Active Metastructures for Light-Weight Vibration Suppression

by

Katherine K. Reichl

A dissertation submitted in partial fulfillment
of the requirements for the degree of
Doctor of Philosophy
(Aerospace Engineering)
in The University of Michigan
2018

Doctoral Committee:

Professor Daniel J. Inman, Chair
Professor Jerome P. Lynch
Professor Henry A. Sodano
Associate Professor Veera Sundararaghavan

Katherine K. Reichl

reichl@umich.edu

ORCiD: 0000-0002-9199-050X

DEDICATION

To my husband, Dan.

ACKNOWLEDGEMENTS

I would like to thank everyone who has contributed to my research and my graduate education. I am sincerely grateful for all the support I have received throughout my five years at the University of Michigan.

First, I would like to thank my advisor Dr. Daniel Inman. He has been a truly supportive advisor through my whole graduate education. He has helped me develop the various skills necessary to become a good researcher. The lessons I have learned from him will help me throughout my career and life. He has always been supportive of my chosen career path and helped me find a faculty position which was a good fit for me.

I would also like to thank my committee for their input into my research and their support throughout my graduate career. I met both Dr. Daniel Inman and Dr. Jerome Lynch at the Los Alamos Dynamics Summer School. My experience meeting with them and others had a significant influence on my decision to pursue graduate school. Dr. Veera Sundararaghavan taught some of my structures courses during my first year in graduate school, and I also got the opportunity to work with him as a graduate student instructor. Dr. Henry Sodano has always been willing to give me a different perspective on how to become a successful researcher.

There have been many friends who have encouraged me throughout this process. Most importantly, the members of the Adaptive Intelligent Multifunctional Structures (AIMS). Not only have I learned a great deal about becoming a good researcher alongside them, but they have also supported me through all the ups and downs of research. Specifically, I would like to thank Alex Pankonien, Cassio Thome de Faria, Jared Hobeck, Brittany Essink, Lawren Gamble, Andrew Lee, Krystal Acosta, and Lori Groo. Also, I would like to thank

previous students of Dr. Daniel Inman who I never had the chance to work with but have always been willing to provide me with advice, specifically Kaitlin Spak, Steven Anton and Ya Wang.

Beyond research, there have been numerous people who have shaped who I have become throughout my graduate program. The Graduate Society of Women Engineers (GradSWE) was a large part of my experience at Michigan, and I would like to thank every woman who has been a part of that organization. Additionally, Kim Elliot, Tiffany Porties, and Andria Rose from the Office of Graduate Education who encouraged and supported the development of my leadership skills.

I also want to thank everyone at Michigan who has provided me with resources to develop my teaching skills and learn about various teaching-focused career paths. A special thanks to Dr. Susan Montgomery for developing the Teaching Engineering class. Also, thanks to all the staff at CRLT and CRLT-Engin for all their hard work developing programs to support graduate student and faculty in their teaching endeavors and also for providing me with numerous opportunities to learn about teaching and practice teaching, in particular, Tershia Pinder-Grover. Lastly, thanks to the student chapter of the American Society for Engineering Education and the Engineering Education Research group for providing additional opportunities to learn about education research.

Thanks to all my friends and family for their tremendous support. My parents have always been my number one supporters as I pursued my passion to become a professor. My sisters, Laura and Sarah, are always a phone call away and are willing to provide a listening ear. A special thanks to my church family through LifePoint Church, iZosh, and GradCru who have encouraged me throughout the years and helped me see how God is using me and my career to make an impact on the world.

Lastly, a very special thanks to my husband, Dan for being by my side for every step of this process. He has supported me in every possible way. He always makes sure I realize the end goal throughout this process and helps me ensure that I am working towards that goal.

This work is supported in part by the US Air Force Office of Scientific Research under the grant number FA9550-14-1-0246 “Electronic Damping in Multifunctional Material Systems” monitored by Dr. BL Lee and in part by the University of Michigan.

TABLE OF CONTENTS

LIST OF TABLES

TABLE

LIST OF FIGURES

FIGURE

LIST OF APPENDICES

APPENDIX

LIST OF ABBREVIATIONS

ADF Anelastic Displacement Fields

DM Digital Materials

DMA Dynamic Mechanical Analyzer

FD Fractional Derivative

FRF Frequency Response Function

GHM Golla-Hughes-McTavish

MFC Macro Fiber Composite

MSE Modal Strain Energy

PPF Positive Position Feedback

TMD Tuned Mass Damper

ABSTRACT

The primary objective of this work is to examine the effectiveness of metastructures for vibration suppression from a weight standpoint. Metastructures, a metamaterial inspired concept, are structures with distributed vibration absorbers. In automotive and aerospace industries, it is critical to have low levels of vibrations while also using lightweight materials. Previous work has shown that metastructures are effective at mitigating vibrations but does not consider the effects of mass.

This work considers mass by comparing a metastructure to a baseline structure of equal mass with no absorbers. The metastructures are characterized by the number of vibration absorbers, the mass ratio, and the natural frequencies of the vibration absorbers. The metastructure and baseline structure are modeled using a lumped mass model and a distributed mass model. The lumped mass model allows for mass and stiffness parameters to be varied independently without the need to consider geometry constraints. The distributed mass model is a more realistic representation of a physical structure and uses relevant material properties. The steady-state and transient time responses of the structure are obtained. The results of these models examine how the performance of the structure varies with respect to the number of vibration absorbers and the mass ratio. Additionally, the stiffness and mass distributions of the vibration absorbers are considered. When the ratio of stiffness over mass varies linearly, the absorbers create broad-band suppression. Overall, these results show it is possible to obtain a favorable vibration response without adding additional mass to the structure.

The distributed vibration absorbers are realized through geometry modifications on the centimeter scale. To obtain the complex geometry needed for these structures, the metas-

tructures are typically manufactured using 3D printers, specifically the Objet Connex 3D printer. To better understand the damping properties of the materials used by the Objet Connex, the viscoelastic properties are characterized. These properties are characterized by measuring the frequency and temperature dependent complex modulus values using a dynamic mechanical analysis (DMA) machine. The material properties are incorporated into the Golla-Hughes-McTavish (GHM) model to capture the damping effect. Using the time-temperature equivalence, the material properties are transformed to various temperatures, allowing the response of the structures to be modeled at various temperatures. A 3D printed metastructure is experimentally tested and compared to the GHM model. These results show the GHM model can accurately predict the natural frequencies of the vibration absorbers.

Lastly, the concept of adding active vibration control to a metastructure to get additional vibration suppression is explored. This is done by attaching piezoelectric materials to the metastructure and utilizing the positive position feedback (PPF) control law to further reduce vibrations. Two active vibration absorber designs are explored; the first uses a stack actuator to control the position of a single absorber and the second design bonds PZT patches in a bimorph cantilevered configuration to the beam of one absorber. This work shows that the active vibration absorber design utilizing a stack actuator is not practical, but the PZT bimorph configuration is capable of further reducing vibrations. Due to the metastructure design, each mode corresponds to the oscillation of a single absorber. When a single vibration absorber is active, the controller can control the corresponding mode. Overall, this shows that integrating active vibration control into a metastructure design can provide additional performance improvements.

CHAPTER I

Introduction

1.1 Motivation and scope of dissertation

In recent years, advances in manufacturing techniques have led to stronger and lighter materials, specifically composite materials. Often, these advances result in structures with less internal damping making vibrations a more critical issue [1]. Additionally, manufacturing techniques allow more complex assemblies to be made as a single part. For example, in jet engines, traditional fans and compressor stages are assembled from a single rotor and multiple blades. The blades are attached to the rotor via a series of dovetail joints. Dovetail joints are formed by two parts interlocking with corresponding notches. With recent advances, the rotor and the blades can be created as a single part eliminating the dovetail joints, known as a blisk or an integrally bladed rotor. Eliminating the dovetail joints is beneficial since they commonly develop cracks. However, this is disadvantageous because the friction within the joints results in higher internal damping of the assembly [2]. These examples show the need for new lightweight vibration suppression solutions.

A traditional method for suppressing vibrations is through the use of a vibration absorber or a tuned mass damper. These devices are tuned to the frequency at which a structure is experiencing high vibrations and can significantly reduce the vibrations at that frequency. These devices are advantageous but can add up to 30% additional mass to the structure. Instead of adding a single large vibration absorber to the structure, this work looks at adding

many small vibration absorbers distributed throughout the structure. The distributed nature of the absorbers allows them to be integrated into the design of the structure. Since there are many absorbers, there are a higher number of parameters to tune producing more desirable results. Structures with distributed vibration absorbers are defined as *metastructures*. The vibration absorbers are realized through geometry modifications on the centimeter scale. Metastructures typically have complex geometry which is most easily manufactured using 3D printers.

3D printing of polymers has made significant developments in recent years leading to a cost-effective and efficient method to create prototypes of structures with complex geometry [3, 4]. In engineering applications, these prototypes are used to verify models which exhibit a certain behavior. The printed material behavior is usually modeled using an elastic model with viscous damping. When polymer materials are used, it is important to consider the viscoelastic effects of these materials, particularly when used in vibration applications and in scenarios where the temperature varies.

This dissertation focuses on using metastructures to determine light-weight vibration suppression solutions, including methods to accurately model the materials commonly used to create prototypes of the structures. Across the literature, a variety of terminology has been used to describe the same concepts presented here. For consistency, the following terminology will be used throughout this dissertation. References to the terms utilized in the original work will also be included. The term metastructure is used to refer to structures with distributed vibration absorbers designed to suppress vibrations. A metastructure is composed of two parts, the vibration absorber system and the host structure. Vibration absorbers consist of a mass and spring whose parameters may be tuned to absorb vibrations at a specific frequency. The absorbers are connected to the host structure which is the main load-bearing component of the structure. The vibration absorber system aims to reduce vibrations in the host structure. Here, higher performance correlates to greater vibration suppression with a focus on the lower frequencies.

While metastructure concepts are widespread in the literature, there has been little in focus on determining what characteristics lead to higher performance and the effects of additional mass on the structure. The primary objective of this dissertation is to investigate light-weight structures with high vibration suppression properties. This is accomplished by examining a simple one-dimensional metastructure which is modeled using various methods. Additionally, the polymer materials used in 3D printers commonly used to create prototypes of metastructure are characterized, and an appropriate model developed to capture the vibration properties. Lastly, the adding active vibration control to a metastructure is explored to determine methods to increase the performance of the metastructures further.

1.2 Proposed design

This dissertation examines one-dimensional metastructures. The aim is to suppress vibrations in the longitudinal direction of the bar. The one-dimensional model was chosen for simplicity. One-directional vibrations are straightforward to model allowing the dynamics to be understood easily. In the future, the same ideas presented here could be applied to bending motion. To provide a basis for performance improvement, the results for each metastructure are compared to a baseline structure. The baseline structure is a comparable structure with no vibration absorbers. The baseline structure is chosen such that it has a similar design to the host structure without the absorbers, and so that the fundamental natural frequencies of the baseline structure and the metastructure are relatively close. All designs have the same mass to isolate the results from the effects of mass. The performance metric used when evaluating the response of these structures is the area under the Frequency Response Function (FRF) and the settling time. A lower area under the FRF corresponds to increased suppression and subsequently higher performance. The settling time is a measure of how quickly the time response of the structure dies out. A lower settling time indicates that the vibrations die out more quickly, which is desired. The performance metrics for the metastructure are compared to that of the baseline structure to calculate a percent change.

All prototypes used in the experimental testing are fabricated using the Objet Connex 3D printer. This printer was chosen for its ability to print multiple materials in a single print job and its ability to print viscoelastic materials. Viscoelastic materials inherently have high damping but are also temperature dependent. To model the viscoelasticity of the materials, the Golla-Hughes-McTavish (GHM) method is used. A Dynamic Mechanical Analyzer (DMA) machine is used to characterize the complex modulus of the materials. Using the characterization results, the viscoelastic metastructure is modeled using the GHM model.

Active vibration control is added to the metastructure design using piezoelectric materials. The piezoelectric materials are added to a vibration absorber to create an active absorber. Two different active absorber designs are considered. The first uses a stack actuator to control the position of a single absorber, and the second design attaches PZT material to the beam of one of the absorbers to create a bimorph configuration. The effects of change the location of the active absorber are explored along with how the design of the metastructure affects the performance.

1.3 Background

This section provides the background on the various technologies used throughout this dissertation. The main focus of this dissertation is on metastructures. Therefore, the beginning of the background section talks about the history of metamaterials and how this work is connected to previous work. The next section goes into detail about the previous work completed on 3D printed materials and how that works fits into the context of metastructures. More detail about the specific 3D printer used in this dissertation is presented. The last background section covers the active vibration control, specifically, control techniques used for structures with piezoelectric actuators and sensors.

1.3.1 Metastructures and metamaterials

Metastructures are a metamaterial inspired concept. Metamaterial research began by investigating electromagnetic metamaterials which exhibited a negative permittivity and or permeability [5, 6]. Inspired by the electromagnetic metamaterials, the concepts were extended to acoustic metamaterials [7]. Traditional metamaterials utilize the theory of Bragg scattering. The lattices are created such that when the waves reflect off the structure, they destructively interfere with each other. For the Bragg scattering mechanism to work, the periodic length of the material must be of a similar length as the wavelength. Thus, for low frequencies very large structures are required [8]. Metamaterials that rely on the Bragg scattering mechanism are commonly called phononic crystals. Phononic crystals are materials which exhibit some periodicity and are reviewed in a paper by Hussein *et al.* [9]. Milton and Willis were the first to conceive the idea of using local absorbers to create structures with a negative effective mass that varies with frequency [10]. Liu *et al.* created the first physical metastructure that was able to create a bandgap at a frequency lower than that of the Bragg scattering mechanism. This structure is designed to suppress acoustic waves above 300 Hz. Their acoustic metamaterial contains lead spheres coated in a silicone rubber within an epoxy matrix. The lead balls in the rubber are referred to as local resonators. The local resonator mechanism is the same mechanism used for vibration suppression [11]. Since then locally resonant metamaterials have been studied extensively for both acoustic and vibration isolation applications. The work presented here deals exclusively with vibration mitigation applications. Structures or materials capable of suppressing vibrations using these local resonators are often referred to as elastic or mechanical metamaterials [12]. In a review paper by Zhu *et al.*, the authors provide a review of various type of plate-type elastic metamaterials and discuss possible applications. They also explain the negative mass density and negative bulk modulus [13]. Here the term metastructure is used to refer to structures with distributed vibration absorbers. These structures use conventional materials with absorbers integrated into the structure through geometry and material changes on the

centimeter scale. The periodic-type nature of these structures was inspired by metamaterials, but the larger scale modifications make the term structure a more fitting term for this work. In the literature, these are also referred to as locally resonant phononic crystals, elastic metamaterials or mechanical metamaterials. The field of auxetics also has considerable overlap with metastructures. Auxetics are materials that exhibit a negative Poisson's ratio. These materials are realized by creating periodic lattice structures. Because of the periodic nature of auxetics, they affect how waves propagate through them and thus can be used for vibration suppression among other applications [14].

As Hussein *et al.* describes in his review paper, metastructures are at the crossroads of vibration and acoustics engineering, and condensed matter physics [9]. Thus, it is crucial that strengths from both fields are considered and reviewed for relevancy. Sun *et al.* and Pai looked into the working mechanism of metastructures for both bending and longitudinal motion. They were able to conclude that the working mechanism that leads to vibration suppression is based on the concept of mechanical vibration absorbers that do not need to be small or closely spaced [15, 16]. Therefore, it is also relevant to explore the literature regarding vibration absorbers. A vibration absorber can also be called a Tuned Mass Damper (TMD) or a dynamic vibration absorber. TMDs typically consist of mass-spring-damper systems, while a vibration absorber does not use a damper to add significant localized damping. Although there is no localized damper added to the vibration absorber, there is still a small amount of material damping which is inherent in all structures. TMDs are studied widely in the field of earthquake engineering. Igusa and Xu were the first researchers to look at the effects of using multiple TMDs to suppress a single mode of a structure [17, 18]. Later, this was also studied by Yamaguchi and Harnprnchai [19]. Their work focuses on attaching multiple TMDs to a single degree of freedom system and shows that multiple TMDs can be more effective than a single TMD. These results can be leveraged in metastructure research.

Another important aspect of the TMD literature is how the optimal parameters for the

TMDs were determined. Many methods have been used and applied to various systems. DenHartog developed the optimal parameters for a single TMD as an analytical expression [20] and this result has since been studied by many others as summarized in Sun *et al.*s review paper [21]. The work presented here focuses on some of the numerical methods utilized by many TMD researchers specifically the H_2 norm. Parameters are chosen such that the H_2 norm is minimized. This performance metric describes the response of a structure excited across all frequencies [22, 23]. The H_2 norm provides different results than those obtained by suppressing a specific frequency range and tend to suppress the fundamental mode which typically has the largest magnitude response.

The model used in this paper is a one-dimensional lumped mass model, which was chosen for its simplicity, and allows the dynamics to be understood more thoroughly. Some of the most relevant work related to 1D metastructures is from Pai who models a longitudinal metastructure consisting of a hollow tube with many small mass-spring systems distributed throughout the bar. He suggests that the ideal design for a metastructure involves absorbers with varying tuned frequencies [16]. Xiao *et al.* looks at a similar structure as Pai but considers multiple degree of freedom resonators. Their work focuses on modeling procedures and understanding the bandgap formation mechanisms [24]. Banerjee *et al.* examines a frequency graded 1D metamaterial, using a similar model to this work using a mass-in-mass mechanical model. The mass-in-mass model is similar to the lumped mass model used in this work but assumes an infinite structure during the analysis [25]. The favorable dynamics response of these structures can also be described as having a negative effective mass which has been shown analytically and experimentally [10, 26, 27]. In addition, other researchers have conducted experiments on longitudinal metastructures. Zhu *et al.* looked at a thin plate with cantilever absorbers cut out of the plate. They were able to show the ability to accurately predict the band-gap and also compared various absorber designs [28]. Wang *et al.* tested a glass bar with cantilever absorbers made out of steel slices and a mass [29]. With the rise in additive manufacturing, 3D printing has become a good method to realize

the complex geometry needed for these structures [30]. Hobeck *et al.* and Nobrega *et al.* both created longitudinal 3D metastructures and obtained experimental results [31, 32].

The work of Igusa and Xu is similar to the work presented here, but there are some important differences. They are comparing the effectiveness of a single TMD and multiple TMDs whereas this work compares multiple vibration absorbers to no absorbers. Thus their structure with vibration suppression is heavier than their structure without suppression. In this work, the suppression system does not add weight to the structure. Additionally, Igusa and Xu use TMDs so they can tune the mass, stiffness and damping of each absorber [18]. The work presented here does not add dampers with high levels of localized damping to the vibration absorbers, thus only mass and stiffness can be tuned.

1.3.2 3D printing

3D printing of polymers has made significant developments in recent years leading to a cost-effective and efficient method to create prototypes of structures with complex geometry [3, 4]. Over the recent years, research has looked at modeling and improving the printing process [33, 34] and the effects of varying printing parameters on the material properties of the printed materials [35]. In engineering applications, these prototypes are used to verify models which exhibit a certain behavior. Structures with complex geometry and are most easily manufactured via 3D printing. In metastructure and metamaterial applications, the printed material is typically modeled using an elastic model with viscous damping. When polymer materials are used, it is important to consider the viscoelastic effects of these materials, particularly when used in scenarios where there are vibrations and when the temperature varies. Of these papers studying the material properties, the dynamic modulus of the printed materials has only been explored a few times [36, 37] and even fewer papers have used the dynamic modulus data to model the dynamic response of the resulting structure [38]. Additionally, vibration suppression systems are required to function across a range of temperatures, yet the literature ignores the effects of temperature on printed

materials.

1.3.2.1 Objet Connex printer

This work will focus on a single 3D printer which has frequently been used in the area of vibration suppression [30, 39, 40, 41, 42] and known to exhibit viscoelastic behavior [37, 43, 38]. The 3D printer being investigated in this work is the Objet Connex printer by Stratasys. This printer is capable of printing rubber-like and stiff materials. These materials exhibit viscoelastic properties [44]. The Object Connex printer uses PolyJet printing technology which works like an inkjet printer. The parts are made by depositing many small dots of material and then curing the resin resulting in a printed material that appears homogeneous. Because of the digital nature of this method, these materials are referred to as Digital Materials (DM). This approach allows the printer to easily mix two different base materials in various ratios to create a gradient of materials with multiple hardness levels [45]. Additionally, this method also allows for parts made in a single print with both rigid and viscoelastic components. Using this technique and the many base materials available, the Object Connex printer can create many combinations with varying properties. For this paper, the focus will be on the digital materials created using the two base materials, VeroWhitePlus^{TM} and TangoPlus^{TM}. VeroWhitePlus^{TM} is a rigid opaque material and TangoPlus^{TM} is a rubber-like transparent material [46]. Using these two base materials, the printer can print ten different digital materials [47]. In the field of active composites and origami, Qi *et al.* has done extensive work using the Objet Connex 3D printer, and his papers provide many details the actual mechanisms the 3D printer utilizes [37, 48, 49, 50].

1.3.3 Viscoelastic materials

Viscoelastic materials are a common method for adding vibration damping to structures. Many materials exhibit viscoelastic behavior such rubbers, adhesives, and plastics [44]. A typical application method is constrained layer damping where a layer of viscoelastic ma-

terial is added to a structure, and a stiffer material is attached to the top [51, 52]. When subjected to oscillatory motion, the response of viscoelastic material has a phase lag, leading to hysteresis which causes energy dissipation. Due to the phase lag of the response, the ratio of stress, $\sigma(t)$, over strain, $\varepsilon(t)$, leads to a complex number, known as the complex modulus, $G^{\star}(\omega)$, which is a frequency dependent value

$$\frac{\sigma(t)}{\varepsilon(t)} = G^{\star}(\omega) = G'(\omega) + \jmath G''(\omega) = G'(\omega)[1 - \mu(\omega)] \tag{1.1}$$

where $G'(\omega)$ is the strong modulus, $G''(\omega)$ is the loss modulus, and $\mu(\omega)$ is the loss factor. Viscoelastic materials are known to have both frequency and temperature dependent material properties [53, 54]. The complex modulus can also be written in the Laplace domain as $s\tilde{G}(s)$ and is referred to as the material dissipation function.

1.3.3.1 Modeling of viscoelastic materials

There is a range of modeling methods that can be used to model the viscoelasticity of materials. The usefulness of the models depends on the application and the desired accuracy. The classic viscoelastic models are the Maxwell and Kelvin-Voigt models. For these models, the materials are represented as series of spring and dashpots. These models are not applicable over a wide range of frequencies thus are not useful for vibration applications [55].

For vibration applications, the Modal Strain Energy (MSE) method is widely used [56, 57]. The MSE energy method is easy to implement but is only applicable at a single frequency [58]. To capture the effects of the frequency variance, a class of modeling methods known as internal variable methods has been developed. These methods approximate the material dissipation function over a range of frequencies. There are three commonly used interval variable methods. The Fractional Derivative (FD) model was developed by Bagley and Torvik in 1983 and closely fits experimental data over an extensive frequency range. The FD model approximates the material dissipation function as

$$s\tilde{G}(s) = \frac{G_0 + G_1 s^{\alpha}}{1 + bs^{\beta}} \tag{1.2}$$

where G_0, G_1, b, α, and β are all parameters used to curve fit experimental data of the material dissipation to the approximation [59, 60]. The Anelastic Displacement Fields (ADF) model was developed by Lesieutre and Mingori in 1990 and approximates the material dissipation function as

$$s\tilde{G}(s) = G_0 \left[1 + \sum_{j=1}^{n} \Delta_j \frac{s}{\omega^2 + \Omega_k^2} \right] \tag{1.3}$$

where G, E_k, and b_k are parameters used to curve fit the experimental data and n is the number of terms used in the approximation [61]. The last internal variable method is the GHM model developed by Golla and Hughes in 1985 and expanded upon by McTavish and Hughes in 1987 [62, 63]. The GHM model is used to model viscoelastic materials in this dissertation. The material dissipation function is approximated as

$$s\tilde{G}(s) = G^{\infty} \left[1 + \sum_{j=1}^{n} \hat{\alpha}_j \frac{s^2 + 2\hat{\zeta}_j \hat{\omega}_j s}{s^2 + 2\hat{\zeta}_j \hat{\omega}_j s + \hat{\omega}_j^2} \right] \tag{1.4}$$

where G^{∞}, $\hat{\alpha}_j$, $\hat{\zeta}_j$ and $\hat{\omega}_j$ are the parameters of the model [62].

Since the original GHM model was published, many researchers have made developments using the GHM model. Inman extended the model to be used with distributed parameters [64]. Friswell *et al.* created a reduced parameter model [65]. Friswell and Inman developed a method for creating a reduced order GHM model [66]. Lam *et al.* used the GHM method to model active constrained layer damping [67]. de Lima provides a nice overview of all of the internal variable methods and describes how they can be incorporated into finite element models [68].

1.3.3.2 Characterizing viscoelastic materials

To use the internal variable methods described in the previous section, the approximation of the material dissipation function must be curve-fit to experimental data. The book by Jones describes different methods to obtain this experimental data [44]. Additionally, Vasques *et al.* also provides a nice review [69]. The dynamic modulus of a material must be obtained experimentally at various frequencies. There are two ways to accomplish this. The first method is by applying an excitation force at varying frequencies and measuring the magnitude and phase of the response. This is typically accomplished using DMA machine according to ASTM standards D5026 and D5418 [70, 71]. The second method involves measuring the natural frequency and damping in some simple structure such as a cantilevered beam. Using the geometric dimensions of the sample, the dynamic modulus can be calculated. If multiple natural frequencies are measured, then the dynamic modulus can be found at multiple frequencies. This method is outlined in ASTM standard E756 [72]. Using both of these methods, only a limited range of frequencies are feasible for these testing methods. In order get the modulus values over a larger range, the time-temperature superposition method is utilized. The same procedure outlined above is performed at multiple temperatures. A relationship between the frequency and temperature is determined experimentally. Using this relationship, the values at various temperatures can be expressed at a single temperature but over a wide frequency range [44]. Once the complex modulus data is determined for a single temperature over the application frequency range, the GHM material dissipation function is evaluated along the imaginary axis ($s = \jmath\omega$) and curve fit to the experimental data [62].

1.3.4 Active vibration control

Active vibration control is a common method to suppress vibration is structures and has been utilized by many researchers [73, 74]. Instead of simply taking an active approach, this work looks at integrating active and passive vibration control into a single structure.

Other researchers have implemented active control in conjunction with viscoelastic materials [75, 76, 77]. This work looks at specifically implementing active vibration control into metastructures. Much work has been completed in the field of active metamaterials [78, 79, 80, 81, 82, 83], similar to Section 1.3.1 the focus of these metamaterials is typically on higher frequency vibrations. The focus of this work is on the fundamental mode of the structure and therefore lower frequencies. In addition to using metastructure for vibration suppression, other research has also investigated using metastructures for simultaneous energy harvesting and vibration suppression [84, 85, 86]. These works integrate active elements into a metastructure design but do not have a focus on active vibration control.

The specific control law utilized in this work is the Positive Position Feedback (PPF) which was originally proposed by Goh and Caughey [87]. This control law is easy to implement in vibration control scenarios and can be based on an experimental FRF [73]. The PPF control law has effectively reduced vibrations in many scenarios [76, 88, 89].

The active vibration control in this work will be implemented using piezoelectric materials. When a voltage is applied to a piezoelectric material, the material produces a strain. Additionally, the converse effect also occurs; if the piezoelectric material strains, a voltage is produced [90]. Because of these properties, piezoelectric materials can be used as both actuators and sensors in control scenarios. Leo provides specific information on how to use piezoelectric materials for active vibration control [91]. A single piezoelectric element can be used simultaneously as a sensor and an actuator; this is called self-sensing or collocated control. Dosch *et al.* and Jones *et al.* provide details about how this can be implemented [92, 93].

1.4 Outline of dissertation

This dissertation is divided into six chapters. This first chapter provides motivation, defines the scope of the dissertation and provides a literature review of the various concepts covered in this dissertation.

Chapter II introduces the lumped mass metastructure model which is used to determine the feasibility of a mass-conserved metastructure. This simple model allows the various parameters of the system to quickly be modified and integrated into an optimization scheme. The lumped mass model is characterized by the mass and stiffness of the various components. These lumped parameters are influenced by a geometric design, but there is no geometry of material properties associated with the model.

Chapter III examines the viscoelastic properties of materials printed on the Objet Connex 3D printer. This work steams from the need to have a more accurate model of the 3D printed materials used to print prototypes of the metastructure. The GHM model is used to model the viscoelastic properties of the 3D printed material. This model is also able to capture the effects of temperature on the structures. Experimental verification of the GHM model using a simple cantilevered beam is performed at various temperatures.

Chapter IV expands the concepts learned from the lumped mass model in the previous chapter and applies them to a realistic distributed mass model. The distributed mass model utilizes realistic geometry and viscoelastic material properties to model the response of the metastructure. A design methodology for design the distributed mass metastructures is presented. The metastructure GHM model is also experimentally verified.

Chapter V implements active vibration control methods into a metastructure model. The chapter starts by looking at a lumped mass model to determine the general trends that the addition of active vibration control can provide to the structure using the PPF control law. Next, the concepts are extended to a distributed mass model and piezoelectric materials are used to create an active vibration absorber. The effects of varying the position of the active absorber are explored along with examining how well different metastructure designs can be controlled.

Lastly, the conclusion provides a summary of the work complemented in this dissertation. The contributions of this work on the fields of vibration suppression and 3D printing are also stated.

CHAPTER II

Mass-Conserved Lumped Mass Metastructure

This work begins by examining a one-dimensional lumped mass model, chosen for its simplicity. The one-dimensional nature of this model allows the dynamics to be understood more thoroughly. The metastructure models used in this chapter are compared to a baseline structure of equal mass but with no distributed vibration absorbers. The mass-conserved constraint implies that any increase in performance can be attributed to the addition of the absorbers and not due to additional mass. The methodology used for this chapter begins by introducing the model used and the parameter characterizing this model. The main parameters varied throughout this study are the number of absorbers, the mass ratio, the natural frequencies of the individual absorbers, and the mass distributions of vibration absorbers. Other variables in the model are calculated such that the mass of the structure is constant and the fundamental frequency of the entire structure stays relatively constant throughout the analysis. Both steady state and transient responses are examined. A performance measure is introduced, namely the H_2 norm, which measures the total energy of the system. An optimization procedure is used to minimize H_2 norm. Various forms of the optimization procedure are used to highlight the trade-offs between the various parameters. The effects of the mass ration, the number of vibration absorbers and the distribution of the mass and stiffness values of the vibration absorbers are examines. The last part of this chapter compares the performance of the metastructure to a structure with a tuned mass damper (TMD) attached

to the tip of the structure. The TMD damper is a common vibration suppression method making it a nice comparison to better quantify the performance of the metastructure.

2.1 Description of lumped mass models

The design of the lumped mass model was chosen to behave similarly to an one-dimensional axial bar but with vibration absorbers distributed throughout the length of the bar. The metastructure bar lumped mass model is shown in Figure 2.1(a). This model consists of masses and springs connected in series. Since this is a one dimensional model, all the deformation occurs in the horizontal direction. The model consist of two parts, the host structure and the vibration absorbers. The larger masses and springs make up the host structure while the smaller masses and springs represent the vibration absorbers. Small deformation is desired in the host structure. To provide a basis for performance improvement, the results for the metastructure are compared to a baseline structure. A simple uniform bar is utilized as the baseline structure and is modeled as mass and springs connected in series, seen in Figure 2.1(b). The baseline structure and the metastructure have the same mass, which shows that better performance from the metastructure is due to the addition of the absorbers and not from the additional mass. Throughout this chapter, the bars and absorbers are modeled as lumped mass systems so the dynamics of the system are easily understood and computational time is small.

The design of these structures was chosen such that the dynamics of structures will be comparable between the metastructure and the baseline structure. Most importantly, they will have fundamental natural frequencies near each other. The metastructure is characterized by the number of absorbers it has, denoted n. Therefore, $n+1$ masses make up the host structure. All masses in the host structure, except the far right mass, have a small absorber connected to it, modeled as a mass and spring. The larger masses will be referred to as the host masses since these make up the host structure whereas the smaller masses are called the absorber masses. The host masses all have the same mass to represent a uniform bar but

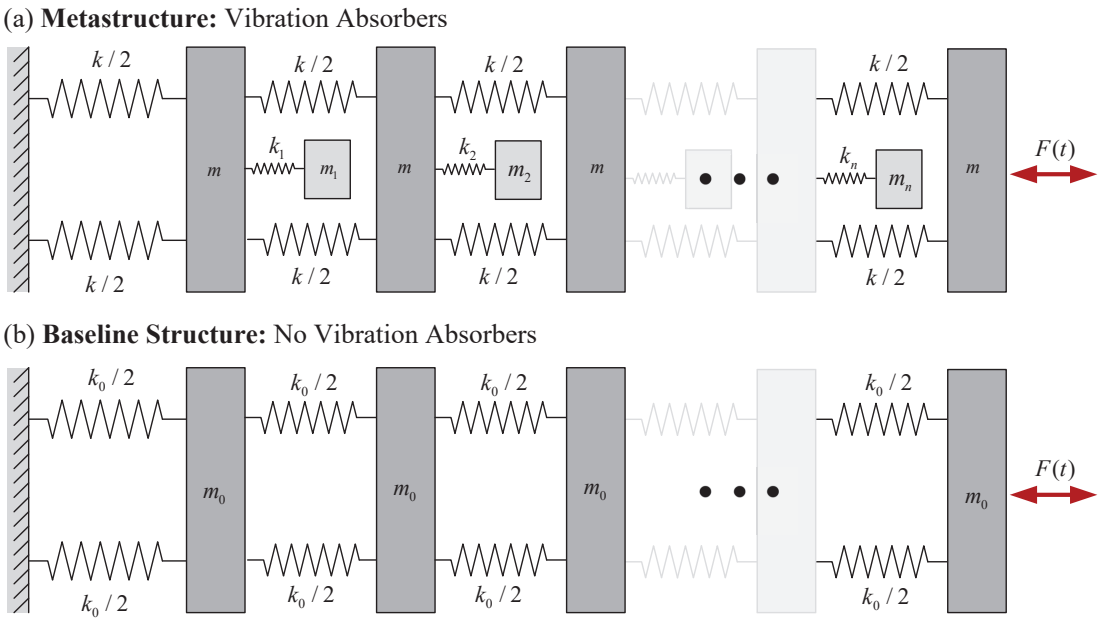

Figure 2.1: Lumped mass models of (a) the metastructure and (b) the baseline structure

the mass of the absorbers is allowed to vary throughout the structure. These masses have values of m and m_i respectively where the i refers to the ith absorber mass from the left and ranges from 1 to n. The springs connecting the host masses are called the host springs and are denoted k. The mass ratio, μ is the ratio of the mass of the absorber system to the mass of the entire structure, and is calculated by

$$\mu = \frac{\sum_{i=1}^{n} m_i}{m_{\text{total}}} = \frac{\sum_{i=1}^{n} m_i}{(n+1)m + \sum_{i=1}^{n} m_i} \tag{2.1}$$

The baseline structure has the same number of masses at the host structure, $N = n + 1$. The mass of each one of these masses, m_0 is calculated by taking the total mass of the metastructure divided by the number of masses. The springs in the baseline structure have the same stiffness as the host springs in the metastructure. For all simulations, structural damping is utilized to approximate the total material damping in the structure.

Table 2.1: Continuous bar parameters

Property	**Values**
Young's Modulus, E	1970 MPa
Density, ρ	1.168 g cm^{-3}
Length, ℓ	0.45 m
Cross Sectional Area, A	9.00 cm^2
Total Mass, m_{total}	597 g

2.1.1 Model parameters

In this section the specific parameters for both the baseline structure and the metastructure are described. The baseline structure is fully characterized by the number of vibration absorbers. The metastructure is also characterized by the number of vibration absorbers, but the mass ratio, μ and the distributions of the mass and stiffness of the vibration absorbers also effect the dynamics of the structure. This chapter begins by characterizing the baseline model then explains the metastructure used for the most general metastructure model, and lastly goes into detail showing the various constraints that can be placed on the vibration absorber mass and stiffness distributions. For ease of comparison, the fundamental natural frequencies of the baseline structure and metastructure should be approximately equal. In order to achieve relatively constant fundamental frequencies, the mass and stiffness values are chosen based on a continuous uniform fixed-free bar with a rectangular cross section and parameters shown in Table 2.1.

2.1.1.1 Baseline structure parameters

A finite element type approach is used to obtain m and k. This approach results in a relatively constant natural frequency for varying degrees of freedom. The uniform fixed-free bar of length ℓ is discretized into n elements so that the length of each element, ℓ_{element} is calculated as $\ell_{\text{element}} = \ell/n$. The mass and springs values are calculated for the baseline structure as

$$k_0 = \frac{EAn}{\ell} \tag{2.2a}$$

$$m_0 = \frac{m_{\text{total}}}{n+1} \tag{2.2b}$$

where k_0 and m_0 represent the stiffness and mass values for the baseline structure from Figure 2.1, and m_{total}, E, A, and ℓ are defined in Table 2.1. These values fully define the lumped mass baseline structure model.

2.1.1.2 Metastructure parameters

For the lumped mass metastructure model, the value of the host spring stiffness equals the stiffness from the spring in the baseline structure. The mass of the host mass must change in order to keep the mass constant between the two models and can be calculated using the the mass ratio, μ.

$$k = k_0 \tag{2.3a}$$

$$m = (1-\mu)\frac{m_{\text{total}}}{n+1} \tag{2.3b}$$

where k and m are the values of the host mass and host stiffness as shown in Figure 2.1. Once again to ensure the mass is conserved between the baseline structure and the metastructure, the masses of the absorber masses must satisfy the following equation.

$$\sum_{i=1}^{n} m_i = \mu m_{\text{total}} \tag{2.4}$$

The values of the vibration absorber spring constants are calculated based on the desired frequency of the absorbers. All the absorbers can be tuned to a single frequency or each one can be tuned to a unique frequency, ω_i

$$\omega_i = \sqrt{\frac{k_i}{m_i}} \tag{2.5}$$

These equations provide the most general case of parameters for the metastructure.

2.1.1.3 Distribution simplifications for vibration absorber mass and stiffness

In this section, various constraints are set for the vibration absorber mass and stiffness values. These constraints are used in the simulations through the rest of this chapter. These simplify the problem to varying degrees and allow various trends to be observed. The distributions of both the absorber masses and the absorber stiffness are modified. The most restrictive case, constrains all the vibration absorbers to have to same mass and stiffness values resulting in the natural frequencies of all the vibration absorbers to be the same. Relaxing the constraints on the stiffness distribution, the stiffness values are allowed to vary in a quadratic sense, resulting in linearly varying natural frequencies for the vibration absorbers. The mass distribution of the vibration absorbers can also be allowed be allowed to varying linearly. Lastly, the least restrictive configuration puts no restrictions on the distributions of the mass or stiffness of the vibration absorbers.

For the constant absorber mass the mass of each vibration absorber is constrained to be constant throughout the length of the bar. For these cases, the mass of the vibration absorbers can be calculated directly using the mass ratio, μ as

$$m_i = \mu \frac{m_{\text{total}}}{n} \tag{2.6}$$

When the vibration absorber stiffness is also constrained to be constant, the stiffness value can be calculated based on the desired frequency of the vibration absorbers, ω as

$$k_i = m_i \omega^2 = \mu \frac{m_{\text{total}}}{n} \omega^2 \tag{2.7}$$

The constant absorber mass constraint can be relaxed and the masses can be allowed to varying linearly throughout the length of the beam. The amount of variation allowed is represented by a percentage change in mass, Δm. The distribution is constrained such that

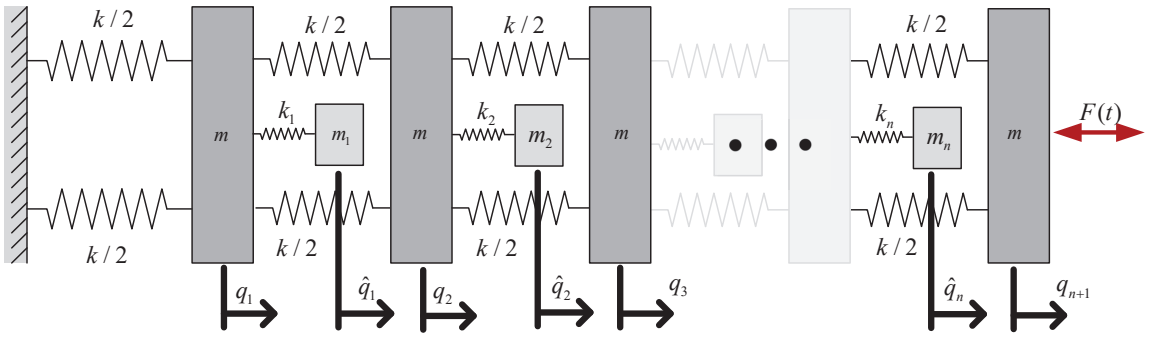

Figure 2.2: Definition of mass displacements

the sum of the absorber masses still meets the requirements of Equation 2.4.

$$m_{\min} = (1 - \Delta m)\mu \frac{m_{\text{total}}}{n} \tag{2.8a}$$

$$m_{\max} = (1 + \Delta m)\mu \frac{m_{\text{total}}}{n} \tag{2.8b}$$

$$m_i = \begin{bmatrix} m_{\min} & \cdots & m_{\max} \end{bmatrix} \in \mathbb{R}^{(1\times n)} \tag{2.8c}$$

Other simulations restrict the natural frequencies of the vibration absorbers to vary linearly. This range is defined using the minimum and maximum frequencies, $\omega_{\min}$ and $\omega_{\max}$. From these defined parameters, the individual spring constants, k_i can be calculated as

$$\Delta\omega = \frac{\omega_{\max} - \omega_{\min}}{n - 1} \tag{2.9a}$$

$$k_i = m_i[\omega_{\max} - \Delta\omega(i - 1)]^2 \tag{2.9b}$$

2.1.2 Development of mass, stiffness and damping matrices

Next, the model is assembled into mass, stiffness and damping matrices. The displacements of the masses are defined in Figure 2.2. In formulas, the hat refers to displacements of the absorber masses and the subscript refers the absorber number. The individual displacements are arranged into vectors as

$$\mathbf{q}_0 = \begin{bmatrix} q_1^0 & q_2^0 & \dots & q_n^0 & q_{n+1}^0 \end{bmatrix}^{\mathrm{T}} \in \mathbb{R}^{(n+1)\times 1} \tag{2.10a}$$

$$\mathbf{q}_0 = \begin{bmatrix} q_1 & q_2 & \dots & q_n & q_{n+1} & \hat{q}_1 & \hat{q}_2 & \dots & \hat{q}_n \end{bmatrix}^{\mathrm{T}} \in \mathbb{R}^{(2n+1)\times 1} \tag{2.10b}$$

where the 0 superscript refers to the displacements of the baseline structure masses. Since the structure is a lumped mass model, all the masses are arranged on the diagonal of the global mass matrix. The mass matrices are arranged as

$$\mathbf{M}_0 = \mathrm{diag}(\begin{bmatrix} m_0 & \cdots & m_0 \end{bmatrix}) \in \mathbb{R}^{(n+1)\times(n+1)} \tag{2.11a}$$

$$\mathbf{M}_0 = \mathrm{diag}(\begin{bmatrix} m & \cdots & m & m_1 & \cdots & m_n \end{bmatrix}) \in \mathbb{R}^{(2n+1)\times(2n+1)} \tag{2.11b}$$

where diag$(\cdot)$ indicates a square matrix with the vector components arranged on the diagonal of the matrix. The stiffness matrices are arranged as follows

$$\mathbf{K}_0 = \begin{bmatrix} 2k & -k & -k & \cdots & 0 & 0 & 0 \\ -k & 2k & -k & \cdots & 0 & 0 & 0 \\ 0 & -k & 2k & \cdots & 0 & 0 & 0 \\ \vdots & \vdots & \vdots & \ddots & \vdots & \vdots & \vdots \\ 0 & 0 & 0 & \cdots & 2k & -k & 0 \\ 0 & 0 & 0 & \cdots & -k & 2k & -k \\ 0 & 0 & 0 & \cdots & 0 & -k & k \end{bmatrix} \in \mathbb{R}^{(n+1)\times(n+1)} \tag{2.12a}$$

$$\mathbf{K} = \begin{bmatrix} & & -\mathbf{V} \\ \mathbf{K}_0 + \mathbf{V}_{\text{aug}} & & \mathbf{0} \\ & & \\ -\mathbf{V} & \mathbf{0} & \mathbf{V} \end{bmatrix} \in \mathbb{R}^{(2n+1)\times(2n+1)} \tag{2.12b}$$

$$\mathbf{V} = \text{diag}([\ k_1 \quad k_2 \quad \cdots \quad k_n\ ]) \in \mathbb{R}^{n\times n} \tag{2.12c}$$

$$\mathbf{V}_{\text{aug}} = \text{diag}([\ k_1 \quad k_2 \quad \cdots \quad k_n \quad 0\ ]) \in \mathbb{R}^{(n+1)\times(n+1)} \tag{2.12d}$$

$$\mathbf{0} = [\ 0 \quad \cdots \quad 0\ ]^{\text{T}} \in \mathbb{R}^{n+1} \tag{2.12e}$$

For this model, no dampers are added to the system but since all structures have material damping inherent in them this must be modeled. This damping does not change the dynamics of the system; it simply prevents the simulations from tending to infinity. A proportional damping model is utilized choosing an arbitrary damping constant, α and defining the damping matrices by

$$\mathbf{D} = \alpha\mathbf{K} \tag{2.13a}$$

$$\mathbf{D}_0 = \alpha\mathbf{K}_0 \tag{2.13b}$$

Note that proportionality to the mass matrix, commonly used, is not used here because of the recent result of Kabe and Sako [94]. Results are presented as a pair of plots: the FRF and the impulse response. Each plot shows the baseline structure with no absorbers as a dotted line and the structure with absorbers as a solid line. The FRF is of the far right main mass subjected to an input force, *i.e.* $|[Q^0_{n+1}(s)]/[F_{n+1}(s)]|$. The impulse response function is also calculated by applying a unit impulse to the same mass. As a quantitative measure, the percent decrease of the H_2 norm is also reported. This norm is explained in more detail in the next section.

2.2 Performance measure

This section describes the performance measure used to determine how effectively the structure suppresses vibrations. Here the H_2 will be utilized, which is widely used in control literature to develop optimal control theory. The H_2 norm is related to the total energy in the system. To begin, the system must be transformed into state space. The equations of motion for the structure are

$$\mathbf{M}\ddot{\mathbf{q}} + \mathbf{D}\dot{\mathbf{q}} + \mathbf{K}\mathbf{q} = \mathbf{F} \tag{2.14}$$

where $\mathbf{M}$, $\mathbf{D}$ and $\mathbf{K}$ are the mass, damping and stiffness matrices defined in the previous section, $\mathbf{F}$ is the force vector, and $\mathbf{q}$ are the displacements of the lumped mass. The force vector, F is taken to have a unit value. The corresponding state space matrices are

$$\mathbf{A} = \begin{bmatrix} \mathbf{0} & \mathbf{I} \\ -\mathbf{M}^{-1}\mathbf{K} & -\mathbf{M}^{-1}\mathbf{D} \end{bmatrix} \tag{2.15a}$$

$$\mathbf{B} = \begin{bmatrix} \mathbf{0} \\ \mathbf{M}^{-1}\mathbf{F} \end{bmatrix} \tag{2.15b}$$

$$\mathbf{C} = \begin{bmatrix} \mathbf{I} & \mathbf{0} \end{bmatrix} \tag{2.15c}$$

These can be used to express a transfer function matrix

$$\mathbf{H}(s) = \mathbf{C}(s\mathbf{I} - \mathbf{A})^{-1}\mathbf{B} \tag{2.16}$$

This results in a transfer function matrix, $\mathbf{H}(s)$, which has dimensions $m \times m$ and contains complex numbers, where m is the total number of degrees of freedom in the system. For the baseline structure, $m = n + 1$ and for the metastructure, $m = 2n + 1$. The specific entries of this matrix can be named as

$$\mathbf{H}(s) = \begin{bmatrix} H_{11}(s) & \cdots & H_{1m}(s) \\ \vdots & \ddots & \vdots \\ H_{m1}(s) & \cdots & H_{mm}(s) \end{bmatrix} \tag{2.17}$$

The term of interest to this paper is the $H_{NN}(s)$ entry which describes the relationship between an input at the tip and the response of the tip, where $N = n + 1$. For convenience the following definition is utilized, $H_{NN}(s) = G(s)$. The H_2 norm is a measure of the total vibration energy of the system over all frequencies and can be calculated by taking the norm of frequency response function as follows

$$H_2 = \|G(s)\|_2^2 = \frac{1}{2\pi} \int_{-\infty}^{\infty} \mathrm{tr}[G^\star(\jmath\omega) G(\jmath\omega)] \mathrm{d}\omega \tag{2.18}$$

where the star indicates the complex conjugate of the number. This performance measure is also related to the impulse response function by Parsevals theorem

$$\|G(s)\|_2^2 = \|H(t)\|_2^2 = \int_0^{\infty} \mathbf{h}(t) \mathbf{h}^{\mathrm{T}}(t) \mathrm{d}t \tag{2.19}$$

where $\mathbf{h}(t)$ is the impulse response function defined as

$$\mathbf{h}(t) = \mathbf{C} e^{\mathbf{A}t} \mathbf{B} \tag{2.20}$$

The norms of the metastructure and the baseline structure are compared and presented as a percent decrease in the following section defined as

$$H_2 \text{ percent decrease} = \frac{|(H_2)_{\text{baseline}} - (H_2)_{\text{metastructure}}|}{(H_2)_{\text{baseline}}} \times 100 \tag{2.21}$$

where $(H_2)_{\text{metastructure}}$ is the H_2 norm calculated for the metastructure and $(H_2)_{\text{baseline}}$ is the norm of the baseline structure calculated in the same manner as for the metastructure but with the $\mathbf{M}_0$, $\mathbf{D}_0$ and $\mathbf{K}_0$ matrices replacing the $\mathbf{M}$, $\mathbf{D}$ and $\mathbf{K}$ matrices in Equation 2.14.

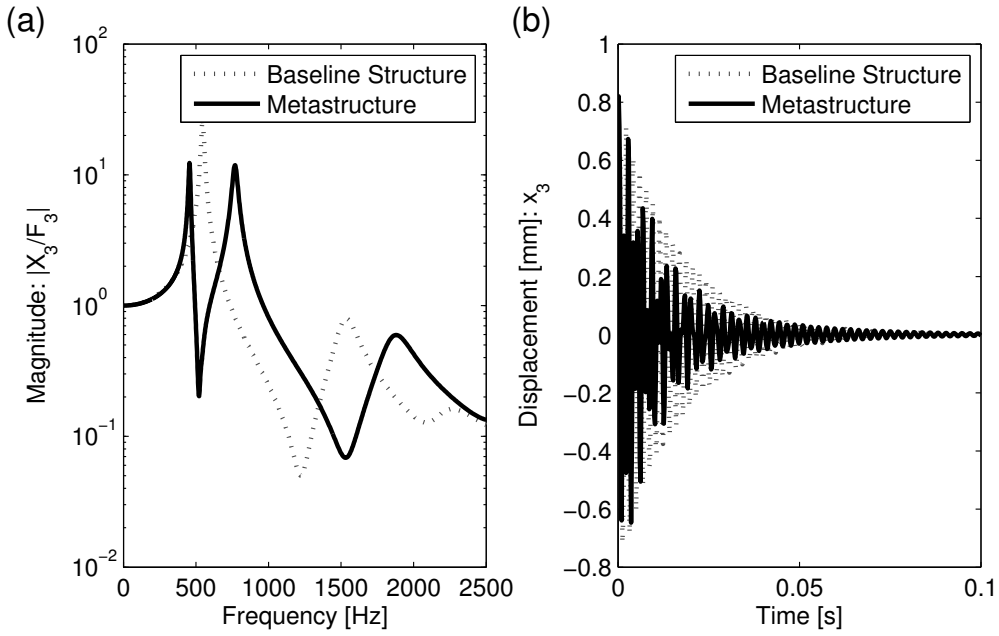

Figure 2.3: (a) FRF and (b) the impulse response of a structure with 2 absorbers tuned to the same frequency

A larger percent decrease represents better performance.

2.3 Initial simulation results

Initially, a metastructure model with three main masses, two absorbers, and a mass ratio of $\mu = 0.3$ is examined. The corresponding baseline structure has a fundamental natural frequency of 546 Hz. The two absorbers in the metastructure are tuned to that same frequency, 546 Hz. Using Equations 2.6 and 2.7, m_1 and k_1 are calculated.

The results of this simulation are shown in Figure 2.3. The FRF on the left clearly shows that the natural frequency peak of the baseline model gets split into two slightly smaller peaks. If the metastructure system is excited around 546 Hz the response will be minimal but deviation from that excitation frequency will cause in increase in response. This correlates to a 26.3% decrease in the H_2 norm. Looking at the impulse response plot on the right, it is clear that overall, the response of the structure with the absorbers has smaller amplitudes.

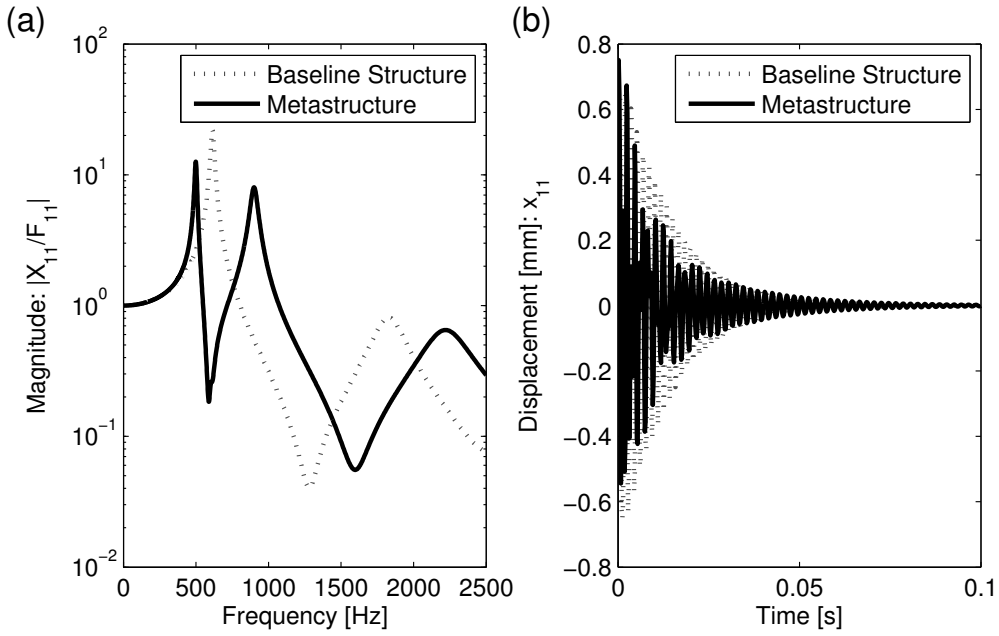

Figure 2.4: (a) FRF and (b) impulse response of structure with 10 absorbers with constant frequency

The next set of results looks at a system with 10 absorbers. Once again, all the absorbers are tuned to a natural frequency that is equal to the fundamental natural frequency of the baseline structure, which is at 614 Hz for this system. This system produces very similar results to the previous system. The H_2 decrease is slightly larger at 28.2%, but overall the trends look the same. This indicates that if all the absorbers are tuned to the same natural frequency, increasing the number of absorbers does not greatly affect the response of the system.

Simply increasing the number of absorbers while keeping the natural frequency the same for all absorbers does not make a significant impact, but it does allow for greater flexibility in the tuning of the parameters. From the previous results, the frequency at which the absorbers were tuned causes a dip in the FRF at that frequency. Instead of setting all the absorbers to a single frequency and getting one large dip, the next case tunes the absorbers to varying frequencies ranging from 350 to 950 Hz in an effort to smooth out the peak instead of simply splitting the peak. The results displayed in Figure 2.5 show that this produces

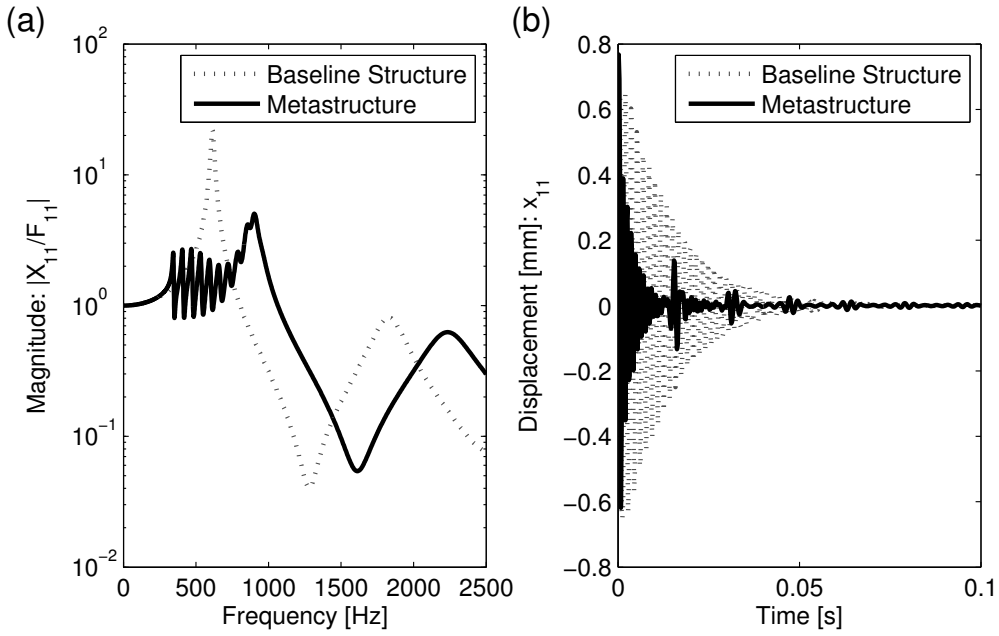

Figure 2.5: (a) FRF and (b) impulse response of a structure with 10 absorbers with linearly varying frequencies

favorable results. The peak is smoothed out and the H_2 norm has a decrease of 49.9%. In the impulse response function, the magnitude of the vibrations is also greatly reduced. Towards the end of the impulse response, beating phenomenon becomes apparent. Beating behavior occurs when there are closely spaced natural frequencies causing the amplitude of the impulse response to increase for a short period of time. Even with the increased levels due to beating, the displacement levels remain below the baseline model. In a zoomed version of the FRF, shown in Figure 2.6, the closely spaced peaks are visible. The inverse of difference between the peaks corresponds to the time period of the beat seen in the time response.

2.4 Optimization procedure

Next, an optimized version of this model is examined using a similar procedure to that of Zuo and Nayfeh, who applied their methods to multiple degree of freedom tuned mass dampers [23]. Zuo and Nayfeh optimized their model by minimizing the H_2 norm. A similar approach is taken in this model, but will maximize the percent decrease in the H_2 norm from

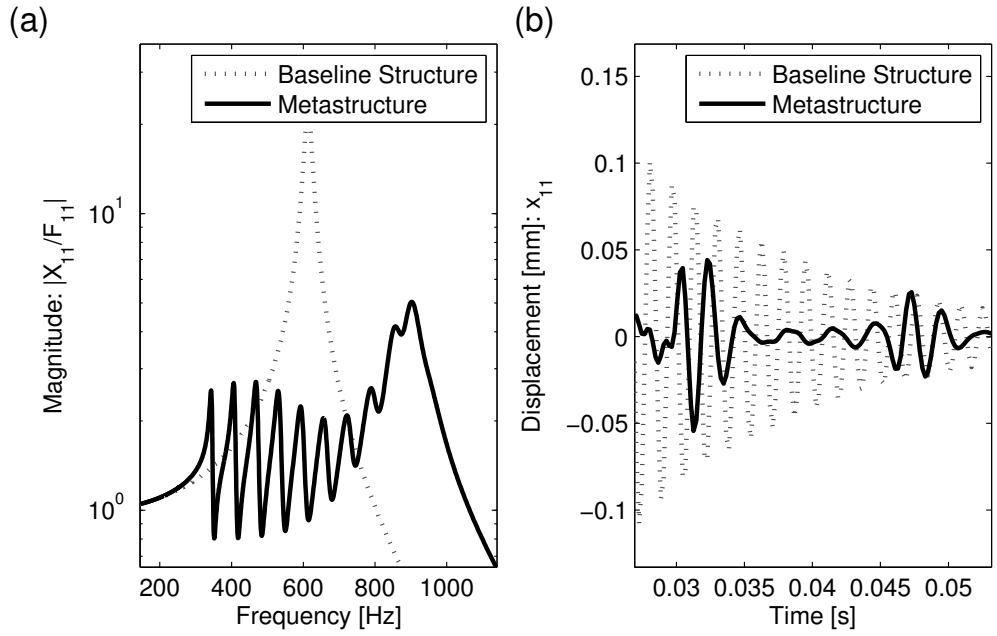

Figure 2.6: Close-up view of beating behavior in the (a) FRF and (b) the impulse response of a structure with 10 absorbers with linearly varying frequency

the baseline structure to the metastructure as described in Equation 2.21. The negative of this percentage is used as the objective function and is minimized. The optimization is performed in MATLAB using a constrained non-linear interior point algorithm (`fmincon`). During the optimization, the mass distribution of the vibration absorbers is constrained to be constant and the natural frequencies of the vibration absorbers are allowed to vary linearly. When the optimization is performed, the number of vibration absorbers is constrained to a single value and the algorithm determines the optimal values of the frequency range and mass ratio. The number of absorbers was not used as a parameter of the optimization since it does not take an optimal value. More absorbers lead to higher performance but also lead to a more complex structure. The complexity of a structure is difficult to quantity. This trade-off between performance and complexity is described in more detail in Section 2.5.1. When this optimization procedure is applied to the system with ten absorbers from Section 2.3, the optimal range of frequencies is calculated as 406 to 1260 Hz and the optimal mass ratio is $\mu = 0.31$. The frequency range deviates slightly from the range estimated in Section

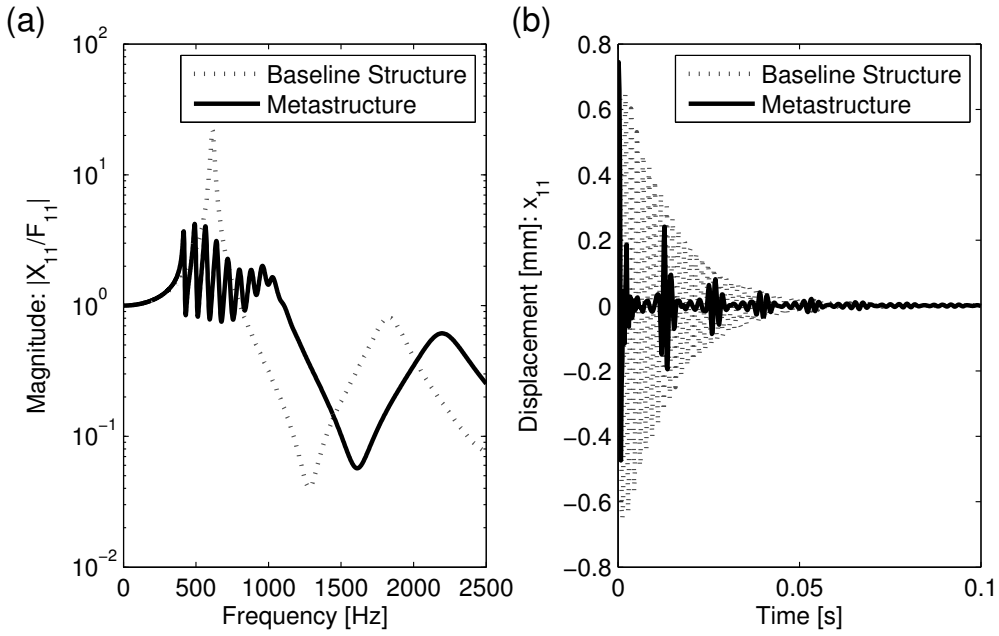

Figure 2.7: (a) FRF and (b) the impulse response of a structure with 10 absorbers of linearly varying optimized frequencies

2.3, 350 to 950 Hz and the mass ratio increases slightly from the estimated value of $\mu = 0.30$. These new values used in the optimized model result in a 58.2% reduction in the H_2 norm, which is a greater reduction compared to the non-optimized model; see Table 2.2 . The FRF and impulse response can be seen in Figure 2.7. Through out the rest of this chapter, the same basic optimization procedure is used but with slightly different parameters which allows various trends to be examined.

2.5 Parameters trends

In this section, a variety of parameters are examined. This allows the capability of the model to be understood and to help understand basic phenomenon. The various parameters of the models are altered to determine how these parameters affect the performance of the structure. The results for these various studies can be found in Table 2.2.

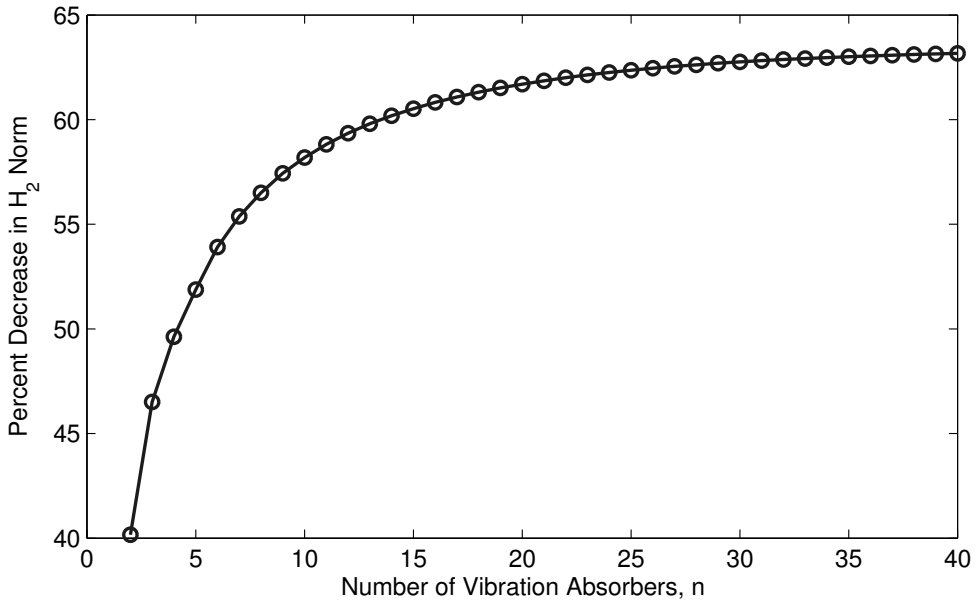

Figure 2.8: Optimal percent decrease in H_2 norm for varying number of absorbers

2.5.1 Number of absorbers

Here, the effect of the number of absorbers is examined for a structure where the mass of the absorbers is constrained to be constant and the frequencies of the absorbers is allowed to vary linearly. This analysis is run using the optimization procedure described in Section 2.4. For each data point shown in Figure 2.8 an optimization procedure is run to determine the optimal mass ratio, and distribution of absorber frequencies. The results show there is not an optimal number of absorbers, but the performance tends towards an asymptote. The response improves as more absorbers are used, but at some point there is a trade-off between increased performance and increased complexity. For this paper, ten absorbers is chosen because any structure with more than ten absorbers provides only marginally better performance. The FRFs for systems with 2, 26, and 50 absorbers are plotted in Figure 2.9.

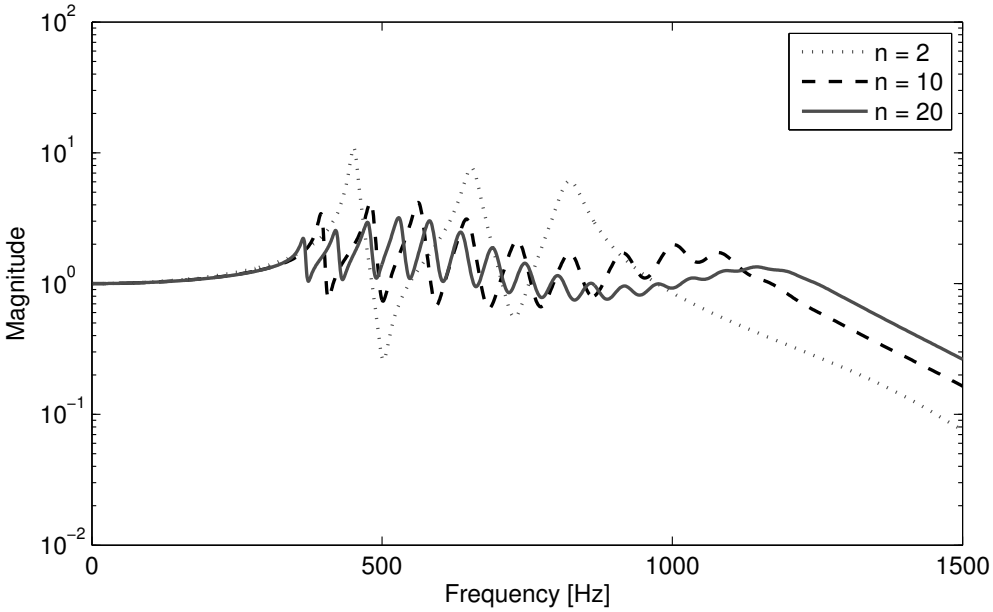

Figure 2.9: Optimal FRFs for various number of absorbers

2.5.2 Mass ratio

Next, the effect of the mass ratio on the system is determined for a structure where the mass of the vibration absorbers is restricted to be constant and the frequencies of the absorbers are allowed to vary linearly. Here, the mass ratio is not included in the optimization procedure. Looking at the effects of varying the mass ratio provides insight into the behavior of the system. Recall, the definition of the mass ratio is the ratio of the mass of the absorbers over the mass of the entire structure, Equation 2.1. Once a mass ratio and a total mass is defined, the mass of the absorbers can be calculated; see Equation 2.6 for details. Then the optimization procedure is used to calculate the stiffness values of the absorber springs. For each data point in Figure 2.10, the number of absorbers is set to ten, the mass ratio is varied, and the optimization procedure is performed. The resulting percent decrease is plotted and the shape of the plot shows there is an optimal mass ratio value which is why the mass ratio was added to the optimization procedure in Section 2.4. The existence of an optimal mass value shows that there is a trade-off between mass in the absorber system and mass in

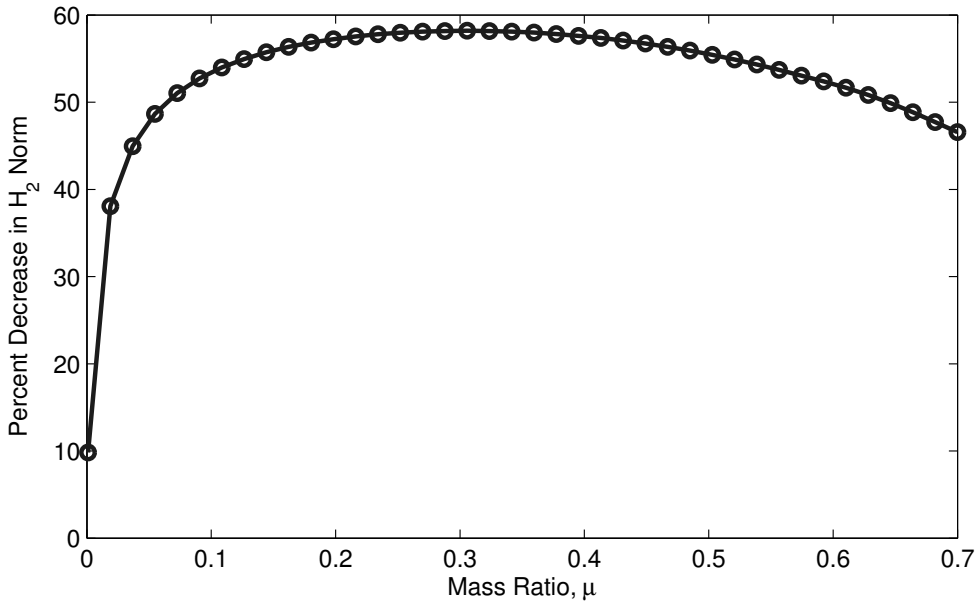

Figure 2.10: Optimal percent decrease in H_2 norm for varying mass ratios

the host structure. Too little mass in the absorber system does not allow sufficient energy transfer to the absorber mass and too much mass produces a large response from a higher mode. From these results, a mass ratio of $\mu = 0.31$ is optimal for this specific structure. The shape of the plot has a flat curve; thus a slightly lower mass ratio value could be used with only a slight loss in performance. Figure 2.11 shows the resulting FRF for four of the mass ratios.

2.5.3 Distribution of stiffness

As shown previously, the models in which the absorbers are tuned to frequencies that vary linearly provide better performance than those that are all tuned to a single frequency. Next, other distributions are examined. Instead of constraining the distribution to be linear, the optimization code allows each absorber to take on any value for its natural frequency. Figure 2.12 shows the optimal distribution for a structure with 10 absorbers alongside the distributions for the linear and constant cases. The x-axis denotes the absorber number, ranging from 1 to n and the y-axis shows the natural frequency of that absorber. It is

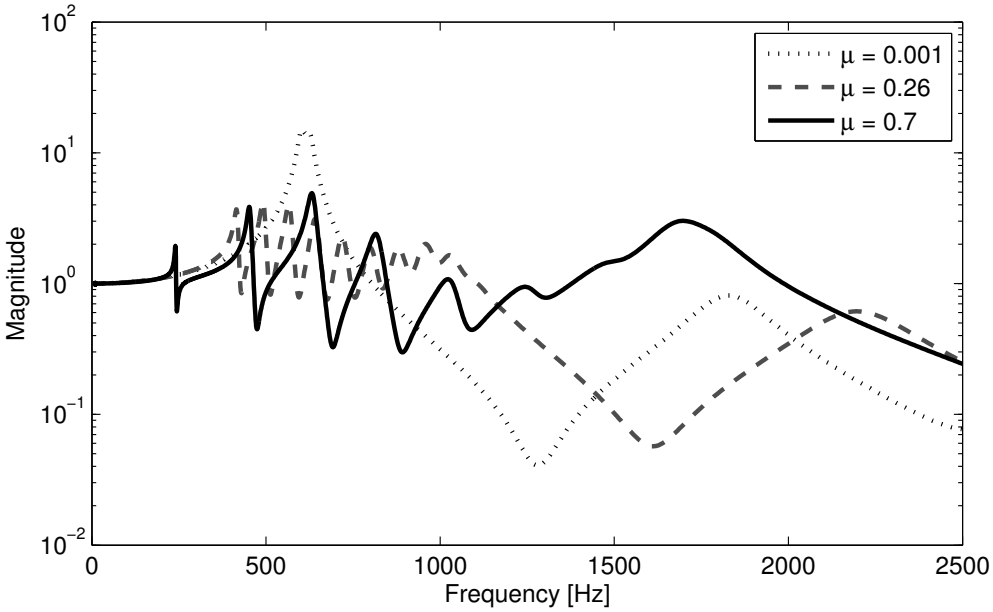

Figure 2.11: Optimal FRFs for various mass ratios

interesting to note the pattern of the optimal distribution, but it must also be noted that transitioning from the linear to the unconstrained distribution produces less than a 1% additional decrease. The decrease goes from 58.2% to 58.9%. The results are summarized in Table 2.2. This is deemed not beneficial enough to outweigh the extra time it takes the optimization code to run. For a majority of the following analyses, a linear distribution is utilized.

2.5.4 Distribution of absorber mass

In this section, the effect of these absorber mass distribution is studied. Three different distributions of absorber masses are examined. For the first case, the distribution of the mass is uniformly distributed throughout the length of the bar and the stiffness of each absorber was chosen such that the natural frequencies of each absorber vary linearly. For the second case, the mass is allowed vary linearly and once again, the stiffnesses are chosen to produce linearly varying natural frequencies. The last case has no constraints on the distributions of the mass and stiffness of the absorbers. For each of these cases, an optimization is

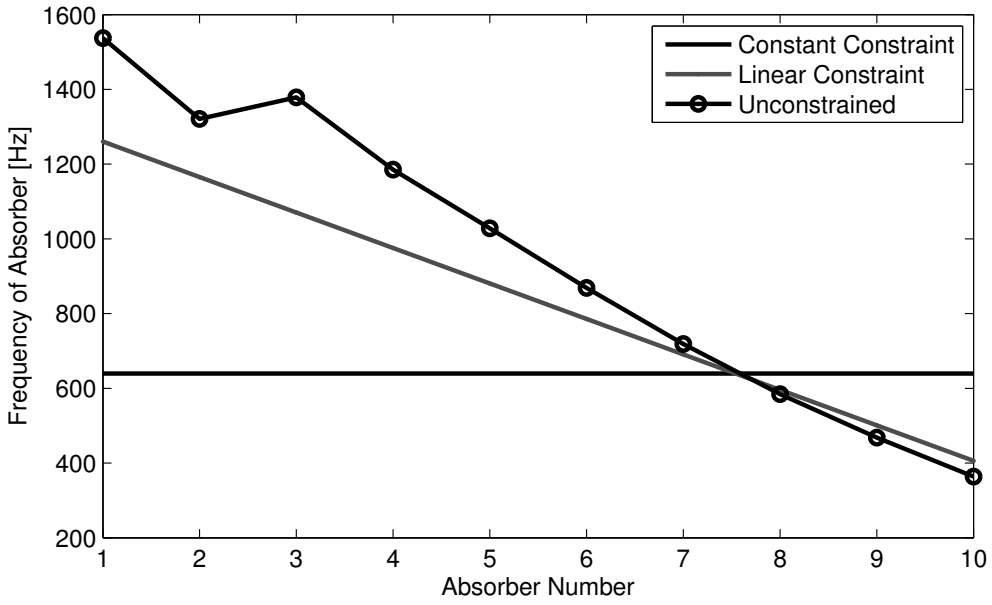

Figure 2.12: Natural frequencies of individual vibration absorbers

Table 2.2: Summary of optimized results for various configurations. *indicates mass ratio values that are not optimized

Number absorbers	**Mass ratio**	**Mass distribution**	**Frequency distribution**	**Minimum frequency**	**Maximum frequency**	H_2 **decrease**
2	0.165	constant	constant	583 Hz	583 Hz	28.33 %
10	0.323	constant	constant	640 Hz	640 Hz	28.39 %
10	0.323	linear	constant	472 Hz	472 Hz	28.86 %
10	0.305	constant	linear	406 Hz	1260 Hz	58.19 %
10	0.318	linear	linear	381 Hz	1354 Hz	58.50 %
10	0.300*	constant	unconstrained	430 Hz	1260 Hz	58.91 %
10	0.400*	constant	unconstrained	430 Hz	1260 Hz	56.09 %
10	0.300*	unconstrained	unconstrained	405 Hz	2267 Hz	59.01 %
10	0.400*	unconstrained	unconstrained	364 Hz	1537 Hz	59.22 %

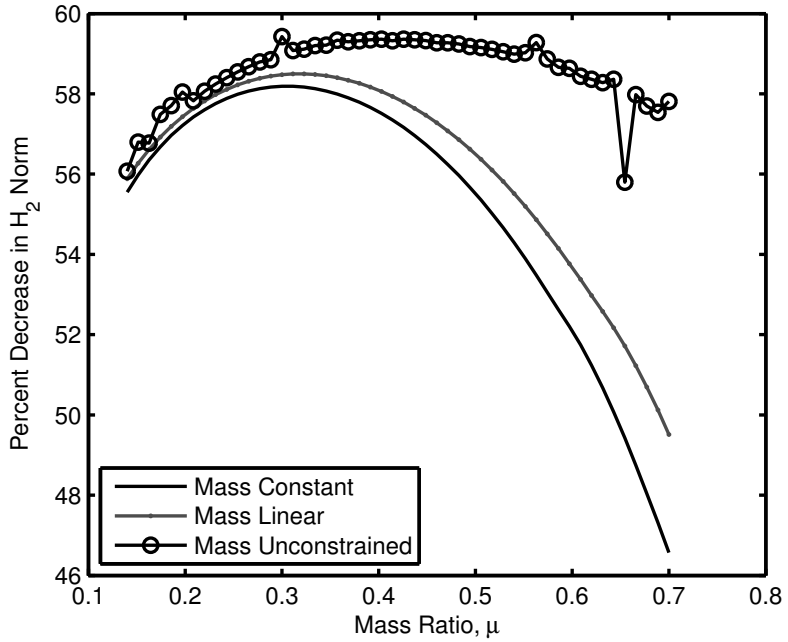

Figure 2.13: Effects of varying the absorber mass distribution on performance measure versus the mass ratio for uniform distribution, linear distribution and unconstrained distribution

performed at varying mass ratio values. The optimal distribution for each mass ratio is found by minimizing the H_2. In Figure 2.13 the performance measure is plotted for each of the mass ratios. The unconstrained distribution case gives the best performance results for all mass ratio values. As the mass ratio increases, the unconstrained case has a greater increase in performance compared to the linearly varying case. For a mass ratio of $\mu = 0.40$, Figure 2.14 shows the values that the absorber mass takes on for the various distributions. For these, the unconstrained distribution follows the linear distribution closely with some changes. The dynamic responses of this structure can be seen in Figure 2.15 for the three different absorber mass distributions.

2.6 Tuned mass damper comparison

In addition to comparing the metastructure design to a baseline structure, the metastructure design is also compared to a traditional tuned mass damper. The use of a tuned

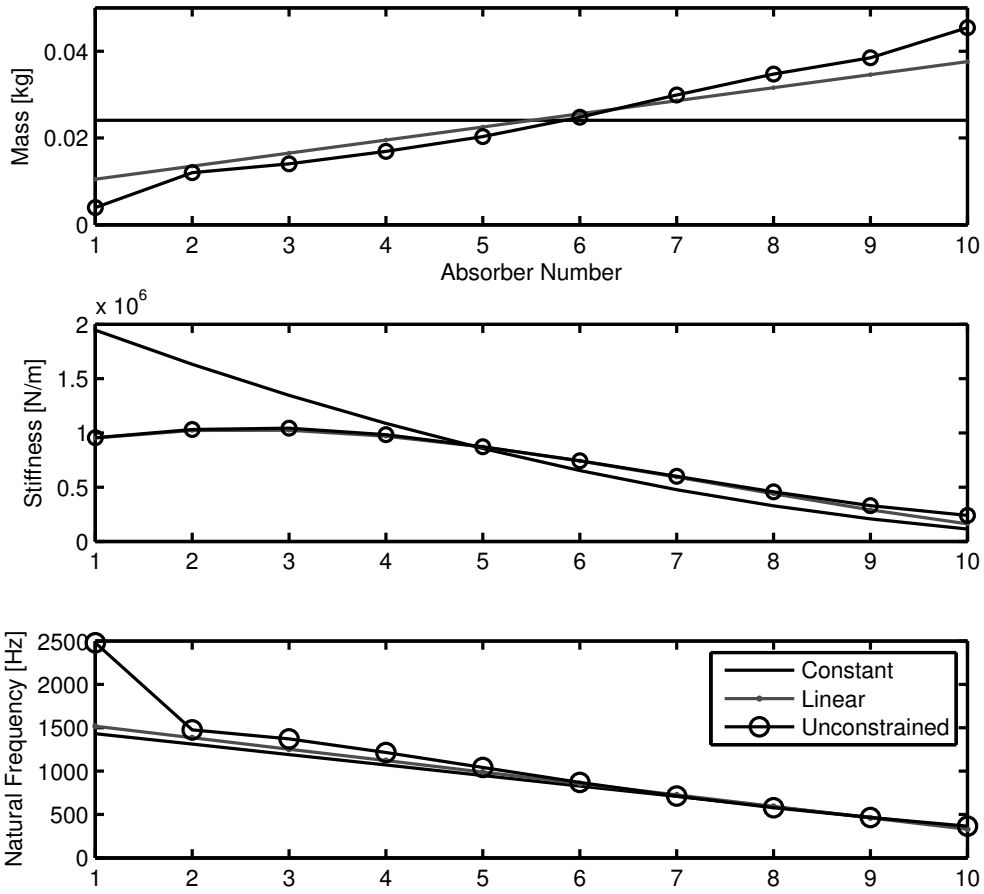

Figure 2.14: Optimal distribution of absorber mass for uniform distribution, linear distribution and unconstrained distribution for a metastructure with a mass ratio of $\mu = 0.40$

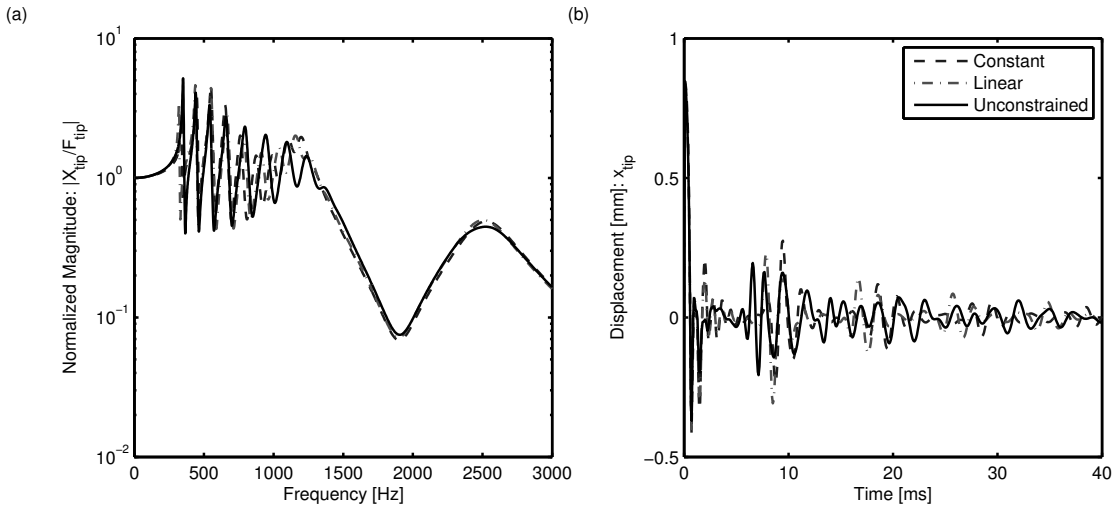

Figure 2.15: The (a) frequency response function and the (b) impulse response function of the metastructure for uniform, linear and unconstrained absorber mass distributions for a mass ratio of $\mu = 0.40$

mass damper is a traditional vibration suppression method and is used here to show the differences between a tuned mass damper solution and a metastructure solution. A TMD is similar to a vibration absorber but additionally contains a damper.

2.6.1 Tuned mass damper model

The model used in these simulations is shown in Figure 2.16 where $k_{\text{TMD}}, c_{\text{TMD}}$ and m_{TMD} are the stiffness, damping and mass parameter of the TMD. The mass ratio of the structure is defined in a similar way to as the metastructure as

$$\mu = \frac{m_{\text{TMD}}}{m_{\text{total}}} = \frac{m_{\text{TMD}}}{(n+1)m + m_{\text{TMD}}} \tag{2.22}$$

For these simulations the mass of the baseline structure, the metastructure, and the structure with the TMD area all constrained to have the same mass, such that

$$m_{\text{metastructure}} = (n+1)m + \sum_{i=1}^{n} m_i = m_{\text{baseline}} = (n+1)m + m_{\text{TMD}} \tag{2.23}$$

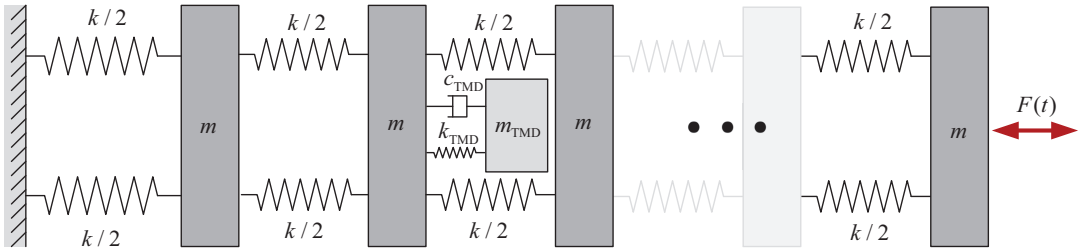

Figure 2.16: Lumped mass model of a bar with a single tuned mass damper

2.6.2 Tuned mass damper comparison results

Here, the performance of a metastructure is compared to that of a structure with TMD. As before, the performance of the structure is plotted versus the mass ratio as seen in Figures 2.17 and 2.18. For each mass ratio, an optimized metastructure, with absorber masses values varying linearly, is used as described in the previous section. For the structure with the TMD, the TMD parameters, $k_{\text{TMD}}, c_{\text{TMD}}, m_{\text{TMD}}$, are determined using optimization where the H_2 norm is minimized. For these cases structural damping was utilized as shown in Equation 2.18 with two different damping values, $\alpha = 2 \times 10^{-5}$ and $\alpha = 4 \times 10^{-5}$. These values correspond to 2.03% and 4.11% of critical damping for the fundamental mode of the metastructure. For the instance in which $\mu = 0.23$ and $\zeta_1 = 0.0203$ the frequency response function and the impulse response of the tip subjected to a tip excitation are plotted in Figure 2.19. This figure shows that using a TMD and a metastructure with vibration absorbers of varied frequencies achieve a similar effect, where the fundamental peak of the structure is flattened out allowing for boarder band suppression around the fundamental natural frequency of the structure. The optimal parameters for various mass ratios are shown in Table 2.3. When the structure has more structural damping, the metastructure performs comparatively better compared to a case with less structural damping. The amount of structural damping added to the structure significantly affects the comparison. Thus, for this comparison to be useful, the amount of structural damping in the structure must be determined. Additionally, in these

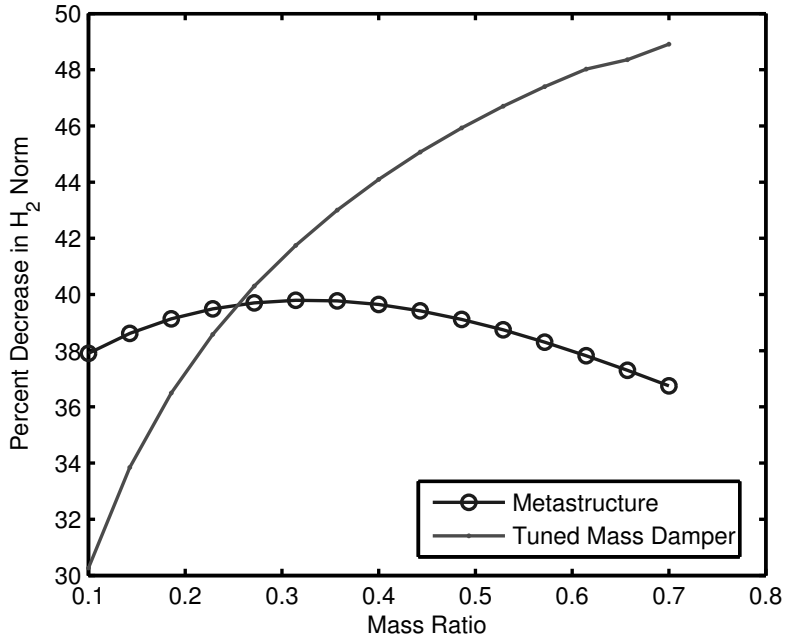

Figure 2.17: Percent decrease in the H_2 norm plotted versus varying mass ratio values for a metastructure and a structure with a tuned mass damper for a damping ratio of $\zeta_1 = 0.0411$

simulations the additional weight necessary to achieve the damping values for the TMD has not been considered. The point here is that while the TMD and metastructure are capable of producing similar results, the metastructure is able to produce vibration suppression without increasing the mass and takes up less space, critical in some applications.

2.7 Chapter summary

The results of these simulations show that it is possible to use distributed vibration absorbers to reduce the response of a system without adding additional mass to the structure. These simulations found that the distributed absorbers should be designed such that their natural frequencies span a range of frequencies. For this specific structure, the results show that the mass ratio (mass of the absorbers over the mass of the host structure) should be around 0.30 and the number of absorbers should be around 20 or lower. The natural frequencies of the vibration absorbers should be tuned such that their frequencies vary linearly.

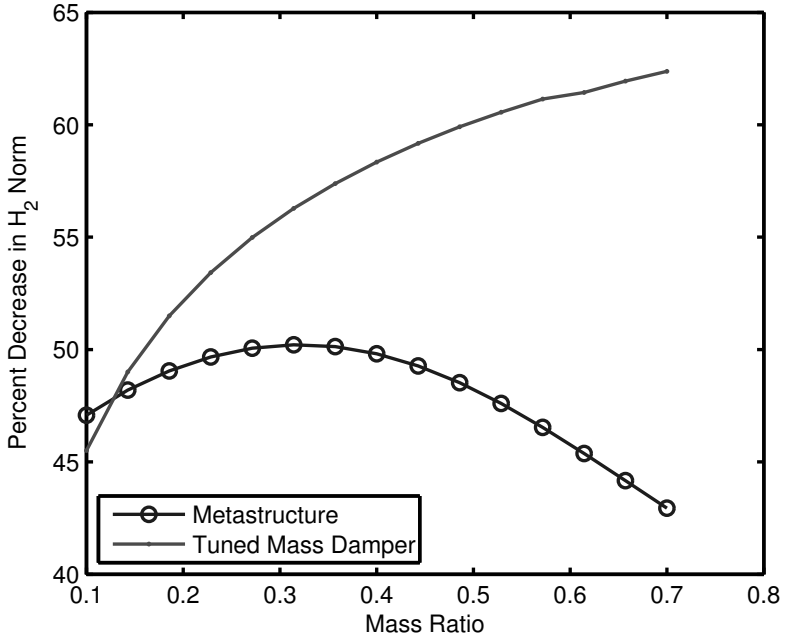

Figure 2.18: Percent decrease in the H_2 norm plotted versus varying mass ratio values for a metastructure and a structure with a tuned mass damper for a damping of $\zeta_1 = 0.0203$

Table 2.3: Optimal tuned mass damper parameters for various mass ratios and structural damping values

Mass ratio	**Damping value of TMD [kg/s]**		**Natural frequency of TMD [Hz]**	
	$\zeta_1 = 0.0203$	$\zeta_1 = 0.0411$	$\zeta_1 = 0.0203$	$\zeta_1 = 0.0411$
0.100	85.73	83.21	552.4	545.2
0.143	139.85	135.46	531.3	523.9
0.186	198.64	192.24	511.8	504.6
0.229	260.52	252.18	493.7	486.8
0.271	324.47	314.38	476.9	470.3
0.314	389.75	378.27	461.2	454.9
0.357	455.90	443.46	446.4	440.6
0.400	522.53	509.69	432.6	427.3

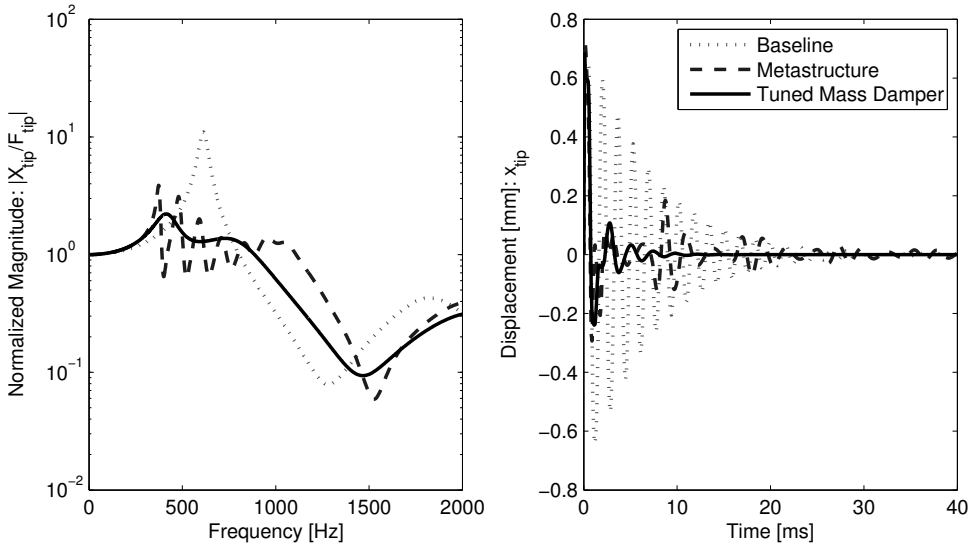

Figure 2.19: The (a) frequency response function and (b) impulse response function for a metastructure versus a structure with a tuned mass damper for $\mu = 0.229$ and $\zeta_1 = 0.0203$

If higher mass ratio are used, then using an unconstrained distribution of absorber mass and stiffness should be considered. For mass ratios about 0.30, it is sufficient to use a constant absorber mass distribution with linearly varying natural frequencies.

Additionally, the metastructure design is compared to that of a structure with a TMD. The comparison of these structures has a strong dependence on the amount of structural damping in the structure making it challenging to examine from a lumped mass model perspective. In general, for lower mass ratios the metastructure can perform slightly better than the TMD. The additional weight needed to achieve the high level of damping required for the optimally tuned TMD has not been considered. Future work could consider the additional weight necessary to achieve the required levels of damping and consider modeling the amount of damping in the structure to get a better comparison. The metastructure is able to provide good levels of suppression by integrating the vibration absorbers into the structural design. The formulation and procedures outlined above provide a scenario for designing metastructures and for helping designers to decide between a traditions TMD approach versus a metastructure approach for their particular application.

CHAPTER III

Dynamic Characterization of 3D Printed Viscoelastic Materials

This chapter characterizes the viscoelastic properties of materials printed using the Objet Connex 3D printer and presents a modeling method used to capture the effects of the viscoelastic behavior. The 3D printer being explored is used in Chapter IV to create a metastructure prototype. Metastructures tend to have complex geometry, thus are easily manufactured on 3D printers. The most cost-effective and readily available 3D printers today, use polymer resins to create the parts. Polymers materials are composed of long molecular chains, which lead to energy dissipation during cyclic deformation. The energy dissipation experienced by polymer materials can be modeled using a viscoelastic model [44]. This chapter begins by explaining the modeling procedure used the characterize the viscoelastic material properties which involve the complex modulus and the temperature-frequency equivalence. After these modeling methods are described, the characterization of the Objet Connex materials is presented. The characterization is performed using a DMA machine which can measure the complex modulus of the specimen. The complex modulus values are found for various frequencies and temperatures. The temperature-frequency equivalence is used to determine a relationship between those variables. The characterization is performed on four out of ten of the materials that the 3D printer is capable of printing. For one of these materials, the testing configuration and the print direction are explored. For the complex

modulus data to be used in a transient setting, the frequency dependence of the material must be modeled. This work uses the GHM model, which utilizes an approximation for the complex modulus versus frequency data. The GHM approximation is curve-fit to the experimental data, and the resulting parameters are used to develop finite element mass, damping and stiffness matrices for the viscoelastic materials. This allows the viscoelastic material to be modeled in various dynamic applications. This chapter ends by using the GHM model to examine the dynamic response of a simple bar and beam, specifically looking at how a temperature change affects the response. For the simple beam case, these results are experimentally verified.

3.1 Viscoelastic modeling

This section describes the modeling methods used in this work to model the viscoelastic material behavior. In steady-state dynamic applications, the viscoelastic material behavior can be described using the complex modulus model. The complex modulus of a viscoelastic material varies with both frequency and temperature at which the specimen is excited. The complex modulus data can be experimentally obtained using various methods which will be described later. The temperature-frequency equivalence develops a relationship between the frequency and temperature dependence of the complex modulus data, allowing the complex modulus data to be represented at a wider range of frequencies and temperatures than those obtained experimentally.

3.1.1 Complex modulus method

For dynamic applications, the most common method used to describe the dynamic response of viscoelastic materials is to identify the response of the material subjected to a sinusoidal load. When a harmonically varying stress is applied to an elastic material, the strain response will have the same frequency and phase as the load. This is not the case for a viscoelastic material; the response remains at the same frequency as the input but will

have a phase lag. When the following time-varying stress $\sigma(t)$ is applied to a viscoelastic material

$$\begin{aligned} \sigma(t) &= \sigma_0 \sin(\omega t) \\ \varepsilon(t) &= \varepsilon_0 \sin(\omega t - \delta) \end{aligned} \tag{3.1}$$

where ω is the frequency of the forcing function, $\varepsilon(t)$ is the strain-response of the material and the phase lag is denoted as δ the dynamic modulus can be expressed as the following complex number

$$G^\star(\omega, T) = \frac{\sigma(t)}{\varepsilon(t)} = G' + \jmath G'' \tag{3.2}$$

where $G^\star$ is the complex modulus, also referred to as the dynamic modulus. Because of the phase lag, the modulus is a complex number and can be decomposed into its real and imaginary components, where G' is the storage modulus and G'' is the loss modulus. The complex modulus can also be expressed by factoring out the storage modulus

$$G^\star(\omega, T) = G'[1 + \jmath\eta] \tag{3.3}$$

where η is the loss factor. The modulus values vary with both frequency and temperature [44]. This relationship can also be expressed in the Laplace domain as

$$\tilde{\sigma}(s) = s\tilde{G}(s)\tilde{\varepsilon}(s) \tag{3.4}$$

where the tilde represents the Laplace transform of the variable and the function $s\tilde{G}(s)$ is called the material dissipation function. When evaluated along the imaginary axis ($s = \jmath\omega$) the material dissipation function is equivalent to the complex modulus representation in Equation 3.2.

3.1.2 Temperature-frequency equivalence

Using the temperature-frequency equivalence, a relationship between the frequency and temperature can be determined to reduce the number of the variables necessary to describe the response of the material. We can assume that the complex modulus value at a frequency, f_1 and a temperature, T_1 is equal to the value at any other frequency f_2 and some temperature, T_2 such that the following relationship can be made

$$G^{\star}(f_1, T_1) = G^{\star}(f_2 \cdot \alpha(T_2)) \tag{3.5}$$

where $\alpha(T_2)$ is the shift factor and describes the relationship between frequency and temperature. Using the shift factor, the effects of both temperature and frequency can be combined into a single variable called the reduced frequency, $f_r(f, T) = f \cdot \alpha(T)$. The shift factor relationship is determined by testing a material at multiple frequencies and temperatures. For each temperature, a shift factor value is determined graphically by examining the modulus versus reduced frequency plots. Varying the shift factor causes the data at a specific temperature to shift on the reduced frequency scale. Once the shift factors for each temperature are determined, the $\log[\alpha(T)]$ is plotted versus $1/T$. This relationship resembles a slightly curved line, which is approximated by a straight line using the Arrhenius shift factor equation and takes on the following form

$$\log[\alpha(T)] = T_A \cdot \left(\frac{1}{T} - \frac{1}{T_0}\right) \tag{3.6}$$

where T_0 is an arbitrarily selected reference temperature, and T_A is related to the activation energy and is represented by the slope of the line. Using this relationship, the storage modulus and loss factor can be expressed as

$$G'(f, T) = G'\left(f \cdot \exp\left[\frac{-2.303 T_A}{T}\right] \cdot \exp\left[\frac{-2.303 T_A}{T_0}\right]\right) \tag{3.7a}$$

$$\eta(f,T) = \eta\left(f \cdot \exp\left[\frac{-2.303T_A}{T}\right] \cdot \exp\left[\frac{-2.303T_A}{T_0}\right]\right) \tag{3.7b}$$

These relationships allow the storage modulus and the loss factor to be expressed each as single curves plotted with respect to reduced frequency. Using the Arrhenius equation, Equation 3.6, this curve can be shifted to show properties at any temperature [44].

3.2 Viscoelastic material characterization of Objet Connex 500 3D printer

This section describes the procedure used to characterize the material properties of the Objet Connex 3D printer. This section begins by describing the 3D printer used in this work. This printer can print ten different materials with varying moduli. Four of these materials are characterized. Next, the characterization procedure is detailed. A DMA machine is utilized for this characterization which can measure the complex modulus. The DMA machine can test the specimens in various configurations using different clamping mechanisms. Here, the two different configurations, tensile and cantilevered, are used, and the resulting properties are compared. Additionally, the two different print directions are tested and compared. This section ends by comparing and contrasting the different testing configurations and the print directions.

3.2.1 Description of the 3D printer

The 3D printer investigated in this work is the Objet Connex 500 printer by Stratasys. This printer is capable of printing many different materials. Of interest to this paper are the rubber-like and rigid materials. The Objet Connex printer uses inkjet printing technology. The parts are made by depositing many small dots of liquidized polymer base materials and curing the resin using ultraviolet light, resulting in a printed material that appears homogeneous. Because of the digital nature of this method, these materials are called digital materials. This approach allows the printer to easily mix two distinct base materials in

Table 3.1: Manufacturer provided material properties of Objet Connex digital materials printed using base materials VeroWhitePlus and TangoPlus [46, 47]

Material	**Young's modulus [MPa]**	**Shore A value**	**Tensile strength [MPa]**	**Tested**
VeroWhitePlus	2000 - 3000	-	50 - 65	×
DM 8420	1400 - 2000	-	35 - 45	×
DM 8430	1100 - 1700	-	29 - 38	×
DM 9795	-	9 - 95	8.5 - 10.0	
DM 9785	-	80 - 85	5.0 - 7.0	
DM 9770	-	68 - 72	3.5 - 5.0	
DM 9760	-	57 - 63	2.5 - 4.0	
DM 9750	-	45 - 50	1.9 - 3.0	
DM 9740	-	35 - 40	1.3 - 1.8	
TangoPlus	-	26 - 28	0.8 - 1.5	×

various ratios to create a gradient of materials with multiple hardness levels [45]. Additionally, this method allows for parts made in a single print with both rigid and rubber-like components. Using this technique and the many base materials available, the Objet Connex printer can create many combinations with varying properties. The focus of this work will be on the digital materials created using the two base materials, VeroWhitePlus (RGD835) and TangoPlus (FLX930). VeroWhitePlus is a rigid opaque material, and TangoPlus is a rubber-like transparent material [47]. The printer can print ten different digital materials using these base materials [46]. The manufactured provided properties of these materials are shown in Table 3.1.

Previous work has shown that the materials produced from the Objet Connex printer exhibit viscoelastic behavior, making the materials both frequency and temperature dependent [39, 41, 37]. The work of Yu *et al.* measured the storage modulus and the loss modulus versus temperatures for seven of the ten digital materials. Their work shows the storage modulus varies by two orders of magnitude between 10° to 100° C [50]. These findings are expanded upon by characterizing the frequency and temperature dependence of four digital materials printed using VeroWhitePlus and TangoPlus on the Objet Connex 500 and by examining the effects of print direction and testing configuration on the complex modulus.

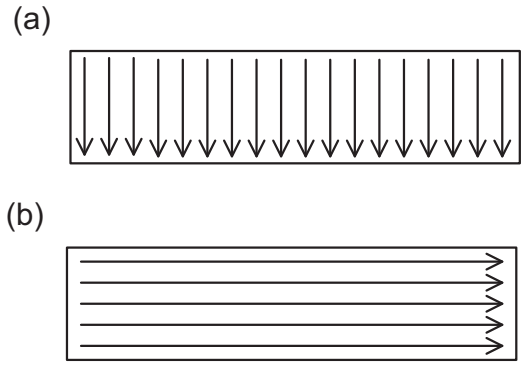

Figure 3.1: Schematic of (a) horizontal and (b) vertical print direction

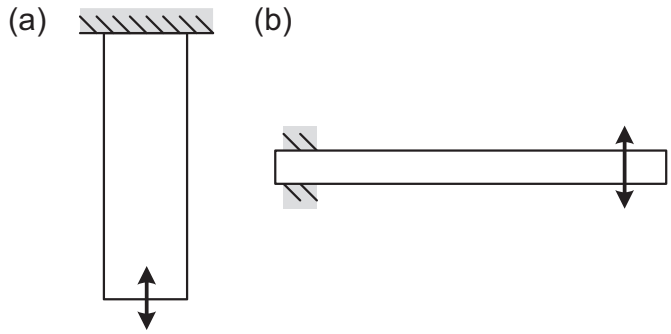

Figure 3.2: Schematic of (a) tensile and (b) cantilevered configurations

3.2.2 Experimental characterization methods

The complex modulus of these materials is characterized by varying both frequency and temperature. Also, the effects of print direction and testing configuration on the complex modulus are presented. The print direction is varied by rotating the orientation of the part on the print bed of the 3D printer as seen in Figure 3.1. The material properties are measured using a DMA machine with two different fixtures, cantilevered and tensile, shown in Figure 3.2.

The characterization of the materials is conducted using a DMA machine which applies

Table 3.2: Material characterizations performed [97]

Material	**Temperature Range [°C]**	**Testing Configuration**
VeroWhitePlus	0 - 100	Tensile
DM 8420	0 - 100	Tensile
DM 8430	0 - 100	Tensile
TangoPlus	-40 - 60	Tensile
DM 8430	35 - 60	Cantilevered
DM 8430	25 - 105	Tensile

a sinusoidal load and measures the magnitude and phase shift of response which can be used to calculate the complex modulus as seen in Equation 3.2. The DMA machine varies the excitation frequency and uses a thermal chamber allowing the temperature of the specimen also to vary. Using the raw data, the temperature-frequency equivalence can be used to transform the data to a single temperature and a wider range of frequencies. This testing method was chosen over other testing methods because other testing methods can only determine the complex modulus at the resonance frequency of the structure where this method can determine the modulus at any frequency [95].

Using these relationships described in Section 3.1.2, the curves can be shifted to any temperature. When shifting the data, the frequency range that the data covers will change, so it is important, to start with a sufficient number of data points to ensure the shifted data covers the entire desired frequency range for the temperature of interest. For this paper, the frequency range of interest is 10 to 2,000 Hz. Table 3.2 shows a summary of the material characterizations performed in this work [96, 97].

3.2.2.1 Sample preparation

When exploring the effects of printing direction and testing configuration, DM 8430 was used. The complex modulus properties for VeroWhitePlus, DM 8420, DM 8430 and TangoPlus are presented for comparison to each other and tested over a wider temperature range. The samples were printed on an Objet Connex 500 printer using the digital material

mode and the two base materials, VeroWhitePlus and TangoPlus. For parts oriented in the vertical configuration, the samples were positioned on the print bed such that the print direction aligned with the long edge of the sample. The parts were rotated 90° on the print bed for parts with the horizontal print direction as seen in Figure 3.1. After the printing was completed, the support material was removed from the parts using a metal scraper and water.

3.2.2.2 Dynamic mechanical properties

Rectangular specimens, having a size of approximately 9 × 1 × 5 mm, were used for the tensile dynamic mechanical experiments and 17 × 3 × 12 mm for the cantilevered configuration. The data were obtained using a DMA Q800 machine by Thermal Analysis. The tensile configuration testing followed the ASTM D5026 standard [98]. Figure 3.3 shows a setup of the test. The sample specimen was held in place by two clamps, the upper of which was fixed while the bottom moved cyclically. For the cantilevered configuration, the sample was tested using a single cantilevered set-up where a fixed clamp held one end of the beam and excited at the tip shown in Figure 3.2. These tests closely followed the ASTM D5418 standard. The standard pertains to a dual cantilever beam, and here a single cantilever was used [71].

All the samples were tested at nine to ten temperatures, varied linearly. The DM 8430 samples comparing print direction and testing configuration were tested at temperatures between 25° and 105° C for the tensile and 35° and 90° C for the cantilever configuration. VeroWhitePlus, DM 8420 and DM 8430 were tested at temperatures between 0°, and 100° C. TangoPlus was tested between -40° and 60° C. A soak time of five minutes was used at each temperature to ensure the sample reached the isothermal state. At each temperature, the sample was tested at ten frequencies, varied logarithmically between 100 and 0.10 Hz.

The DMA Q800 software collected and analyzed the data for each temperature and frequency. Based on the geometry of the testing specimen, the software outputs the storage

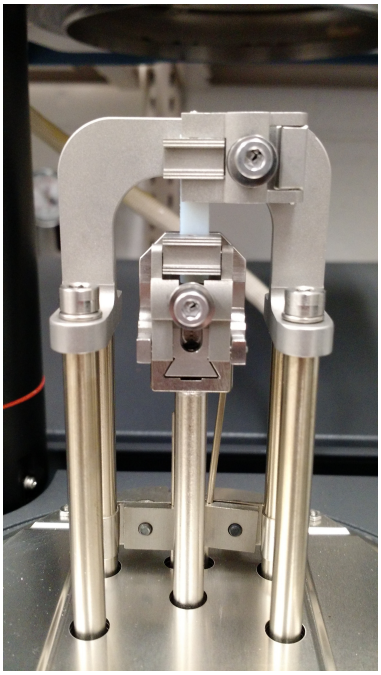

Figure 3.3: Experimental set-up of the tensile configuration in the DMA machine

modulus and the loss factor for the material at the specified temperatures and frequencies.

3.2.3 Characterization results

To identify potential errors in the data, a Wicket plot of the experimental data is created for all materials tested, displayed in Figure 3.4. The Wicket plot can be used to identify possible sources of error through the identification of points which deviate significantly from the primary sequence. The basis for a Wicket plot is because both the storage modulus and the loss factors are functions of the reduced frequency, thus must also be unique functions of each other. When the experimental data is plotted, the Wicket plot should be a unique curve with all data points lying close to the curve [44]. As seen in Figure 3.4, this trend holds for the four materials tested here. The Wicket plots for all characterizations can be found in Appendix A.

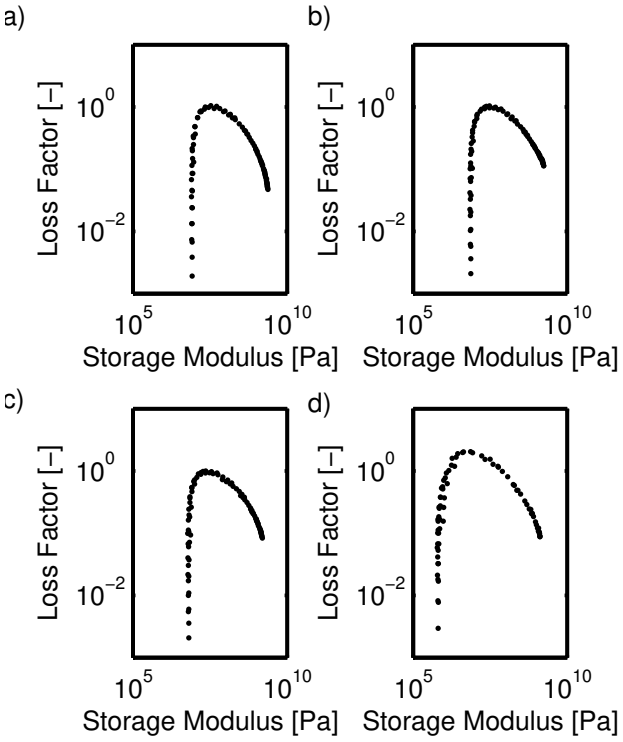

Figure 3.4: Wicket plots of experimental data for a) VeroWhitePlus, b) DM 8420, c) DM 8430 and d) TangoPlus

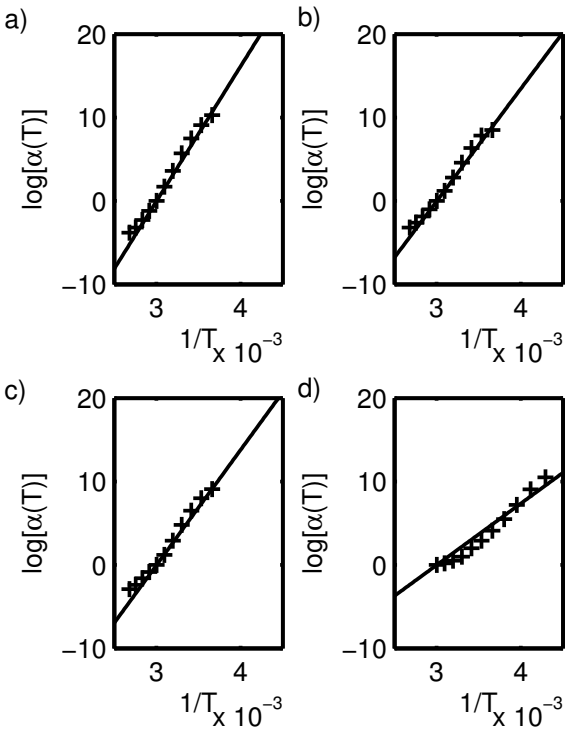

Figure 3.5: Plot of the logarithmic value of the shift factor versus the inverse of the temperature with the experimentally determined values plotted as plus symbols, and an Arrhenius fit plotted as a solid black line for a) VeroWhitePlus, b) DM 8420, c) DM 8430 and d) TangoPlus

Table 3.3: Arrhenius fit data for materials tested

Material	**Reference Temperature [°C]**	**Arrhenius Temperature [K]**
VeroWhitePlus	60	16,183
DM 8430	60	13,492
DM 8420	60	13,831
TangoPlus	60	7,385

3.2.3.1 Temperature effects

The data outputted from the DMA machine is manually analyzed to determine the relationship between temperature and frequency. This is accomplished using a shifting procedure to determine the relationship between the shift factors, α and the temperature, T as described in section 3.2.2.1. The resulting master curve is the complex modulus data plotted against reduced frequency. The relationship between the shift factor and the temperature along with the Arrhenius fit, from Equation 3.6, are plotted in Figure 3.5. For the materials tested, the reference temperature and the Arrhenius temperature are reported in Table 3.3. The details for all characterization can be found in Appendix A.

3.2.3.2 Dynamic mechanical results

The storage modulus and loss factor as defined in Equation 3.2 are respectively plotted in Figures 3.6 and 3.7 for each of the four materials tested. The storage modulus for the three stiffest materials, VeroWhitePlus, DM 8420, and DM 8430, vary by over three orders of magnitude from low frequencies to high frequencies. For TangoPlus, the storage modulus varies by over four orders of magnitude, and at low frequencies, is an order of magnitude lower compared to the other materials. Examining the loss factor plot (Figure 3.7), the TangoPlus material achieves significantly higher values, which is expected from a more rubbery material. The peak loss factor value occurs at a higher frequency, which corresponds to a lower temperature using the temperature-frequency equivalence. See Appendix A for tables with the data presented here.

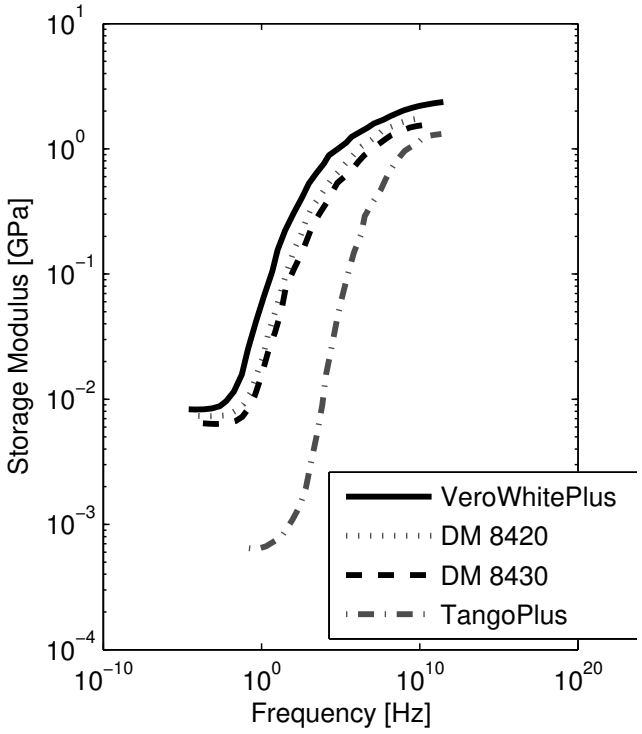

Figure 3.6: Master curve of storage modulus versus frequency for a reference temperature of 60° C

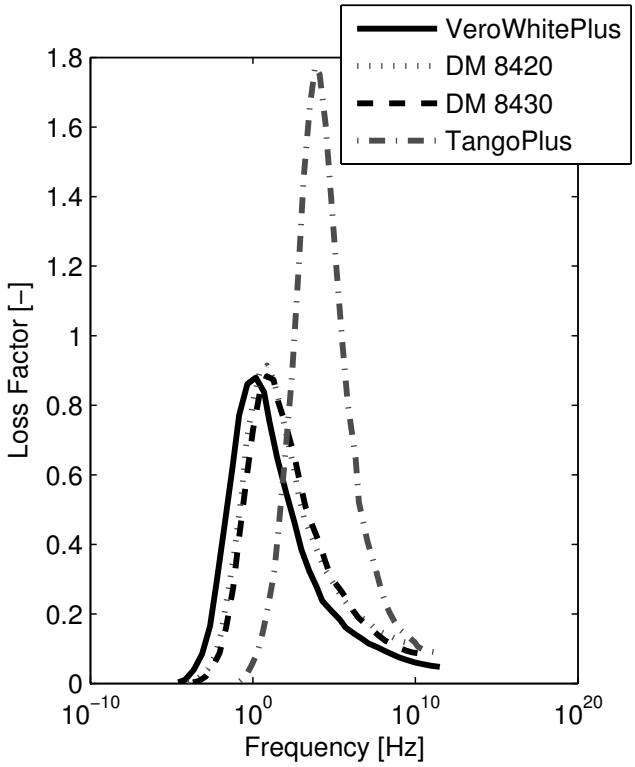

Figure 3.7: Master curve of loss factor versus frequency for a reference temperature of 60° C

3.2.3.3 Effect of print direction

A horizontal and vertical print direction were tested, where vertical refers to the orientation in which the print direction is along the long edge of the sample, and horizontal refers to when the part is rotated 90° on the print bed as seen in Figure 3.1. Figure 3.8 shows the results of these tests, where the results are virtually indistinguishable from each other, leading us to conclude the in-plane print direction does not affect the complex modulus results.

3.2.3.4 Effect of testing configuration

The testing configuration of the samples appears to have a slight influence on the complex modulus of the printed materials. Both a tensile and a cantilevered configuration were tested, and their results are shown in Figure 3.9. A schematic of these configurations is shown in Figure 3.2. The tensile configuration leads to a slightly higher loss factor peak value and higher storage modulus.

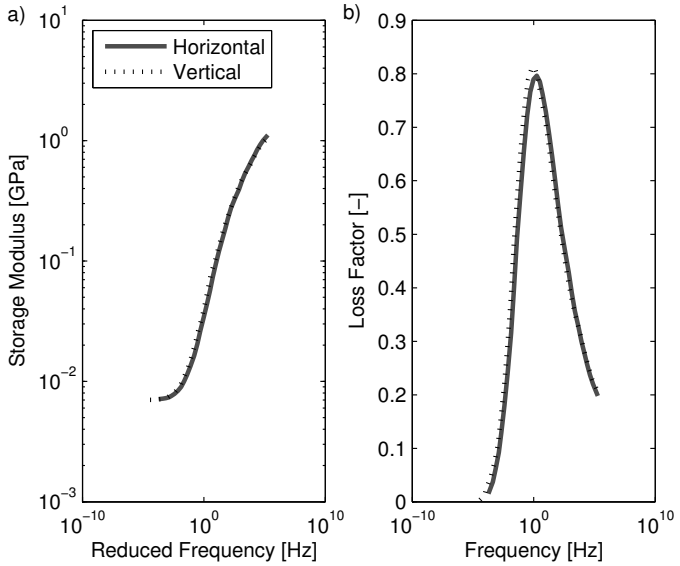

Figure 3.8: Effect of print direction on a) storage modulus and b) loss factor with a reference temperature of 65° C

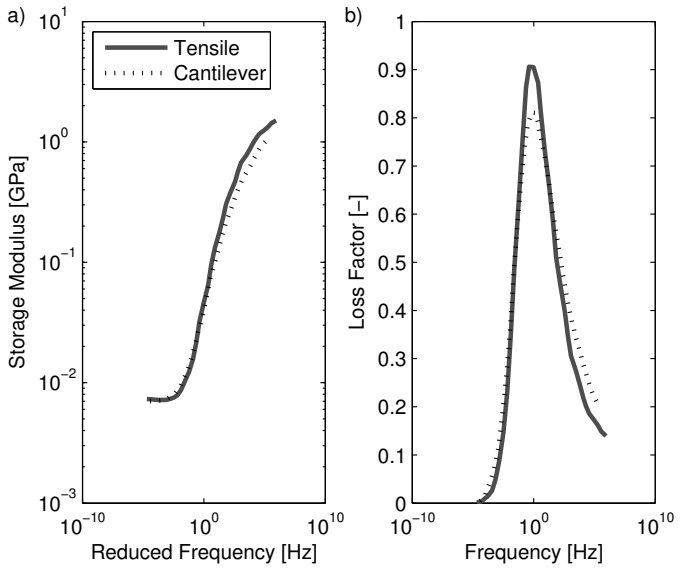

Figure 3.9: Effect of testing configuration on a) storage modulus and b) loss factor with a reference temperature of 65° C

3.2.4 Summary of characterization

The complex modulus properties of the inkjet printed material from the Objet Connex printer have been determined. These materials show viscoelastic effects, which should be considered when modeling these materials for use in vibration applications, particularly in situations where there are significant temperature changes. Although all materials show viscoelastic effects, the TangoPlus material exhibits greater variations in the storage modulus and loss factor than the VeroWhitePlus, DM 8430, and DM 8420. The master curves from Figures 3.6 and 3.7 can be used to curve fit viscoelastic models to the experimental data and can also be used for design purposes. Additionally, the effects of testing configuration and print direction were also investigated. The results show that variations in the in-plane print direction do not affect the response of the material for both the tensile and cantilevered configurations. The testing configuration does have a slight effect on the complex modulus values.

3.3 Frequency-dependent modeling of viscoelastic materials

The complex modulus model can be used to model steady-state applications but for situations in which the frequency in varying, the frequency dependence of the modulus values must be accounted for. Three common models are used in the field of vibration suppression to account the frequency variation and are shown in Table 3.4 [66, 68]. These models are characterized by the form of the equation used to represent the complex modulus data. The fractional derivative model developed by Bagley and Torvik uses a derivative of fractional order and is advantageous because five parameters are sufficient to represent the frequency-dependent behavior over a broad range of frequencies [59, 60]. The anelastic displacement fields model was developed by Lesieutre and his coworkers [99, 61, 100]. This model looks at elastic and the anelastic parts and represents the anelastic part by a first order differential equation. This model is formulated directly in the time-domain. The model that will be

Table 3.4: Material dissipation function approximations for selected viscoelastic models

Model	**Form of Material Dissipation Function**
Fractional Derivatives (FD)	$s\tilde{G}(s) = \dfrac{G_0 + G_1 s^\alpha}{1 + bs^\beta}$
Golla-Hughers-McTavish (GHM)	$s\tilde{G}(s) = G^\infty \left[1 + \sum_{j=1}^{n} \hat{\alpha}_j \dfrac{s^2 + 2\hat{\zeta}_j \hat{\omega}_j s}{s^2 + 2\hat{\zeta}_j \hat{\omega}_j s + \hat{\omega}_j^2}\right]$
Anelastic Displacement Fields (ADF)	$s\tilde{G}(s) = G_0 \left[1 + \sum_{j=1}^{n} \Delta_j \dfrac{s}{\omega^2 + \Omega_k^2}\right]$

used in the paper is the GHM model developed by representing the complex modulus as a series of mini-oscillators [62, 101].

3.3.1 GHM method

This section provides an overview of the GHM modeling method used here to account for the frequency dependence of the complex modulus. The GHM method was first introduced in 1985 by Golla and Hughes [62] and expanded upon by McTavish and Hughes in 1987 [102, 63]. The GHM method was originally developed to analyze damping in large flexible space-structures but can be used wherever there are viscoelastic materials are present. This internal-variable method uses auxiliary dissipation coordinates to model the frequency-dependent loss factor inherent in viscoelastic materials. These dissipation coordinates are augmented to the system adding degrees of freedom to the overall system. This method is valuable because it produces mass, stiffness and damping matrices in the familiar second-order time-domain format. The resulting matrices can be easily integrated into existing finite element theory or analytical models following from Newtons laws. The only additional information required is curving-fitting parameters from the complex modulus curve. These parameters are obtained from material testing by curve-fitting the complex modulus versus reduced frequency curve. These curve-fitting parameters are inherent of the materials, not of the system.

The GHM method approximates the material modulus using the following second-order rational function involving three parameters. This approximation is comprised of terms called mini-oscillator terms which come from the single degree of freedom physical realization. In the Laplace domain, the material dissipation function takes the form

$$s\tilde{G}(s) = G^{\infty}\left[1 + \sum_{j=1}^{n_{\mathrm{MOT}}} \hat{\alpha}_j \frac{s^2 + 2\hat{\zeta}_j\hat{\omega}_j s}{s^2 + 2\hat{\zeta}_j\hat{\omega}_j s + \hat{\omega}_j^2}\right] \tag{3.8}$$

where G^{∞} is the equilibrium value of the modulus and $\hat{\alpha}_j$, $\hat{\omega}_j$, $\hat{\zeta}_j$ are the parameters determined by the shape of the curve. The number of terms utilized depends on the test data, target frequency-range and desired accuracy. The following conditions, $\hat{\alpha}_j > 0, \quad \hat{\omega}_j > 0, \quad \hat{\zeta}_j > 0$ ensure that the representation dissipates energy [62].

The viscoelastic finite element matrices will be developed for a material dissipation function with a single term ($n_{\mathrm{MOT}} = 1$) and then generalized for any number of terms. For more details see McTavish and Hughes [63]. A typical finite element formulation, has the following equation of motion

$$\mathbf{M}^e\ddot{\mathbf{q}}(t) + G\bar{\mathbf{K}}^e\mathbf{q}(t) = \mathbf{f}(t) \tag{3.9}$$

where $\mathbf{M}^e$ and $\mathbf{K}^e = G\bar{\mathbf{K}}^{\mathbf{e}}$ are the classical elastic finite element matrices and $\mathbf{f}(t)$ is the elemental nodal force vector corresponding the elemental degrees of freedom, $\mathbf{q}(t)$. This equation can be generalized by replacing the constant elastic constant with a viscoelastic representation resulting in

$$\mathbf{M}^e\ddot{\mathbf{q}}(t) + G(t)\bar{\mathbf{K}}^e\mathbf{q}(0) + \int_0^t G(t-\tau)\bar{\mathbf{K}}^e\frac{\mathrm{d}}{\mathrm{d}\tau}\mathbf{q}(\tau) = \mathbf{f}(t) \tag{3.10}$$

where $\mathbf{q}(t)$ is restricted to be zero for $t \in (-\infty, 0)$. Transforming Equation 3.10 into the Laplace domain yields

$$s^2\mathbf{M}^e\tilde{\mathbf{q}}(s) + s\tilde{G}(s)\bar{\mathbf{K}}^e\tilde{\mathbf{q}}(s) = \tilde{\mathbf{f}}(s) + s\mathbf{M}^e\mathbf{q}_0 + \mathbf{M}^e\dot{\mathbf{q}}_0 \tag{3.11}$$

Introduce a column of dissipation coordinates $\tilde{\hat{\mathbf{z}}}$ such that

$$\tilde{\hat{\mathbf{z}}} = \frac{\omega^2}{s^2 + 2\hat{\zeta}\hat{\omega}s + \hat{\omega}^2}\tilde{\mathbf{q}}(s) \tag{3.12}$$

Using the approximation given in Equation 3.8 and the relationship for Equation 3.12, the following equation of motion is equivalent to Equation 3.11

$$\begin{bmatrix} \mathbf{M}^e & \mathbf{0} \\ \mathbf{0} & \frac{\hat{\alpha}}{\hat{\omega}^2}\mathbf{K}^e \end{bmatrix} \begin{Bmatrix} \ddot{\mathbf{q}} \\ \ddot{\hat{\mathbf{z}}} \end{Bmatrix} + \begin{bmatrix} \mathbf{0} & \mathbf{0} \\ \mathbf{0} & \frac{2\hat{\alpha}\hat{\zeta}}{\hat{\omega}}\mathbf{K}^e \end{bmatrix} \begin{Bmatrix} \dot{\mathbf{q}} \\ \dot{\hat{\mathbf{z}}} \end{Bmatrix} + \begin{bmatrix} (1+\hat{\alpha})\mathbf{K}^e & -\hat{\alpha}\mathbf{K}^e \\ -\hat{\alpha}\mathbf{K}^e & \hat{\alpha}\mathbf{K}^e \end{bmatrix} \begin{Bmatrix} \mathbf{q} \\ \hat{\mathbf{z}} \end{Bmatrix} = \begin{Bmatrix} \mathbf{f} \\ \mathbf{0} \end{Bmatrix} \tag{3.13}$$

Next, a spectral decomposition on the stiffness matrix is utilized to simplify the equations. The elastic stiffness matrix possesses n_q non-negative eigenvalues. The zero eigenvalues represent rigid body modes which cannot dissipate energy thus they are neglected. Considering only the positive eigenvalues (λ_p) and their corresponding eigenvectors $\mathbf{r}_p$ of $\bar{\mathbf{K}}^e$, the following matrices are constructed

$$\bar{\mathbf{R}} = \text{row}\{\mathbf{r}_p\}, \quad \bar{\mathbf{\Lambda}} = \text{diag}\{\lambda_p\}, \quad \bar{\mathbf{R}}^{\mathrm{T}}\bar{\mathbf{R}} = \mathbf{I} \tag{3.14}$$

Leading to this spectral decomposition

$$\mathbf{K}^e = G^{\infty}\bar{\mathbf{R}}\bar{\mathbf{\Lambda}}\bar{\mathbf{R}}^{\mathrm{T}} \tag{3.15}$$

Taking Equation 3.13 and pre-multiplying the bottom row by $\bar{\mathbf{R}}^{\mathrm{T}}$ and letting $\mathbf{z} = \bar{\mathbf{R}}^{\mathrm{T}}\hat{\mathbf{z}}$ the equations of motion become

$$\mathbf{M}^v \begin{Bmatrix} \ddot{\mathbf{q}} \\ \ddot{\mathbf{z}} \end{Bmatrix} + \mathbf{D}^v \begin{Bmatrix} \dot{\mathbf{q}} \\ \dot{\mathbf{z}} \end{Bmatrix} + \mathbf{K}^v \begin{Bmatrix} \mathbf{q} \\ \mathbf{z} \end{Bmatrix} = \begin{Bmatrix} \mathbf{f} \\ \mathbf{0} \end{Bmatrix} \tag{3.16}$$

Where the viscoelastic mass, stiffness and damping matrices have the following form

$$\mathbf{M}^v = \begin{bmatrix} \mathbf{M}^e & \mathbf{0} \\ \mathbf{0} & \dfrac{\hat{\alpha}}{\hat{\omega}^2}\boldsymbol{\Lambda} \end{bmatrix} \tag{3.17a}$$

$$\mathbf{D}^v = \begin{bmatrix} \mathbf{0} & \mathbf{0} \\ \mathbf{0} & \dfrac{2\hat{\alpha}\hat{\zeta}}{\hat{\omega}}\boldsymbol{\Lambda} \end{bmatrix} \tag{3.17b}$$

$$\mathbf{K}^v = \begin{bmatrix} \mathbf{K}^e(1+\hat{\alpha}) & \hat{\alpha}\mathbf{R} \\ \hat{\alpha}\mathbf{R}^{\mathrm{T}} & \hat{\alpha}\boldsymbol{\Lambda} \end{bmatrix} \tag{3.17c}$$

where $\boldsymbol{\Lambda} = G^{\infty}\bar{\boldsymbol{\Lambda}}$ and $\mathbf{R} = \bar{\mathbf{R}}\boldsymbol{\Lambda}$. Since the spectral decomposition determines the number dissipation coordinates that will be augmented onto the total system, the eigenvalue problem must be completed before the total degrees of freedom are known. The degrees of freedom depend on the number of non-negative eigenvalues of the stiffness matrix in addition to the size of the stiffness matrix and the number of terms in the complex modulus approximation. Generalizing this to a GHM approximation with n_{MOT} terms, the viscoelastic mass, damping and stiffness matrices have the following form

$$\mathbf{M}^v = \begin{bmatrix} \mathbf{M}^e & \mathbf{0} & \cdots & \mathbf{0} \\ \mathbf{0} & \dfrac{\hat{\alpha}_1}{\hat{\omega}_1^2}\boldsymbol{\Lambda} & \cdots & \mathbf{0} \\ \vdots & \vdots & \ddots & \vdots \\ \mathbf{0} & \mathbf{0} & \cdots & \dfrac{\hat{\alpha}_n}{\hat{\omega}_n^2}\boldsymbol{\Lambda} \end{bmatrix} \tag{3.18a}$$

$$\mathbf{D}^v = \begin{bmatrix} \mathbf{0} & \mathbf{0} & \cdots & \mathbf{0} \\ \mathbf{0} & \dfrac{2\hat{\alpha}_1\hat{\zeta}_1}{\hat{\omega}_1}\boldsymbol{\Lambda} & \cdots & \mathbf{0} \\ \vdots & \vdots & \ddots & \vdots \\ \mathbf{0} & \mathbf{0} & \cdots & \dfrac{2\hat{\alpha}_n\hat{\zeta}_n}{\hat{\omega}_n}\boldsymbol{\Lambda} \end{bmatrix} \tag{3.18b}$$

$$\mathbf{K}^v = \begin{bmatrix} \left(1 + \sum_{i=1}^{n} \hat{\alpha}_i\right) \mathbf{K}^e & -\hat{\alpha}_1 \mathbf{R} & \cdots & -\hat{\alpha}_n \mathbf{R} \\ \hat{\alpha}_1 \mathbf{R}^{\mathrm{T}} & \hat{\alpha}_1 \mathbf{\Lambda} & \cdots & \mathbf{0} \\ \vdots & \vdots & \ddots & \vdots \\ \hat{\alpha}_n \mathbf{R}^{\mathrm{T}} & \mathbf{0} & \cdots & \hat{\alpha}_n \mathbf{\Lambda} \end{bmatrix} \tag{3.18c}$$

The viscoelastic matrices are square matrices with a dimension $n_q + n_z$ where n_q is the number of physical coordinates and n_z is the number of dissipation coordinates dictated by the number of terms included in the approximation from Equation 3.8. To arrive at the global system of equations, the element matrices must be assembled into the global matrices. The degrees of freedom associated with the physical degrees of freedom are assembled using traditional finite element methods and the dissipation coordinate are simplify augmented to the system since the dissipation degrees of freedom for neighboring elements do not interact with each other.

3.3.2 Determination of damped natural frequency and damping values

For this system, the damping matrix is not necessarily a linear combination of the mass and stiffness matrices thus the system must be transformed into state space to determine the eigenvalues and eigenvectors. The method shown here does not require any matrix inversion thus is computationally fast compared than other methods [73]. The coordinates, $\mathbf{y}_1$ and $\mathbf{y}_2$ are defined as

$$\mathbf{y}_1 = \begin{bmatrix} \mathbf{q} \\ \mathbf{z} \end{bmatrix}, \quad \mathbf{y_2} = \begin{bmatrix} \dot{\mathbf{q}} \\ \dot{\mathbf{z}} \end{bmatrix} \tag{3.19}$$

Using the fact that, $\dot{\mathbf{y}}_1 = \mathbf{y}_2$ and by rearranging the viscoelastic equation of motion, Equation 3.16, the following relationships can be written

$$-\mathbf{K}^v \dot{\mathbf{y}}_1 = -\mathbf{K}^v \mathbf{y}_2 \tag{3.20a}$$

$$\mathbf{M}^v\dot{\mathbf{y}}_2 = -\mathbf{D}^v\mathbf{y}_2 - \mathbf{K}^v\mathbf{y}_1 \tag{3.20b}$$

Putting these equations into matrix form

$$\begin{bmatrix} -\mathbf{K}^v & \mathbf{0} \\ \mathbf{0} & \mathbf{M}^v \end{bmatrix} \begin{bmatrix} \dot{\mathbf{y}}_1 \\ \dot{\mathbf{y}}_2 \end{bmatrix} = \begin{bmatrix} \mathbf{0} & -\mathbf{K}^v \\ -\mathbf{K}^v & \mathbf{D}^v \end{bmatrix} \begin{bmatrix} \mathbf{y}_1 \\ \mathbf{y}_2 \end{bmatrix} \tag{3.21}$$

This leads to the following eigenvalue problem

$$\lambda\mathbf{A}\mathbf{v} = \mathbf{B}\mathbf{v} \tag{3.22}$$

The resulting complex eigenvalues can be related to the natural frequencies and damping ratios using the following relationships

$$\lambda_i = \zeta_i\omega_i - \omega_i\sqrt{1-\zeta_i^2}\jmath \tag{3.23a}$$

$$\lambda_{i+1} = \zeta_i\omega_i + \omega_i\sqrt{1-\zeta_i^2}\jmath \tag{3.23b}$$

with ω_i is the ith natural frequency and ζ_i is the damping factor of the ith natural frequency. Inverting these equations, the natural frequencies and damping ratios are calculated as

$$\omega_i = \sqrt{\mathrm{Re}[\lambda_i]^2 + \mathrm{Im}[\lambda_i^2]} \tag{3.24a}$$

$$\zeta_i = \frac{-\mathrm{Re}[\lambda_i]}{\sqrt{\mathrm{Re}[\lambda_i]^2 + \mathrm{Im}[\lambda_i]^2}} \tag{3.24b}$$

where Re[$\cdot$] represents the real part of the complex argument and Im[$\cdot$] represents the imaginary part.

3.3.3 Determining the GHM parameters

To use the GHM model, the form of Equation 3.8, evaluated along the imaginary axis ($s = \jmath\omega$) must be curve-fit to the complex modulus data from the 3D printed materials. The curve fit is performed in a logarithmic sense with equal weighting given to the real and imaginary parts. The number of terms necessary to obtain a good fit of the GHM approximation depends on the material, the frequency range, and the desired accuracy. In this paper, the frequency range of interest is 10 to 2,000 Hz. Depending on the shape of the curve at the temperature and frequency of interest dictates the number of GHM parameters used. For a complete data table of the GHM parameters for all materials tested, see Appendix B.

The DM 8430 tensile configuration data tested from 0° to 100° C, is shifted to various temperatures and a curve fit is performed on the resulting curves. The GHM fits are plotted over the frequency range of interest for temperatures ranging from 20° to 100° C in Figure 3.10. This figure shows the significant variation resulting from changes in temperature in both the storage modulus and the loss factor.

3.4 Dynamic response of structure made from viscoelastic materials

This section utilizes the GHM model described in the previous section and applies the model to specific structures to study the effect of the viscoelastic properties on the dynamic response of the structure, including the effects of changing the temperature. Additionally, the differences in the dynamic response due to the two testing configurations, tensile and cantilever described above will be explored. Lastly, an experimental prototype of a beam undergoing temperature change is used to validate the experimental characterization.

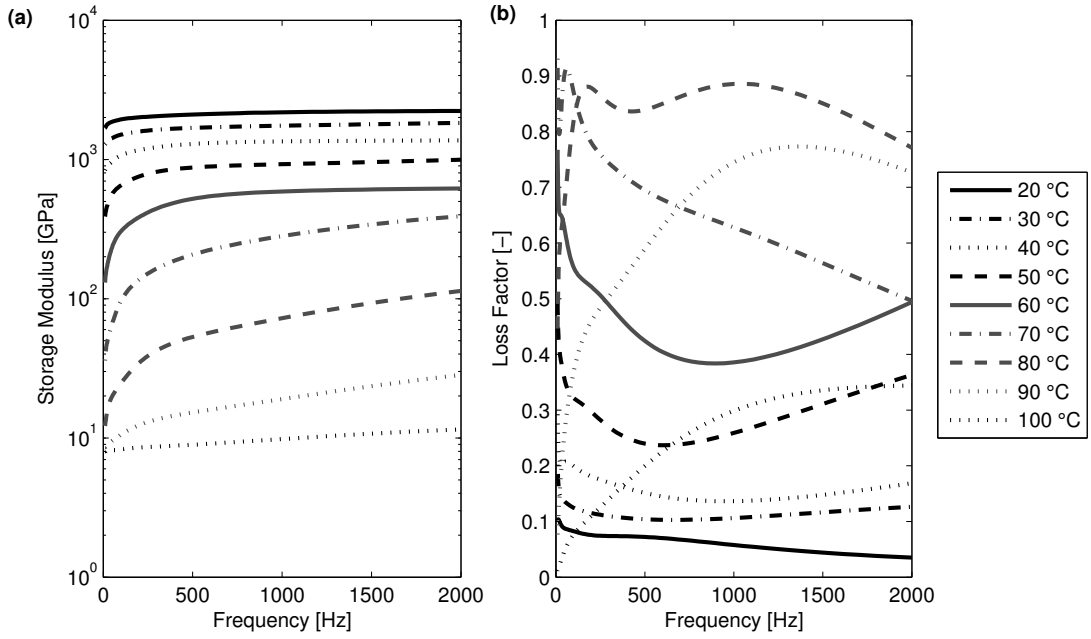

Figure 3.10: (a) Storage modulus and (b) loss factor data for DM 8430 at various temperatures

Table 3.5: Geometry properties of the bar model

Property	**Value**
Density [kg/m^3]	1168
Cross-section area [m^2]	1.131×10^{-3}
Length of bar [m]	45

3.4.1 Dynamic response of a viscoelastic solid bar

A uniform bar with a hollow rectangular cross-section made from a 3D printed viscoelastic material is modeled using a GHM model. The geometry and material properties of the bar are shown in Table 3.5. The bar is discretized into ten finite elements, with two nodes for each element. The bar is fixed at the base.

The elastic mass and stiffness elastic finite element matrices are given as [62]

$$\mathbf{M}^e_{\text{bar}} = \frac{\rho A \ell}{6} \begin{bmatrix} 2 & 1 \\ 1 & 2 \end{bmatrix} \tag{3.25a}$$

$$\mathbf{K}^{e}_{\text{bar}} = \frac{A}{\ell}\begin{bmatrix} 1 & -1 \\ -1 & 1 \end{bmatrix} \tag{3.25b}$$

By performing an eigenvalue analysis on the stiffness matrix, two degrees of freedom can be eliminated since they correspond to eigenvalues of zero.

$$\bar{\mathbf{R}}^{\text{T}}_{\text{bar}} = \begin{bmatrix} -\frac{-\sqrt{2}}{2} & \frac{\sqrt{2}}{2} \end{bmatrix} \tag{3.26a}$$

$$\bar{\mathbf{\Lambda}}_{\text{bar}} = \frac{2A}{\ell} \tag{3.26b}$$

Using Equations 3.18 the resulting viscoelastic finite elements matrices are

$$\mathbf{M}^{v}_{\text{bar}} = \begin{bmatrix} \frac{\rho A\ell}{3} & 0 & \cdots & 0 & \frac{\rho A\ell}{3} \\ 0 & \frac{2A}{\ell}\frac{\hat{\alpha}_1}{\hat{\omega}_1^2} & \cdots & 0 & 0 \\ \vdots & \vdots & \ddots & \vdots & \vdots \\ 0 & 0 & \cdots & \frac{2A}{\ell}\frac{\hat{\alpha}_{n_{\text{MOT}}}}{\hat{\omega}_{n_{\text{MOT}}}^2} & 0 \\ \frac{\rho A\ell}{6} & 0 & \cdots & 0 & \frac{\rho A\ell}{3} \end{bmatrix} \tag{3.27a}$$

$$\mathbf{D}^{v}_{\text{bar}} = \begin{bmatrix} 0 & 0 & \cdots & 0 & 0 \\ 0 & \frac{4A}{\ell}\frac{\hat{\alpha}_1\hat{\zeta}_1}{\hat{\omega}_1} & \cdots & 0 & 0 \\ \vdots & \vdots & \ddots & \vdots & \vdots \\ 0 & 0 & \cdots & \frac{4A}{\ell}\frac{\hat{\alpha}_{n_{\text{MOT}}}\hat{\zeta}_1}{\hat{\omega}_{n_{\text{MOT}}}} & 0 \\ 0 & 0 & \cdots & 0 & 0 \end{bmatrix} \tag{3.27b}$$

$$\mathbf{K}^{v}_{\text{bar}} = \frac{G^{\infty}A}{\ell}\begin{bmatrix} 1+\sum\hat{\alpha}_j & \sqrt{2}\hat{\alpha}_1 & \cdots & \sqrt{2}\hat{\alpha}_{n_{\text{MOT}}} & -(1+\sum\hat{\alpha}_j) \\ \sqrt{2}\hat{\alpha}_1 & 2\hat{\alpha}_1 & \cdots & 0 & -\sqrt{2}\hat{\alpha}_1 \\ \vdots & \vdots & \ddots & \vdots & \vdots \\ \sqrt{2}\hat{\alpha}_{n_{\text{MOT}}} & 0 & \cdots & 2\hat{\alpha}_{n_{\text{MOT}}} & -\sqrt{2}\hat{\alpha}_{n_{\text{MOT}}} \\ -(1+\sum\hat{\alpha}_j) & -\sqrt{2}\hat{\alpha}_1 & \cdots & -\sqrt{2}\hat{\alpha}_{n_{\text{MOT}}} & 1+\sum\hat{\alpha}_j \end{bmatrix} \tag{3.27c}$$

where the degrees of freedom have been rearranged to facilitate the assembly process

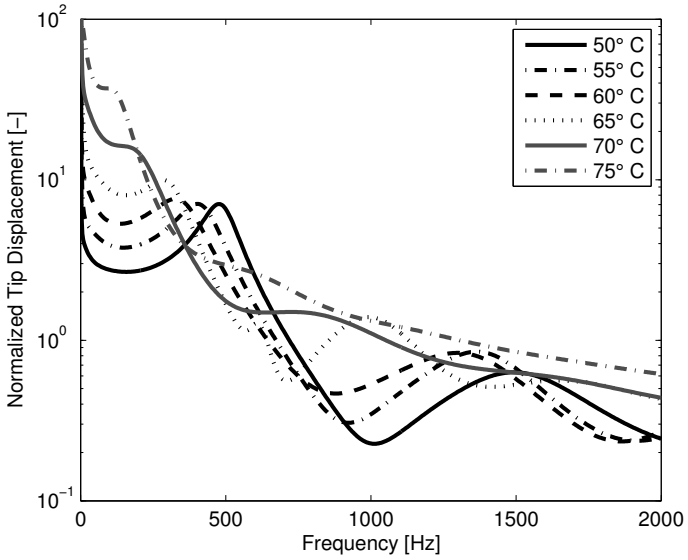

Figure 3.11: FRFs for a solid bar at varying temperatures

and to reduce the bandwidth of the final assembled matrices. Using the GHM parameters obtained at various temperatures, the FRFs are shown in Figure 3.11. These results show changing the temperature of a viscoelastic bar can cause a shift in the natural frequency and also affect the amount of damping at each natural frequency.

Next, the response of the same structure subjected to an impulse load at the tip of the bar is considered. The settling time of the response is calculated for the bar subjected to different temperatures. A plot of the settling time versus temperature is shown in Figure 3.12. Initially, as the temperature increases, the settling time decreases. This is due to the increasing damping in the material. After a certain temperature, an increase in temperature causes an increase in the settling time. As the temperature increases, the storage modulus decreases causing the material to be more compliant.

3.4.2 Dynamic response of a viscoelastic solid beam

A uniform beam made from a 3D printed viscoelastic material is modeled using a GHM model. The geometry and material properties of the beam are shown in Table 3.6. The

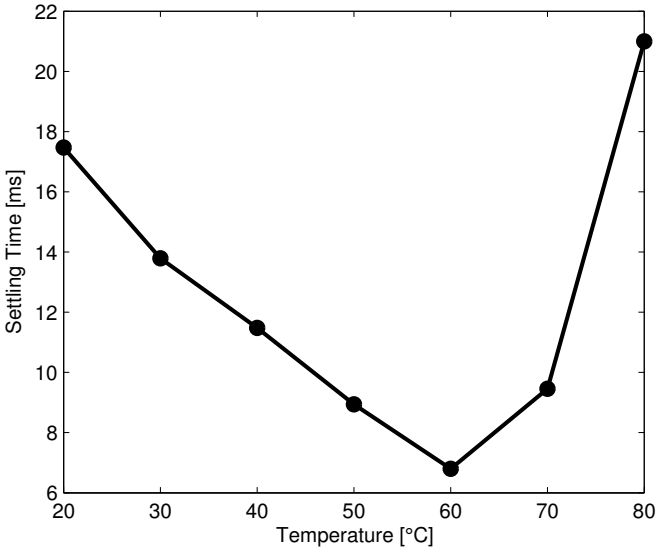

Figure 3.12: Settling time of a solid bar subjected to a unit impulse at varying temperatures

Table 3.6: Geometry and material properties of beam model

Property	**Value**
Density [kg/m^3]	1168
Cross-sectional width [mm]	12.71
Cross-sectional height [mm]	2.96
Length of beam [cm]	20.32
Cross-sectional area moment of inertia [m^4]	2.747×10^{-11}

VeroWhitePlus material properties are used for the model. The beam is discretized into five finite elements, with two nodes and four degrees of freedom, a displacement and rotational degree of freedom at each node.

The elastic mass and stiffness elastic finite element matrices are given as

$$\mathbf{M}^e_{\text{beam}} = \frac{\rho A \ell}{420} \begin{bmatrix} 156 & 22\ell & 54 & -13\ell \\ 22\ell & 4\ell^2 & 13\ell & -3\ell^2 \\ 54 & 13\ell & 156 & -22\ell \\ -13\ell & -3\ell^2 & -22\ell & 4\ell^2 \end{bmatrix} = \begin{bmatrix} \mathbf{M}_{11} & \mathbf{M}_{12} \\ \mathbf{M}_{21} & \mathbf{M}_{22} \end{bmatrix} \tag{3.28a}$$

$$\mathbf{K}^e_{\text{beam}} = \frac{G^\infty I}{\ell^3}\begin{bmatrix} 12 & 6\ell & -12 & 6\ell \\ 6\ell & 4\ell^2 & -6\ell & 2\ell^2 \\ -12 & -6\ell & 12 & -6\ell \\ 6\ell & 2\ell^2 & -6\ell & 4\ell^2 \end{bmatrix} = \begin{bmatrix} \mathbf{K}_{11} & \mathbf{K}_{12} \\ \mathbf{K}_{21} & \mathbf{K}_{22} \end{bmatrix} \tag{3.28b}$$

where ℓ is the length of the beam, ρ is the density of the material, and I is the area moment of inertia [62]. By performing an eigenvalue analysis on the stiffness matrix, two degrees of freedom can be eliminated since they correspond to eigenvalues of zero. The spectral decomposition results in

$$\bar{\mathbf{R}}^{\mathrm{T}}_{\text{beam}} = \begin{bmatrix} 0 & -\frac{\sqrt{2}}{2} & 0 & \frac{\sqrt{2}}{2} \\ \frac{2}{\ell\sqrt{8/\ell^2+2}} & \frac{1}{\ell\sqrt{8/\ell^2+2}} & \frac{-2}{\ell\sqrt{8/\ell^2+2}} & \frac{1}{\ell\sqrt{8/\ell^2+2}} \end{bmatrix} \tag{3.29a}$$

$$\bar{\mathbf{\Lambda}}_{\text{beam}} = \begin{bmatrix} \frac{2I}{\ell} & 0 \\ 0 & \frac{6I(\ell^2+4}{\ell^3} \end{bmatrix} \tag{3.29b}$$

$$\mathbf{R}^{\mathrm{T}}_{\text{beam}} = \frac{G^\infty I}{\ell^3}\begin{bmatrix} 6\sqrt{2(\ell^2+4)} & 3\sqrt{2(\ell^2+4)} & -6\sqrt{2(\ell^2+4)} & 3\sqrt{2(\ell^2+4)} \\ 0 & -\sqrt{2}\ell^2 & 0 & \sqrt{2}\ell^2 \end{bmatrix} = \begin{bmatrix} \mathbf{R}^{\mathrm{T}}_1 \\ \mathbf{R}^{\mathrm{T}}_2 \end{bmatrix} \tag{3.29c}$$

Using Equations 3.18, the viscoelastic finite element matrices are

$$\mathbf{M}^v_{\text{beam}} = \begin{bmatrix} \mathbf{M}_{11} & \mathbf{0} & \cdots & \mathbf{0} & \mathbf{M}_{12} \\ \mathbf{0} & \frac{\hat{\alpha}_1}{\hat{\omega}_1^2}\mathbf{\Lambda}_{\text{beam}} & \cdots & \mathbf{0} & \mathbf{0} \\ \vdots & \vdots & \ddots & \vdots & \vdots \\ \mathbf{0} & \mathbf{0} & \cdots & \frac{\hat{\alpha}_n}{\hat{\omega}_n^2}\mathbf{\Lambda}_{\text{beam}} & \mathbf{0} \\ \mathbf{M}_{21} & \mathbf{0} & \cdots & \mathbf{0} & \mathbf{M}_{22} \end{bmatrix} \tag{3.30a}$$

$$\mathbf{D}^{v}_{\text{beam}} = \begin{bmatrix} \mathbf{0} & \mathbf{0} & \cdots & \mathbf{0} & \mathbf{0} \\ \mathbf{0} & 2\frac{\hat{\alpha}_1\hat{\zeta}_1}{\hat{\omega}_1}\mathbf{\Lambda}_{\text{beam}} & \cdots & \mathbf{0} & \mathbf{0} \\ \vdots & \vdots & \ddots & \vdots & \vdots \\ \mathbf{0} & \mathbf{0} & \cdots & 2\frac{\hat{\alpha}_n\hat{\zeta}_n}{\hat{\omega}_n}\mathbf{\Lambda}_{\text{beam}} & \mathbf{0} \\ \mathbf{0} & \mathbf{0} & \cdots & \mathbf{0} & \mathbf{0} \end{bmatrix} \tag{3.30b}$$

$$\mathbf{K}^{v}_{\text{beam}} = \begin{bmatrix} \phi\mathbf{K}_{11} & \hat{\alpha}_1\mathbf{R}_1 & \cdots & \hat{\alpha}_n\mathbf{R}_1 & \phi\mathbf{K}_{12} \\ \hat{\alpha}_1\mathbf{R}_1^{\mathrm{T}} & \hat{\alpha}_1\mathbf{\Lambda} & \cdots & \mathbf{0} & \hat{\alpha}_1\mathbf{R}_2^{\mathrm{T}} \\ \vdots & \vdots & \ddots & \vdots & \vdots \\ \hat{\alpha}_n\mathbf{R}_1^{\mathrm{T}} & \mathbf{0} & \cdots & \hat{\alpha}_n\mathbf{\Lambda} & \hat{\alpha}_n\mathbf{R}_2^{\mathrm{T}} \\ \phi\mathbf{K}_{21} & \hat{\alpha}_1\mathbf{R}_2 & \cdots & \hat{\alpha}_n\mathbf{R_2} & \phi\mathbf{K}_{22} \end{bmatrix} \tag{3.30c}$$

where $\phi = 1 + \sum_{j=1}^{n_{\text{MOT}}} \hat{\alpha}_j$ and the degrees of freedom have been rearranged to facilitate global matrix assembly and reduce the bandwidth of the stiffness matrix reducing the computational time required for matrix inversion. This model is used to model a beam at various temperatures. Figure 3.13 shows how the settling time changes with temperature. The beam shows similar trends to the bar explained in the previous section.

3.4.3 Effects of testing configuration on dynamic response

This section looks at how using a tensile versus a cantilevered testing configuration during the material characterization affects the GHM model results. During the characterization of the viscoelastic material properties of the 3D printed materials, two different testing configurations were utilized, cantilevered and tensile. The DMA machine has various clamps which can be utilized to obtain the dynamic modulus values. The cantilevered clamp fixes one end of the beam while forcing the other end to move cyclically. The tensile clamp places the specimen in tension with one end staying fixed and the other end moving cyclically [103]. The comparison in testing configuration was completed on the DM 8430 material, which is slightly less stiff than the VeroWhitePlus material used in the previous sections. Using the

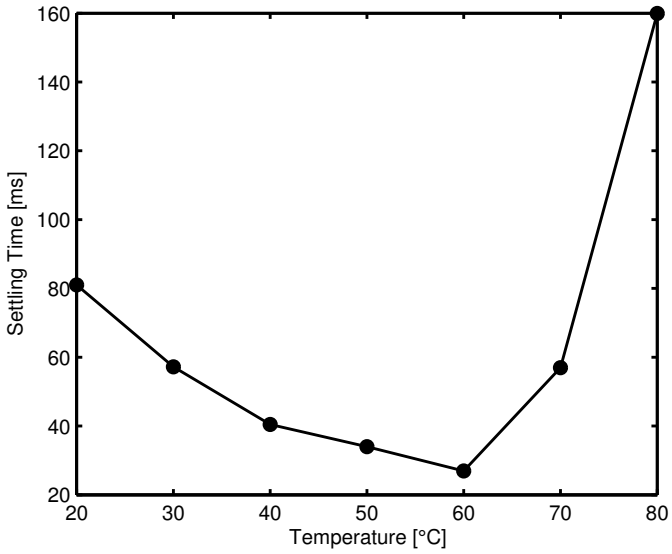

Figure 3.13: Settling time of a solid beam subjected to a unit impulse at varying temperatures

dynamic modulus data produced from the DMA machine, GHM parameters were fit to the data for both testing configurations described above. The GHM parameters were then used to model the solid beam described above. The natural frequency and damping of the first two modes were obtained for temperatures ranging from 50° to 70° C. The focus of this work is on the first mode, since this mode dominates the response in metastructure applications. The second mode was obtained to see how accurate the model is. These natural frequency and damping values are plotted in Figure 3.14. These results show that the tensile testing configuration leads to a higher natural frequency than the cantilevered configuration. This difference is more pronounced in the second mode than the first. Additionally, the tensile configuration results in lower damping values than the cantilevered configuration. The FRF for these two cases at a temperature of 50° C can be seen in Figure 3.15. This shows that the testing configuration used to obtain the material properties can make a significant difference in the results from the GHM model.

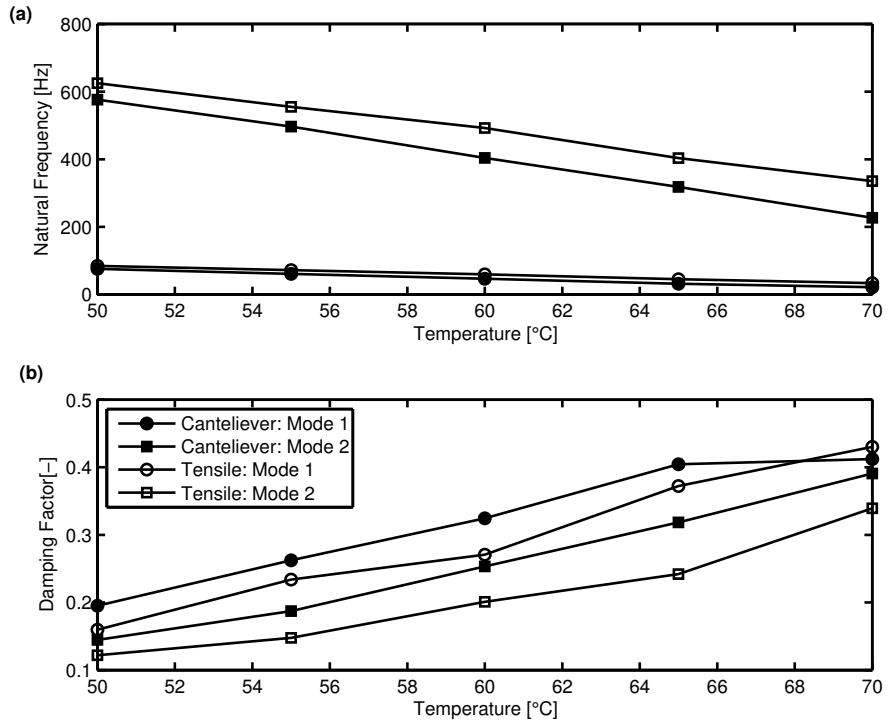

Figure 3.14: Variations in the (a) natural frequency and (b) damping factor of a cantilevered beam modeling using GHM parameters obtained from a cantilevered and tensile testing configuration

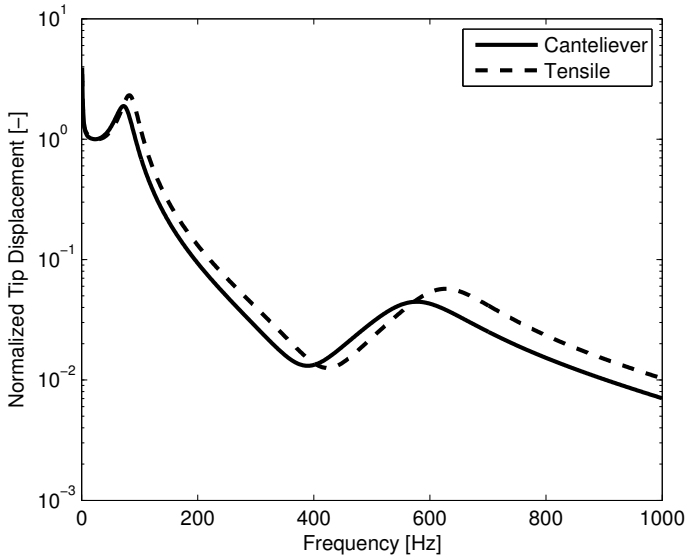

Figure 3.15: Variations in the FRF factor of a cantilevered beam at 50° C modeling using GHM parameters obtained from a cantilevered and tensile testing configuration

3.4.4 Experimental verification of material characterization

Next, the trends are experimentally validated using a beam model. The experimental model was printed using the Objet Connex 3D printer with dimensions of $8 \times 12 \times 120$ mm. The beam was clamped at the base and placed in a thermal chamber. The chamber tested the beam at 20°, 30°, and 40° C. Once the chamber reached the desired temperature, a soak time of 30 mins was used to allow the entire specimen to reach a uniform temperature. A small magnetic disk was glued to the tip of the beam, and a magnetic transducer provided an excitation force to the tip. The response of the beam was measured as the tip using a laser Doppler vibrometer mounted to the outside of the chamber and measured through a glass window. A National Instruments data acquisition system was used provide the excitation signal to the magnetic transducer via a voltage amplifier and to collect the signals from the laser vibrometer. Ten sine sweeps from 0 Hz to 1500 Hz were conducted and the resulting FRFs averaged together. A curve fitting procedure was then performed on the averaged FRF to obtain the natural frequencies and damping factors for the first two modes. During the tests at temperatures higher than 40° C, the beam became complaint resulting in the tip of the beam getting stuck to the magnetic transducer.

For the GHM model used in the comparison, the material characterization from VeroWhitePlus tested in the tensile configuration was used. The tensile configuration was performed at lower temperatures allowing overlap between the experimental data and the modeled results. The GHM model was created as described in the solid beam section above.

The results comparing the experimental results to the GHM model at various temperatures are shown in Figure 3.16. For the natural frequency, the results show good agreement of the first mode, which is the focus of this paper. The second mode has more significant deviations. This could be attributed to a number of issues. The shift could be due to the effect of testing configuration as described in the previous section. The experimental beam was tested in a cantilevered configuration, but the material characterization data was obtained using a tensile configuration. The tensile configuration produced higher natural

frequency values than the cantilevered configuration, which was also more evident in the second mode. Additionally, the frequency range of the curve fit could be increased and more GHM parameters used to improve the accuracy of the model. This would also increase the degrees of freedom of the model. Since the focus of this work is on the first mode, this was not explored.

Based on the results from the previous section, it would be expected that the GHM model would predict damping factors lower than that of the experimental results, but this is not the case. This shows that the GHM mode is not able to accurately predict the amount of damping in the beam for this example. This could be due to the mismatch in the dimensions of the material characterization testing specimen compared to the beam used for these experimental results. Additionally, the testing clamp used to obtain the dynamic modulus could have introduced damping into the structure that was not produced from the viscoelastic effects of the 3D printed material. The beam used for the experimental results used a non-contact excitation method along with a non-contact transducer which introduces less damping into the system. Although the GHM model is not able to predict the correct amount of damping in the structure, it can capture the trends due to a temperature change which will allow us to explore the effects of temperature change using a GHM model.

3.5 Chapter summary

The complex modulus properties of the inkjet printed material from the Objet Connex printer have been determined. These materials show viscoelastic effects, which should be considered when modeling these materials for use in vibration applications, particularly in situations where there are significant temperature changes. Although all materials show viscoelastic effects, the TangoPlus material exhibits greater variations in the storage modulus and loss factor than the VeroWhitePlus, DM 8430, and DM 8420. Additionally, the effects of testing configuration and print direction were also investigated. The results show that variations in the in-plane print direction do not affect the response of the material for both

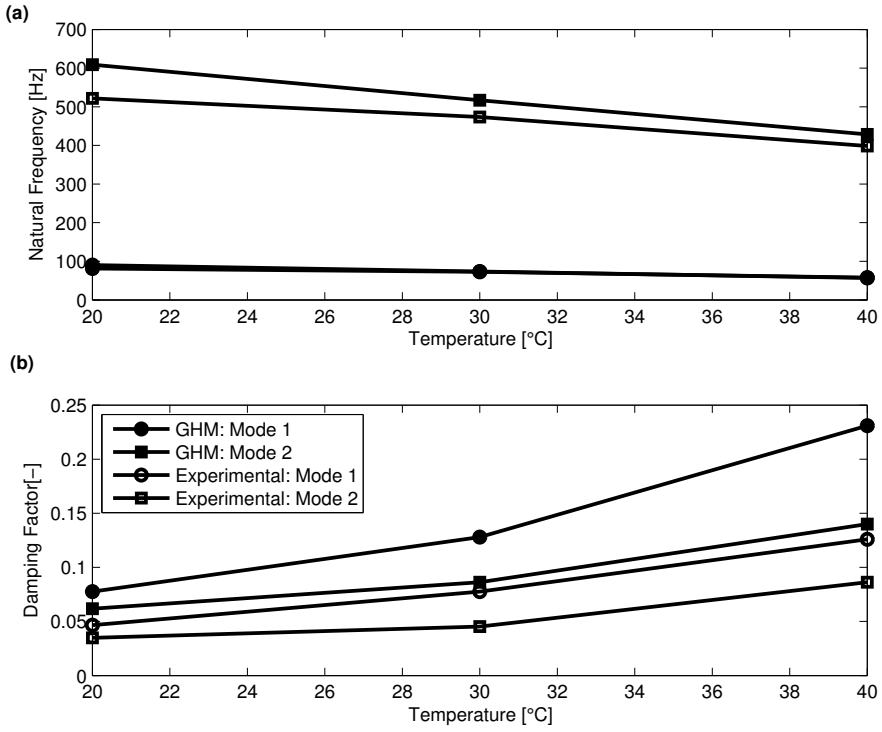

Figure 3.16: Comparison of the (a) natural frequencies and (b) damping factors of a GHM model and experimental results for a 3D printed VeroWhitePlus cantilevered beam

the tensile and cantilevered configurations. The testing configuration does have a slight effect on the complex modulus values.

These results show that the GHM model can accurately predict the fundamental natural frequency of a structure printed using the Objet Connex 3D printer. It can also predict the changes in the natural frequency due to temperature changes. This paper shows the complete process required to accurately use the GHM model; starting from the material characterization of the viscoelastic material properties to the experimental verification of the model.

The change in temperature can significantly alter both the storage modulus and the loss modulus of the material; these changes lead to changes in the natural frequencies and the damping of the resulting structure. When experimentally characterizing the viscoelastic material properties of the 3D printed material, the testing configuration of the specimen should be carefully considered. This work showed that the tensile testing configuration led to higher natural frequencies and lower damping values than the cantilevered configuration. The experimental verification results also had lower damping values than the modeled results.

Lastly, the GHM model developed was used to model the dynamics of a metastructure and studies the effects of a changing temperature. The results showed that the changes in the natural frequency of the host structure and the vibration absorbers changed at a similar rate, resulting in similar trends in the dynamic response as the temperature increase. This was true up to a specific temperature when the performance of the metastructure significantly decreased resulting in the baseline structure have better performance.

CHAPTER IV

Mass-Conserved Distributed Mass Metastructure

This chapter builds off of the previous two chapters. The lumped mass metastructure concept developed in Chapter II is expanded to a distributed mass model to allow for a potentially more accurate model. Additionally, the viscoelastic modeling methods developed in Chapter III are applied to the distributed mass metastructure model to capture the effects of damping inherent in the 3D printed materials. Additionally, this model is used to explore the effects of temperature on the performance of the metastructure. This chapter begins by explaining the metastructure design used throughout the rest of this dissertation. Similar to Chapter II, the metastructures in this chapter look to suppress vibrations along the axial direction of the bar. Starting with a simple 1D model, allows the effects to be explored more easily. Cantilevered beams with tip masses are used for the distributed vibration absorbers. Similar to the lumped mass metastructures, the main design parameters of the metastructure are the number of absorbers, the mass ratio and the natural frequencies of the absorbers. Initially, this design concept is verified using commercial finite element software and experimental testing. The next section develops an elastic model of the absorbers and the metastructure using finite element techniques. The following section extends the elastic model to a viscoelastic model using the GHM model as described in the previous chapter. Next, the effects of varying the metastructure parameters on the performance of the structure are explored. This is accomplished by examining many different configurations with a

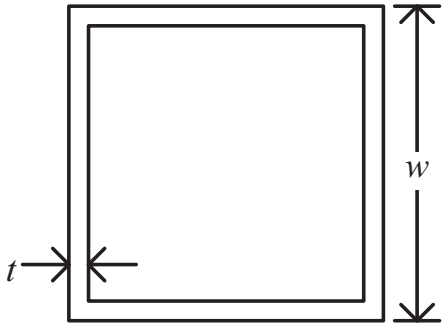

Figure 4.1: Cross-section of the host and baseline structure

different number of absorbers and different mass ratios. For each one of these configurations, the optimal natural frequencies of the absorbers are found. Of these different metastructure designs, one design is printed and experimentally tested. This design is printed on the Objet Connex 3D printer, and a modal analysis is performed to compare the results. Lastly, the effects of temperature on the metastructure are explored using the viscoelastic GHM model.

4.1 Metastructure design

The metastructure design used here has been studied in previous work [97, 104] and is designed to suppress vibrations along the axial direction of the metastructure bar. The metastructure is composed of the host structure and the vibration absorber system. The host structure has a hollow square cross-section as seen in Figure 4.1 and is the component of the structure in which lower vibrations are desired. The vibration absorbers are cantilevered beams with a tip mass arranged such that the bending motion of the cantilevered beams absorbs vibrations along the axial direction of the bar as seen in Figure 4.2, where the axial vibrations are in the horizontal direction.

The performance of the metastructure is compared to a baseline structure which has the same weight as the metastructure but with no vibrations absorbers distributed throughout the length of the bar. The baseline structure has the same cross-section design as the host

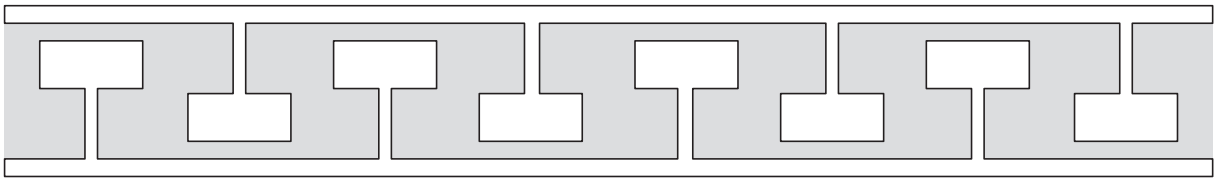

Figure 4.2: Schematic of metastructure. Vibrations occur along the horizontal direction.

section as depicted in Figure 4.1 but with a slightly different thicknesses to account for the weight constraint. Restricting the metastructure and the baseline structure to have the same weight allows any performance gains in the metastructure to be attributed to the addition of the distributed vibration absorbers and not due to any mass added to the structure.

4.1.1 Design parameters

The design of the metastructure is characterized by the number of vibration absorbers, N, the mass ratio, μ, and the natural frequency of the individual vibration absorbers, ω_i. The mass ratio is the ratio of the mass of the absorbers over the total mass of the structure and is defined as

$$\mu = \frac{\sum_{i=1}^{N} m_i}{\sum_{i=1}^{N} m_i + m_{\text{host}}} \tag{4.1}$$

where m_i is the mass of the ith absorber and m_{host} is the mass of the host structure. Similar to the lumped mass metastructure described in Chapter II, this mass ratio provides a measure of how much mass is being redistributed to the absorber system. A higher mass ratio represents more mass in the absorber system.

The natural frequencies of the vibrations absorbers are varied by changing the geometry of the absorbers. For example, making the tip mass larger and therefore heavier will lead to a lower natural frequency, but increasing the thickness of the beam leads to a higher stiffness and therefore a higher natural frequency. Throughout this chapter, various methods are used

to determine the relationship between the geometric parameters and the resulting natural frequency.

4.1.2 Verification of design

This section looks at the proposed design and verifies that the design produces the desired effects by looking a commercial finite element model and experimental results. The finite element model is based on an elastic model. Verifying that an elastic model produces similar trends as the experimental results is a necessary first step. This verification gives us confidence in the actual design of the metastructure and provides an intermediate step before using more complicated models.

The specific design used for this verification is based on the optimal lumped mass metastructure design from Section 2.5.3. The metastructure has ten vibration absorbers and a mass ratio of 0.206. This section begins by explaining how the natural frequencies of the vibration absorbers were chosen then goes into the details of the finite element and the experimental results. The results of the finite element verification are based off two papers by the authors [97, 104]. These results look at two different metastructure designs, one where all the vibration absorbers are tuned to the same frequency and another design where the vibration absorbers are tuned to linearly varying natural frequencies. The finite element results compare both metastructure designs to the baseline structure. The experimental results test the baseline structure and the metastructure with vibration absorbers having a constant natural frequency.

The material properties utilized are those from the Objet Connex 3D printer by Stratasys, specifically the DM 8430 digital material, which has been studied in detail in Chapter III. The parameters used for the baseline structure and metastructures are detailed in Table 4.1. Both the host structure and the baseline structure have cross-sections as shown in Figure 4.1. The parameters are chosen such that the baseline structure and the metastructure have the same mass, cross-sectional width, and length. The other parameters are varied such that

Table 4.1: Parameters for baseline structure and metastructure used in the design verification

Parameter	**Value**
Young's Modulus, E	1970 MPa
Density, ρ	1.168 g/cm^3
Mass ratio, μ	0.206
Number of absorbers, N	10
Host width, w_{host}	50 mm
Host thickness, t_{host}	5 mm
Host cross-sectional area, A_{host}	9.00 cm^2
Host length, ℓ_{host}	45 cm
Host mass, m_{host}	474 g
Total absorber mass, $\sum_{i=1}^{N} m_i$	123 g
Individual absorber mass, m_i	12.3 g
Total metastructure mass, $m_{\text{metastructure}}$	597 g
Baseline width, w_{baseline}	50 mm
Baseline thickness, t_{baseline}	6.5 mm
Baseline cross-sectional area, A_{baseline}	11.3 cm^2
Baseline mass, m_{baseline}	595 g
Baseline length, ℓ_{baseline}	45 cm

the mass ratio and number of absorber parameters are met.

To determine the desired natural frequencies of the absorbers, a 1D finite element model was created in MATLAB. Because of the simplicity of the 1D model, the simulation runs quickly and can be optimized easily in order the find the ideal range of natural frequencies of the absorbers. This 1D finite element model is depicted in Figure 4.3. The host structure is modeled as a distributed mass bar represented as the grey rectangle, and the vibration absorbers are modeled as lumped masses. The host structure is discretized into 110 elements

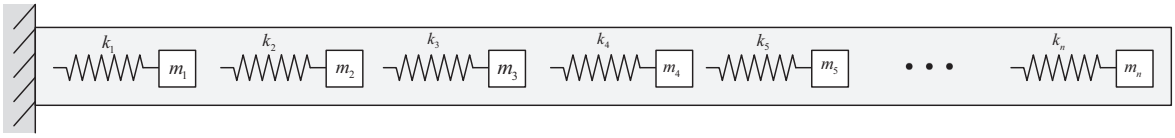

Figure 4.3: 1D finite element model with lumped mass vibration absorbers

along the length of the bar, and a simple 2-noded bar element is utilized. The vibration absorbers are modeled as lumped masses and springs. The absorbers are distributed evenly throughout the length of the bar. The necessary parameters for the finite element model are calculated using the parameters from Table 4.1. The bar finite element matrices are

$$\mathbf{M} = \frac{m_e}{6}\begin{bmatrix} 2 & 1 \\ 1 & 2 \end{bmatrix} \tag{4.2a}$$

$$\mathbf{K} = k_e\begin{bmatrix} 1 & -1 \\ -1 & 1 \end{bmatrix} \tag{4.2b}$$

where k_e and m_e for the metastructure are calculated by

$$k_e = \frac{nEA_{\text{host}}}{\ell_{\text{host}}} \tag{4.3a}$$

$$m_e = \frac{\rho A_{\text{host}}\ell_{\text{host}}}{n} \tag{4.3b}$$

where n is the number elements along the length of the bar. The lumped parameters, m_i and k_i are added to the corresponding degrees of freedom. The value for m_i is found in Table 4.1 and k_i is varied during the optimization. Varying the stiffness of the vibration absorbers results in different natural frequencies of the of the absorbers leading to a different response in the structure. All other parameters are kept constant, and just the stiffness values are varied. The stiffness values are constrained to vary in a linear fashion; thus the minimum and maximum values characterize these values. The objective function of the optimization is the area under frequency response function, the H_2 norm, as described in Section 2.2. The optimization is done in MATLAB using a constrained non-linear interior point algorithm (`fmincon`). The results of the optimization show that the natural frequencies of the absorbers should vary from 1100 to 450 Hz in order the achieve the best performance. The natural frequency of the host structure is 721 Hz.

To vary the natural frequency of the absorber, the cross-sectional area of the beam is varied. A larger thickness of the beam leads to a stiffer absorber which raises the natural frequency. To keep the mass of all the vibration absorbers constant, the cross-sectional area of the beam is restricted to be constant throughout the entire structure. Thus, an increased thickness of the beam will result in a decrease in the width of the beam. To determine the natural frequencies of the vibration absorbers, a 3D finite element model was used. Each absorber was modeled by itself attached to the host structure and a modal analysis performed. This allowed the stiffness of the host structure to be accounted for while eliminating the interactions between the various vibration absorbers. The results of this modeling are shown in Table 4.2. The entire range of frequencies from the optimization procedure described above was not able to be achieved with the geometry constraints given. The optimization called for frequencies ranging from 1100 to 450 Hz. To reach frequencies above 940 Hz, the thickness of the beam needed to be greater than 21 mm. The absorber mass is 21 mm in length on each side; thus the dimensions of the beam must be less than 21 mm. The dimensions are shown in Table 4.2 are used for the final design of the metastructure with varying frequencies. The metastructure with vibration absorbers having a single frequency used absorber 7 for all ten of the vibration absorbers which has a natural frequency closest to that of the host structure, 721 Hz.

4.1.2.1 Finite element modeling

The 3D finite element modeling is done in Abaqus using the geometry provided in the previous section. The finite element models compare three different structures all of which have the same weight as described in the previous section. Three-dimensional models of the baseline structure and the metastructure with vibration absorbers of linearly varying natural frequencies are shown in Figure 4.4.

Symmetry conditions were used, requiring only half of the model to be used as seen in Figure 4.5. The model used 3D tetrahedral elements, and the mesh for the metastructure

Table 4.2: Geometric properties of the vibration absorbers and the resulting natural frequencies

Absorber	**Thickness [mm]**	**Width [mm]**	**Area [mm^2]**	**Distance from root [cm]**	**Finite element frequency [Hz]**
1	20.3	4.93	100.1	40.9	939.8
2	18.7	5.30	99.1	36.8	913.9
3	17.2	5.81	99.9	32.7	875.4
4	15.6	6.38	99.5	28.6	839.2
5	14.1	7.07	99.7	24.5	794.8
6	12.6	7.94	100.0	20.5	764.0
7	11.1	9.05	100.0	16.4	648.3
8	9.5	10.5	99.9	12.3	610.6
9	8.0	12.6	100.4	8.2	564.2
10	4.9	20.5	100.0	4.1	426.5

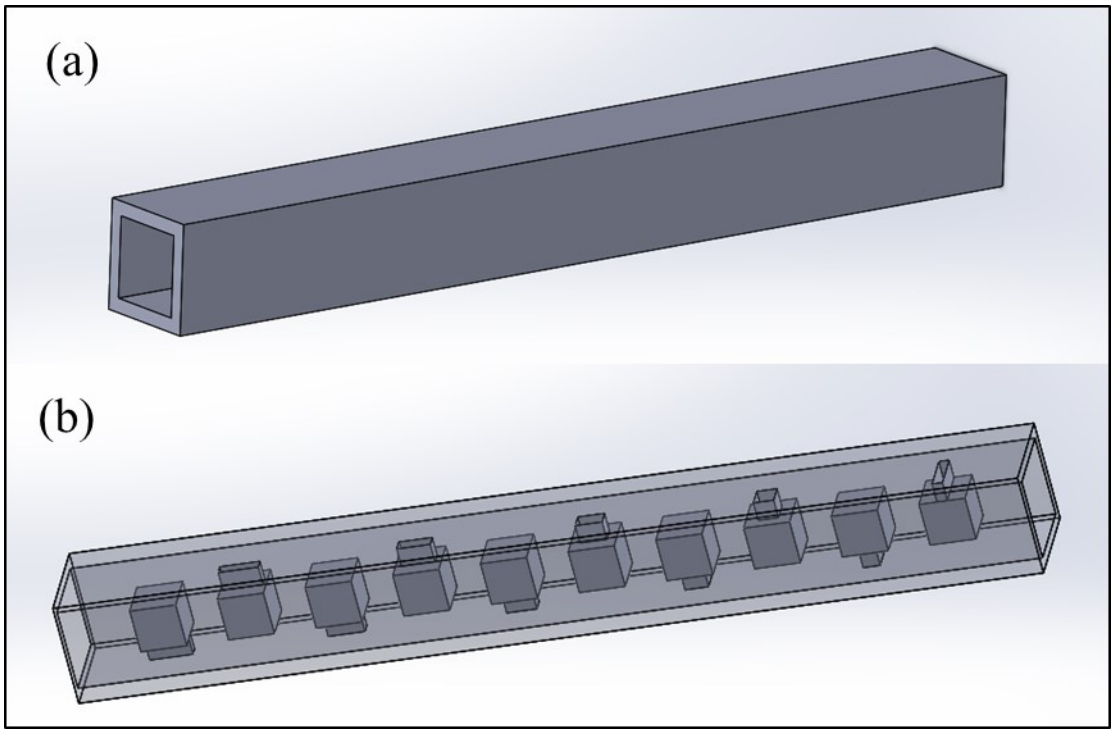

Figure 4.4: Three dimensional models of (a) baseline structure and (b) metastructure with vibration absorbers with linearly varying natural frequencies

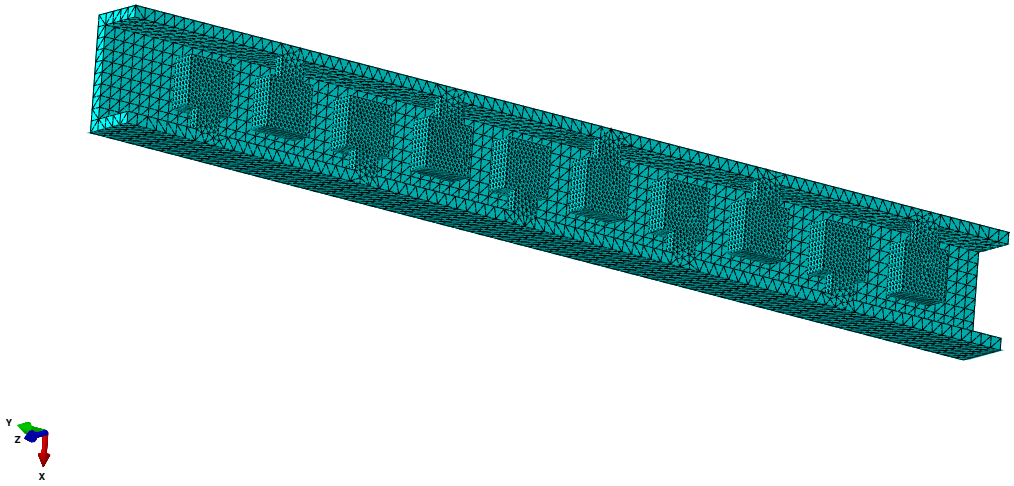

Figure 4.5: Mesh used for the metastructure with vibration absorbers having constant natural frequencies

with vibration absorbers with constant frequencies can be seen in Figure 4.5. The other two structures had similar meshes. One end of the structure was fully constrained to simulate a clamped condition. A cyclically varying force was applied to the other end in the axial direction. The frequency of the force varied from 0 to 1500 Hz, the frequency range of interest. At each frequency, the steady-state amplitude was calculated, and the resulting FRF was plotted. All the FRFs plotted are normalized with respect to the static response of the baseline structure.

4.1.2.2 Experimental testing

An experimental FRF was obtained using the set-up shown in Figure 4.6. The baseline structure and the structure with absorbers tuned to a single frequency were tested experimentally. The structure is secured to the surface of a large object to emulate the clamped boundary condition. For these structures, a base with through holes for fasteners was added to the CAD model and printed with the structure. The fasteners were inserted into tapped holes on a large table as seen in Figure 4.7.

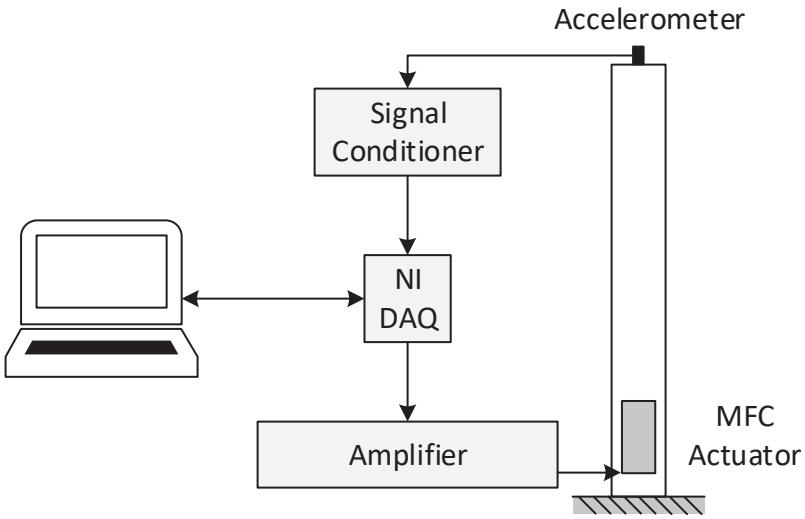

Figure 4.6: Experimental set-up used for testing of metastructure

Two Macro Fiber Composite (MFC) patches were added to each side of the structure. The MFC patches used are P1-type actuators manufactured by Smart Materials Corporation with an active area of 85 by 28 mm (M8528-P1). The patches were attached to the surface of the structure using 3M^{TM} Scotch-Weld^{TM} Epoxy Adhesive DP460. The adhesive was applied to the surface of the MFC and placed onto the surface of the metastructure. Next, the structure was placed in a vacuum bag to ensure the adhesive was evenly applied with no air bubbles. The adhesive cured for 8 hours in the vacuum bag. After the MFCs were bonded to the surface of the metastructure, wire leads were soldered to the electrodes of the MFCs and arranged in parallel such that the same voltage is applied to each MFC. This produces an elongation force along the axial direction of the structure.

The voltage applied to the MFC actuators is controlled using a National Instruments Data Acquisition (NI DAQ) system and LabVIEW. The voltage signal is fed through an amplifier to provide a sine signal with a peak-to-peak amplitude of 40 volts.

The response of the structure is measured using an accelerometer mounted to the top of the structure oriented to measure accelerations along the axial direction of the structure. The voltages are feed through a signal conditioner and read using the NI DAQ. The LabVIEW

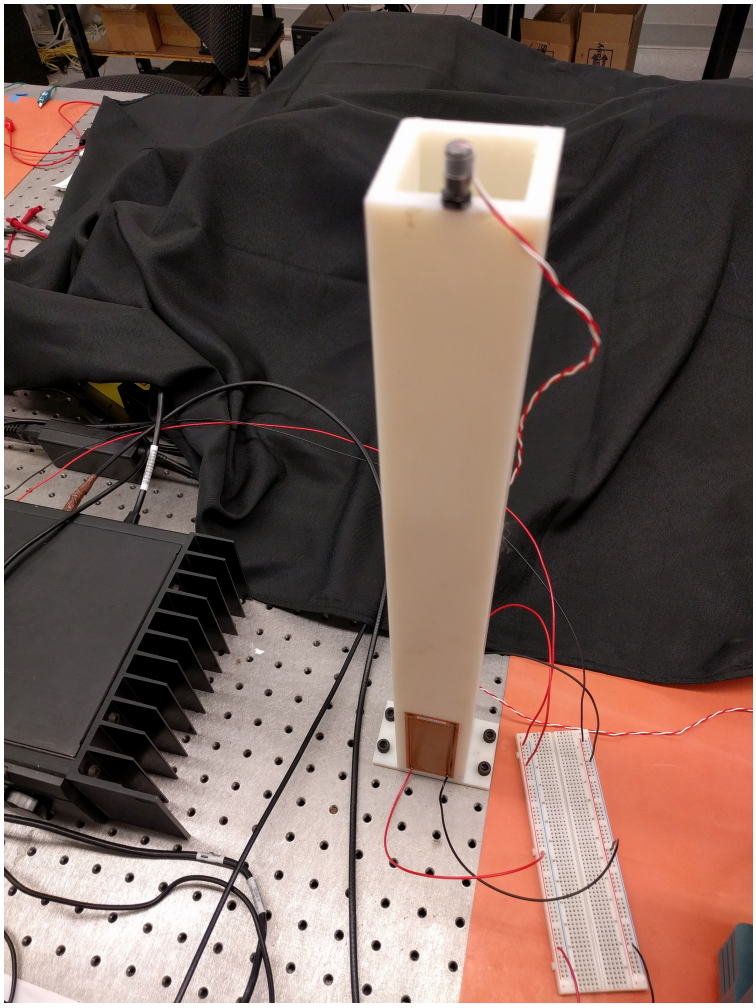

Figure 4.7: Experimental set-up for testing

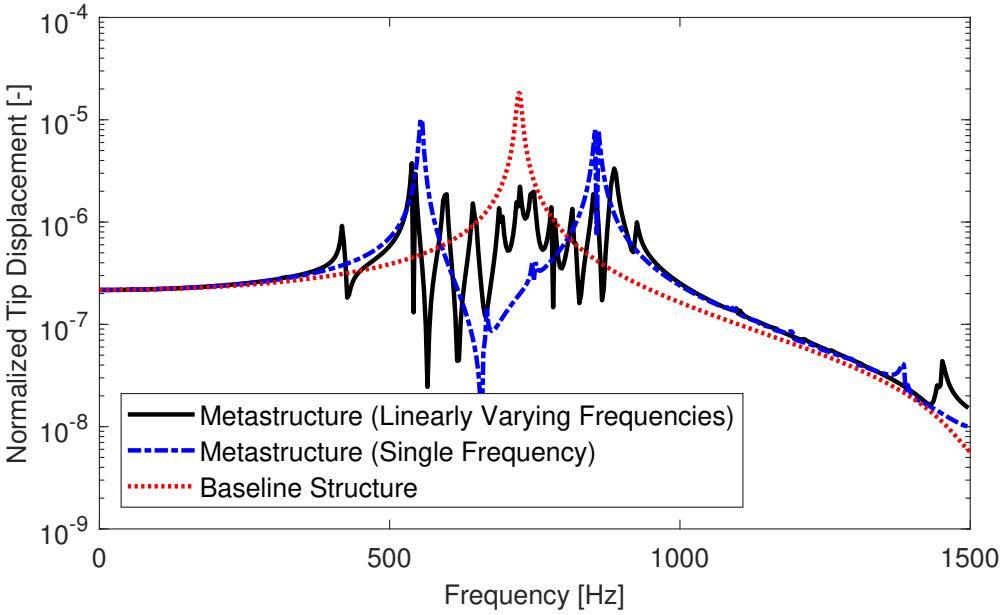

Figure 4.8: FRFs for the finite element models of the metastructures and baseline structure

software calculates an FRF of the tip acceleration due to an excitation force at the base using these signals. The accelerations are then converted to displacements in the frequency domain.

4.1.2.3 Results

This section presents the results from the finite element model and the experimental tests described in the previous two sections. The FRFs from the finite elements models are shown in Figure 4.8. For the metastructure with a single vibration absorber, there are clearly two peaks on either side of the natural frequency of the baseline structure. The metastructure with multiple frequencies has many small peaks which can be seen throughout the range of frequencies of interest. These trends match those from the lumped mass models.

Figure 4.9 shows the experimental FRFs for the two structures tested experimentally, the baseline structure and the metastructure with absorbers tuned to a single frequency. Once again, the expected trend of the metastructure having two split peaks is clearly shown in the experimental results. These results show that the proposed design leads to the desired

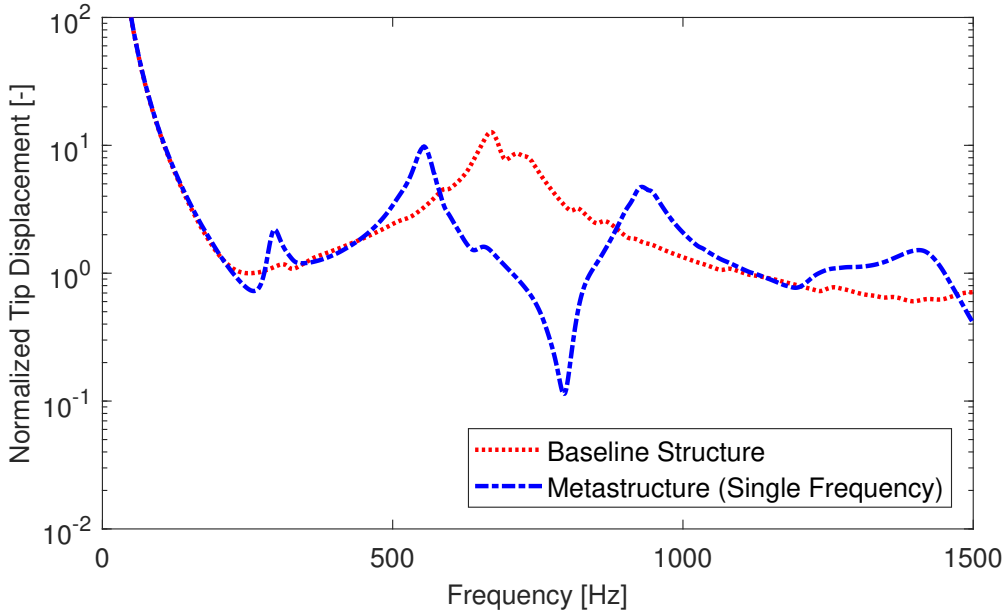

Figure 4.9: FRFs from experimental testing of the metastructure and baseline structure

trends in the resulting FRF of the structures.

4.2 Elastic metastructure modeling

To develop a viscoelastic finite element model using the GHM model, the elastic model finite element model must be developed first. This section explains the elastic modeling procedure used to model the vibration absorbers and the whole metastructure. These models are based on the beam and bar models developed in the previous chapter and are expanded upon here to be used for this specific metastructure design. This section begins by developing the model for a single vibration absorber, then incorporates that model into a full metastructure model.

4.2.1 Elastic model of a single vibration absorber

A single vibration absorber is composed of a beam with a tip mass. The dimensions of the vibration absorber are defined in Figure 4.10a and Figure 4.10b shows the equivalent

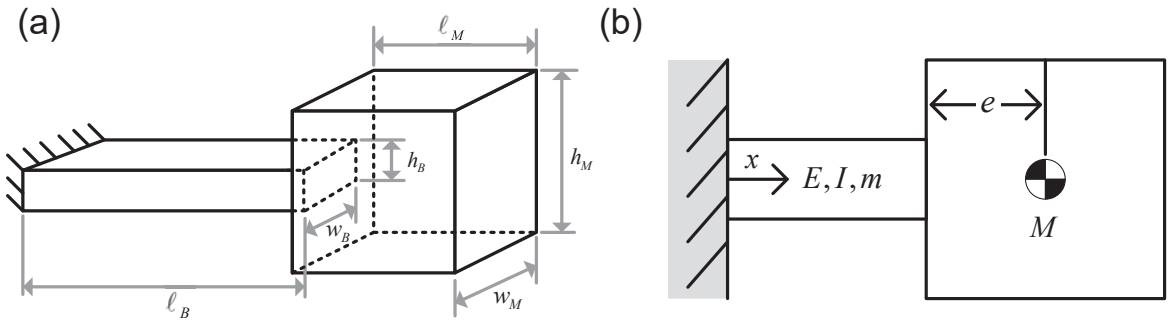

Figure 4.10: Schematics of the vibration absorber consisting of a cantilevered beam with a tip mass where (a) shows the dimensions of the vibration absorber and (b) shows the effective properties used for modeling

Table 4.3: Effective properties of the vibration absorber

Property	**Equation**
Area moment of inertia of beam	$I = \frac{1}{12} w_B h_B^3$
Cross-sectional area of beam	$A = w_B h_B$
Eccentricity of tip mass	$e = \frac{\ell_M}{2}$
Mass of tip mass	$m_M = \rho \ell_M w_M h_M$
Polar moment of inertia of tip mass	$J = \frac{1}{12} m_M (h_M^2 + \ell_M^2) + \frac{1}{2} m_M e^2$

properties used in the finite element model. These equivalent properties are calculated using the equations shown in Table 4.3.

The vibration absorber is discretized into elements along the length of the beam and the typical beam finite elements from the solid beam section are used for all elements except the element closest to the tip. The tip element must also include the effects of the tip mass. Since the tip mass is relatively large, both the rotational and translational motion of the tip mass must be accounted for. This is derived using energy methods. The kinetic energy expression of the tip element is

$$T = \frac{1}{2} \int_{x_1}^{x_2} \rho A \dot{w}^2 \mathrm{d}x + \frac{1}{2} m_M \left[\dot{w}(x_2) + e\dot{w}'(x_2) \right]^2 + \frac{1}{2} J \dot{w}'(x_2)^2 \tag{4.4}$$

where $w(x)$ is the vertical displacement of the beam, x_1 and x_2 are the coordinates of the

first and second node of the element, the dot represents the partial derivative with respect to time, and the prime represents the partial derivative with respect to x. Using typical finite element methods, the vertical displacement of the beam can be represented using the following separation of variables

$$w(x,t) = \mathbf{H}(x)\mathbf{r}(t) \tag{4.5}$$

where $\mathbf{H}(x)$ is a vector of shape functions and $\mathbf{r}(t)$ is a vector of the time-varying components of each shape function

$$\mathbf{r}(t) = \begin{bmatrix} r_1 & r_1' & r_2 & r_2' \end{bmatrix}^{\mathrm{T}} \tag{4.6}$$

The shape functions are defined as

$$\mathbf{H}(\xi) = \frac{1}{4}\begin{bmatrix} (1-\xi)^2(2+\xi) & \frac{2}{\ell}(1-\xi)^2(\xi+1) & (1+\xi)^2(2-\xi) & \frac{2}{\ell}(1-\xi)^2(\xi-1) \end{bmatrix} \tag{4.7}$$

where the shape function is defined in terms of ξ instead of x. The transformation between the two variables is described as

$$x = \frac{x_1 + x_2}{2} + \frac{x_2 - x_1}{2}\xi \tag{4.8}$$

Substituting Equation 4.5 into Equation 4.4

$$T = \frac{1}{2}\dot{\mathbf{r}}^{\mathrm{T}}\left\{\rho AL\int_{x_1}^{x_2}\mathbf{H}^{\mathrm{T}}(\xi)\mathbf{H}(\xi)\frac{\ell}{2}\mathrm{d}\xi + m_M[\mathbf{H}(x_2) + e\mathbf{H}'(x_2)]^{\mathrm{T}}[\mathbf{H}(x_2) + e\mathbf{H}'(x_2)] + J\mathbf{H}'(x_2)^{\mathrm{T}}\mathbf{H}'(x_2)\right\}\dot{\mathbf{r}} \tag{4.9}$$

where ℓ is the length of the element. Using the fact that $T = \mathbf{r}^{\mathrm{T}}\mathbf{M}\mathbf{r}$, the elastic mass matrix for the tip element becomes

$$\mathbf{M}^{e}_{\text{tipmass}} = \frac{\rho A \ell}{420}\begin{bmatrix} 156 & 22\ell & 54 & -13\ell \\ 22\ell & 4\ell^2 & 13\ell & -3\ell^2 \\ 54 & 13\ell & 156 & -22\ell \\ -13\ell & -3\ell^2 & -22\ell & 4\ell^2 \end{bmatrix} + \begin{bmatrix} 0 & 0 & 0 & 0 \\ 0 & 0 & 0 & 0 \\ 0 & 0 & m_M & m_M e \\ 0 & 0 & m_M e & m_M e^2 + J \end{bmatrix} \tag{4.10}$$

Since the tip mass only affects the kinetic energy of vibration absorber, the stiffness matrix stays the same for all elements in the vibration absorber. This elastic tip mass element is used for the elastic finite element model and also in the derivation of the viscoelastic finite element matrices using a procedure similar to the one described above.

4.2.2 Elastic model of metastructure

The elastic model of the metastructure is created by assembling simple bar finite element matrices and the vibration absorber finite element matrices explained in the previous section. This section gives the details for that process starting with the process used to develop the host structure finite element matrices.

The host structure is modeled using a simple bar finite element model. The bar finite element matrices are given in Section 3.4.1. The number of elements used along the length of the bar is one greater than the number of absorbers, $n_e = N + 1$. This guarantees there are nodes at the locations in which the absorbers are to be attached to the host structure, allowing for easier assembly.

As described in Section 4.2.1, the finite element matrices for each vibration absorber are developed. When the vibration absorber is attached to the host structure, it is done such that the cantilever is fixed to the host structure. This arrangement constricts the slope at the base of the cantilever to be fixed, but the displacement at the base is equal to axial displacement at the corresponding location of the host structure. These boundary conditions are accomplished by constraining the slope at the base of each absorber to be

zero and assembling the finite element matrices such that the vertical displacement at the base of the absorber is equal to the axial displacement at the location of the absorber. Mathematically, this is described as

$$w_i'(0) = 0 \tag{4.11a}$$

$$w_i(0) = u(z_i) \tag{4.11b}$$

where w_i is the transverse displacement of the ith vibration absorber, $u(z)$ is the axial displacement of the host structure, and z_i is the location of the ith vibration absorber from the base of the host structure. Using these constraints, the metastructure finite element matrices are assembled. The degrees of freedom are arranged in such a way to minimize the bandwidth of the matrices which allows for a faster matrix inversion.

4.3 Viscoelastic modeling

This section takes the elastic model developed in the previous section and extends it to a GHM viscoelastic model, this is first done for a single vibration absorber and then for the entire metastructure. Next, the approach used to determine various designs for the metastructure is explained.

4.3.1 Viscoelastic model of a single vibration absorber

The viscoelastic model for a single vibration absorber was developed using the beam viscoelastic elements developed in Section 3.4.2 and adding the inertial effects of the tip mass using the mass matrix in Section 4.2.1. The natural frequency of the absorber is calculated by fixing the base degrees of freedom (both displacement and slope) and using the methods described in Section 3.3.2 to determine the natural frequencies. Knowing the natural frequency of the absorber is helpful when developing the design of the metastructure.

For a vibration absorber, clamped at the base, the resulting FRF of the tip displacement

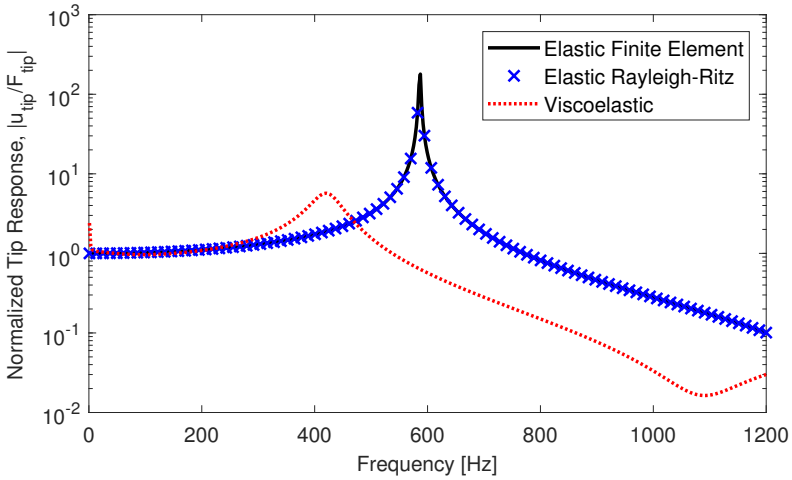

Figure 4.11: Elastic and viscoelastic comparison of the FRF for a single vibration absorber

response due to a force at the tip is shown in Figure 4.11. This figure shows the FRF for the viscoelastic model and the elastic model developed in Section 4.2.1. Additionally, an elastic Rayleigh-Ritz model is also shown. The Rayleigh-Ritz model has good agreement with the elastic finite element model giving us confidence in the development of the finite element model. The FRF for the viscoelastic model predicts a slightly lower natural frequency with higher levels of damping. A mesh convergence study was used to determine that two elements are sufficient to accurately predict the natural frequency of the absorber using the GHM model.

4.3.2 Viscoelastic model of metastructure

The viscoelastic model for the entire metastructure combines the viscoelastic bar elements developed in Section 3.4.1 and the vibration absorber model from the previous section and assembles them using the process described in Section 4.2.2. To show how this model performs, it is applied to an actual metastructure. The metastructure has a mass ratio, $\mu = 0.23$ as defined in Equation 4.1 and 12 absorbers throughout the length of the bar. The vibration absorbers have geometries such that the natural frequency of the absorbers varying linearly from 980 to 500 Hz with the higher frequency absorbers located close to the base. The mass

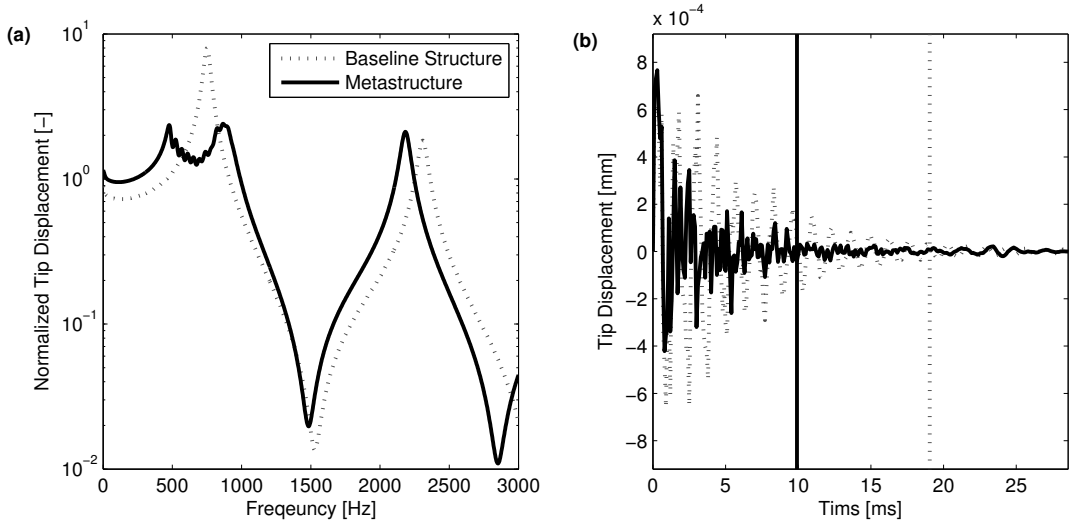

Figure 4.12: (a) FRF and (b) impulse response of the a metastructure bar with vertical lines representing the setting time of the corresponding structures

of each vibration absorber is constrained to have a constant value of 12 g. Later sections will go into more details about how these various parameters affect the performance. The results from this model are shown in Figure 4.12. The FRF shows that the linearly varying nature of the vibration absorbers leads to more board-band absorption near the fundamental natural frequency. The response of the tip of the metastructure subjected to a unit impulse also at the tip is shown in Figure 4.12b. The setting time of each structure is represented by a vertical line. This plot shows that the metastructure design significantly decreases the setting time of the structure.

4.3.3 Metastructure design approach

The basics of the metastructure design were shown in Section 4.1. The next step in the design process for the metastructure is to choose the geometric parameters of the absorbers to get the desired frequencies. In Section 4.1.2, the parameters of the metastructure were chosen using a trail and error method and a commercial finite element model. For many absorber geometries, the natural frequencies were calculated, and the absorbers with the desired natural frequencies were used. In this section, instead of using a commercial finite

element software to find the natural frequencies, a GHM finite element model of the absorbers is used. This model is created in MATLAB. This allows the viscoelastic effects to be taken into account while also speeding up the process by using a 1D model instead of a 3D model.

In Chapter II, choosing the parameters for the metastructure model was fairly straightforward because mass and stiffness values could be chosen independently. When designing real structures, changing the geometric parameters changes both the mass and the stiffness. Additionally, the geometry of absorbers is defined by six different geometric parameters, as seen in Figure 4.10. Here, an iterative approach is taken. For many different absorber geometries, the frequency of the absorber is calculated using the GHM model of the absorber. If the natural frequency of the absorber falls within the desired frequency range, 100 to 1500 Hz, then that absorber geometry is stored along with its frequency. In addition to the frequency being within the desired frequency range, a number of other constraints must also be met. First, there is a constraint on the total overall length of the absorber. The length of the beam plus the length of the tip mass must be less than 35 mm so that the absorber can fit inside the host structure which has an inside width of 40 mm. Additionally, the maximum height of the absorber must be less than 30 mm, allowing for all the absorbers to fit along the length of the host structure. The last constraint is on the slenderness ratio, SR, of the absorber beam. The slenderness ratio must be high enough to ensure the Euler-Bernoulli assumptions are valid. For this work, the slenderness ratio must take on a value higher than 4. The slenderness ratio is calculated as

$$\mathrm{SR} = \frac{\ell_B}{r} \tag{4.12}$$

where r is the radius of gyration, calculated as

$$r = \sqrt{\frac{I}{A}} \tag{4.13}$$

where I and A are defined in Table 4.3. Different combinations of the six geometric

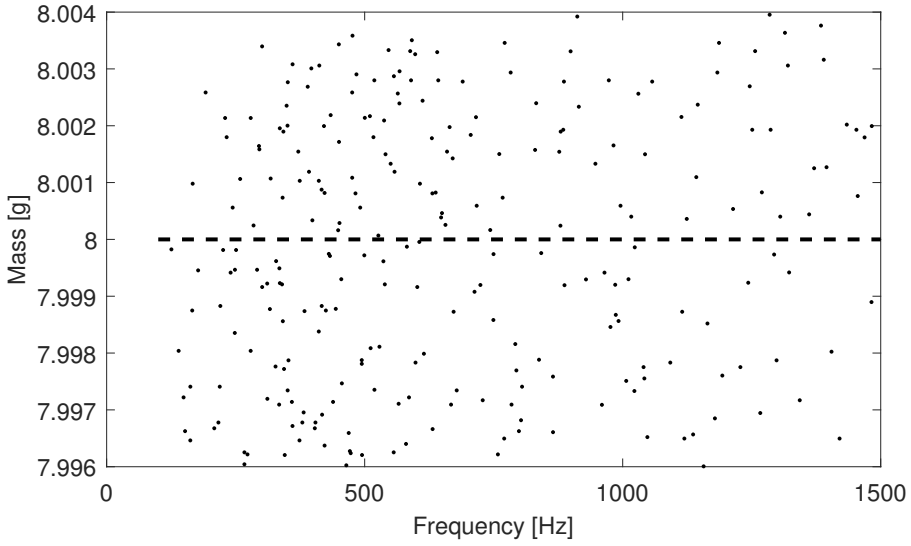

Figure 4.13: Actual mass of various absorber designs versus natural frequency for absorbers with a desired weight of 8 g. Black dashed line indicates desired weight.

parameters are used. Each combination of parameters leads to a different vibration absorber design, and the various constraints must be met in order for that absorber to be a viable option. For each metastructure design, the mass of the absorbers is constrained to be the same mass which is informed by the analysis done in Section 2.5.4. When calculating the natural frequency of the absorbers, the mass of the absorber is also calculated. The mass of the absorber must be within 0.05 % of the desired mass in order for that specific absorber geometry to stored. Fourteen different absorber mass values are used during this analysis, ranging from 8 to 24 g in increments of 2 g. For absorbers with a desired weight of 8 g, a plot of actual absorber mass versus natural frequency is shown in Figure 4.13. For each of these absorber masses, the tip mass height and the tip mass width are constrained to have specific value; these values are given in Table 4.4. For the other four geometric parameters, a range of values is used. Within each range, 100 different values are used. The ranges are shown in Table 4.5.

For the vibration absorber designs weighing 8 g, the values of the geometric properties versus natural frequency of the absorber are shown in Figure 4.14. The values for the tip mass height and tip mass width are constrained, as seen in the plot. These plots show

Table 4.4: Values of the constrained geometric parameters

Absorber Mass [g]	**Tip Mass Height [mm]**	**Tip Mass Width [mm]**
8	16	30
10	19	30
12	19	32
14	22	35
16	22	35
18	22	35
20	24	35
22	27	35
24	27	35

Table 4.5: Absorber geometry parameter ranges

Dimension	**Symbol**	**Range**
Beam Length	ℓ_B	5 - 20 mm
Beam Width	w_B	5 - 35 mm
Beam Height	h_B	3 - 15 mm
Tip Mass Length	ℓ_M	10 - 25 mm

different trends about how the natural frequency of the absorber varies with the geometry. For example, lower values of the beam height led to lower natural frequencies, which is expected. Figure 4.15 shows the values of the slenderness ratio versus natural frequency for the absorbers weighing 8 g. This plot shows that absorber designs with lower slenderness ratios have higher natural frequencies. The slenderness ratio constraint is also shown on the plot. If this constraint is set too high, then vibration absorbers with higher natural frequencies cannot be achieved.

The method described above leads to tables of absorber designs for various absorber weights ranging from 8 to 24 g. For all metastructure designs, the same host structure geometry is used. As defined in Figure 4.1, the width of the cross-section is 50 mm, and the thickness is 5 mm. The length of the host structure is 45 cm. Different metastructure configurations are studied by varying the number of absorbers and the mass of the absorbers. The number of absorbers varies from 5 to 13, and the weight of the absorbers varies from

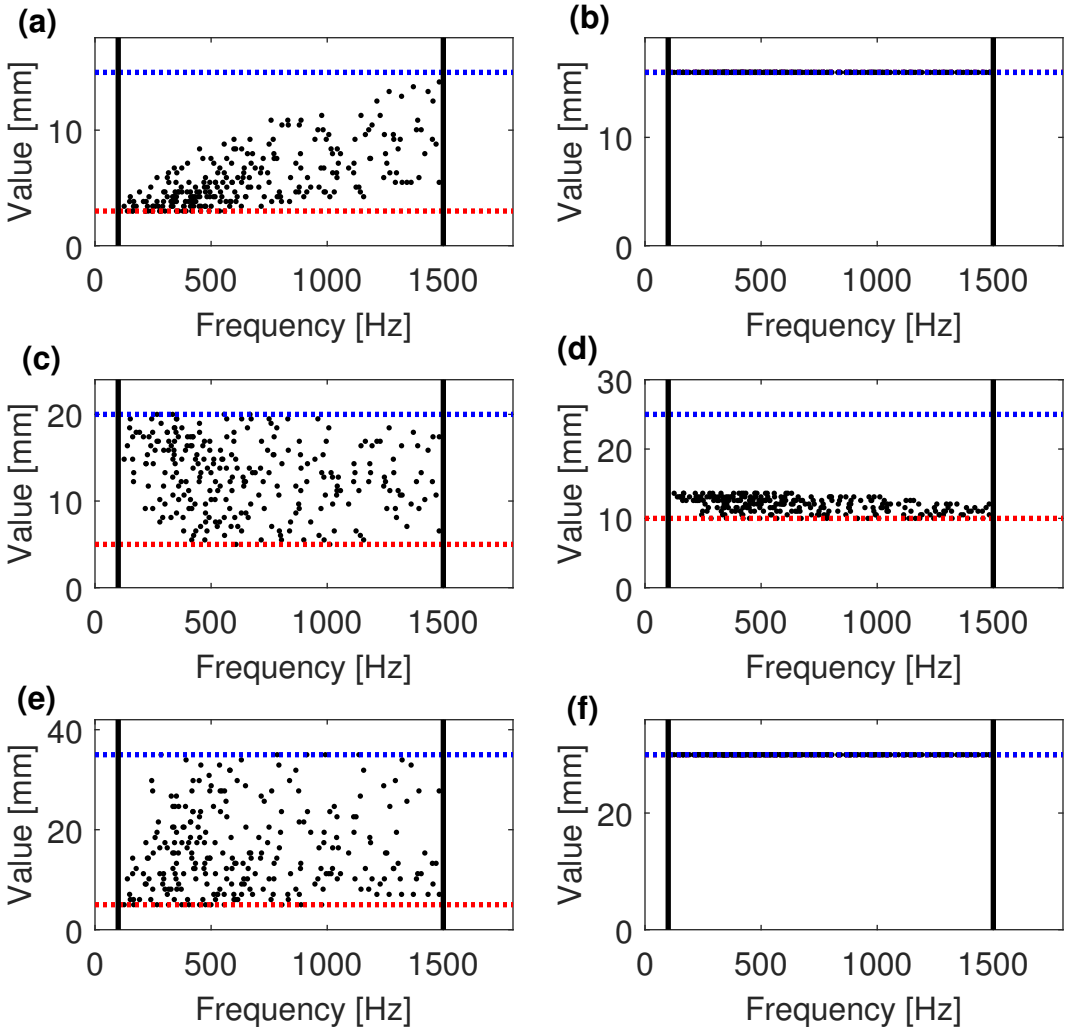

Figure 4.14: Values of the geometric parameters versus frequency of the absorber weighing 8 g for the six geometric parameters: (a) beam height, (b) tip mass height, (c) beam length, (d) tip mass length, (e) beam width, (f) tip mass width. The blue dotted line represents the upper limit of the range used and the red dotted line represents the lower limit.

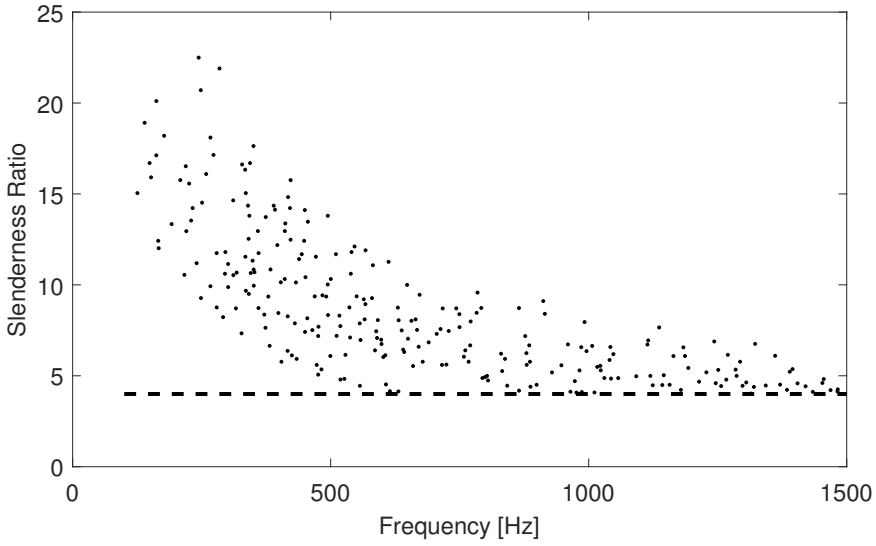

Figure 4.15: Trend of slenderness ratio versus natural frequency for absorber designs weight 8 g. Black dashed line shows slenderness ratio constraint.

8 g to 24 g. These two parameters dictate the weight of the absorber system. Using that weight, the mass ratio of the metastructure can be calculated using Equation 4.1. Table 4.6 lists all the different configurations and the associated mass ratio. The mass ratio values vary from 0.077 to 0.395. For each mass ratio, a baseline structure with the same weight as the metastructure is used as a comparison.

For each of these configurations, various absorber frequency ranges are explored using the absorber tables described above. For all designs, the natural frequencies of the absorbers are constrained to vary linearly along the length of the beam. For each of the varying ranges, both the H norm and the settling time, t_s are calculated and compared the baseline structure. In Chapter II, the H_2 norm was calculated by calculating the area under the FRF from negative infinity to infinity. In this section, simply the frequency range of interest is used for the H norm calculation

$$H \text{ norm} = \int_0^{2{,}500 \text{ Hz}} G(\jmath\omega)\mathrm{d}\omega \tag{4.14}$$

where $G(\jmath\omega)$ is the FRF of the tip displacement due to an input force at the tip. For

each configuration, the optimal frequency range is determined based on the design with the lowest settling time. Table 4.6 reports the optimal frequency range. The first number in the range is the frequency of the absorber closest to the base, and the last number is the frequency of the tip absorber. Additionally, the percent decreases in the settling time and the H norm are reported. These are calculated as

$$H \text{ percent decrease} = \frac{(H)_{\text{metastructure}} - (H)_{\text{baseline}}}{(H)_{\text{baseline}}} \times 100 \tag{4.15a}$$

$$t_s \text{ percent decrease} = \frac{(t_s)_{\text{metastructure}} - (t_s)_{\text{baseline}}}{(t_s)_{\text{baseline}}} \times 100 \tag{4.15b}$$

Table 4.6: Optimal results for metastructure designs for varying number of absorbers and absorber weights

Number of Absorbers	**Weight of Absorber [g]**	**Mass Ratio**	**Frequency Range [Hz]**	**H Percent Decrease**	**t_s Percent Decrease**
5	8	0.077	767 - 494	4.63	67.7
6	8	0.091	838 - 469	4.98	69.8
7	8	0.105	830 - 434	4.46	70.0
8	8	0.118	838 - 421	4.29	73.7
9	8	0.131	865 - 421	4.12	74.0
10	8	0.144	915 - 412	4.21	73.8
11	8	0.156	899 - 371	2.94	72.2
12	8	0.168	899 - 374	2.59	71.6
13	8	0.179	899 - 360	1.84	71.4
5	10	0.095	811 - 465	4.57	67.8
6	10	0.112	864 - 451	4.64	69.9
7	10	0.128	856 - 440	4.21	74.1
8	10	0.144	874 - 415	3.70	75.5
9	10	0.159	897 - 400	3.28	73.7
10	10	0.173	864 - 373	1.96	70.9
11	10	0.187	874 - 360	1.39	71.0
12	10	0.201	939 - 360	1.70	72.5
13	10	0.214	874 - 336	0.31	70.6
5	12	0.112	813 - 484	4.66	63.1
6	12	0.131	813 - 440	3.96	71.9
7	12	0.150	856 - 404	3.47	75.6
8	12	0.168	856 - 371	2.12	73.3
9	12	0.185	878 - 359	1.32	73.2

Table 4.6: Optimal results for metastructure designs for varying number of absorbers and absorber weights

Number of Absorbers	**Weight of Absorber [g]**	**Mass Ratio**	**Frequency Range [Hz]**	**H Percent Decrease**	**t_s Percent Decrease**
10	12	0.201	937 - 330	1.09	73.5
11	12	0.217	937 - 348	0.32	71.7
12	12	0.232	962 - 330	0.13	73.2
13	12	0.246	878 - 303	2.43	70.9
5	14	0.128	829 - 482	4.57	63.1
6	14	0.150	840 - 424	3.47	75.6
7	14	0.170	912 - 404	3.12	73.4
8	14	0.190	893 - 370	1.65	73.9
9	14	0.209	926 - 337	0.74	73.5
10	14	0.227	926 - 321	0.30	73.9
11	14	0.244	912 - 343	1.11	74.9
12	14	0.260	912 - 234	3.34	72.9
13	14	0.276	1017 - 255	2.43	72.5
5	16	0.144	762 - 403	2.13	64.9
6	16	0.167	825 - 394	1.87	69.7
7	16	0.190	913 - 403	2.28	74.1
8	16	0.212	853 - 366	0.12	73.6
9	16	0.232	942 - 374	0.35	74.8
10	16	0.251	933 - 287	2.66	71.7
11	16	0.269	974 - 225	2.76	72.8
12	16	0.287	933 - 211	4.87	78.7
13	16	0.304	933 - 220	5.99	77.1
5	18	0.159	758 - 400	1.42	58.8
6	18	0.185	826 - 394	1.57	73.4
7	18	0.209	884 - 374	0.61	74.0
8	18	0.232	955 - 367	0.19	75.4
9	18	0.253	924 - 283	3.05	74.5
10	18	0.274	942 - 301	3.62	75.0
11	18	0.293	900 - 236	6.43	72.9
12	18	0.312	942 - 184	7.81	79.6
13	18	0.329	924 - 165	8.42	76.1
5	20	0.173	782 - 436	2.10	65.5
6	20	0.201	827 - 395	0.89	71.0
7	20	0.227	845 - 350	1.09	73.0
8	20	0.251	912 - 337	1.76	77.5
9	20	0.274	944 - 323	3.08	74.6
10	20	0.295	912 - 217	5.16	72.5
11	20	0.316	924 - 196	6.92	75.3
12	20	0.335	896 - 223	10.13	77.0

Table 4.6: Optimal results for metastructure designs for varying number of absorbers and absorber weights

Number of Absorbers	**Weight of Absorber [g]**	**Mass Ratio**	**Frequency Range [Hz]**	**H Percent Decrease**	**t_s Percent Decrease**
13	20	0.353	912 - 178	9.98	75.3
5	22	0.187	778 - 421	1.49	65.0
6	22	0.217	787 - 383	0.73	67.0
7	22	0.244	827 - 332	2.56	72.7
8	22	0.269	851 - 267	5.57	72.4
9	22	0.293	880 - 267	6.60	74.0
10	22	0.316	893 - 169	8.24	74.3
11	22	0.337	880 - 191	9.47	76.5
12	22	0.356	880 - 179	11.40	75.5
13	22	0.375	893 - 133	13.64	75.0
5	24	0.201	769 - 416	0.52	65.2
6	24	0.232	753 - 335	3.33	67.1
7	24	0.260	827 - 277	4.55	72.3
8	24	0.287	918 - 348	3.34	74.7
9	24	0.312	964 - 357	4.11	75.8
10	24	0.335	860 - 218	10.44	76.5
11	24	0.356	918 - 174	10.73	74.5
12	24	0.376	873 - 172	12.74	75.7
13	24	0.395	1108 - 297	10.63	74.0

4.4 Metastructure trends

This section examines the trends exhibited in the metastructure when various parameters are varied. This section begins by looking at the effect of varying the absorber natural frequency. The previous section provided the optimal ranges for the absorber frequencies (Table 4.6); this section will look into the non-optimal designs also. Next, the effect of mass ratio and the number of absorbers are explored. Understanding these trends allows a final metastructure design to be chosen and used going forward for experimental testing.

4.4.1 Effects of absorber natural frequency variation

This section will explore the effects of varying the natural frequency range of a metastructure with ten absorbers each weighing 8 g, leading to a mass ratio of 0.144. Figure

4.16 shows a contour plot depicting the performance of the structure for various frequency ranges. The x-axis is the frequency of the tip absorber and the y-axis is the frequency of the base absorber. The frequencies of the other absorbers varying linearly between those two values. The color of the contour plot represents the percent decrease in the performance measures of the structure, where yellow represents better performance and blue represents worse performance. The top plot, (a) shows the percent decrease in the H norm whereas the bottom plot, (b) shows the percent decrease in the settling time.

The diagonal line where the frequencies of the tip absorber and the base absorber are equal represents metastructures in which all the absorbers are tuned to the same natural frequency. Since the highest values do not lie on this line, we can see that is more beneficial to have vibration absorbers with varying frequencies, as we saw with the lumped mass model. Additionally, the contour plot is not symmetric about that line. The upper half, where the frequency of the base absorber is higher than the frequency of the tip absorber has higher performance values. This shows that placing the absorbers with higher frequencies near the base of the metastructure leads to better performance compared to the opposite arrangement. The agrees with the trends of absorber stiffness observed from the lumped mass models. When the performance measures are compared, similar trends are observed. The H norm has more variation where as good settling times are more localized. Additionally, the H norm percent decrease takes on mostly negative values, meaning the baseline structure is performing better than the metastructure with respect to the H norm. This will be explored in more detail when examining the FRFs of specific metastructure designs.

The other configurations take on similar trends. For comparison, the metastructure design with 13 absorbers weighing 24 g is shown in Figure 4.17. This metastructure has a much higher mass ratio of 0.395. Although the mass ratio is higher, similar trends hold.

Next, specific metastructure designs for the configuration with ten absorbers weighing 8 g will be examined in more detail by looking at the FRFs and the impulse response functions. Figure 4.18 shows the optimal frequency range with respect to settling time where the

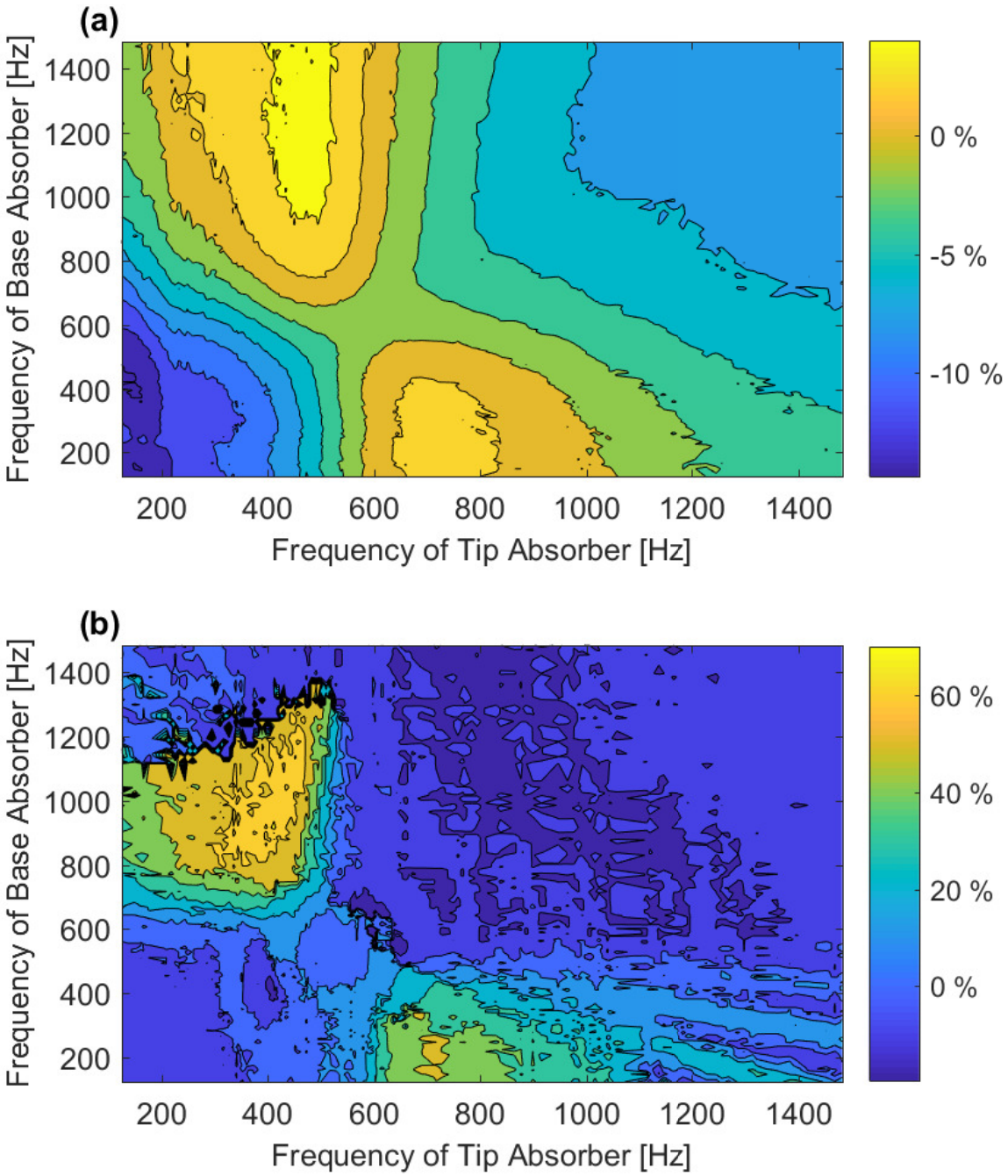

Figure 4.16: Contour plots for a metastructure with 10 absorbers weighting 8 g showing the variation in the percent decrease in the (a) H norm and (b) settling time for varying frequency ranges

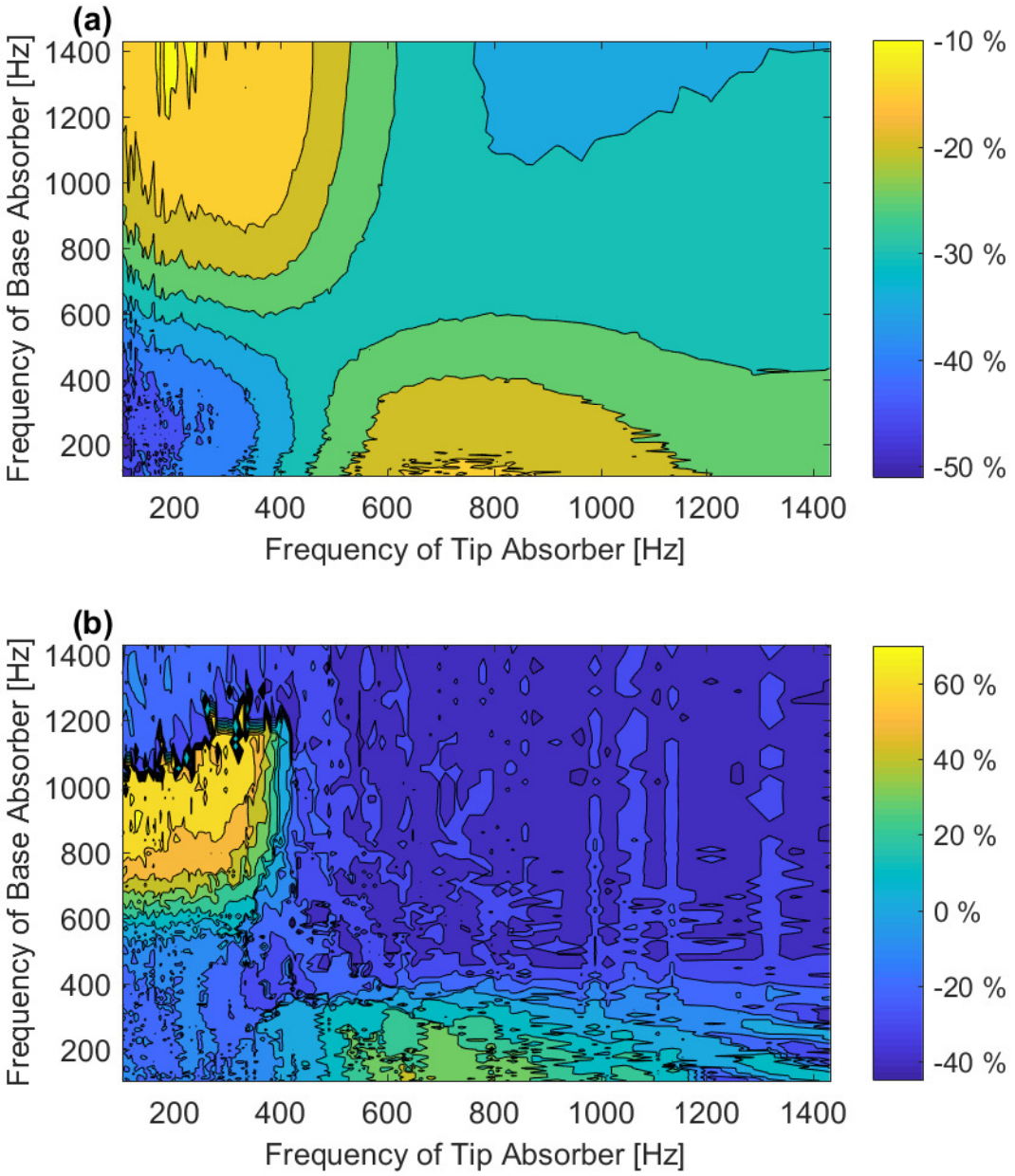

Figure 4.17: Contour plots for a metastructure with 13 absorbers weighting 24 g showing the variation in the percent decrease in the (a) H norm and (b) settling time for varying frequency ranges

absorbers vary from 915 to 412 Hz. The first number of the range is the frequency of the base absorber and the second number is the frequency of the tip absorber. The plot on the left shows the frequency response function of the tip displacement due to an applied force also at the tip. The plot on the right shows the impulse response function of the tip displacement due to a unit impulse applied at the tip. The vertical lines represent the settling time for the corresponding structure. The plots for the optimal structure are compared to the optimal frequency range with response to the H norm where the absorbers vary from 1,114 to 475 Hz shown in Figure 4.19. The configuration optimized with respect to the H norm provides slightly better performance for the H norm but significantly worse performance with respect to the settling time, whereas the design optimized with respect to the settling has good performance for both the H norm and the setting time. This is why the settling time was chosen as the performance measure for choosing the optimal frequency ranges.

As another comparison, the metastructure with absorbers having frequencies varying from 412 to 915 Hz, is shown in Figure 4.20. These absorbers have the same frequencies as the optimal structure shown in Figure 4.18 but with their locations flipped, meaning the higher frequency absorbers are near the tip of the metastructure instead of near the base. The responses of these two structures look very different, showing that the location of the absorbers makes a significant difference in the response of the structure.

Lastly, a metastructure with all the absorbers tuned to the same frequency is shown in Figure 4.21. This design shows the characteristic split peak behavior we expect out of a structure with a single vibration absorber. This aligns with the trends observed in the lumped mass metastructure results.

4.4.2 Effect of mass ratio and number of absorbers

This section looks at how the mass ratio of the metastructure design impacts the performance of the structure. Various configurations with the optimal natural frequency ranges from Table 4.6 are used to examine these trends. Figure 4.22 shows a plot of the percent de-

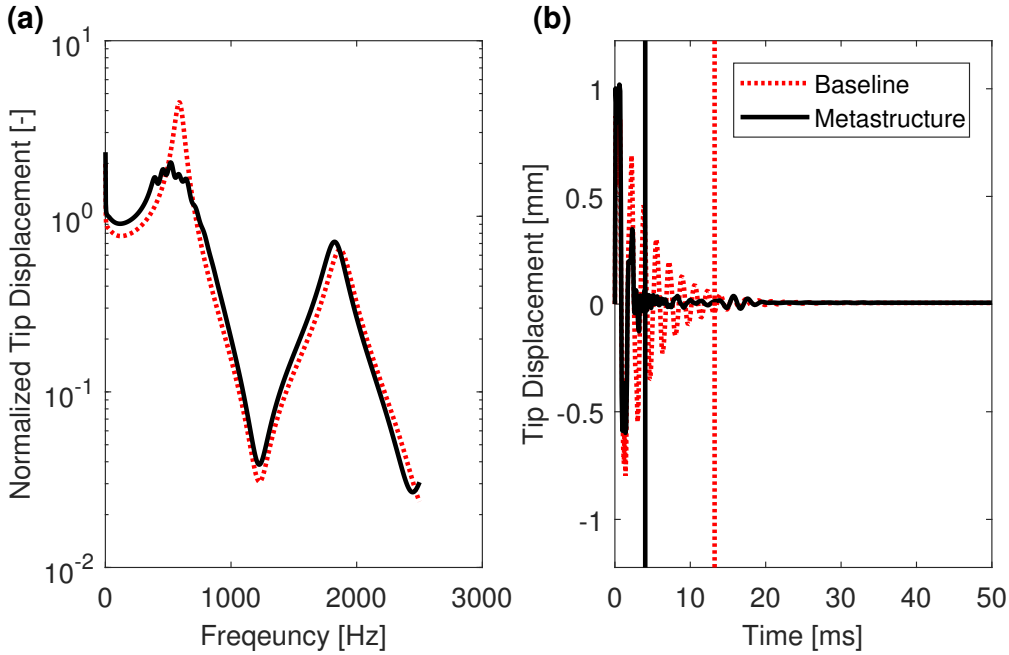

Figure 4.18: Plots of the (a) FRF and (b) impulse response function for a metastructure with 10 absorbers weighing 8 g each and natural frequencies varying from 915 to 412 Hz. The vertical lines represent the settling time of the structures.

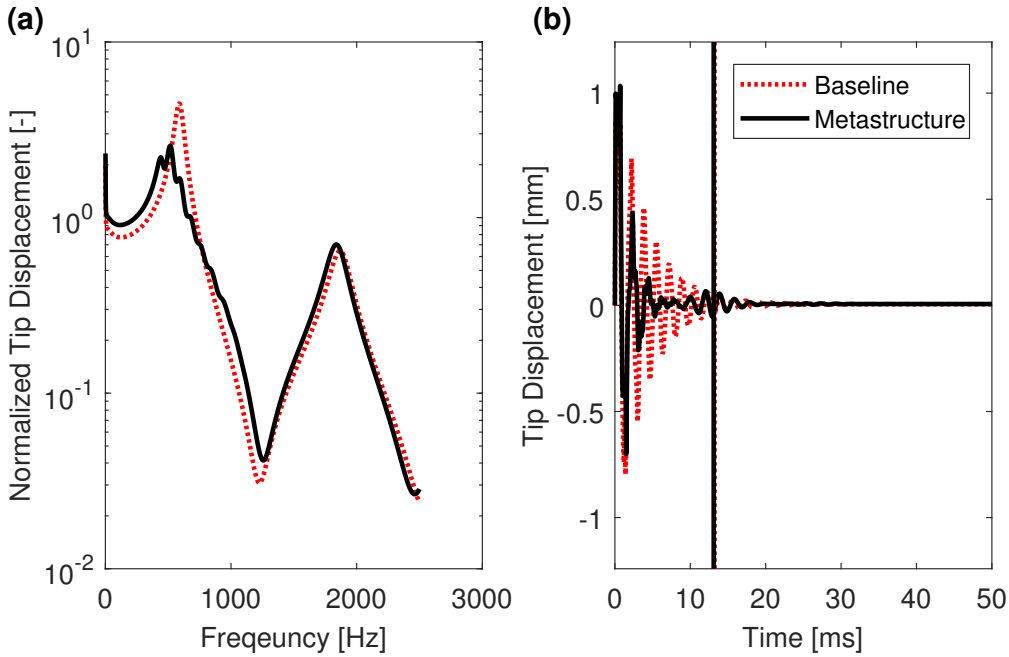

Figure 4.19: Plots of the (a) FRF and (b) impulse response function for a metastructure with 10 absorbers weighing 8 g each and natural frequencies varying from 1,114 to 475 Hz. The vertical lines represent the settling time of the structures.

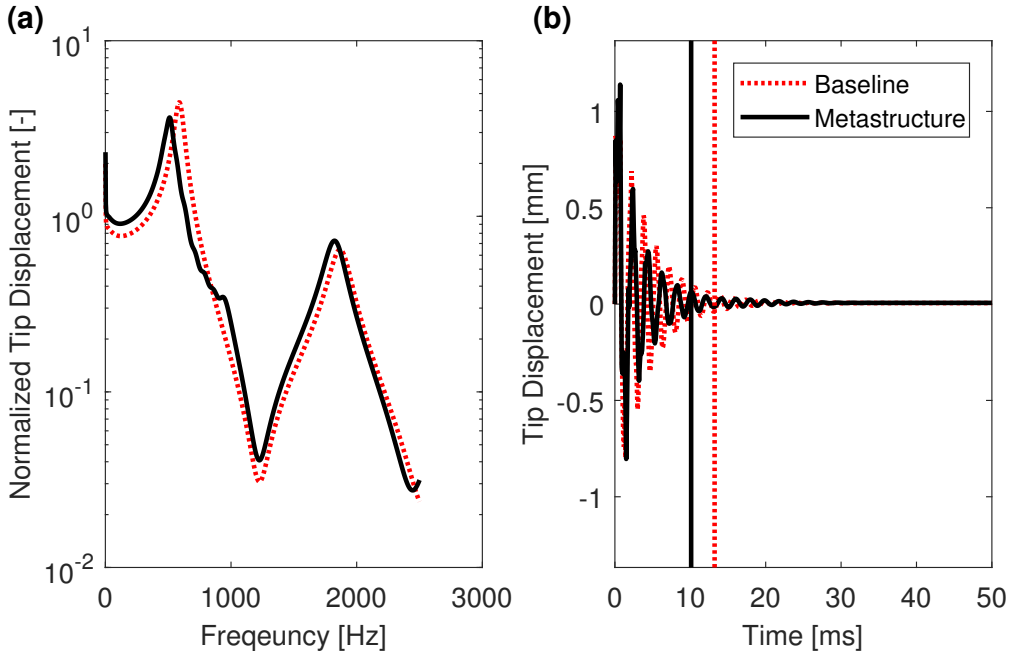

Figure 4.20: Plots of the (a) FRF and (b) impulse response function for a metastructure with 10 absorbers weighing 8 g each and natural frequencies varying from 412 to 915 Hz. The vertical lines represent the settling time of the structures.

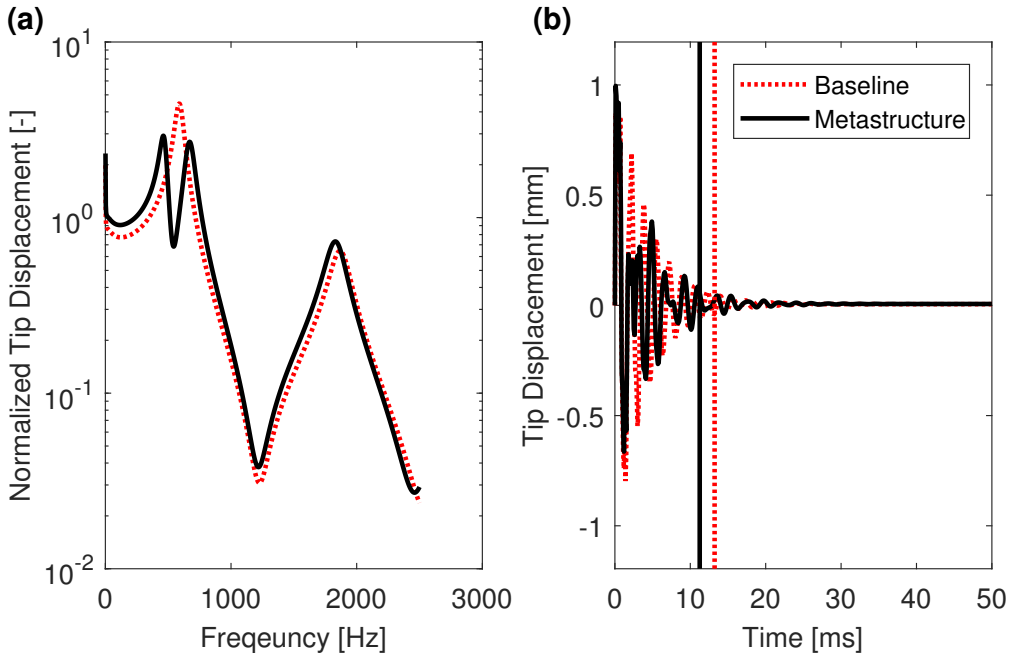

Figure 4.21: Plots of the (a) FRF and (b) impulse response function for a metastructure with 10 absorbers weighing 8 g each and a constant natural frequency of 550 Hz. The vertical lines represent the settling time of the structures.

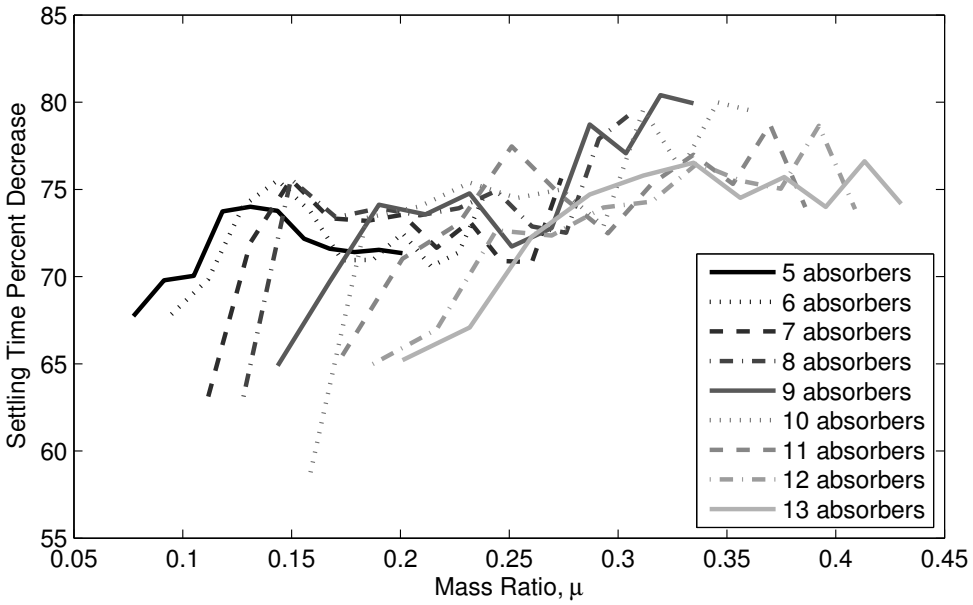

Figure 4.22: Percent decrease in the settling time versus mass ratio for varying number of absorbers

crease in settling time versus mass ratio for various number of absorbers. There is a general trend in this plot; a higher mass ratio leads to better performance. For the individual lines representing the designs with the same number of absorbers, there is significant variance. For example, the line for metastructures with five absorbers has a clear optimal point around a mass ratio value of 0.12 whereas the line for designs with nine absorbers, does not have an optimal value, it simply increases with increasing mass ratio. Figure 4.23 is a similar figure but looks the H norm instead of the setting time. From this plot there is a clear trend, increasing the mass ratio decreases the performance with respect to the H norm, and this holds true for designs with a varying number of absorbers.

4.4.3 Final design

This section describes in detail the final design chosen for the experimental testing and to examine the effects of varying the temperature. Figure 4.24 shows a contour plot of the optimal percent decrease in the settling time for all configurations discussed. This shows that metastructures with few absorbers are less effective than metastructures with more absorbers.

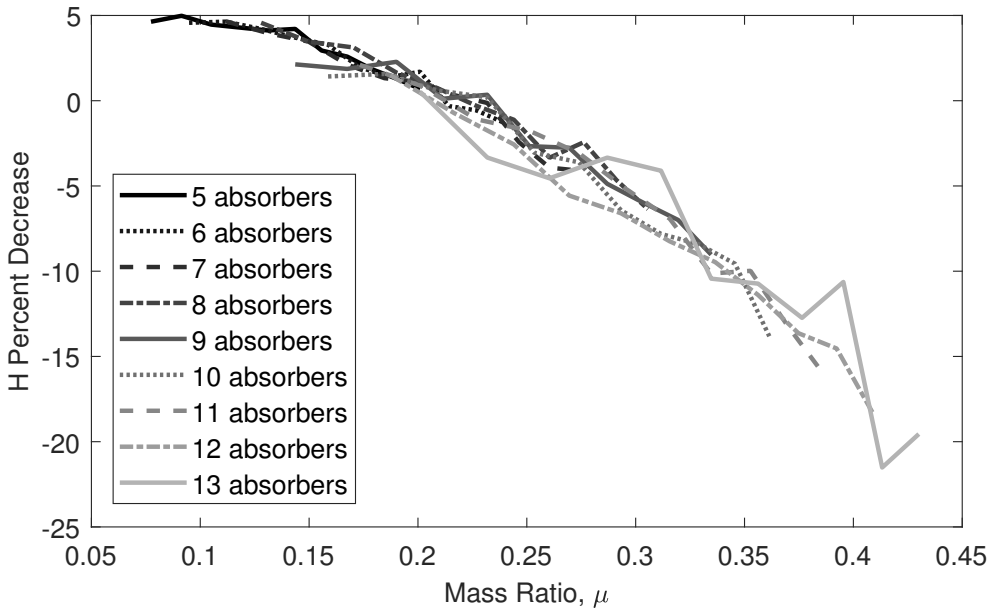

Figure 4.23: Percent decrease in the H norm versus mass ratio for varying number of absorbers

This is likely due to the decreased number of parameters to tune for the structure with only 5 or 6 absorbers. As the number of absorbers increases, there is are more parameters to vary allowing for greater design flexibility and also more variation in the trends.

In the end, a design with ten absorbers weighing 8 g each was chosen to use in the experimental testing. This design has a mass ratio of 0.144. This design has a sufficient number of vibration absorbers allowing for greater flexibility in the design while also providing a lower mass ratio value. A lower mass ratio leads to a better H norm performance while also redistributing less material from the host structure to the absorber system. The absorbers have natural frequencies ranging from 915 to 412 Hz, and the plot of the FRF and impulse response function can be seen in Figure 4.18. The parameters of the final design are summarized in Table 4.7. The geometries used to achieve vibration absorber with frequencies varying from 915 to 412 Hz are shown in Table 4.8. A CAD model of the final design is shown in Figure 4.25.

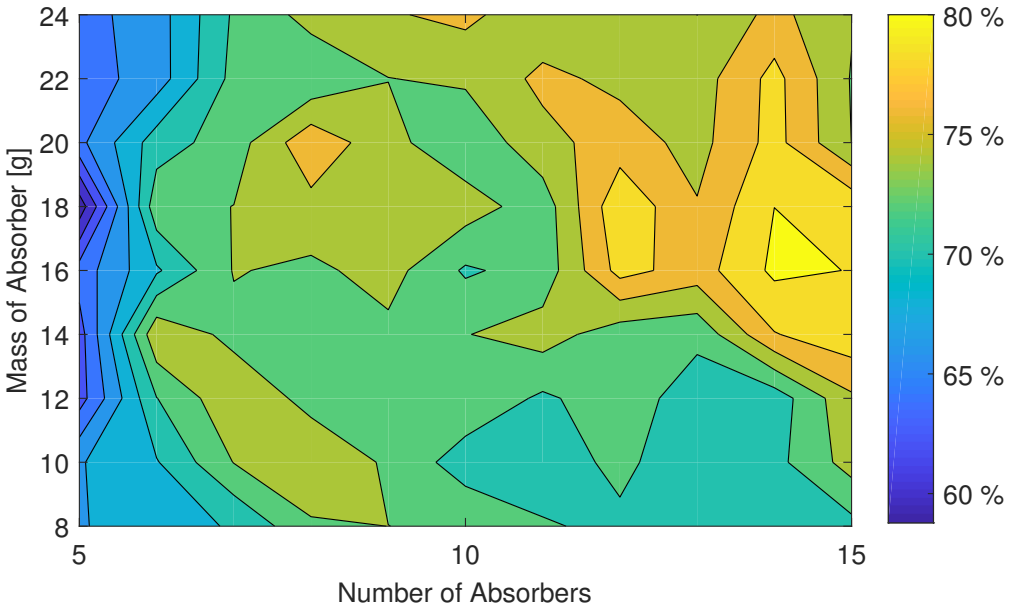

Figure 4.24: Contour plot of the percent decrease in settling time for all configurations

Table 4.7: Parameters of the final metastructure design

Parameter	**Value**
Number of absorbers, n	10
Mass of absorbers, m_i	8 g
Mass ratio, mu	0.144
Host width, w_{host}	50 mm
Host thickness, t_{host}	5 mm
Host length, ℓ_{host}	45 cm
Host mass, m_{host}	473 g
Individual absorber mass, m_i	8 g
Total Absorber mass, $\sum_{i=1}^{N}$	80 g
Total metastructure mass, $m_{\text{metastructure}}$	553 g
Baseline width, w_{baseline}	50 mm
Baseline thickness, t_{baseline}	5.97 mm
Baseline length, ℓ_{baseline}	45 cm
Baseline mass m_{baseline}	553 g

Table 4.8: Absorber parameters for the final metastructure design

Absorber Number	**Frequency [Hz]**	**Beam Length**	**Beam Width**	**Beam Height**	**Tip Mass Length**	**Tip Mass Width**	**Tip Mass Height**
1	915.0	14.31	23.62	5.90	10.0	30.0	16.0
2	842.1	7.59	11.21	5.90	13.1	30.0	16.0
3	803.0	5.52	23.62	3.83	13.1	30.0	16.0
4	743.3	15.86	17.41	6.31	10.5	30.0	16.0
5	689.9	13.28	11.21	6.72	12.1	30.0	16.0
6	631.6	19.48	9.14	8.38	11.0	30.0	16.0
7	567.6	17.41	22.59	5.07	10.0	30.0	16.0
8	518.9	7.59	6.03	5.48	13.6	30.0	16.0
9	464.4	16.38	6.03	7.55	12.6	30.0	16.0
10	412.1	16.38	21.55	4.24	11.0	30.0	16.0

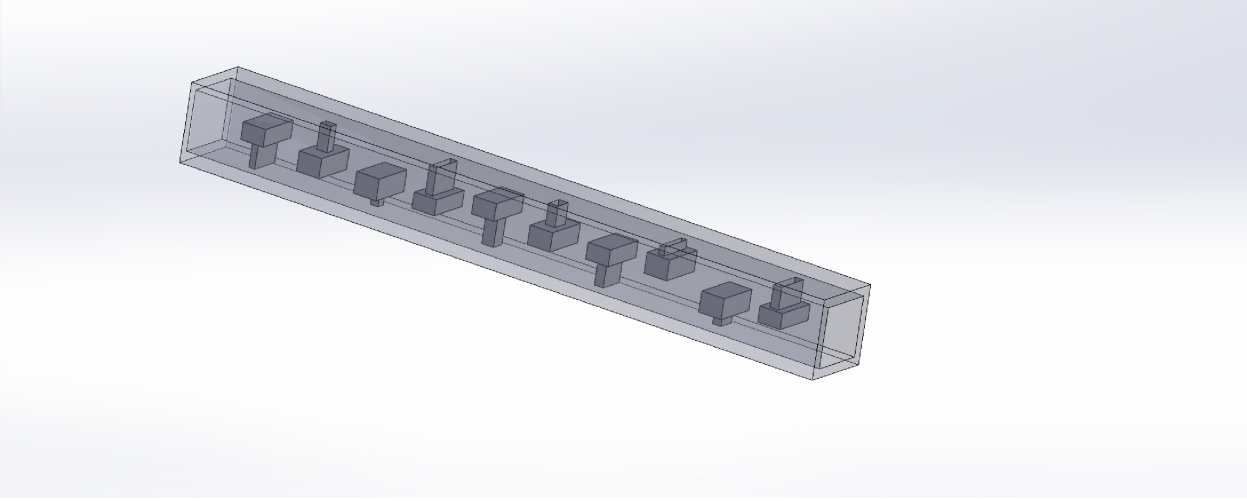

Figure 4.25: Three dimensional CAD model of the final design used with transparent outer walls to show the absorbers

4.5 Temperature effects

This section uses the GHM model described above and looks at the effects of temperature on the performance of the structure. Chapter III details how to incorporate temperature change into the GHM model. First, the effect of temperature on a single vibration absorber is explored. Then the effects on the entire structure are explored.

4.5.1 Temperature effects on a single vibration absorber

Using the same model described in Section 4.3.1, the temperature of the absorber was varied, and the resulting FRFs are plotted in Figure 4.26. This absorber was designed to have a natural frequency of 600 Hz at room temperature (20° C). The figure shows that as the temperatures increases, the natural frequency of the vibration absorber decreases and the level of damping increases which is consistent with results from Chapter III. To ensure this trend holds for a variety of geometries, absorbers with room temperature natural frequencies ranging from 200 to 1,000 Hz were modeled at temperatures from 20° to 100° C. The natural frequencies and damping values are shown in Figure 4.27. These results show that regardless of the design frequency of the vibration absorber, the trends from a temperature change are similar.

4.5.2 Temperature effects on the metastructure

Next, the temperature of the metastructure is changed to determine if similar performance increases are observed at off-design temperatures. The final design described in Section 4.4.3 is used to explore these trends. The temperature is changed for both the baseline structure and the metastructure. The results for various temperatures can be seen in Figure 4.28. For the temperatures, 20° to 40° C, we can see similar trends in FRF. This shows that as the natural frequency of the host structure changes with temperature, the frequencies of the vibration absorbers change at a similar rate leading to similar trends in the FRF. Also, increasing the temperature results in higher damping in the structure leading to a smoother

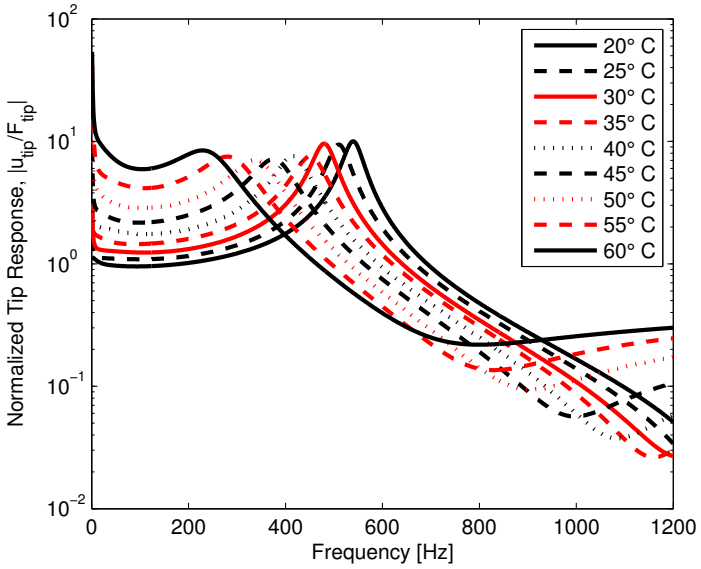

Figure 4.26: FRFs for a single vibration absorber made from VeroWhitePlus at various temperatures

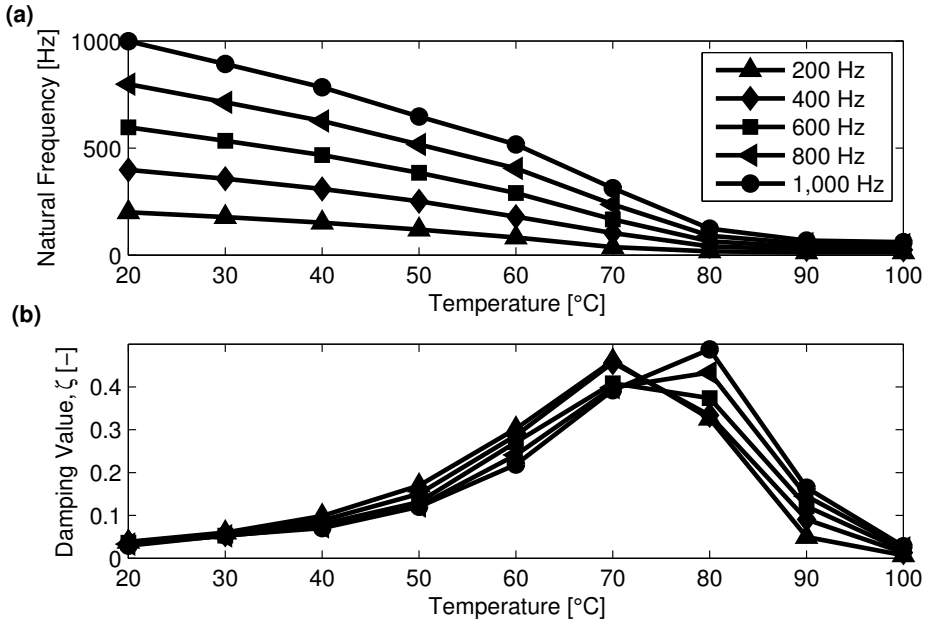

Figure 4.27: Effects of temperature change on the (a) natural frequency and (b) damping values of vibration absorbers with various geometry

FRF. For temperatures above 30° C, the damping in the structure begins to dominate the response, almost completely flatting out the curve and leaving only slight differences in the FRF curves. These trends can also be observed by looking at the impulse response function for various temperatures, shown in Figure 4.29. In this series of plots, the axes are constrained to have the same limits to allow for easier comparison. At the temperature increases, the frequency of the oscillations decreases resulting from the shift in the natural frequency. Additionally, as the temperature of increases, the initial response of the structure increases due to the lower modulus of elasticity.

At temperatures ranging from 20° to 70° C, the settling time of the baseline structure and the metastructure are calculated and plotted in Figure 4.30. Initially, as the temperature increases, the settling time of both the baseline structure and the metastructure varies somewhat but stays relatively constant. At 50° C, the settling time of both the metastructure and the baseline structure rapidly increases. Figure 4.31 shows the same data, but plots the percent decrease in the setting time as temperature changes. Here, there is a general trend that as the temperature of the structures increases, the performance of the metastructure compared to the baseline structure decreases. At temperatures of 60° and 70° C, the baseline structure outperforms the metastructure. This is due to the difference in static response between the two structures, which can be seen in the slight vertical shift in the FRF of the metastructure compared to the baseline structure. Since the baseline structure and the metastructure are constrained to have the same mass, the host structure part of the metastructure must have a slightly smaller wall thickness than that of the baseline structure. The smaller thickness causes a decrease in the stiffness of the structure and an increase in the static response. At higher temperatures, the static response of the structure dominates the response leading to higher settling times. At lower temperatures, the static response has a less-significant role in the response.

These results show that the metastructure design can provide performance benefits for a range of temperatures even if the metastructure is designed for a fixed temperature, but the

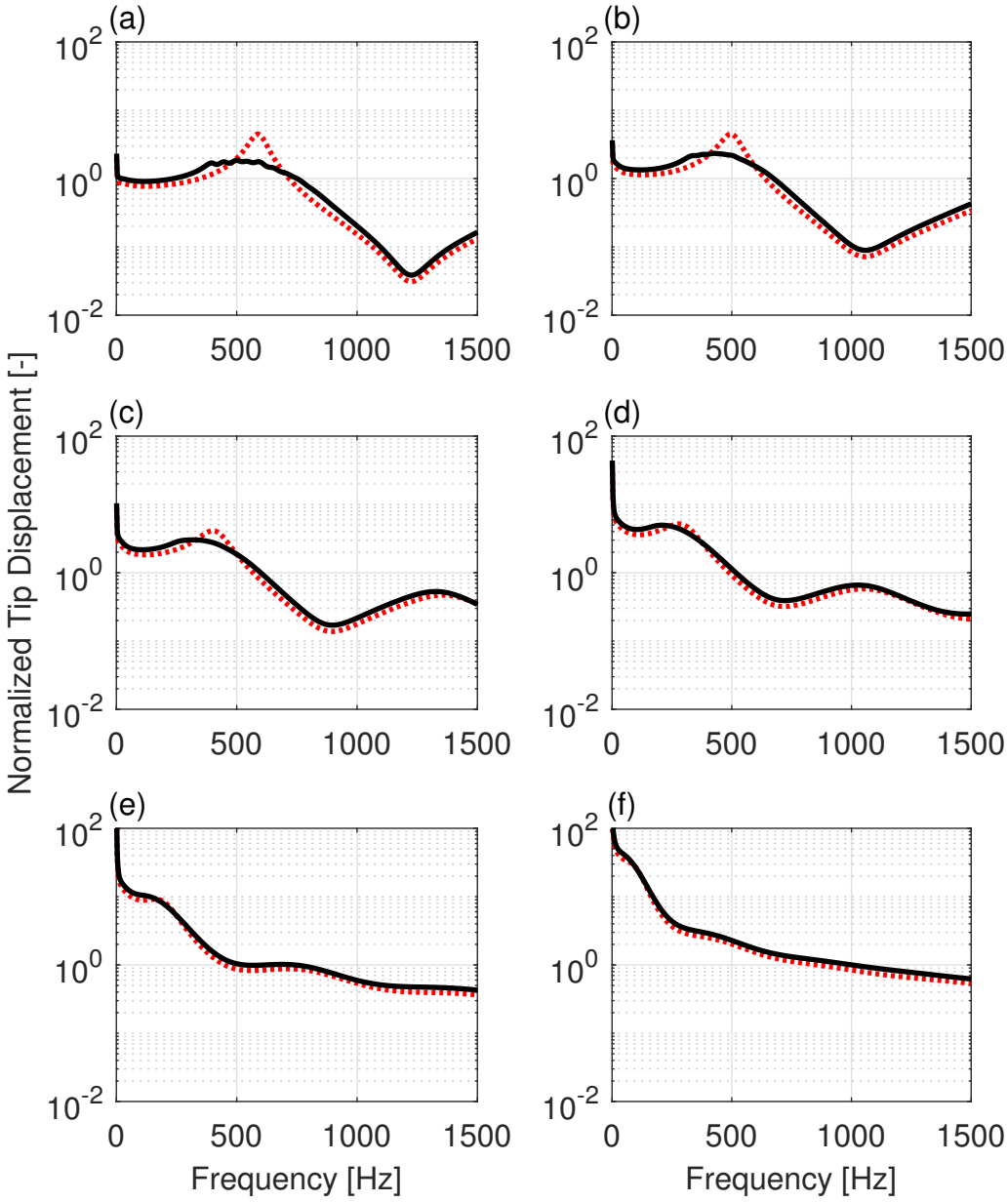

Figure 4.28: FRFs for the metastructure and the baseline structure at temperatures of (a) 20° C, (b) 30° C, (c) 40° C, (d) 50° C, (e) 60° C, (f) 70° C, where the red dotted line represents the metastructure and the black solid line is the baseline structure

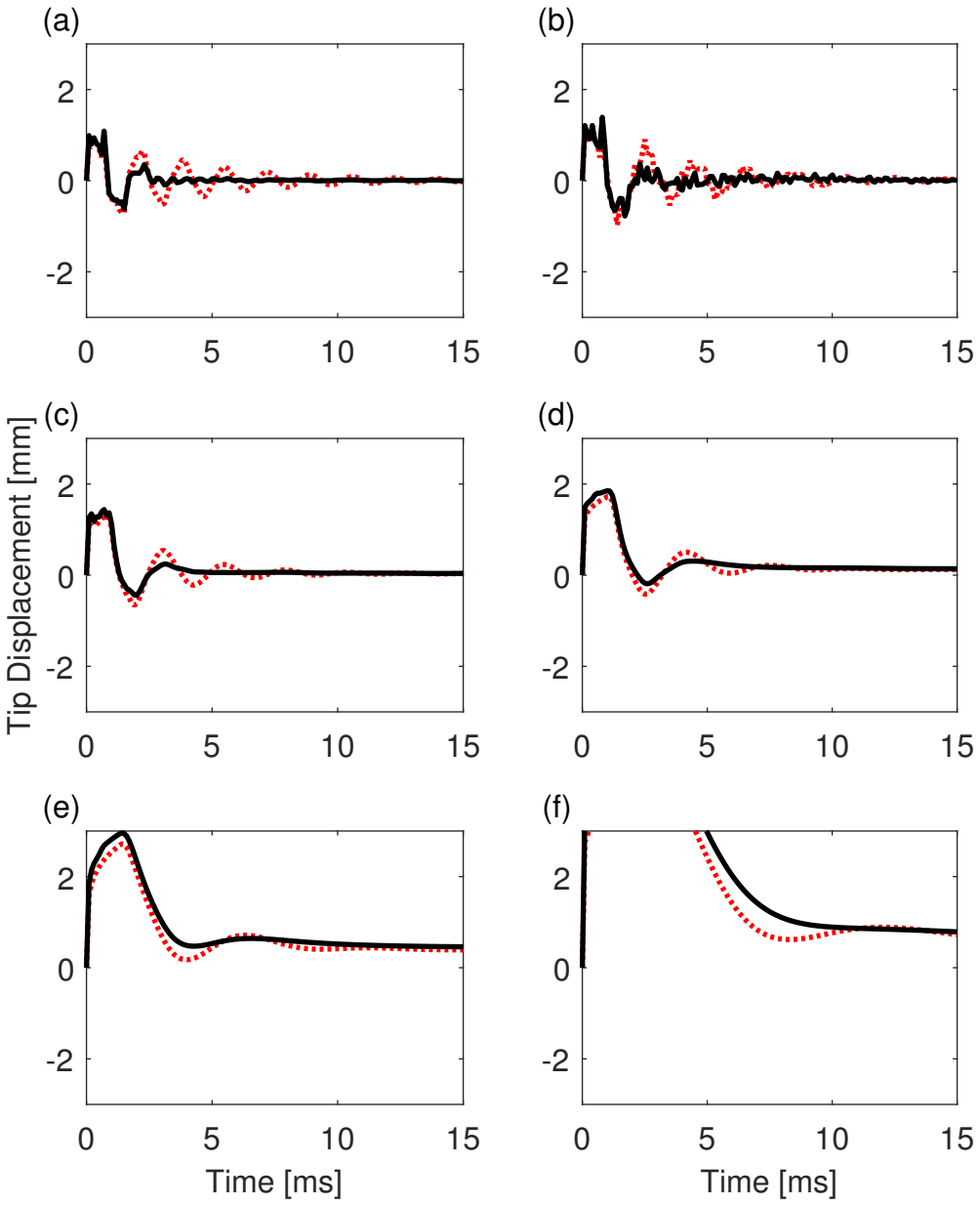

Figure 4.29: Impulse the metastructure and the baseline structure at temperatures of (a) 20° C, (b) 30° C, (c) 40° C, (d) 50° C, (e) 60° C, (f) 70° C, where the red dotted line represents the metastructure and the black solid line is the baseline structure

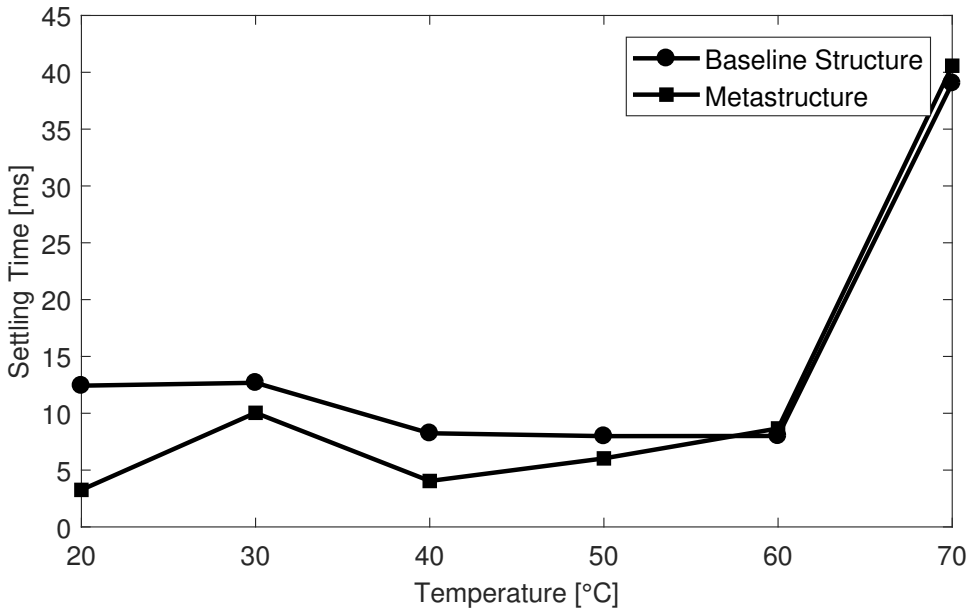

Figure 4.30: Settling time of the baseline structure and the metastructure versus temperature

structure performs best at its design temperature. At high temperatures, the metastructure no longer outperforms the baseline structure. In the end, this shows that operating temperatures of the structure must be considered when determining if a metastructure design should be utilized.

4.6 Experimental verification

This section presents the experimental results on the final design outlined in Section 4.4.3. During this experimental testing, only the metastructure is tested, and the baseline structure is not tested. First, the experimental set-up is described. The set-up is the same as the set-up used in Section 4.1.2. Next, the modeling procedure used to simulate the force that the MCFs provide at the base of the structure is described. The previous sections examined FRF of the tip response due to a force applied at the tip of the structure. Here, the force is applied as the base of the structure, so slight modifications are used to account for that change. Lastly, the experimental results are compared to the GHM model results.

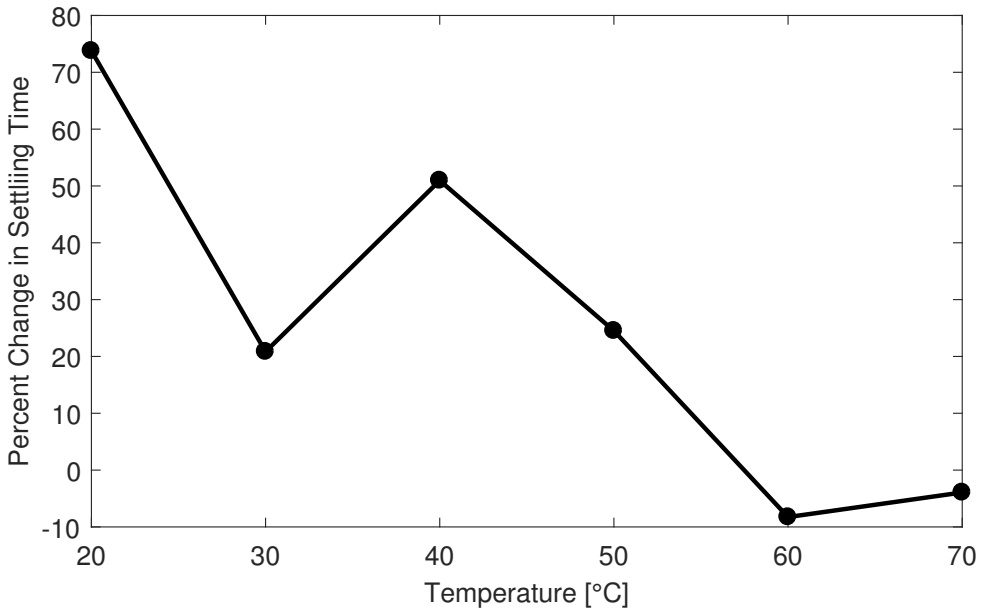

Figure 4.31: Percent change in setting time versus temperature

Table 4.9: Properties of M8528-P1 MFC patches from Smart Materials Corporation used in the experimental testing

Property	**Unit**	**Value**
Active length	mm	85
Active width	mm	28
Capacitance	nF	6.58
Free strain	ppm	1800
Blocking force	N	454

4.6.1 Experimental set-up

As in Section 4.1.2, the experimental model was printed on the Objet Connex 3D printer and two MFC patches were bonded to the base of the structure. The properties of the MFC patches are given in Table 4.9. The experimental set-up can be seen in Figure 4.32. Close-up images of the MFCs and the accelerometer can been seen in Figures 4.33 and 4.34 respectively.

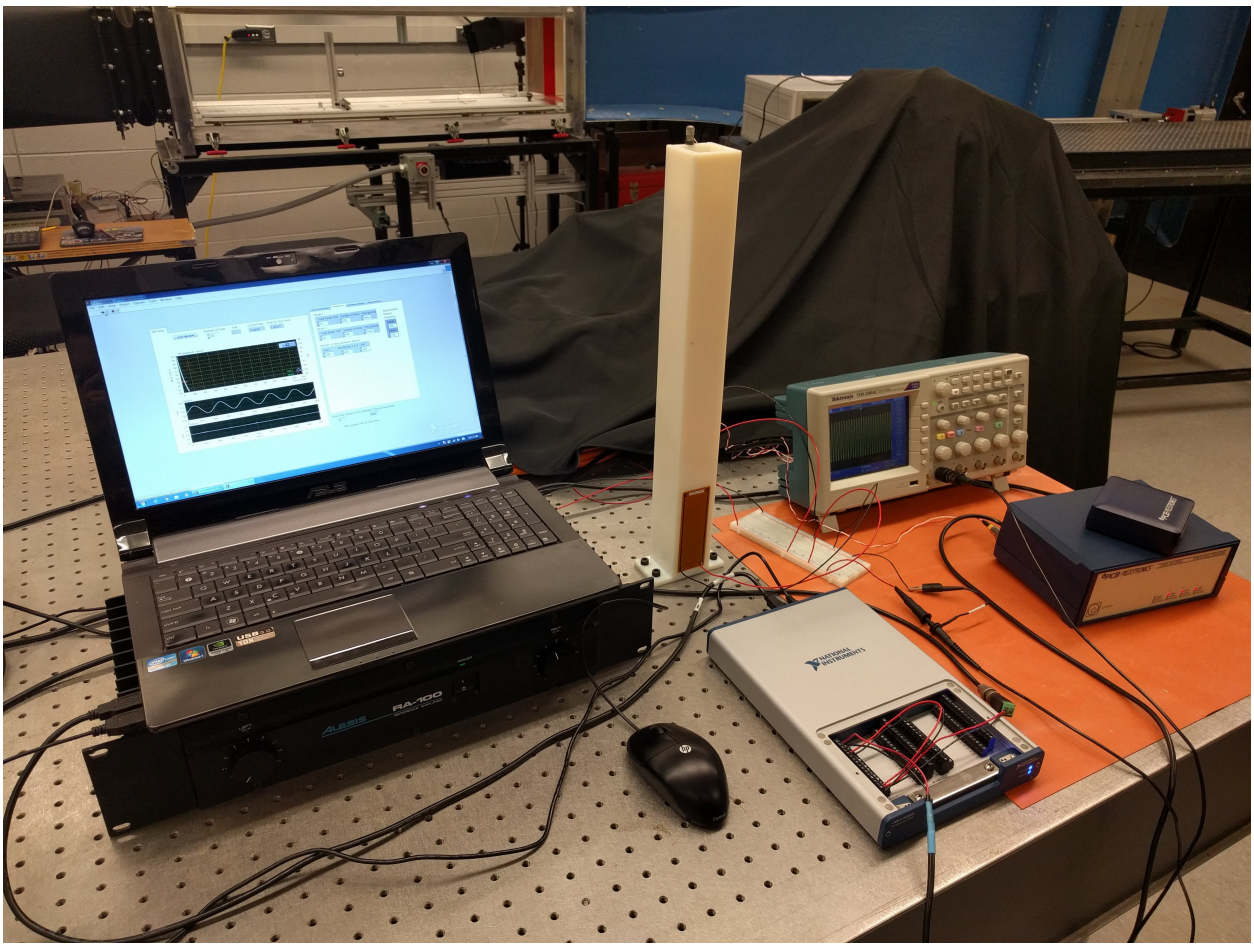

Figure 4.32: Experimental set-up used to test final metastructure design

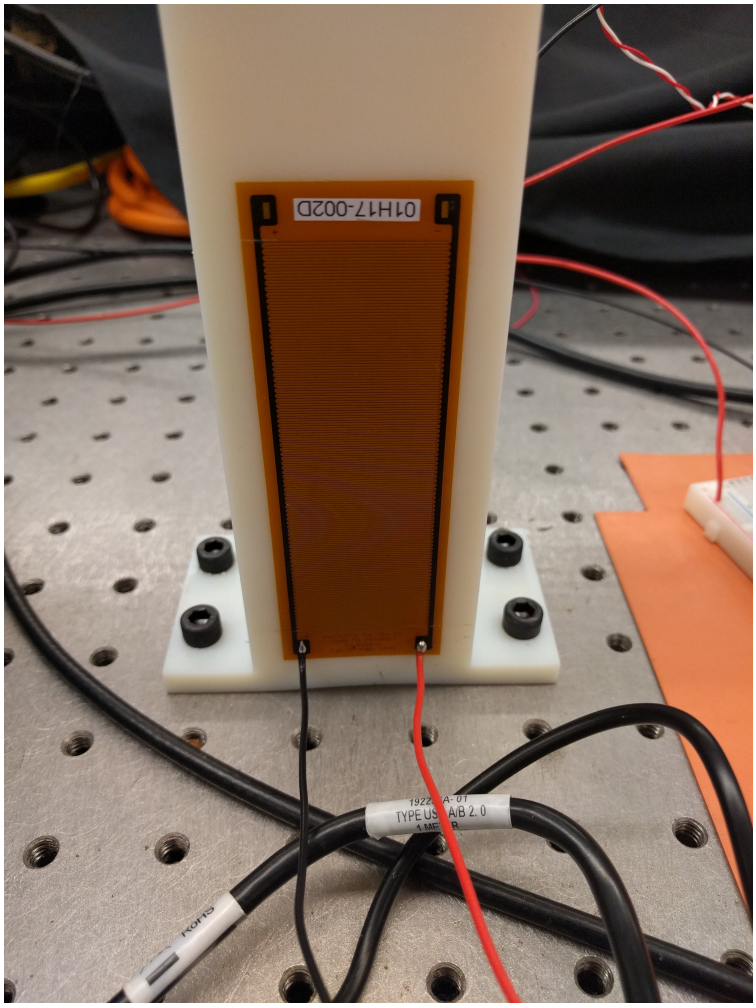

Figure 4.33: Close-up image of MFC bonded to base of metastructure

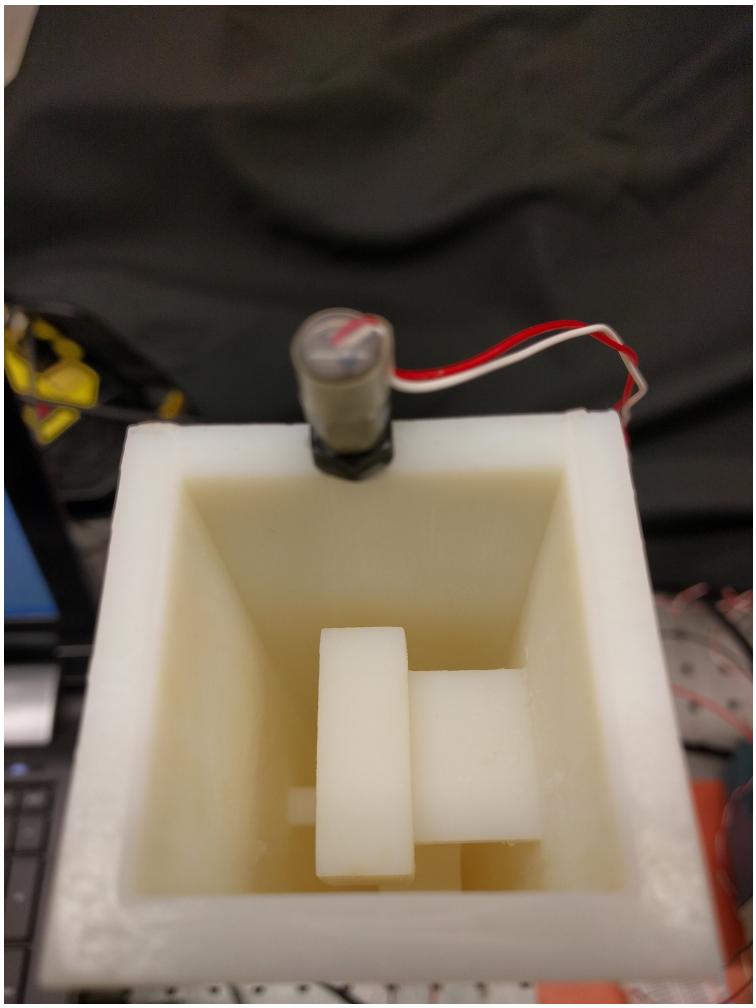

Figure 4.34: Close-up image of accelerometer mounted to tip of metastructure to measure axial accelerations

4.6.2 MFC patch modeling

The viscoelastic GHM model is modified slightly to match the experimental set-up described. The force applied to the metastructure by the MFC patches can be modeled as a traction force applied to the surface of the structure where the patch is bonded. The magnitude of the force depends on the geometry of the metastructure and the properties of the MFCs. This traction will be constant over the applied area and proportional to voltage. The total force applied by the MFC patch is represented as

$$f = \bar{f} v \tag{4.16}$$

where v is the applied voltage. Since the final FRF of the results will be normalized, the specific value of $\bar{f}$ does not need to be calculated. To incorporate this into the GHM model, Equation 4.16 must be converted to finite element form. The MFC patch applies a traction force to the outer edge of the structure. The structure is modeled as a bar, so the two MFC patches can be modeled as a traction force on the corresponding elements.

$$t_x = 2\frac{f}{\ell_p} \tag{4.17}$$

$$\mathbf{F}_i = \frac{t_x \ell_e}{2} \begin{bmatrix} 1 \\ \\ 1 \end{bmatrix} = \frac{\bar{f}\ell_e}{\ell_p} v \begin{bmatrix} 1 \\ \\ 1 \end{bmatrix} \tag{4.18}$$

The assembled force vector takes on the following form

$$\mathbf{F} = \frac{f\ell_e}{\ell_p} \begin{bmatrix} 0 & \cdots & 0 & 1 & 2 & \cdots & 2 & 1 & 0 & \cdots & 0 \end{bmatrix}^{\mathrm{T}} = \bar{\mathbf{F}} v \tag{4.19}$$

where the locations of the nonzero entry depend on the elements on the MFC patch is bonded to the structure. Next, the system must be transformed into state space. The equations of motion for the structure are

$$\mathbf{M}_v\ddot{\mathbf{q}} + \mathbf{D}_v\dot{\mathbf{q}} + \mathbf{K}_v\mathbf{q} = \mathbf{F} = \bar{\mathbf{F}}v \tag{4.20}$$

where $\mathbf{M}_v$, $\mathbf{D}_v$, and $\mathbf{K}_v$ are the mass, damping and stiffness matrices defined in the previous section, and $\mathbf{q}$ are the finite element displacements. The corresponding state space matrices for a voltage input are

$$\mathbf{A} = \begin{bmatrix} \mathbf{0} & \mathbf{I} \\ -\mathbf{M}_v^{-1}\mathbf{K}_v & -\mathbf{M}_v^{-1}\mathbf{D}_v \end{bmatrix} \tag{4.21a}$$

$$\mathbf{B} = \begin{bmatrix} \mathbf{0} \\ \mathbf{M}_v^{-1}\bar{\mathbf{F}} \end{bmatrix} \tag{4.21b}$$

$$\mathbf{C} = \begin{bmatrix} \mathbf{I} & \mathbf{0} \end{bmatrix} \tag{4.21c}$$

These can be used to express a transfer function matrix

$$\mathbf{H}(s) = \mathbf{C}(s\mathbf{I} - \mathbf{A})^{-1}\mathbf{B} \tag{4.22}$$

The transfer function will is an $n \times 1$ matrix with entries corresponding to the finite element degrees of freedom. The degree of freedom corresponding to the tip displacement of the bar will provide the desired FRF.

4.6.3 Comparison

This section looks at the comparison of the GHM model and the experimental results. The experimentally obtained natural frequencies of the vibration absorbers are compared to the natural frequencies predicted using the GHM model. These results are plotted in Figure 4.35. This plot also shows the natural frequencies calculated using an undamped elastic model. These results show that the GHM model is effective at predicting the natural frequencies of the 3D printed absorbers. The elastic model over predicts the natural frequencies at room

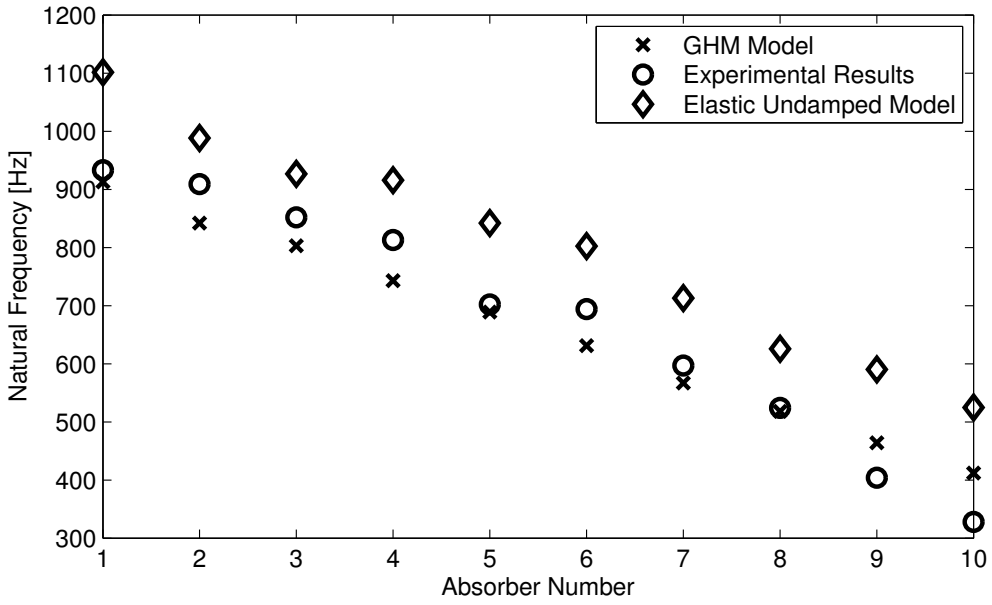

Figure 4.35: Comparison of the experimental absorber natural frequencies to the GHM model and an undamped elastic model

temperature.

Although the GHM model was able to accurately predict the natural frequencies of the absorbers, it did not accurately predict the natural frequencies of the host structure. The GHM model predicted a natural lower than that found experimentally. This led to a non-optimal design of the experimental metastructure. Although the non-optimal design was experimentally tested, the vibration absorbers with closely-spaced natural frequencies can still be observed. In traditional methods, where a single vibration absorber is used, the performance of the vibration absorber is highly dependent on the accuracy of the natural frequencies predictions. If the frequencies do not match, that can be detrimental to the performance. Using vibration absorbers with frequencies that vary leads to a more robust design. If the actual range of the frequencies is off from the predicted range, part of the actual range may still overlap with the critical frequencies to absorb.

4.7 Chapter summary

This chapter presents a metastructure design with vibration absorbers with linearly varying natural frequencies modeled using a distributed mass viscoelastic model. The design used consists of a bar with a hollow square cross-section with vibration absorbers distributed along the length of the bar. The vibration absorbers are cantilevered beams with large tip masses and arranged such that the bending motion of the beam suppresses vibration in the axial direction of the bar. The main contribution of this chapter is showing that a distributed mass metastructure can have better performance than a comparable baseline structure of the same weight. This was previously shown for the lumped mass model, and here it is also shown for the distributed mass viscoelastic model.

This chapter begins by explaining the design used throughout the rest of the chapter and by using a commercial finite element model and experimental results to show this design produces the expected behavior. Next, this chapter goes into detail about how to model the metastructure design proposed using a viscoelastic GHM model. The GHM model incorporates the damping inherent in the 3D printed materials while also providing a model that takes into account temperature change. After the modeling strategies are presented, a detailed design approach is presented. This dissertation shows the complete process necessary to implement the GHM model in a metastructure. It starts with the material characterization of the 3D printed material in Chapter III and then shows how that data can be used to create a GHM model of a metastructure in this chapter.

The benefits of using the GHM model are two-fold. First, the model incorporates damping into the model based on material properties and second, the GHM model can account for temperature change. A change in temperature can significantly alter both the storage modulus and the loss modulus of the material; these changes lead to changes in the natural frequencies and the damping of the resulting structure. The GHM model can capture these effects.

The GHM model developed was used to model the dynamics of a metastructure and

studies the effects of changing temperature. The results showed that the changes in the natural frequency of the host structure and the vibration absorbers changed at a similar rate, resulting in similar trends in the dynamic response as the temperature increase. This was true up until a specific temperature when the performance of the metastructure significantly decreased resulting in the baseline structure have better performance.

Lastly, the GHM model of the metastructure is compared to experimental results. These results showed that the experimental metastructure successfully absorbed vibrations at varying frequencies by using the vibration absorbers with linearly varying natural frequencies. The GHM model was not able to accurately predict the natural frequency of the host structure, producing a non-optimal design where the absorbers were absorbing frequencies lower than necessary based on the predicted design. This shows that although there are many benefits to using the GHM model, more needs to go into ensuring the model can predict the natural frequency of structure made from these 3D printed structures.

This work provides a crucial first step in gaining a better understanding of how to model the viscoelastic natural of 3D printed materials. Future work can explore the variability of the properties of the 3D printed materials and also how the storage modulus and loss factor are experimentally tested and how the GHM model parameters are determined.

CHAPTER V

Active Vibration Control of a Metastructure

As previous chapters have shown, the concept of adding distributed vibration absorbers, to create a metastructure, has been shown to improve the performance of the structure, but these structures still suffer from the effects of temperatures changes. This chapter will examine the effects of adding an active vibration control system to a metastructure to counteract the effects of temperature change. The control system is implemented through a single actuator placed on the structure, and the Positive Position Feedback (PPF) control law is utilized. This chapter begins by explaining the details of the PPF control law then describes the performance measures used. Both the settling time and the H_2 norm are used, but the emphasis is placed on the settling time since it can be measured in real-time.

The active vibration control concept is examined for both a lumped mass model and a distributed mass model, using the models developed in Chapters II and IV. For the lumped mass model, first, the observability and controllability norms are examined to determine how the actuator and sensor locations affect the controllability and observability of the structure. Next, two different lumped mass models designs are examined, a structure that is optimized with respect to the H_2 norm and a structure that is optimized with respect to the settling time. The location of control force varies by the allowing the force to be applied to each absorber. For each location, the controller parameters are optimized using the settling time. This provides insight into how the location of the actuator affects the

performance. The relationship between the gain and the settling time is also explored. For the distributed mass models, the design from Chapter IV is used. The control force is applied to the absorber masses using piezoelectric actuators. Two different concepts are explored, one where a stack actuator is attached to the absorber mass and second where a piezoelectric bimorph configuration is added to the beam of one of the absorbers. The addition of the piezoelectric materials changes the stiffness of the absorbers, thus must be accounted for in the design of the metastructure. For each of these cases, the modeling used is described in addition to how the actuators can be used within the PPF control algorithms.

5.1 PPF control law and settling time

The control law used in this chapter is the PPF control law with a single actuator on the structure. A single actuator is used because of its ease of implementation into a metastructure. PPF was first introduced by Goh and Caughey in 1985 and is a popular control method used in vibration control [87]. This control law adds additional dynamics to the system. PPF is utilized because of its ease of implementation for vibration control; the controller can be designed around an experimental transfer function and does not require an analytic model [73]. Here, the PPF control law will be demonstrated using a single degree of freedom system. Later in this chapter, the formulation will be developed for the metastructure and will use piezoelectric materials. For a single degree of freedom system, the equation of motion is

$$\ddot{x} + 2\zeta\omega_n\dot{x} + \omega_n^2 x = bu \tag{5.1}$$

where ζ and ω_n are the damping ratio and natural frequency of the structure, x is the displacement of the structure, u is the control input, and b is the input coefficient. A compensator is defined as

$$\ddot{\eta} + 2\zeta_f \omega_f \dot{\eta} + \omega_f^2 \eta = g\omega_f x \tag{5.2a}$$

$$u = \frac{g}{b}\omega_f \eta \tag{5.2b}$$

where η is the value of the compensator, ζ_f and ω_f are the damping ratio and natural frequency of the controller, and g is the gain, a constant value. Combining Equations 5.1 and 5.2 results in equations of motion in their usual second-order form

$$\begin{bmatrix} \ddot{x} \\ \ddot{\eta} \end{bmatrix} + \begin{bmatrix} 2\zeta\omega_n & 0 \\ 0 & 2\zeta_f\omega_f \end{bmatrix} \begin{bmatrix} \dot{x} \\ \dot{\eta} \end{bmatrix} + \begin{bmatrix} \omega_n^2 & -g\omega_f \\ -g\omega_f & \omega_f^2 \end{bmatrix} \begin{bmatrix} x \\ \eta \end{bmatrix} = \begin{bmatrix} 0 \\ 0 \end{bmatrix} \tag{5.3}$$

To ensure stability of this system, the augmented stiffness matrix must be positive definite. A matrix is positive definite when the determinant of the matrix is positive, leading to the following stability requirement

$$g^2 < \omega_n^2 \tag{5.4}$$

This chapter references both the H_2 norm and the settling time as performance measures. The H_2 is defined in detail in Section 2.2. The settling time calculation will be described here.

The settling time uses the time response to an impulse response function and determines when the value of the system falls below a predefined threshold. The impulse response, $h(t)$, is calculated once the system is put into state space as

$$h(t) = \mathbf{C}e^{\mathbf{A}t}\mathbf{B} \tag{5.5}$$

The time at which the error falls below a threshold value is known as the setting time, t_s and occurs with the following relationship is met

$$|h(t_s) - h_f| = \delta h_0 \tag{5.6}$$

where h_f is the final steady-state value, δ is the threshold percentage and h_0 is the initial value after the impulse. For this dissertation, the threshold percentage used is 5%.

5.2 Lumped mass metastructure model

This section will examine the lumped mass metastructure model developed in Chapter II. The section begins by examining the controllability and observability of the lumped mass metastructure model to determine the effects of where the controller force is placed. Next, the PPF control law is implemented into two different metastructure designs [105]. Note that the previous work uses $\mathbf{q}(t)$ to represent the displacement of the masses, here $\mathbf{x}(t)$ will be used to avoid confusion with charge used later. The lumped mass model used is seen in Figure 5.1 where Figure 5.1a shows the control force acting on one of the absorber masses and Figure 5.1b shows. the control force acting on one of the host masses.

5.2.1 Observability and controllability

To determine the best placement of the sensor and actuator, we will examine the controllability and observability norms [106, 107]. This analysis is done on a lumped mass model with ten absorbers, a mass ratio of 0.3, and linearly varying natural frequencies optimized with respect to the H_2 norm. The FRF response of this structure is shown in Figure 5.2. The equations of motion of this structure including the control force and sensing are

$$\mathbf{M}\ddot{\mathbf{x}}(t) + \mathbf{D}\dot{\mathbf{x}}(t) + \mathbf{K}\mathbf{x}(t) = \mathbf{B}_f u(t) \tag{5.7a}$$

$$\mathbf{y}(t) = \mathbf{C}_p\mathbf{x}(t) + \mathbf{C}_v\dot{\mathbf{x}}(t) \tag{5.7b}$$

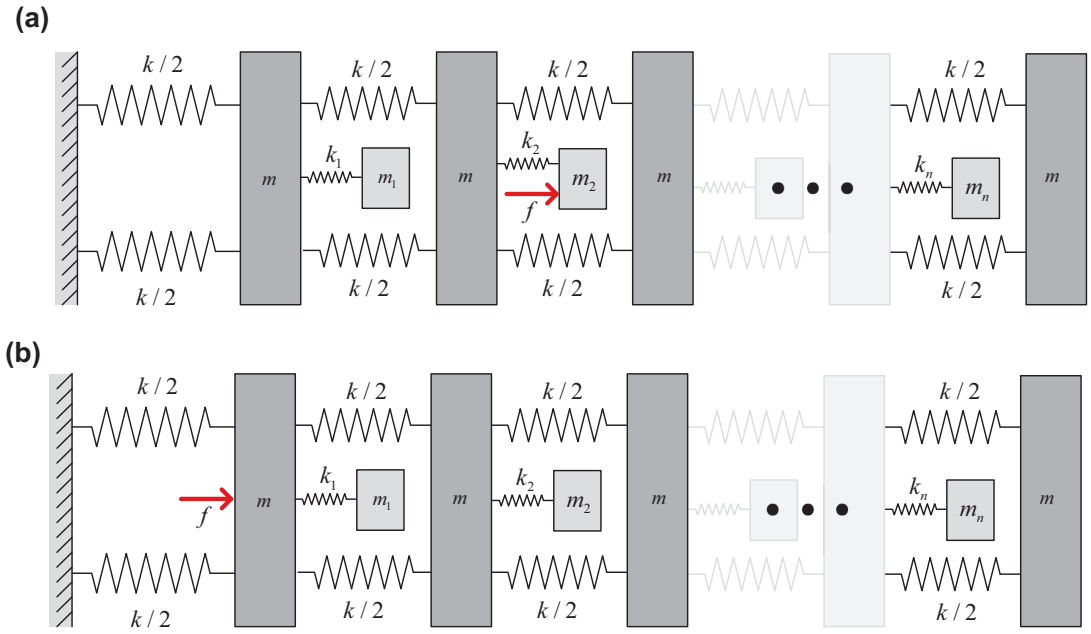

Figure 5.1: Lumped mass model with control force acting on (a) absorber mass and (b) main mass

where u is the control force to the system, $\mathbf{B}_f$ describes the position of the control force, $\mathbf{y}$ is the output vector, and $\mathbf{C}_p$ and $\mathbf{C}_v$ are the displacement and velocity influence coefficients, respectively with their form determined by the placement of the sensors.

To examine the controllability and observability norms, the equations of motion (Equation 5.7) are transformed into modal coordinates using a transformation matrix of eigenvectors, $\mathbf{S}_m$ such that

$$\mathbf{S}_m^T \mathbf{M} \mathbf{S}_m = \mathbf{I} \tag{5.8a}$$

$$\mathbf{S}_m^{\mathrm{T}} \mathbf{K} \mathbf{S}_m = \tilde{\mathbf{K}} = \mathrm{diag}(\omega_1^2, \ldots, \omega_N^2) \tag{5.8b}$$

Letting $\tilde{\mathbf{x}} = \mathbf{S}_m^{\mathrm{T}} \mathbf{x}$ and ignoring the damping, Equation 5.7 becomes

$$\ddot{\tilde{\mathbf{x}}} + \tilde{\mathbf{K}} \tilde{\mathbf{x}} = \tilde{\mathbf{B}}_f u \tag{5.9a}$$

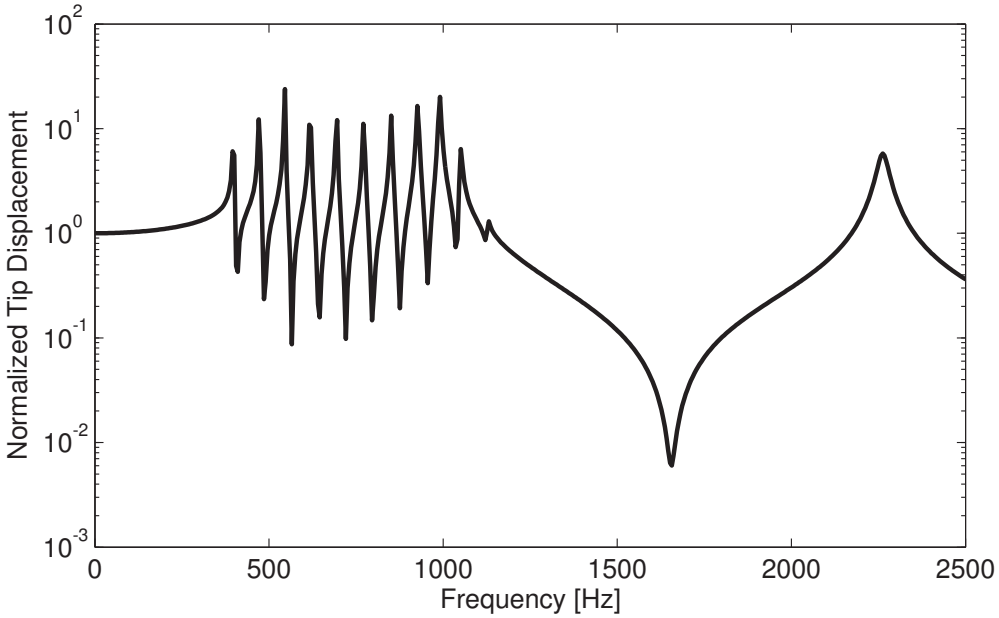

Figure 5.2: Normalized frequency response function of the uncontrolled lumped mass metastructure

$$\mathbf{y} = \tilde{\mathbf{C}}_p\tilde{\mathbf{x}} + \tilde{\mathbf{C}}_v\dot{\tilde{\mathbf{x}}} \tag{5.9b}$$

where $\tilde{\mathbf{B}}_f = \mathbf{S}_m^{\mathrm{T}}\mathbf{B}_f$, $\tilde{\mathbf{C}}_p = \mathbf{C}_p\mathbf{S}_m$ and $\tilde{\mathbf{C}}_v = \mathbf{C}_v\mathbf{S}_m$.

5.2.1.1 Observability norm

Using the modal coordinates, we will examine the cases with a position and rate sensor placed at each absorber. The placements of the position and velocity sensors are dictated by the definitions of the $\mathbf{C}_p$ and $\mathbf{C}_v$ vectors respectively. These are defined as

$$\mathbf{C}_p = \begin{bmatrix} \mathbf{0}_{(n+1)\times 1} & \mathbf{1}_i \end{bmatrix} \tag{5.10a}$$

$$\mathbf{C}_v = \begin{bmatrix} \mathbf{0}_{(n+1)\times 1} & \mathbf{1}_i \end{bmatrix} \tag{5.10b}$$

where n is the number of absorbers, and $\mathbf{1}_i$ is a row of n zeros except for a 1 in the ith position which is the corresponding degree of freedom to the absorber which is being controlled. To determine which absorber can best sense the system, we will examine the

observability norm $\mathcal{O}_q$ which indicates the extent of the observability of the qth mode of the structure and is defined as

$$\mathcal{O}_q = [\det(\mathbf{F}_q \mathbf{F}_q^{\mathrm{T}})]^{1/4N_q} \tag{5.11}$$

where

$$\mathbf{F}_q = \begin{bmatrix} (\tilde{\mathbf{C}}_p)_q & (\tilde{\mathbf{C}}_v)_q \\ -\lambda_q(\tilde{\mathbf{C}}_v)_q & (\tilde{\mathbf{C}}_p)_q \end{bmatrix} \tag{5.12}$$

where $(\tilde{\mathbf{C}}_p)_q$ and $(\tilde{\mathbf{C}}_v)_q$ are the partition of the matrices $\tilde{\mathbf{C}}_p$ and $\tilde{\mathbf{C}}_v$ according to the multiplicities of the eigenvalues. Since this system has distinct eigenvalues ($N_q = 1$), the partitions are simply the rows of the original matrix. The configurations in which there is a position sensor on each absorber and a rate sensor are examined. For a position sensor, $\mathbf{F}_q$ has the following form

$$\mathbf{F}_q = \begin{bmatrix} (\tilde{\mathbf{C}}_p)_q & 0 \\ 0 & (\tilde{\mathbf{C}}_p)_q \end{bmatrix} \tag{5.13}$$

and for a rate sensor, $\mathbf{F}_q$ has the following form

$$\mathbf{F}_q = \begin{bmatrix} 0 & (\tilde{\mathbf{C}}_v)_q \\ \lambda_q(\tilde{\mathbf{C}}_v)_q & 0 \end{bmatrix} \tag{5.14}$$

The observability norm is calculated for different configurations. For each configuration, the sensor is placed on a different absorber. Since there are ten absorbers, ten different configurations are used and labeled based on the absorber number where the sensor is placed. Absorber 1 is the absorber closest to the base and absorber 10 is the absorber at the tip. The values of the observability norms for the position sensors and velocity sensors are shown in Tables 5.1 and 5.2, respectively. These tables show the value of the observability norm for each of the first 11 modes of the structure when a single position sensor is placed on each

Table 5.1: Observability norm values for the first 11 modes of the system, for position sensors located on various absorbers. For each location of the sensor, an average value is calculated.

Mode	**Location of Position Sensor (Absorber Number)**									
	1	**2**	**3**	**4**	**5**	**6**	**7**	**8**	**9**	**10**
1	0.045	0.091	0.140	0.192	0.249	0.318	0.409	0.559	0.930	7.279
2	0.074	0.153	0.237	0.331	0.441	0.587	0.819	1.365	6.931	1.348
3	0.109	0.228	0.359	0.514	0.713	1.021	1.699	6.398	2.269	0.712
4	0.142	0.302	0.488	0.725	1.081	1.817	5.826	3.194	0.970	0.459
5	0.176	0.382	0.644	1.027	1.785	5.379	3.870	1.154	0.573	0.316
6	0.220	0.500	0.905	1.682	5.072	4.286	1.288	0.673	0.398	0.240
7	0.292	0.714	1.505	4.734	4.594	1.427	0.795	0.504	0.328	0.209
8	0.399	1.128	3.789	5.106	1.622	0.981	0.675	0.476	0.330	0.218
9	0.344	1.317	6.104	1.497	1.016	0.773	0.596	0.449	0.325	0.221
10	0.253	7.164	0.205	0.357	0.358	0.322	0.272	0.216	0.162	0.112
11	7.428	0.449	0.067	0.031	0.063	0.071	0.067	0.057	0.044	0.032
Location Average	0.862	1.130	1.313	1.472	1.545	1.544	1.483	1.368	1.206	1.013

absorber. The observability norms are also depicted using a bar graph shown in Figures 5.3 and 5.4. These values take on the highest value along a diagonal line. For example, when the position sensor is placed at the tip absorber (absorber 10), it is best at sensing the first mode. This can be explained by examining what the mode looks like for each natural frequency. When excited at the first natural frequency, most of the motion occurs at the tip mass which experiences significant bending motion. When designing the metastructure, the tip absorber is tuned to have the lowest natural frequency of the absorbers which corresponds to the first natural frequency of the metastructure. Since most of the motion is occurring in the tip absorber, it makes sense that having a sensor at the tip absorber is best at sensing that mode shape. The modes 12 and above correspond to longitudinal modes of the entire host structure with minimal movement of the absorbers. For the velocity sensor, similar trends are observed, but with more variation along that diagonal line. When the velocity sensor is placed closer to the base, it is better at observing its corresponding mode.

These values are also examined by looking at the average observability norm values for each of the sensor locations. These can be seen in Figures 5.5 and 5.6. For each absorber,

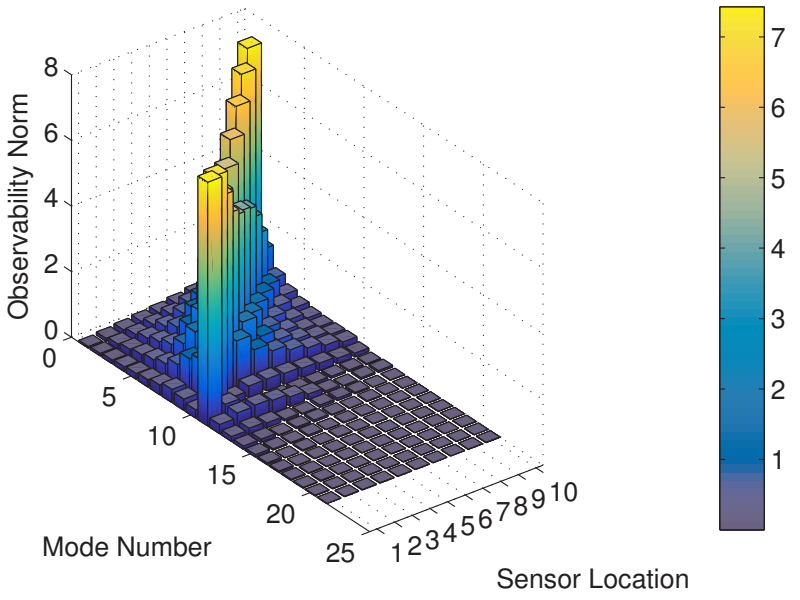

Figure 5.3: Bar graph of observability norm values for position sensors located on various absorbers

Table 5.2: Observability norm values for the first 11 modes of the system, for velocity sensors located on various absorbers. For each location of the sensor, an average value is calculated.

Mode	**Location of Velocity Sensor (Absorber Number)**									
	1	**2**	**3**	**4**	**5**	**6**	**7**	**8**	**9**	**10**
1	112	228	350	480	625	796	1025	1399	2329	18224
2	220	453	704	982	1310	1742	2432	4053	20573	4001
3	374	779	1230	1758	2441	3497	5816	21903	7768	2436
4	552	1171	1895	2817	4198	7058	22631	12406	3770	1782
5	766	1667	2808	4478	7786	23462	16880	5032	2497	1380
6	1068	2427	4393	8162	24611	20797	6251	3268	1933	1163
7	1561	3819	8047	25319	24570	7632	4250	2695	1755	1116
8	2325	6571	22070	29740	9446	5715	3931	2774	1924	1272
9	2139	8196	37982	9312	6320	4811	3708	2796	2022	1373
10	1666	47261	1349	2353	2365	2127	1794	1428	1069	742
11	52614	3181	472	216	449	504	475	404	315	224
Location Average	5763	6887	7391	7783	7647	7104	6290	5287	4178	3065

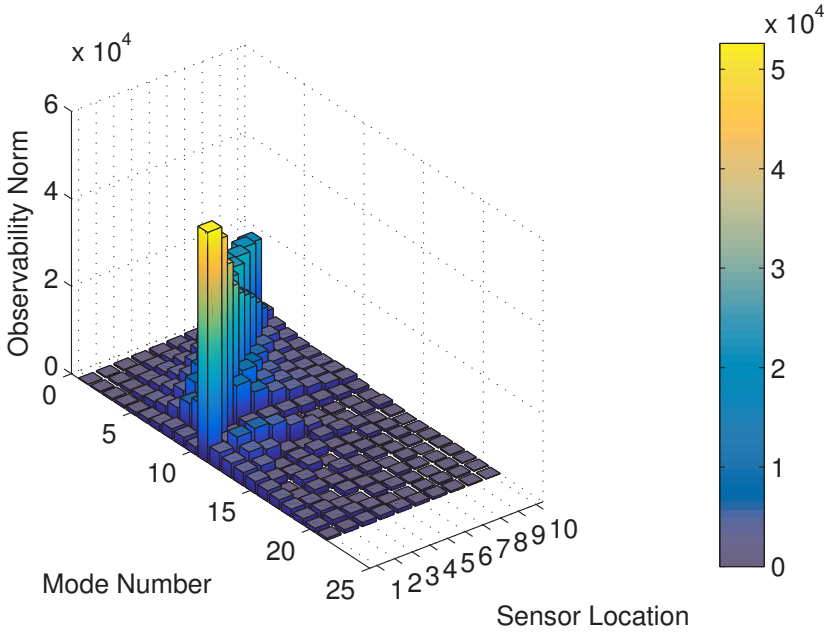

Figure 5.4: Bar graph of observability norm values for velocity sensors located on various absorbers

the average of the observability norm is calculated for all modes and additionally for the modes under 1500 Hz which corresponds to the first 11 modes of the metastructure. These plots give us a sense of which sensor locations are best for observing all the modes of the metastructure. These plots show that the absorbers located more towards the center of the metastructure are better at observing more modes than absorbers located towards the outside. This is because the absorbers near the center tend to oscillate significantly during two modes of vibration. There are ten absorbers and 11 natural frequencies in the range of 0 to 1500 Hz. The mode on the edges of that range corresponds to the movement of a single absorber whereas the ones towards the middle part of that range correspond to the movement of two absorbers.

5.2.1.2 Controllability norm

Next, the controllability norm is examined. Once again, cases in which the actuator is placed at each absorber will be examined. This is dictated by the definition of the $\mathbf{B}_f$ vector,

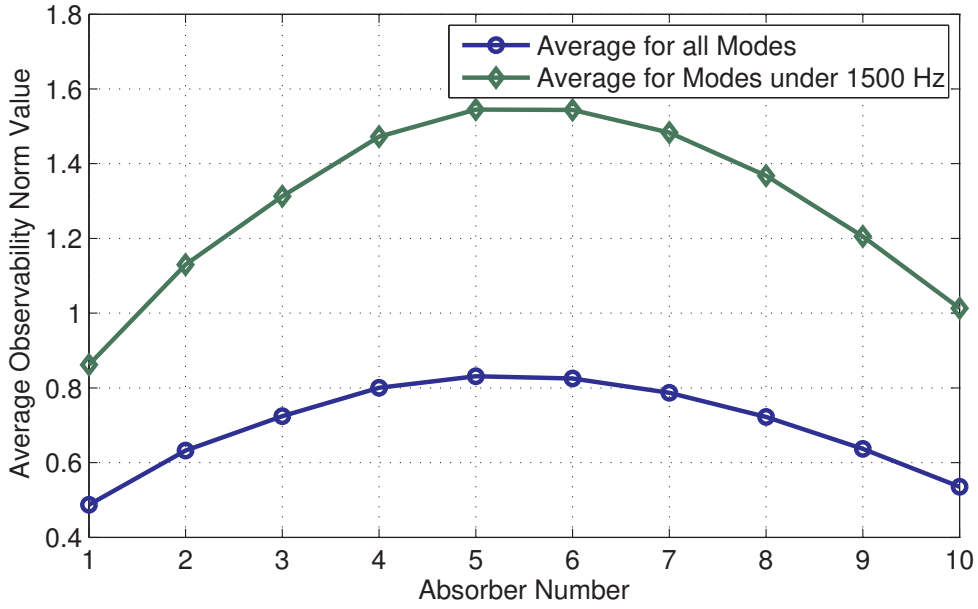

Figure 5.5: Average observability norm values for position sensors placed at each absorber

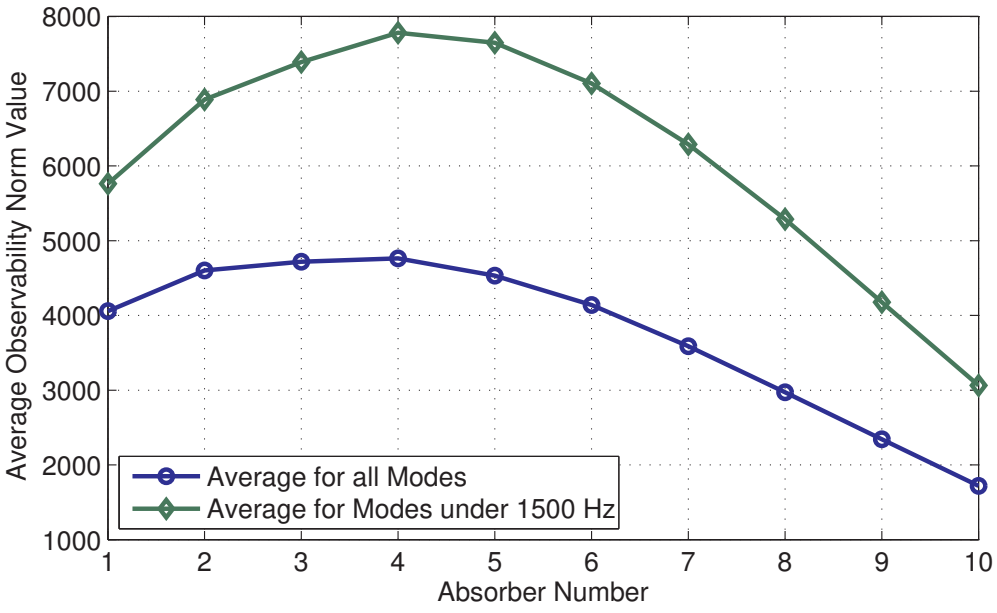

Figure 5.6: Average observability norm values for velocity sensors placed at each absorber

$$\mathbf{B}_f = \begin{bmatrix} \mathbf{0}_{(n+1)\times 1} & \mathbf{1}_i \end{bmatrix} \tag{5.15}$$

where $\mathbf{1}_i$ is a row of n zeros except for a 1 in the ith position which is the corresponding degree of freedom to the absorber which is being controlled. To determine which absorber can exert the most control over the system we will examine the controllability norm $\mathcal{C}_q$ which indicates the extent of the controllability of the qth mode of the structure and is defined as

$$\mathcal{C}_q = [\det(\mathbf{B}_q \mathbf{B}_q^{\mathrm{T}})]^{1/2N_q} \tag{5.16}$$

where $\mathbf{B}_q$ are the partitions of the matrix $\tilde{\mathbf{B}}_f$ according to the multiplicities of the eigenvalues. Since this system has distinct eigenvalues ($N_q = 1$), the partitions $\mathbf{B}q$ are simply the rows of $\tilde{\mathbf{B}}_f$.

Like the observability norm, the controllability norm is calculated for different configurations. For each configuration, the control force is acting on a different absorber. Since there are ten absorbers, ten different configurations are used and labeled based on the absorber number where the control force is acting. The values of the controllability norm are shown in Table 5.3. Once again these values are also depicted using a bar graph as seen in Figure 5.7. The values of the controllability norm take on the same values at the observability norm for a position sensor. This means all the trends that we concluded from the observability norms can also be used to describe how good the placing a sensor on a specific absorber is at controlling the modes. Figure 5.8 shows the average values of the controllability norm for a control force acting on a specific absorber.

5.2.2 PPF lumped mass model implementation

This section will look at the actual implementation of the PPF control law using a lumped mass model. The formulation for a single degree of freedom system was shown in Section 5.1. Here that will be extended to a multiple degree of freedom system. The equations of

Table 5.3: Controllability norm values for the first 11 modes of the system, for control forces acting on various absorbers. For each location of the control force, an average value is calculated.

Mode	**Absorber Number**									
	1	**2**	**3**	**4**	**5**	**6**	**7**	**8**	**9**	**10**
1	0.045	0.091	0.140	0.192	0.249	0.318	0.409	0.559	0.930	7.279
2	0.074	0.153	0.237	0.331	0.441	0.587	0.819	1.365	6.931	1.348
3	0.109	0.228	0.359	0.514	0.713	1.021	1.699	6.398	2.269	0.712
4	0.142	0.302	0.488	0.725	1.081	1.817	5.826	3.194	0.970	0.459
5	0.176	0.382	0.644	1.027	1.785	5.379	3.870	1.154	0.573	0.316
6	0.220	0.500	0.905	1.682	5.072	4.286	1.288	0.673	0.398	0.240
7	0.292	0.714	1.505	4.734	4.594	1.427	0.795	0.504	0.328	0.209
8	0.399	1.128	3.789	5.106	1.622	0.981	0.675	0.476	0.330	0.218
9	0.344	1.317	6.104	1.497	1.016	0.773	0.596	0.449	0.325	0.221
10	0.253	7.164	0.205	0.357	0.358	0.322	0.272	0.216	0.162	0.112
11	7.428	0.449	0.067	0.031	0.063	0.071	0.067	0.057	0.044	0.032
Location Average	0.862	1.130	1.313	1.472	1.545	1.544	1.483	1.368	1.206	1.013

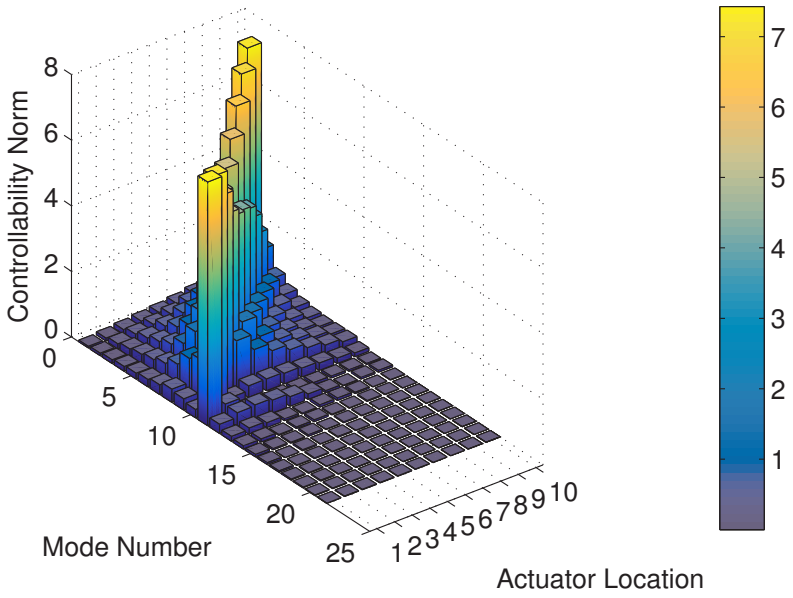

Figure 5.7: Bar graph of controllability norm values for a control force acting on various absorbers

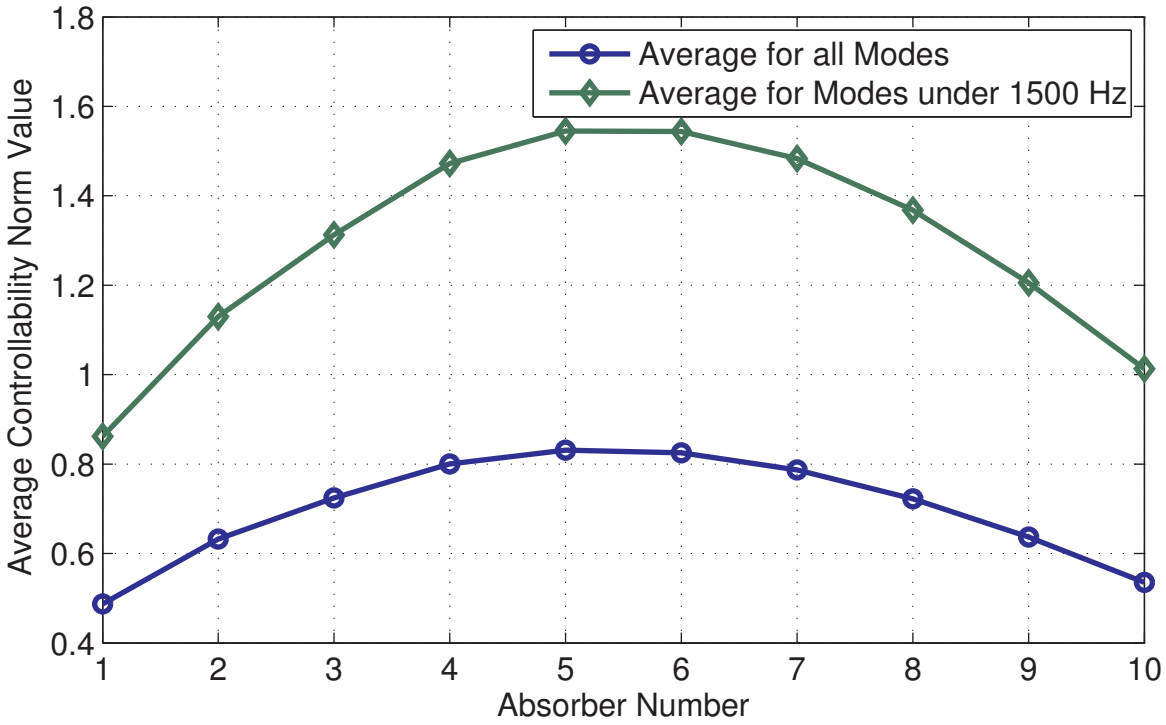

Figure 5.8: Average controllability norm values for control forces acting on each absorber

motion for this multiple degree of freedom system are

$$\mathbf{M}\ddot{\mathbf{x}}(t) + \mathbf{D}\dot{\mathbf{x}}(t) + \mathbf{K}\mathbf{x}(t) = \mathbf{B}_f u(t) \tag{5.17a}$$

$$y(t) = \mathbf{B}_f^{\mathrm{T}}\mathbf{q}(t) \tag{5.17b}$$

where u is the input force to the system provided by the controller, $\mathbf{B}_f$ is based on the location of the input force as shown in Equation 5.15, and y is the output of the sensor. This form of the equations of motion assumes collocated control, where the sensing and the actuating are occurring at the same location. The control is implemented using an auxiliary dynamics system defined using the following equations

$$\ddot{\eta}(t) + 2\zeta_f\omega_f\dot{\eta}(t) + \omega_f^2\eta(t) = g\omega_f y(t) \tag{5.18a}$$

$$u(t) = g\omega_f\eta(t) \tag{5.18b}$$

In which ζ_f and ω_f are the parameters of the controller and g is the gain. Combining the auxiliary system with the equations of motions yields

$$\begin{bmatrix} \mathbf{M} & 0 \\ 0 & 1 \end{bmatrix} \begin{bmatrix} \ddot{\mathbf{q}} \\ \ddot{\eta} \end{bmatrix} + \begin{bmatrix} \mathbf{D} & 0 \\ 0 & 2\zeta_f\omega_f \end{bmatrix} \begin{bmatrix} \dot{\mathbf{q}} \\ \dot{\eta} \end{bmatrix} + \begin{bmatrix} \mathbf{K} & -g\omega_f\mathbf{B}_f \\ -g\omega_f\mathbf{B}_f^{\mathrm{T}} & \omega_f^2 \end{bmatrix} \begin{bmatrix} \mathbf{q} \\ \eta \end{bmatrix} = \begin{bmatrix} \mathbf{0} \\ 0 \end{bmatrix} \tag{5.19}$$

The augmented mass matrix is positive definite and the augmented damping matrix is positive semi-definite. To ensure stability of the system, augmented stiffness matrix must also be positive definite. The augmented stiffness matrix will be defined as

$$\hat{\mathbf{K}} = \begin{bmatrix} \mathbf{K} & -g\omega_f\mathbf{B}_f \\ -g\omega_f\mathbf{B}_f^{\mathrm{T}} & \omega_f^2 \end{bmatrix} \tag{5.20}$$

To test if the augmented stiffness matrix is positive definite, it will be multiplied by an

arbitrary vector, $\mathbf{z}$

$$\mathbf{z}^{\mathrm{T}}\hat{\mathbf{K}}\mathbf{z} = \begin{bmatrix} \mathbf{z}_1^{\mathrm{T}} & \mathbf{z}_2^{\mathrm{T}} \end{bmatrix} \begin{bmatrix} \mathbf{K} & -g\omega_f\mathbf{B}_f \\ -g\omega_f\mathbf{B}_f^{\mathrm{T}} & \omega_f^2 \end{bmatrix} \begin{bmatrix} \mathbf{z}_1 \\ \mathbf{z}_2 \end{bmatrix} \tag{5.21a}$$

$$= \mathbf{z}_1^{\mathrm{T}}\mathbf{K}\mathbf{z_1} - g\omega_f\mathbf{z}_2^{\mathrm{T}}\mathbf{B}_f\mathbf{z}_1 - g\omega_f\mathbf{z}_1^{\mathrm{T}}\mathbf{B}_f\mathbf{z}_2 + \omega_f^2\mathbf{z}_2^{\mathrm{T}}\mathbf{z}_2 \tag{5.21b}$$

where $\mathbf{z}_1$ and $\mathbf{z}_2$ are partitions of $\mathbf{z}$. Completing the square and defining an arbitrary vector, $\mathbf{y}$

$$\mathbf{z}^{\mathrm{T}}\hat{\mathbf{K}}\mathbf{z} = \mathbf{z}_1^{\mathrm{T}}\left(\mathbf{K} - g^2\mathbf{B}_f^{\mathrm{T}}\mathbf{B}_f\right)\mathbf{z}_1 + \left(g\mathbf{B}_f^{\mathrm{T}}\mathbf{z}_1 - \omega_f\mathbf{z}_2\right)^{\mathrm{T}}\left(g\mathbf{B}_f^{\mathrm{T}}\mathbf{z}_1 - \omega_f\mathbf{z}_2\right) \tag{5.22a}$$

$$= \mathbf{z}_1^{\mathrm{T}}\left(\mathbf{K} - g^2\mathbf{B}_f^{\mathrm{T}}\mathbf{B}_f\right)\mathbf{z}_1 + \mathbf{y}^{\mathrm{T}}\mathbf{y} \tag{5.22b}$$

Since $\mathbf{y}^{\mathrm{T}}\mathbf{y}$ will never be negative, the augmented stiffness matrix, $\hat{\mathbf{K}}$ will be positive definite if $\mathbf{K} - g^2\mathbf{B}_f^{\mathrm{T}}\mathbf{B}_f$ is positive definite This provides a stability criterion.

Two different lumped mass metastructure designs are used in the following sections. Both of these designs have ten absorbers, a mass ratio of 0.3, and absorbers with linearly varying natural frequencies. For the first design, the natural frequencies are chosen such that the H_2 norm is minimized. This will be referred to as Design 1, and the frequency response and the impulse response are shown in Figure 5.9. For Design 2, the absorber natural frequencies are chosen such that the settling time of the structure is minimized. The response of Design 2 can be seen in Figure 5.10.

5.2.2.1 Controller design

Two different designs from the previous section will be inspected to determine the effects of a control system on the response of the structure. The best location of the actuator must be determined. This section will examine cases where the control force is being applied to

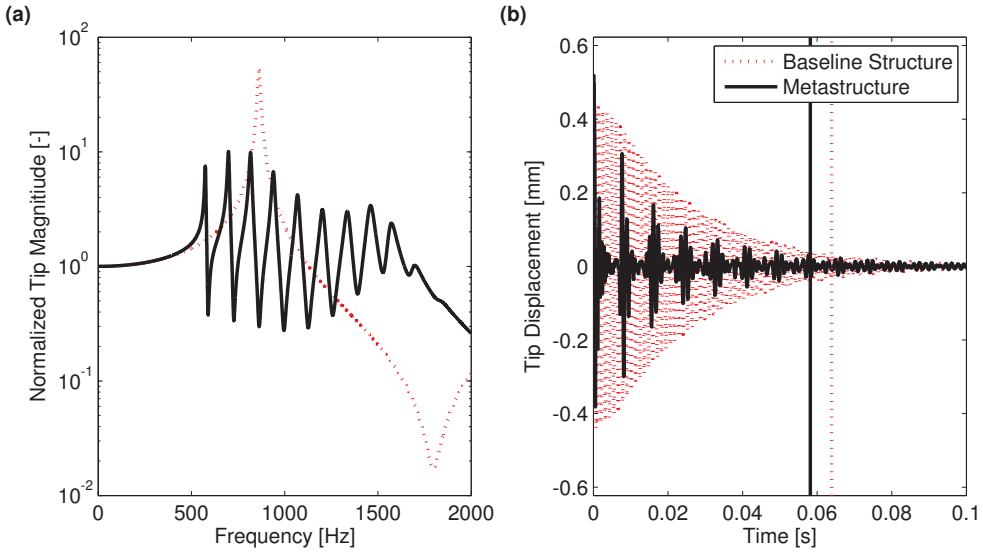

Figure 5.9: The (a) frequency response function and (b) impulse response function of Design 1, where the vertical line in the impulse response function shows the settling time of structures

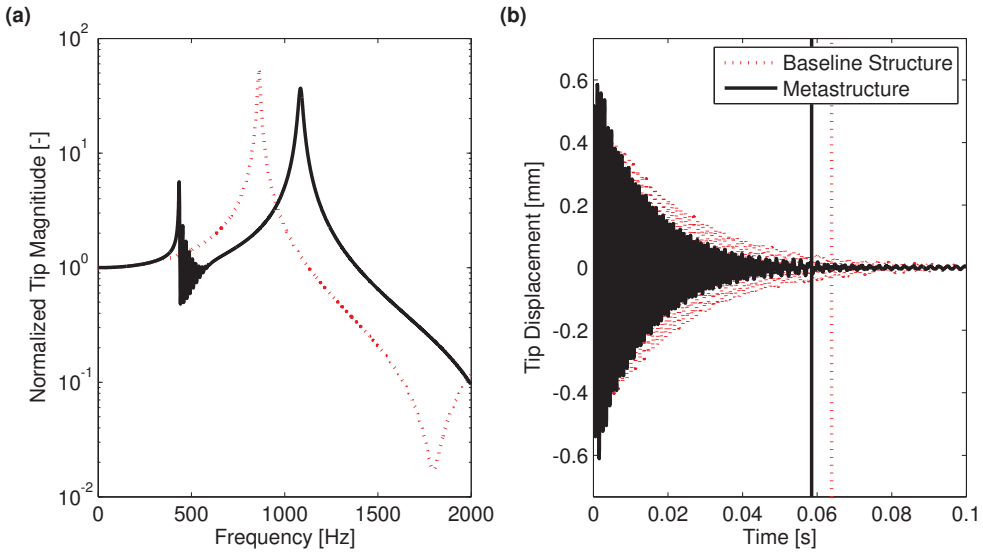

Figure 5.10: The (a) frequency response function and (b) impulse response function of Design 2, where the vertical line in the impulse response function shows the settling time of structures

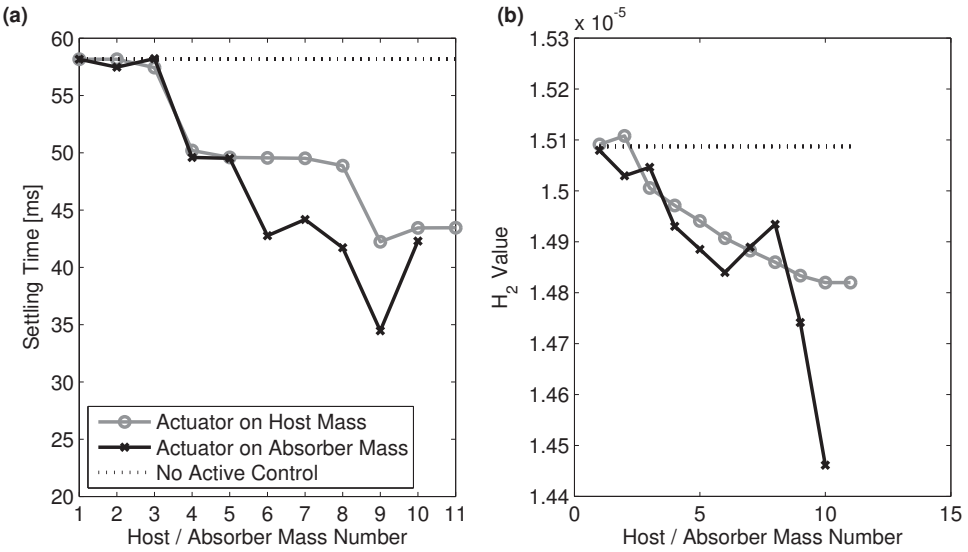

Figure 5.11: The (a) settling time and (b) H_2 norm values for Design 1 when controller values are optimized with respect to the settling time for various actuator locations

the vibration absorbers and the host masses. For each control force location, the structure remains the same, the gain is held constant and the controller parameters are varied to determine the best controller parameters for a each control force location. The structure has 11 host masses and ten absorber masses. The actuator is placed on each one of the masses and then the controller parameters, ω_f and ζ_f are optimized with respect to the settling time. Optimizing the structure with respect to the H_2 norm gave very similar results thus is not included here. This accomplished using a simple a constrained non-linear interior point optimization algorithm (`fmincon`) in MATLAB.

The response of Design 1 without control is shown in Figure 5.9. The time response of this structure has more apparent beating behavior compared to the other design utilized. The optimization of the controller parameters was run, and the performance measures plotted in Figure 5.11. The lower mass and absorber numbers refer to masses closer to the base of the bar. The results show that an actuator placed closer to the tip of the bar is more effective reducing vibrations. The corresponding optimized controller values for each of these cases are shown in Figure 5.12.

Three of the specific cases will be examined in more detail. The first case is when the

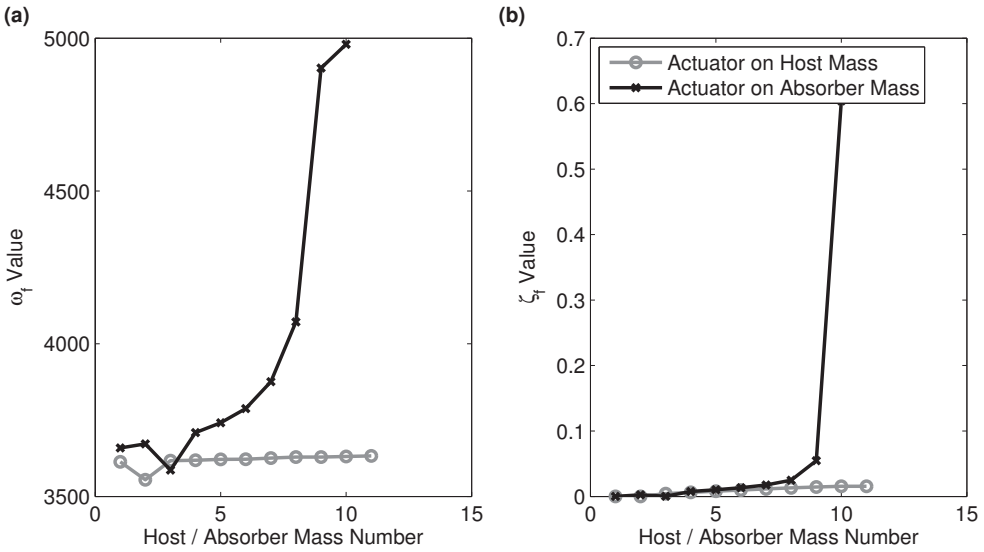

Figure 5.12: Optimized values of controller (a) natural frequency and (b) damping value for various actuator locations for Design 1

actuator is placed on the host mass closest to the tip of the metastructure bar. The response of this structure can be seen in Figure 5.13. On the FRF, there is a slight decrease in the magnitude near the first peak which corresponds to a settling time decrease from 58.2 ms to 43.5 ms. The second case examined is when the actuator is placed on the absorber mass located second from the tip. The response can be seen in Figure 5.14. In this case, you can see that the controller can eliminate the second mode of the metastructure. This results in a settling time decrease from 58.2 ms to 34.4 ms. The last case examined is when the actuator is placed on the absorber mass which is fourth from the tip, and the results are shown in Figure 5.15. For this case, the settling time decreases to 44.2 ms which is slightly higher than the previous case. Looking at the FRF, this case is not able to completely control a single mode but influences a few of the modes. This results in a slight settling time reduction.

Similar to Design 1, the same plots are examined for Design 2. The uncontrolled response of Design 2 is shown in Figure 5.10. This response does not have the beating behavior that dominates the response from design one. Instead, there are two peaks near the fundamental natural frequency of the baseline structure. As with Design 1, the actuator is placed on various masses, and the controller parameters are optimized, and the resulting performance

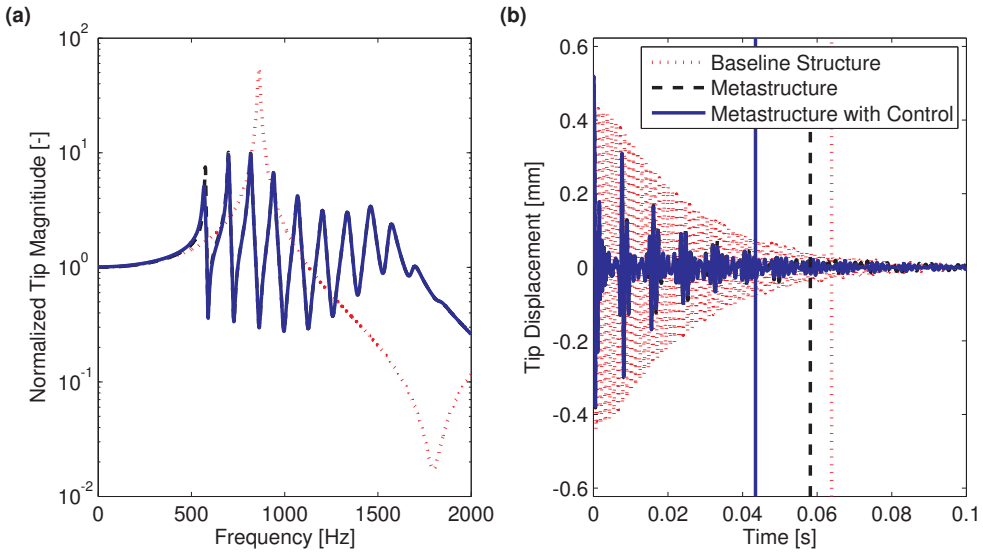

Figure 5.13: The (a) FRF of the tip subjected to a force at the tip and (b) displacement of the tip subjected to a unit impulse at the tip for design 1 when the actuator is placed at the tip host mass

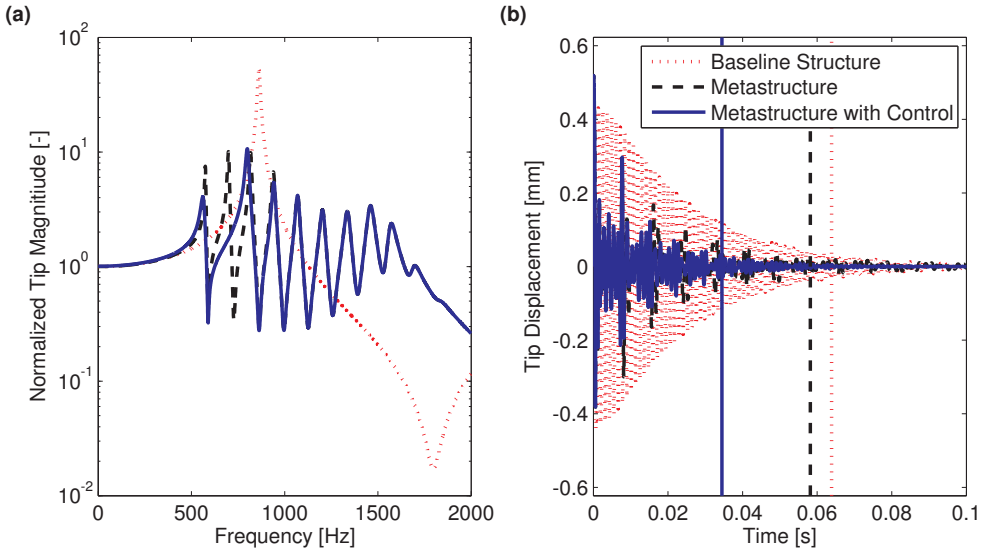

Figure 5.14: The (a) FRF of the tip subjected to a force at the tip and (b) displacement of the tip subjected to a unit impulse at the tip for design 1 when the actuator is placed at the absorber mass second from the tip

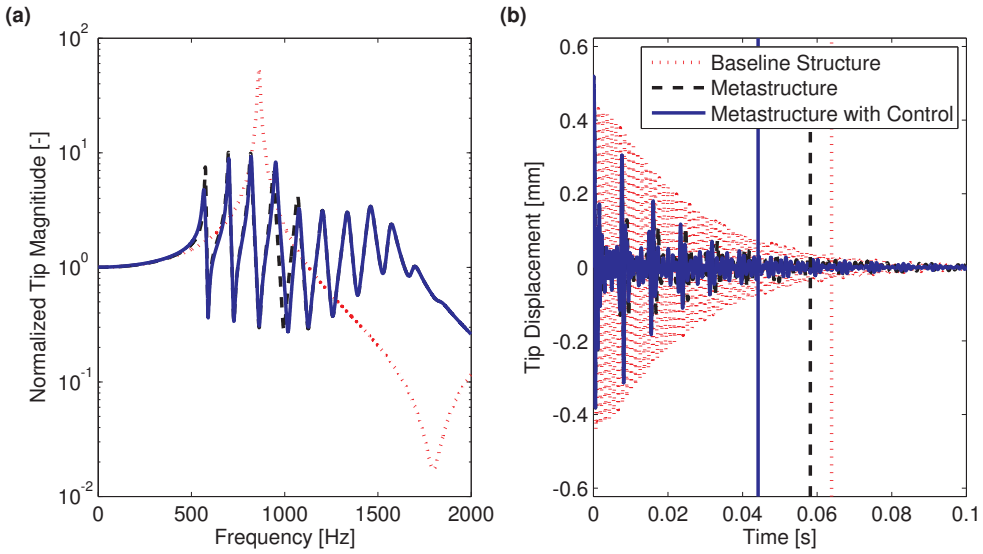

Figure 5.15: The (a) FRF of the tip subjected to a force at the tip and (b) displacement of the tip subjected to a unit impulse at the tip for design 1 when the actuator is placed at the absorber mass fourth from the tip

measures are shown in Figure 5.16. The H_2 norm values are much higher than those from Design 1 but the settling time values are comparable. For this design, the trend between the location of the actuator and performance is less clear for the H_2 norm values but follows a similar trend for the settling time values. Figure 5.17 shows the optimized controller values for the various locations.

The time and frequency responses for three different cases are examined. These are the same three cases examined for Design 1. The FRFs shown for these three cases are zoomed into the first peak of the system so the effects can be seen more easily. Figure 5.18 shows the case when the actuator is placed at the tip host mass. For this situation, the settling time is reduced from 58.5 ms to 52.1 ms. When the actuator is placed at the second absorber from the tip, the response is shown in Figure 5.19. As with Design 1, the second mode is eliminated and the settling time reduces from 58.2 ms to 41.5 ms. For the last case, when the actuator is placed on the absorber mass fourth from the tip, the response is shown in Figure 5.20. For this case, the fourth mode can be eliminated using the control force. This results in a settling time decrease from 58.5 ms to 46.2 ms. In summary for Design 2, when

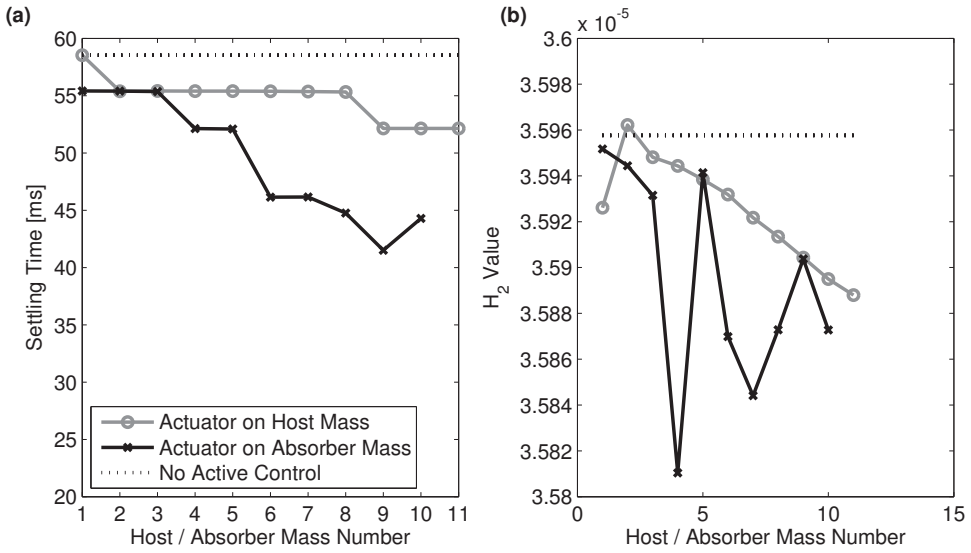

Figure 5.16: The (a) settling time and (b) H_2 norm values for Design 2 when controller values are optimized with respect to the settling time for various actuator locations

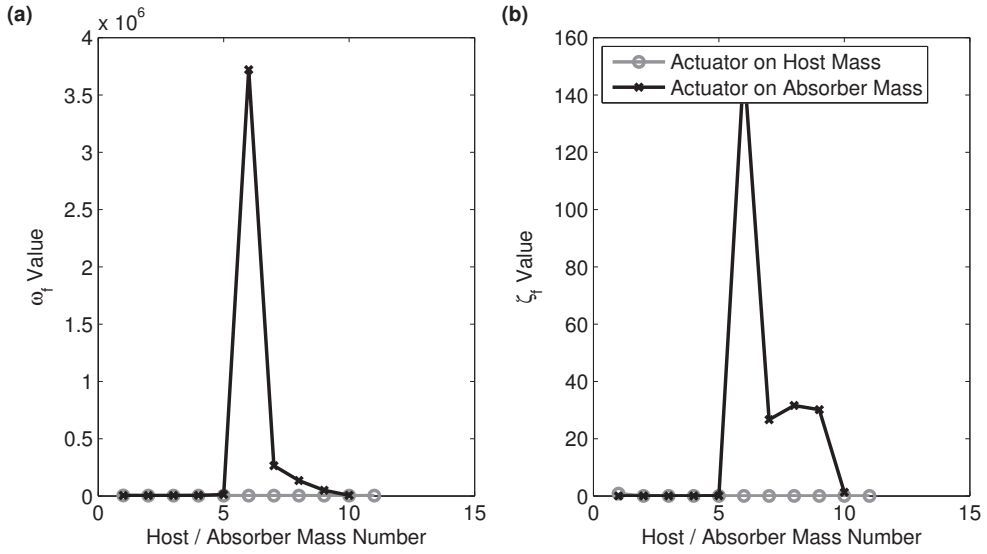

Figure 5.17: Optimized values of controller (a) natural frequency and (b) damping value for various actuator locations for Design 2

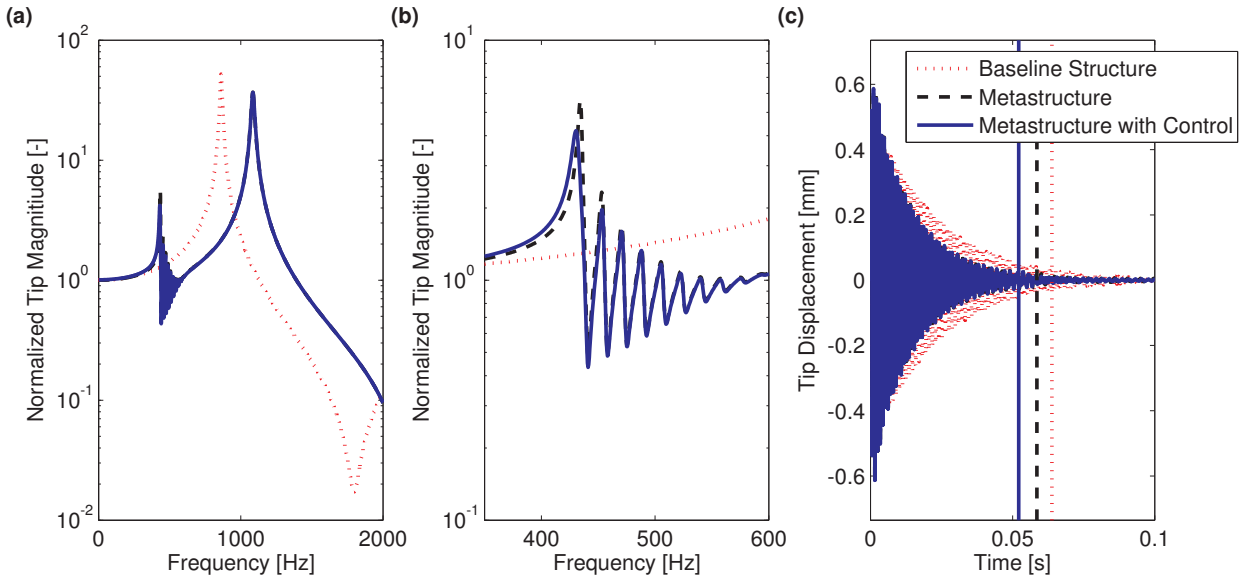

Figure 5.18: The (a) FRF and (b) zoomed in FRF of the tip subjected to a force at the tip and (c) displacement of the tip subjected to a unit impulse at the tip for Design 2 when the actuator is placed at the tip host mass

the actuators are placed on the absorbers masses, a specific mode is damped out, but since the modes of the metastructure with no control system looks different than those in Design 1, the absorber masses which provide substantial performance increases are different.

5.2.2.2 Effects of gain

Examining these designs, a single location for the actuator is chosen and the effects of increasing and decreasing the gain values on the settling time are examined. For Design 1, the actuator will be placed on the tip absorber mass. For Design 2, the absorber mass fourth from the tip will be utilized. Both of these locations provided good performance from the previous investigation. A plot of the gain values versus settling time are shown in Figures 5.21 and 5.22. Because of the beating of the responses, there are jumps in the relationships. Increasing the gain slightly, causes the beating to fall below the threshold value thus providing a jump in the settling time.

The plots also show that there is a limit to the settling times that can be accessed. Once

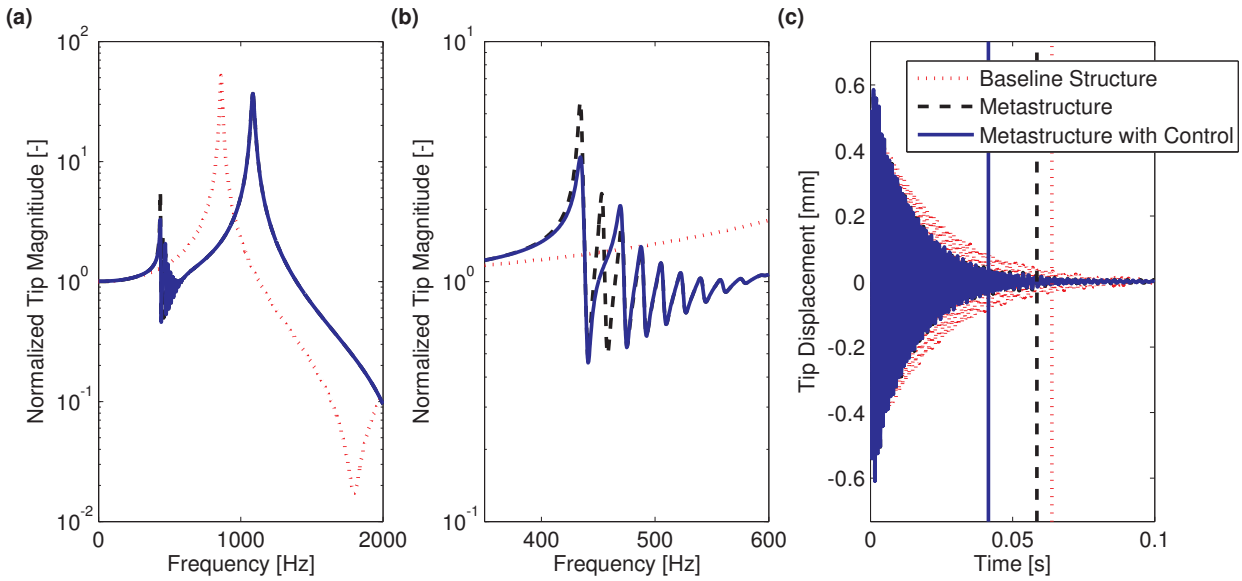

Figure 5.19: The (a) FRF and (b) zoomed in FRF of the tip subjected to a force at the tip and (c) displacement of the tip subjected to a unit impulse at the tip for Design 2 when the actuator is placed at the absorber mass second from the tip

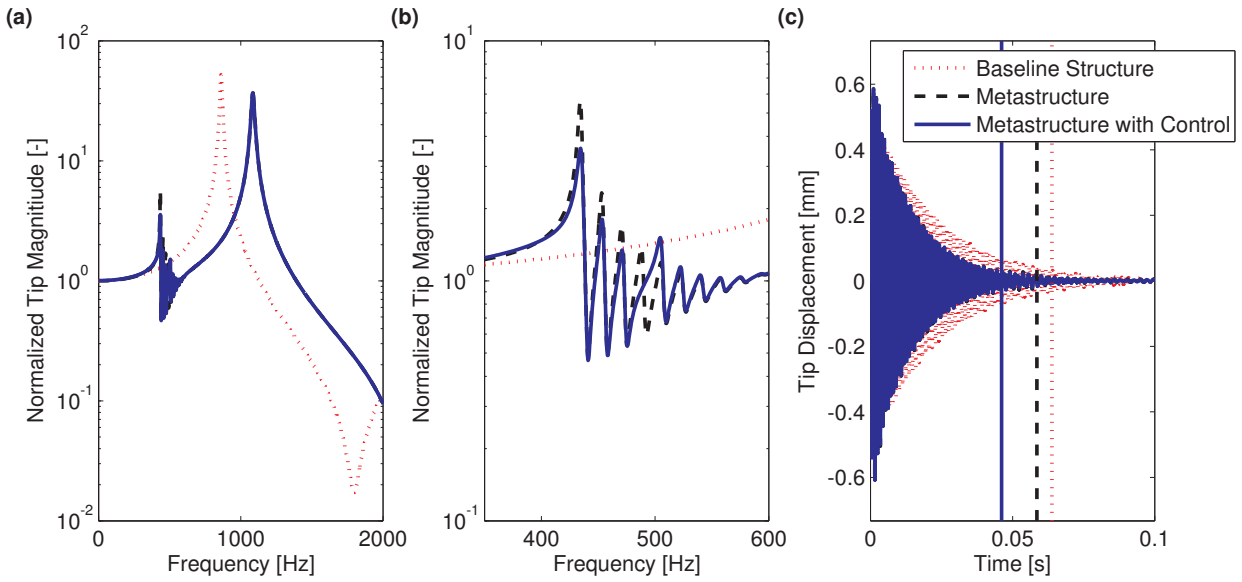

Figure 5.20: The (a) FRF and (b) zoomed in FRF of the tip subjected to a force at the tip and (c) displacement of the tip subjected to a unit impulse at the tip for Design 2 when the actuator is placed at the absorber mass fourth from the tip

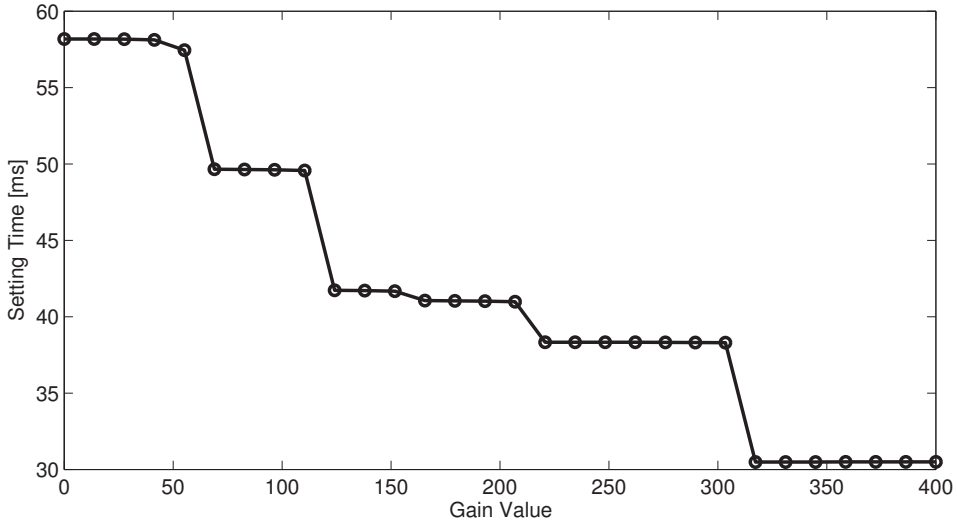

Figure 5.21: The effects of increasing the gain on settling time for Design 1 with the actuator placed on the absorber mass closest to the tip

the gain value is increased to a certain value, the mode that the controller is adding damping to is complete damped out, thus increasing the gain does not change the system.

5.3 Distributed mass metastructure model

This section extends the work from the previous section; a distributed mass model is used instead of a lumped mass model. For the distributed mass model, specific materials and their material properties are used in the modeling. The control force on the metastructure is implemented using piezoelectric materials. These piezoelectric materials are attached to the vibration absorbers to control the movement of the absorber resulting in an active vibration absorber. Two different active vibration absorber designs are used. The first design utilizes a stack actuator; the stack actuator is attached to an absorber on one end of the metastructure. The second designs bonds piezoelectric material to each side of the beam of one of the vibration absorbers, in a bimorph configuration. These two designs are depicted in Figure 5.23. For each of these designs, the modeling procedures for both the piezoelectric material and the metastructure are presented. Then the specifics of the PPF control law are

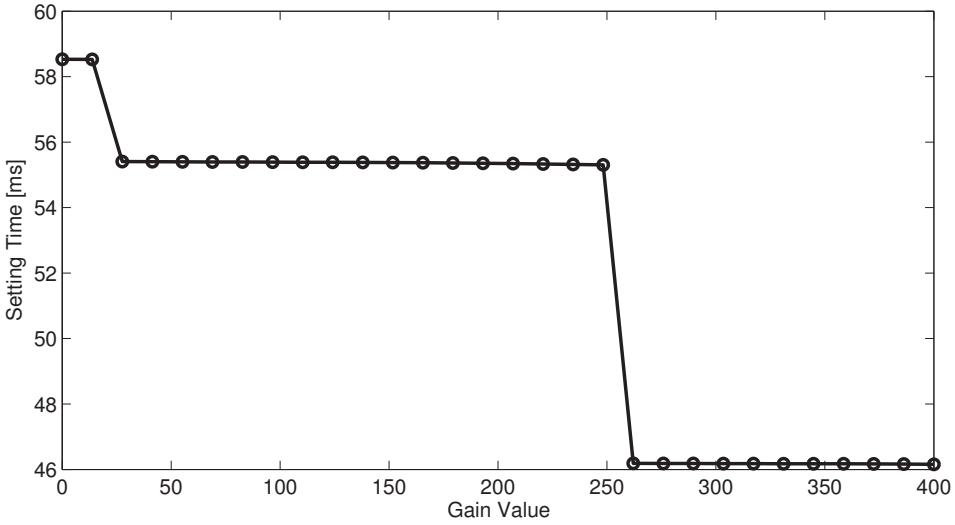

Figure 5.22: The effects of increasing the gain on settling time for Design 2 with the actuator placed on the absorber mass fourth from the tip

Table 5.4: Properties for NAC 2014-H16 stack actuator

Property	**Symbol**	**Value**
Area	A_p	49 mm^2
Length	L_p	16 mm
Layer thickness	t_p	0.05 mm
Number of layers	n_p	320
Coupling coefficient	k_{33}	0.74
Piezoelectric charge constant	d_{33}	433×10^{-9} C/N
Elastic compliance	$s_{33}^T = \frac{1}{Y_3^E}$	19×10^{-12} m^2/N
Dielectric constant	ε_{33}^T	1.89×10^{-8} F/m

explained, and lastly, the results of the two different designs are presented.

5.3.1 Metastructure with stack actuator

For this design, a stack actuator is attached to one of the vibration absorbers at the end of the metastructure as seen in Figure 5.23a. The specific actuator used in the model is the NAC 2014-H16 stack actuator from Noliac. The properties of this stack can be found in Table 5.4.

For the specific metastructure design used during this analysis, the mass of the vibrations

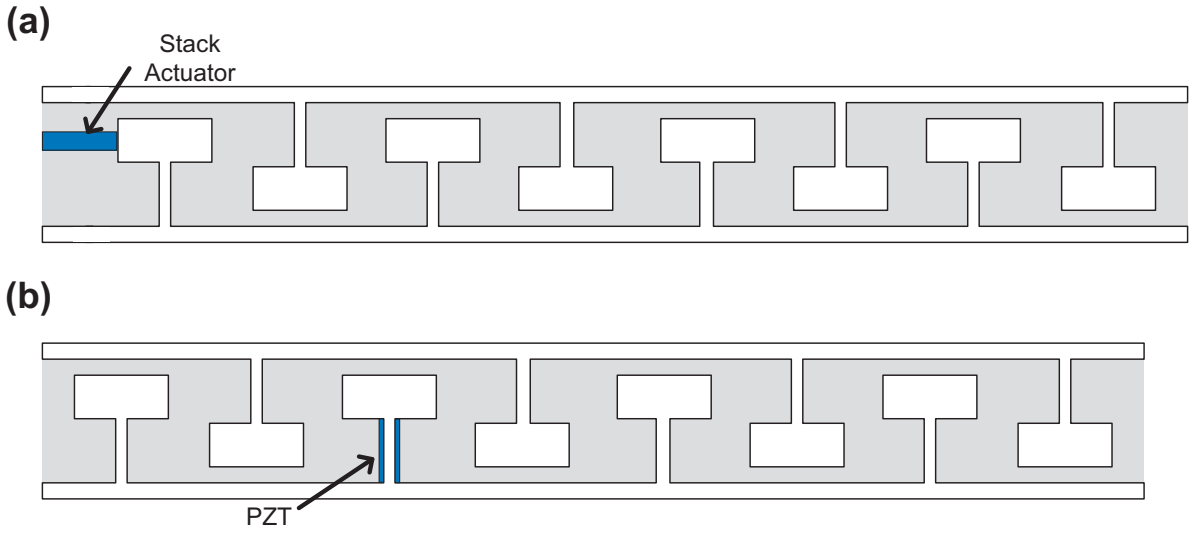

Figure 5.23: Schematics of active vibration absorbers using a (a) stack actuator and (b) piezoelectric bimorph configuration

absorbers is chosen such that the mass ratio, $\mu = 0.26$ is achieved and the stiffness of the absorbers varies such that the natural frequencies vary linearly. There are ten vibration absorbers ($n_a = 10$) with in the hollow section distributed throughout the length of the bar. The host structure is a hollow square bar with an outer width of 50 mm and a thickness of 5 mm. The length of the bar is 45 cm. The host structure has a mass of 473 g leading to the mass of the absorbers to be 123 g. The natural frequencies of the absorbers vary linearly from 426.5 to 939.8 Hz. This gives the structure a total mass of 600 g. The material properties of the structure are those from the Objet Connex 3D printer by Stratasys, specifically the DM 8430 digital material. The Young's modulus and density of the material are 1.97 GPa and 1168 kg/m^3 respectively.

5.3.1.1 Modeling procedure

The model for this active metastructure consists of the structural model and the piezoelectric stack actuator model. Both of these models are presented and the assembly process to couple the structural and piezoelectric models are explained.

The structural model uses a one-dimensional finite element model for the host structure with lumped mass vibration absorbers as depicted in Figure 5.24. The host structure is discretized into 100 elements, n_e along the length of the bar and a simple bar 2-noded bar element is utilized. The vibration absorbers are modeled as lumped masses and springs and are distributed evenly throughout the length of the bar. The structural equations of motion are

$$\mathbf{M}_s\ddot{\mathbf{x}}(t) + \mathbf{D}_s\dot{\mathbf{x}}(t) + \mathbf{K}_s\mathbf{x}(t) = \mathbf{f}(t) \tag{5.23}$$

where the matrices and vectors can be partitioned into the components associated with the host structure and the absorbers

$$\mathbf{x}(t) = \begin{bmatrix} \mathbf{x}_{\text{host}}(t) \\ \mathbf{x}_{\text{absorbers}}(t) \end{bmatrix} \tag{5.24a}$$

$$\mathbf{M}_s = \begin{bmatrix} \mathbf{M}_{\text{host}} & \mathbf{0} \\ \mathbf{0} & \mathbf{M}_{\text{absorbers}} \end{bmatrix} \tag{5.24b}$$

$$\mathbf{K}_s = \begin{bmatrix} \mathbf{K}_{\text{host}} & \mathbf{K}_{\text{ha}} \\ \mathbf{K}_{\text{ha}}^{\text{T}} & \mathbf{K}_{\text{absorbers}} \end{bmatrix} \tag{5.24c}$$

Since the vibration absorbers are modeled as lumped masses, there is no mass coupling between the host structure and the absorbers. For the stiffness matrix, there is coupling between the host structure and the absorbers as represented by the non-zero off-diagonal elements.

The necessary equations to create the piezoelectric model of the stack actuator are summarized here; for more details see Leo [90]. Consider a thin piezoelectric plate operating in its 3-3 mode and the direction of the polarization aligns with the thin direction of the plate; the piezoelectric constitutive equations become

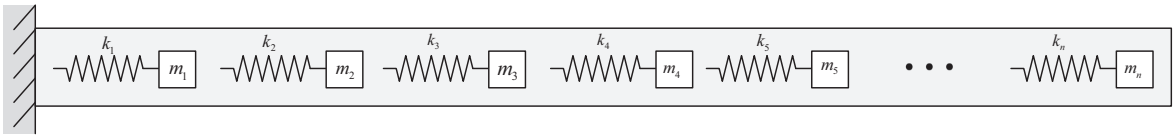

Figure 5.24: One-dimensional finite element model with lumped mass vibration absorbers

$$\begin{bmatrix} S_3 \\ D_3 \end{bmatrix} = \begin{bmatrix} \frac{1}{Y_3^E} & d_{33} \\ d_{33} & \varepsilon_{33}^T \end{bmatrix} \begin{bmatrix} T_3 \\ E_3 \end{bmatrix} \tag{5.25}$$

where S_3 is stress, T_3 is strain, D_s is electric displacement and E_3 is electric field. Assuming stress and strain are uniform through the thickness of the plate, the constitutive equations can be rewritten as

$$u = \frac{t_p}{Y_3^E A_p} f_p + d_3 3v \tag{5.26a}$$

$$q = d_{33} f_p + \frac{\varepsilon_{33}^T A_p}{t_p} v \tag{5.26b}$$

where u is the displacement in the 3direction, t_p is the thickness of the piezoelectric plate, A_p is the area, f_p is the force applied to the plate, v is the applied voltage, and q is the charge. A piezoelectric stack actuator consists of many layers of piezoelectric plates places on top of each other. These plates are wired such that each layer experiences the same voltage and electric field. For a stack actuator with n_p layers and a total length of $L_s = n_p t_s$ the following relationship is obtained.

$$u_s = n_p u = \frac{1}{k_p^E} f_p + \frac{d_{33} L_s}{t_p} v \tag{5.27a}$$

$$q_s = n_p q = \frac{d_{33} L_s}{t_p} f_p + C_p^T v \tag{5.27b}$$

where C_P^T is the stress-free capacitance of the device and k_p^E is the short circuit mechanical stiffness. These are calculated as

$$C_p^T = n_p \frac{\varepsilon_{33}^T A_p}{t_p} \tag{5.28a}$$

$$k_p^E = \frac{Y_3^E A_p}{L_s} \tag{5.28b}$$

Interchanging the dependent and independent variables from Equation 5.27

$$f_p = k_p^D u_s - \frac{d_{33} L_p}{t_p} \frac{k_p^E}{C_p^S} q \tag{5.29a}$$

$$v = -\frac{d_{33} L_p}{t_p} \frac{k_p^E}{C_p^S} u_s + \frac{1}{C_p^S} q \tag{5.29b}$$

where

$$k_p^D = \frac{k_p^E}{1 - k_{33}^2} \tag{5.30a}$$

$$C_p^S = (1 - k_{33}^2) C_p^T \tag{5.30b}$$

The stack actuator equations are coupled to the structural system via the applied force vector, $\mathbf{f}(t)$ from Equation 5.23. The stack actuator will be attached to the tip vibration absorber and the tip of the structure. The tip of the structure is the n_e degree of freedom and displacement of the absorber is the n_t degree of freedom, where $n_t = n_e + n_a$. Assuming there are no other external forces being applied to the structure, the force vector is composed of all zeros except for $\mathbf{f}[n_e] = +f_p$ and $\mathbf{f}[n_t] = -f_p$ where $\mathbf{v}[i]$ refers to the ith component of the vector, $\mathbf{v}$. The displacement of the stack is equal to the difference between the displacement of the tip of the bar and the displacement of the absorber closest to the tip, $u_s = \mathbf{u}[n_e] - \mathbf{u}[n_t]$. This leads to

$$\mathbf{f}[n_e] = +f_p = +k_p^D \mathbf{u}[n_e] - k_p^D \mathbf{u}[n_t] - \frac{d_{33} L_p}{t_p} \frac{k_p^E}{C_p^S} q \tag{5.31a}$$

$$\mathbf{f}[n_t] = -f_p = -k_p^D \mathbf{u}[n_e] + k_p^D \mathbf{u}[n_t] + \frac{d_{33} L_p}{t_p} \frac{k_p^E}{C_p^S} q \tag{5.31b}$$

substituting Equation 5.31 to Equation 5.23, the equations of motion of the smart structure have the following form

$$\mathbf{M}_s \ddot{\mathbf{x}}(t) + \mathbf{D}_s \dot{\mathbf{x}}(t) + \mathbf{K}_s^D \mathbf{x}(t) - \mathbf{\Theta} q(t) = \mathbf{0} \tag{5.32a}$$

$$-\mathbf{\Theta}^{\mathrm{T}} \mathbf{x}(t) + (C_p^s)^{-1} q(t) = v(t) \tag{5.32b}$$

where

$$\begin{aligned} \mathbf{K}_s^D &= \mathbf{K}_s + \mathbf{K}^D \\ \mathbf{K}^D[n_e, n_e] &= \mathbf{K}^D[n_t, n_t] = k_p^D \\ \mathbf{K}^D[n_e, n_t] &= \mathbf{K}^D[n_t, n_e] = -k_p^D \end{aligned} \tag{5.33a}$$

$$\begin{aligned} \mathbf{\Theta}[n_e] &= \tfrac{d_{33} L_p}{t_p} \tfrac{k_p^E}{C_p^S} \\ \mathbf{\Theta}[n_t] &= -\tfrac{d_{33} L_p}{t_p} \tfrac{k_p^E}{C_p^S} \end{aligned} \tag{5.33b}$$

Eliminating $q(t)$ from Equation 5.32 the equations of motion can be reduced to

$$\mathbf{M}_s \ddot{\mathbf{x}}(t) + \mathbf{D}_s \dot{\mathbf{x}}(t) + \mathbf{K}^E \mathbf{x}(t) = \mathbf{B}_c v(t) \tag{5.34}$$

where

$$\mathbf{K}^E = \mathbf{K}_s - \mathbf{\Theta} C_p^s \mathbf{\Theta}^{\mathrm{T}} \tag{5.35a}$$

$$\mathbf{B}_c = \mathbf{\Theta} C_p^S \tag{5.35b}$$

Equation 5.34 is the equation of motion for the metastructure with the active vibration absorber.

5.3.1.2 PPF implementation

Next, the implementation of the PPF control law will be explained for a multiple degree of freedom system. The general equations of motion for a system with piezoelectric materials are

$$\mathbf{M}_s \ddot{\mathbf{x}}(t) + \mathbf{D}_s \dot{\mathbf{x}}(t) + \mathbf{K}_s^D \mathbf{x}(t) - \mathbf{\Theta} \mathbf{q}(t) = \mathbf{0} \tag{5.36a}$$

$$-\mathbf{\Theta}^{\mathrm{T}} \mathbf{x}(t) + (\mathbf{C}_p^s)^{-1} \mathbf{q}(t) = \mathbf{B}_v v(t) \tag{5.36b}$$

where $\mathbf{B}_v$ describes the position where the voltage is being applied. Rearranging Equation 5.36b an expression for charge is

$$\mathbf{q}(t) = \mathbf{C}_p^s \mathbf{B}_v v(t) + \mathbf{C}_p^s \mathbf{\Theta}^{\mathrm{T}} \mathbf{x}(t) \tag{5.37}$$

Substituting Equation 5.37 in Equation 5.36a results in the following equations of motion

$$\mathbf{M}_s \ddot{\mathbf{x}}(t) + \mathbf{D}_s \dot{\mathbf{x}}(t) + \mathbf{K}^E \mathbf{x}(t) = \mathbf{B}_c v(t) \tag{5.38}$$

where

$$\mathbf{K}^E = \mathbf{K}_s^D - \mathbf{\Theta} \mathbf{C}_p^s \mathbf{\Theta}^{\mathrm{T}} \tag{5.39a}$$

$$\mathbf{B}_c = \mathbf{\Theta} \mathbf{C}_p^s \mathbf{B}_v \tag{5.39b}$$

Self-sensing actuation or collocated control will be utilized. This is where the same piezoelectric element is used simultaneously as a sensor and an actuator. The charge generated by the piezoelectric element is a linear combination of voltage and displacement of the structure, as seen in Equation 5.37. Since the applied voltage is known, we can eliminate the dependence on the applied voltage by measuring the following

$$y(t) = \mathbf{B}_v^{\mathrm{T}}\mathbf{q}(t) - \mathbf{B}_v^{\mathrm{T}}\mathbf{C}_p^s\mathbf{B}_v v(t) \tag{5.40}$$

where $y(t)$ is the output. Substituting the charge expression (Equation 5.37) the output becomes

$$y(t) = \mathbf{B}_v^{\mathrm{T}}\mathbf{C}_p^s\boldsymbol{\Theta}^{\mathrm{T}}\mathbf{x}(t) = \mathbf{B}_c^{\mathrm{T}}\mathbf{x}(t) \tag{5.41}$$

Measuring the specific output shown in Equation 5.40 can be accomplished by combining the piezoelectric element with a bridge circuit that adds the associated capacitance of the piezoelectric element into the output. Details on implementing this experimentally for a stack actuator can be found in Jones and Garcia [93].

The auxiliary dynamics system is the same as before

$$\ddot{\eta}(t) + 2\zeta_f\omega_f\dot{\eta}(t) + \omega_f^2\eta(t) = g\omega_f y(t) \tag{5.42a}$$

$$v(t) = g\omega_f\eta(t) \tag{5.42b}$$

Combining Equations 5.38, 5.41 and 5.42 leads to the closed-loop equations of motion are

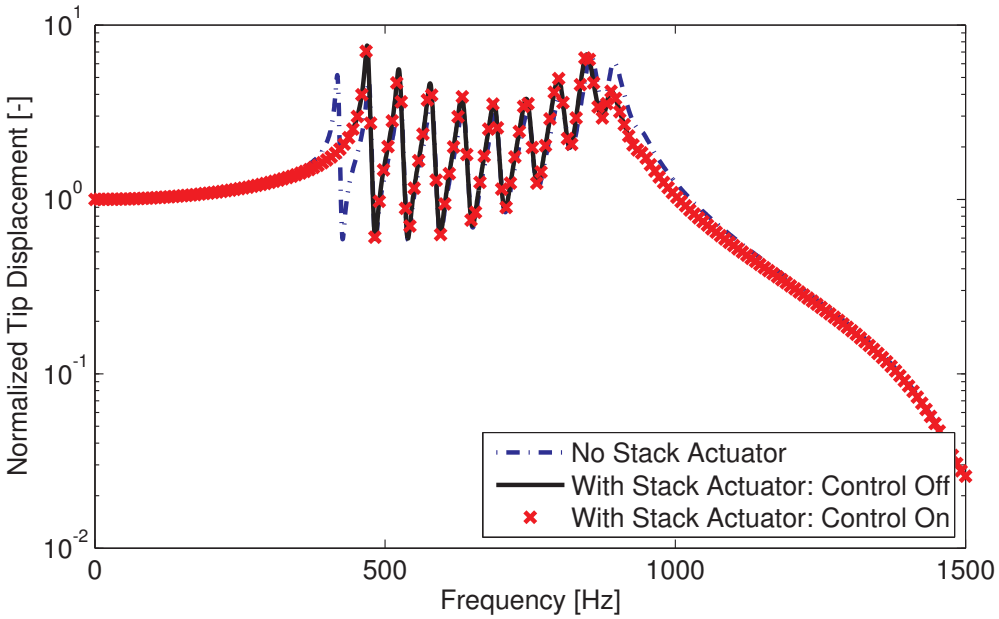

Figure 5.25: FRF of normalized tip displacement due to a force at the tip for a metastructure both with and without a a stack actuator

$$\begin{bmatrix} \mathbf{M}_s & 0 \\ 0 & 1 \end{bmatrix} \begin{bmatrix} \ddot{\mathbf{x}} \\ \ddot{\eta} \end{bmatrix} + \begin{bmatrix} \mathbf{D}_s & 0 \\ 0 & 2\zeta_f\omega_f \end{bmatrix} \begin{bmatrix} \dot{\mathbf{x}} \\ \dot{\eta} \end{bmatrix} + \begin{bmatrix} \mathbf{K}^E & -g\omega_f\mathbf{B}_c \\ -g\omega_f\mathbf{B}_c^{\mathrm{T}} & \omega_f^2 \end{bmatrix} \begin{bmatrix} \mathbf{x} \\ \eta \end{bmatrix} = \begin{bmatrix} \mathbf{0} \\ 0 \end{bmatrix} \tag{5.43}$$

This closed-loop expression is almost identical to the expression found in Equation 5.19 with $\mathbf{B}_c$ substituted in for $\mathbf{B}_v$. By the same reasoning explained in Section 5.2.2, to ensure stability of the controller, the matrix $\mathbf{K}^E - g^2\mathbf{B}_c\mathbf{B}_c^{\mathrm{T}}$ must be positive definite.

5.3.1.3 Results

Using the modeling methods developed in the previous section, the results will be presented and discussed here. The results will be presented for the metastructure without the stack actuator and for the metastructure with the stack actuator attached. Both the open loop and closed loop responses are shown. The FRF of for these three cases is shown in Figure 5.25 and the time response due to an impulse at the tip is shown in Figure 5.26.

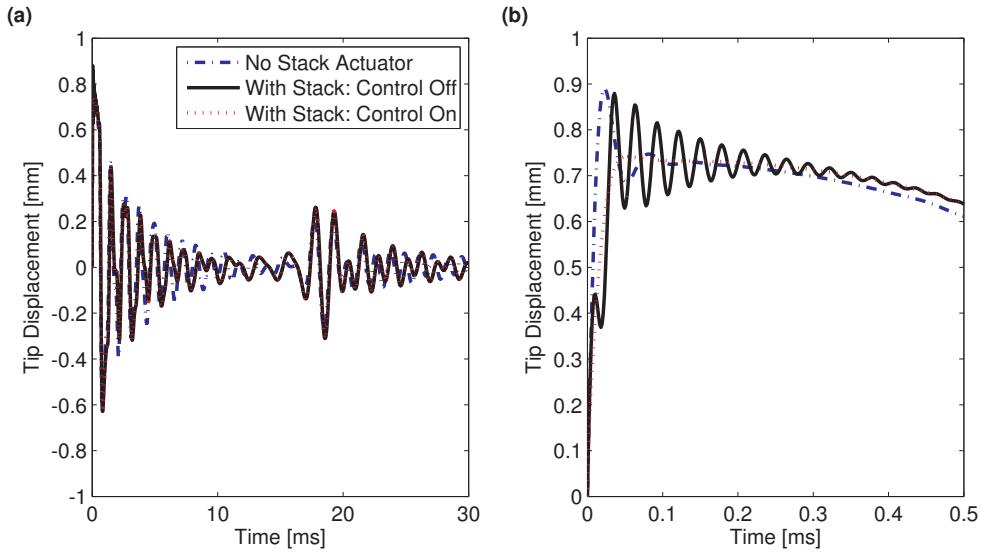

Figure 5.26: Time response of the tip displacement due to an impulsive force at the tip for a metastructure both with and without a stack actuator shown (a) zoomed out and (b) zoomed in

The FRF shows that the addition of the stack actuator eliminates the first mode of vibration. This can be understood by looking at the shape of the mode shapes. When the structure is excited at its first natural frequency, the vibration absorber at the tip of the structure oscillates significantly whereas the rest of the structure stays relatively still. When the stack actuator is attached to that absorber, the absorber becomes stiffer and its natural frequency increases significantly this it no longer appears the same in the FRF. This can also be observed in the time response. Once the stack actuator is added to the structure, the tip of the metastructure initial exhibits high-frequency vibrations. Once the control system is turned on, the stack actuator can eliminate those high-frequency vibrations. Although this is somewhat beneficial, it does not influence the lower frequency vibrations that dominate the response. These trends showed up in all the designs examined using a stack actuator. From these results, it can be concluded that using a stack actuator for active vibration control in a metastructure is ineffective because of the added stiffness resulting in the control of higher frequency vibrations that do not contribute significantly to the response of the structure.

Table 5.5: Properties of the active vibration absorber

Property	**Value**
Young's modulus of substrate	E_s
Density of substrate	ρ_s
Thickness of substrate	t_s
Thickness of piezoelectric material	t_p
Width of substrate and piezoelectric material	w
Area moment of inertia of substrate	$I_s = wt_s^3/12$
Area moment of inertia piezoelectric material	$I_p = wt_p^3/12$
Thickness ratio	$\tau = t_s/t_p$

5.3.2 Metastructure with a piezoelectric bimorph actuator

This section presents the derivation for a metastructure with a piezoelectric bimorph actuator as seen in Figure 5.23b. The metastructure design has a mass ratio of 0.26 and has ten vibration absorbers located along the length of the bar. One of these absorbers uses piezoelectric materials to act as an active vibration absorber. The geometry of the host structure is the same as used in the stack actuator design for Section 5.3.1. The geometry of the vibration absorbers will be different since the addition of the piezoelectric material affects the frequency of the absorber.

5.3.2.1 Modeling procedure

The metastructure is modeled using a combination of a finite element approach and a Rayleigh-Ritz approach. The host structure is modeled using one-dimensional bar finite elements and the absorbers are modeled using a Rayleigh-Ritz approach. First, the modeling approach for the absorbers is shown and then integrated into the finite element model of the host structure to create the final metastructure model. The host structure uses 11 finite elements which creates nodes at the locations at which the absorbers are attached. A schematic of the active vibration absorber is shown in Figure 5.27. The relevant properties are given in Table 5.5.

The constitutive equations for a transversely isotropic material piezoelectric material are

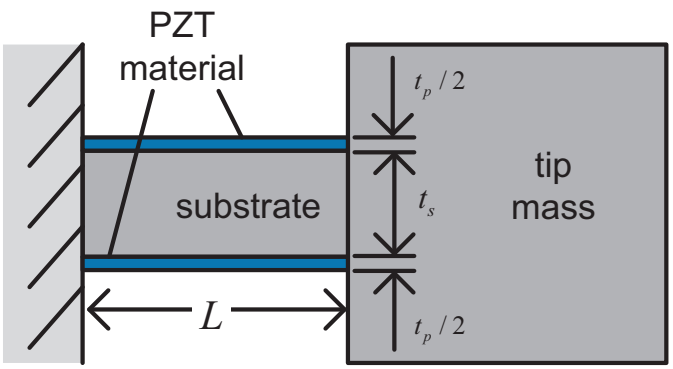

Figure 5.27: Schematic of the active vibration absorber using a piezoelectric cantilevered bimorph concept

$$\begin{Bmatrix} S_1 \\ S_2 \\ S_3 \\ S_4 \\ S_5 \\ S_6 \end{Bmatrix} = \begin{bmatrix} s_{11}^E & s_{12}^E & s_{13}^E & 0 & 0 & 0 \\ s_{12}^E & s_{11}^E & s_{13}^E & 0 & 0 & 0 \\ s_{13}^E & s_{13}^E & s_{33}^E & 0 & 0 & 0 \\ 0 & 0 & 0 & s_{55}^E & 0 & 0 \\ 0 & 0 & 0 & 0 & s_{55}^E & 0 \\ 0 & 0 & 0 & 0 & 0 & s_{66}^E \end{bmatrix} + \begin{Bmatrix} T_1 \\ T_2 \\ T_3 \\ T_4 \\ T_5 \\ T_6 \end{Bmatrix} + \begin{bmatrix} 0 & 0 & d_{31} \\ 0 & 0 & d_{31} \\ 0 & 0 & d_{33} \\ 0 & d_{15} & 0 \\ d_{15} & 0 & 0 \\ 0 & 0 & 0 \end{bmatrix} \begin{Bmatrix} E_1 \\ E_2 \\ E_3 \end{Bmatrix} \quad (5.44a)$$

$$\begin{Bmatrix} D_1 \\ D_2 \\ D_3 \end{Bmatrix} = \begin{bmatrix} 0 & 0 & 0 & 0 & d_{15} & 0 \\ 0 & 0 & 0 & d_{15} & 0 & 0 \\ d_{31} & d_{31} & d_{33} & 0 & 0 & 0 \end{bmatrix} \begin{Bmatrix} T_1 \\ T_2 \\ T_3 \\ T_4 \\ T_5 \\ T_6 \end{Bmatrix} + \begin{bmatrix} \varepsilon_{11}^T & 0 & 0 \\ 0 & \varepsilon_{11}^T & 0 \\ 0 & 0 & \varepsilon_{33}^T \end{bmatrix} \begin{Bmatrix} E_1 \\ E_2 \\ E_3 \end{Bmatrix} \quad (5.44b)$$

where $\{\mathbf{S}\}$ is the strain, $\{\mathbf{T}\}$ is the stress, $\{\mathbf{D}\}$ is the electric displacement and $\{\mathbf{E}\}$ is the electric field. For the piezoelectric material, PZT-5A, the values of the matrices are given in Table 5.6 [108]. Equations 5.44 can be rearranged to get the following relationships

Table 5.6: Materials properties of PZT-5A piezoceramic [108]

Property	**Value**
s_{11}^E	16.4 pm^2/N
s_{12}^E	-5.74 pm^2/N
s_{13}^E	-7.22 pm^2/N
s_{33}^E	18.8 pm^2/N
s_{55}^E	47.5 pm^2/N
s_{66}^E	44.3 pm^2/N
d_{31}	-171 pm/V
d_{31}	374 pm/V
d_{31}	584 pm/V
ε_0	8.854 pF/m
$\varepsilon_{11}^T/\varepsilon_0$	1730
$\varepsilon_{33}^T/\varepsilon_0$	1700
ρ_p	7750 kg/m^3

$$\{\mathbf{T}\} = [\mathbf{c}^D]\{\mathbf{S}\} - [\mathbf{h}]\{\mathbf{D}\} \tag{5.45a}$$

$$\{\mathbf{E}\} = -[\mathbf{h}]^{\mathrm{T}}\{\mathbf{S}\} + [\boldsymbol{\beta}^S]\{\mathbf{D}\} \tag{5.45b}$$

The absorber is modeled using a Rayleigh-Ritz model. The transverse deflection of the ith absorber, w_i is approximated as

$$w_i(x,t) = u_i + \sum_{j=1}^{N_r} r_{ij}(t)\phi_j(x) = \tilde{\boldsymbol{\Phi}}^{\mathrm{T}}(x)\tilde{\mathbf{r}}_i(t) \tag{5.46a}$$

$$\dot{w}_i(x,t) = \tilde{\boldsymbol{\Phi}}^{\mathrm{T}}(x)\dot{\tilde{\mathbf{r}}}_i(t) \tag{5.46b}$$

where u_i is the motion at the base of the ith absorber and $\phi_j(x)$ is an admissible function approximating the displacement of the beam. The admissible functions can be arranged into vector form as

$$\mathbf{\Phi}(x) = \begin{bmatrix} \phi_1 \\ \vdots \\ \phi_{N_r} \end{bmatrix}, \qquad \tilde{\mathbf{\Phi}} = \begin{bmatrix} 1 \\ \mathbf{\Phi}(\mathbf{x}) \end{bmatrix} \tag{5.47}$$

The admissible functions are defined as

$$\phi_j(x) = \left(\frac{x}{L}\right)^{j+1} \tag{5.48}$$

which meets the geometric boundary condition of zero slope and zero displacement at the base of the absorber. The time-varying coefficients of the admissible functions for the ith absorbers can also be written in vector form as

$$\mathbf{r}_i = \begin{bmatrix} r_{i1}(t) \\ \vdots \\ r_{iN_r} \end{bmatrix}, \quad \tilde{\mathbf{r}}_i(t) = \begin{bmatrix} u_i \\ \mathbf{r}_i(t) \end{bmatrix} \tag{5.49}$$

The total kinetic energy of the ith absorber, T_i is

$$T_i = T_s + T_p = T_{\text{beam}} + T_{\text{mass}} + T_p \tag{5.50}$$

where T_s and T_p represent the kinetic energy of the structure and the piezoelectric material respectively. The kinetic energy of the structure consists of the kinetic energy from the beam and the tip mass. These are defined as

$$T_{\text{beam}} = \frac{1}{2}\int_0^L \rho_s A_s \dot{w}_i^2(x,t)\mathrm{d}x = \frac{1}{2}\dot{\tilde{\mathbf{r}}}_i \mathbf{M}_{\text{beam}} \dot{\tilde{\mathbf{r}}}_i \tag{5.51a}$$

$$T_{\text{mass}} = \frac{1}{2}M\left[\dot{w}_i(L) + e\dot{w}_i'(L)\right]^2 + \frac{1}{2}J\dot{w}_i'(L)^2 = \frac{1}{2}\dot{\tilde{\mathbf{r}}}_i \mathbf{M}_{\text{mass}} \dot{\tilde{\mathbf{r}}}_i \tag{5.51b}$$

$$T_p = \frac{1}{2}\int_0^L \rho_p w_p t_p \dot{w}_i^2(x,t)\mathrm{d}x = \frac{1}{2}\dot{\tilde{\mathbf{r}}}_i \mathbf{M}_p \dot{\tilde{\mathbf{r}}}_i \tag{5.51c}$$

Substituting the Rayleigh-Ritz approximation into Equations 5.51a and 5.51c results in the following mass matrices

$$\mathbf{M}_{\text{beam}} = \rho_s w t_s \int_0^L \tilde{\mathbf{\Phi}}(x)\tilde{\mathbf{\Phi}}^{\mathrm{T}}(x)\mathrm{d}x \tag{5.52a}$$

$$\mathbf{M}_p = \rho_p w t_p \int_0^L \tilde{\mathbf{\Phi}}(x)\tilde{\mathbf{\Phi}}^{\mathrm{T}}(x)\mathrm{d}x \tag{5.52b}$$

The mass matrix for the tip mass requires slightly more derivation

$$T_{\text{mass}} = \frac{1}{2}M\left\{\dot{\tilde{\mathbf{r}}}_i^{\mathrm{T}}\tilde{\mathbf{\Phi}}_L\tilde{\mathbf{\Phi}}_L^{\mathrm{T}}\dot{\tilde{\mathbf{r}}}_i + 2e\dot{\tilde{\mathbf{r}}}_i^{\mathrm{T}}\tilde{\mathbf{\Phi}}_L[\tilde{\mathbf{\Phi}}']_L^{\mathrm{T}}\dot{\tilde{\mathbf{r}}} + e^2\dot{\tilde{\mathbf{r}}}_i^{\mathrm{T}}[\tilde{\mathbf{\Phi}}']_L[\tilde{\mathbf{\Phi}}']_L^{\mathrm{T}}\dot{\tilde{\mathbf{r}}}_i\right\} + \frac{1}{2}J\dot{\tilde{\mathbf{r}}}_i^{\mathrm{T}}[\tilde{\mathbf{\Phi}}']_L[\tilde{\mathbf{\Phi}}']_L^{\mathrm{T}}\dot{\tilde{\mathbf{r}}}_i \tag{5.53a}$$

$$= \frac{1}{2}\dot{\tilde{\mathbf{r}}}_i^{\mathrm{T}}\left\{M\left(\tilde{\mathbf{\Phi}}_L\tilde{\mathbf{\Phi}}_L^{\mathrm{T}} + 2e\tilde{\mathbf{\Phi}}_L[\tilde{\mathbf{\Phi}}']_L^{\mathrm{T}} + e^2[\tilde{\mathbf{\Phi}}']_L[\tilde{\mathbf{\Phi}}']_L^{\mathrm{T}}\right) + J[\tilde{\mathbf{\Phi}}']_L[\tilde{\mathbf{\Phi}}']_L^{\mathrm{T}}\right\}\dot{\tilde{\mathbf{r}}} \tag{5.53b}$$

$$= \frac{1}{2}\dot{\tilde{\mathbf{r}}}^{\mathrm{T}}\left\{M\tilde{\mathbf{\Phi}}_L\tilde{\mathbf{\Phi}}_L^{\mathrm{T}} + 2Me\tilde{\mathbf{\Phi}}_L[\tilde{\mathbf{\Phi}}']_L^{\mathrm{T}} + (Me^2 + J)[\tilde{\mathbf{\Phi}}']_L[\tilde{\mathbf{\Phi}}']_L^{\mathrm{T}}\right\}\dot{\tilde{\mathbf{r}}}_i \tag{5.53c}$$

leading to the following mass matrix

$$\mathbf{M}_{\text{mass}} = M\tilde{\mathbf{\Phi}}_L\tilde{\mathbf{\Phi}}_L^{\mathrm{T}} + 2Me\tilde{\mathbf{\Phi}}_L[\tilde{\mathbf{\Phi}}']_L^{\mathrm{T}} + (Me^2 + J)[\tilde{\mathbf{\Phi}}']_L[\tilde{\mathbf{\Phi}}']_L^{\mathrm{T}} \tag{5.54}$$

The potential energy of the ith vibration absorber is

$$U_i = U_s + U_p = U_{\text{beam}} + U_p \tag{5.55}$$

where U_s and U_p represent the potential energy of the structure and the piezoelectric material. The tip mass has no potential energy, so the potential energy of the structure solely consists of the potential energy of the beam and is given by

$$U_{\text{beam}} = \frac{1}{2}\int_0^L EI(w'')^2\mathrm{d}x = \dot{\tilde{\mathbf{r}}}_i^{\mathrm{T}}\mathbf{K}_s\dot{\tilde{\mathbf{r}}}_i \tag{5.56}$$

leading to a structural stiffness matrix

$$\mathbf{K}_s = \frac{EI}{2}\int_0^L [\tilde{\mathbf{\Phi}}''(x)][\tilde{\mathbf{\Phi}}''(x)]^{\mathrm{T}}\mathrm{d}x \tag{5.57}$$

The potential energy for a system containing both elastic materials and piezoelectric materials is given as

$$U_p = \frac{1}{2}\dot{\tilde{\mathbf{r}}}_i^{\mathrm{T}}\left[\mathbf{K}_s + \mathbf{K}_p^D\right]\dot{\tilde{\mathbf{r}}}_i - \dot{\tilde{\mathbf{r}}}_i^{\mathrm{T}}\mathbf{\Theta}\mathbf{q} + \frac{1}{2}\mathbf{q}^{\mathrm{T}}(\mathbf{C}_p^S)^{-1}\mathbf{q} \tag{5.58}$$

where $\mathbf{q}$ is a vector of the generalized charge coordinates [109]. For a cantilevered piezoelectric bimorph beam the following relationships can be derived

$$\mathbf{K}_p^D = \frac{\hat{c}^D I_p}{L^4}(1+3\tau+3\tau^2)\int_0^L [\tilde{\mathbf{\Phi}}''(x)][\tilde{\mathbf{\Phi}}''(x)]^{\mathrm{T}}\mathrm{d}x \tag{5.59a}$$

$$\mathbf{\Theta} = \frac{\tilde{h}t_p^2}{8L^3}(2\tau+1)\left\{[\tilde{\mathbf{\Phi}}']_L - [\tilde{\mathbf{\Phi}}']_0\right\} \tag{5.59b}$$

$$\mathbf{C}_p^s = \frac{\beta_{33}^s t_p}{wL^2}\begin{bmatrix} 1 & 0 \\ 0 & 1 \end{bmatrix} \tag{5.59c}$$

where $\hat{c}^D$ and $\tilde{h}$ are calculated using the components of the matrices defined in Equation 5.45

$$\hat{c}^D = c_{11}^D - 2\nu_{12}c_{12}^D - 2\nu_{13}c_{13}^D + \nu_{12}^2 c_{22}^D + \nu_{12}\nu_{13}c_{23}^D + \nu_{13}^2 c_{33}^D \tag{5.60a}$$

$$\tilde{h} = h_{13} - \nu_{12}h_{23} - \nu_{13}h_{33} \tag{5.60b}$$

and using the alternate definition of $[\mathbf{s}^E]$ to obtain values for ν_{12} and ν_{13}

$$[\mathbf{s}^E] = \begin{bmatrix} \frac{1}{Y_1^E} & -\frac{\nu_{12}}{Y_1^E} & -\frac{\nu_{13}}{Y_1^E} & 0 & 0 & 0 \\ -\frac{\nu_{12}}{Y_1^E} & \frac{1}{Y_1^E} & -\frac{\nu_{13}}{Y_1^E} & 0 & 0 & 0 \\ -\frac{\nu_{13}}{Y_1^E} & -\frac{\nu_{13}}{Y_1^E} & \frac{1}{Y_3^E} & 0 & 0 & 0 \\ 0 & 0 & 0 & \frac{1}{G_{23}^E} & 0 & 0 \\ 0 & 0 & 0 & 0 & \frac{1}{G_{13}^E} & 0 \\ 0 & 0 & 0 & 0 & 0 & \frac{1}{G_{12}^E} \end{bmatrix} \tag{5.61}$$

The host structure of the metastructure is modeled using finite element techniques. The bar is discretized into 11 finite elements allowing for nodes where the absorbers will attach to the host structure. The displacement of the nodes range from u_0 to u_{N_a+1} where u_0 is the displacement of the base of the metastructure, which will be constrained to zero, and u_{N_a+1} is the displacement of the tip of the structure. The displacements in between, u_i, correspond to the displacement of the bar where the absorber is attached and show up in the degree of freedom vector, $\tilde{\mathbf{r}}_i(t)$ from Equation 5.49. Using this the final metastructure mass and stiffness matrices can be assembled, and the final equation of motion of the active structure has the form

$$\mathbf{M}_s\ddot{\mathbf{x}}(t) + \mathbf{D}_s\dot{\mathbf{x}}(t) + \mathbf{K}^E\mathbf{x}(t) = \mathbf{B}_c v(t) \tag{5.62}$$

where $\mathbf{K}^E$ and $\mathbf{B}_c$ are defined in Equation 5.35.

5.3.2.2 PPF implementation

For the piezoelectric bimorph configuration, the PPF control law using collocated charge feedback is implemented using the same equations as the stack actuator design. Refer to Section 5.3.1.2 for these equations. See Dosch *et. al.* for more information about how to implement collocated control using piezoelectric materials on a cantilever beam [92].

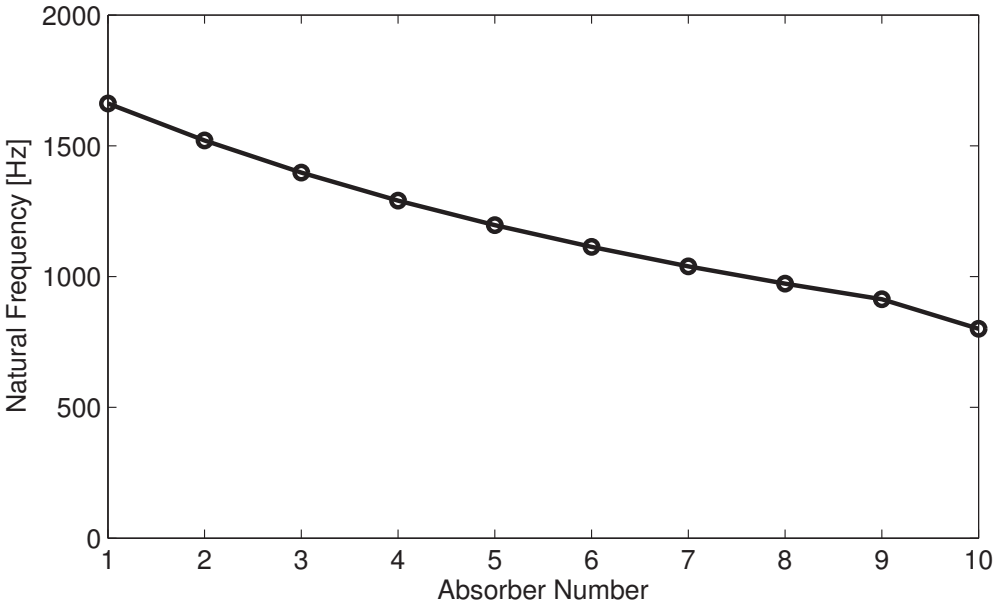

Figure 5.28: Natural frequencies of the vibration absorbers for the wide frequency range design where absorber 1 is closest to the base and absorber 10 is closest to the tip

5.3.2.3 Results

This section examines the design for three different metastructures and the effects using an active vibration absorber for these designs. The three designs examined differ in the natural frequencies of the absorbers. These designs are referred to as the higher frequency range design, lower frequency range design, and constant frequency design. Plots of the natural frequencies of the absorbers from the higher and lower frequency range designs are shown in Figures 5.28 and 5.29. For the higher frequency range design, the active absorber is the absorber closest to the tip whereas, for the lower frequency range, the active absorber is the absorber second from the base of the structure. This corresponds to the absorber mode with the largest response in the FRF. The design in which all the absorbers are tuned to the same frequency and the tip vibration absorber acting as the active absorber.

These frequency ranges are obtained by varying the geometry of the absorbers. The geometry for the higher frequency design is shown in Figure 5.30. For this specific design, the tip absorber has the piezoelectric material bonded to the beam. Since the addition of the

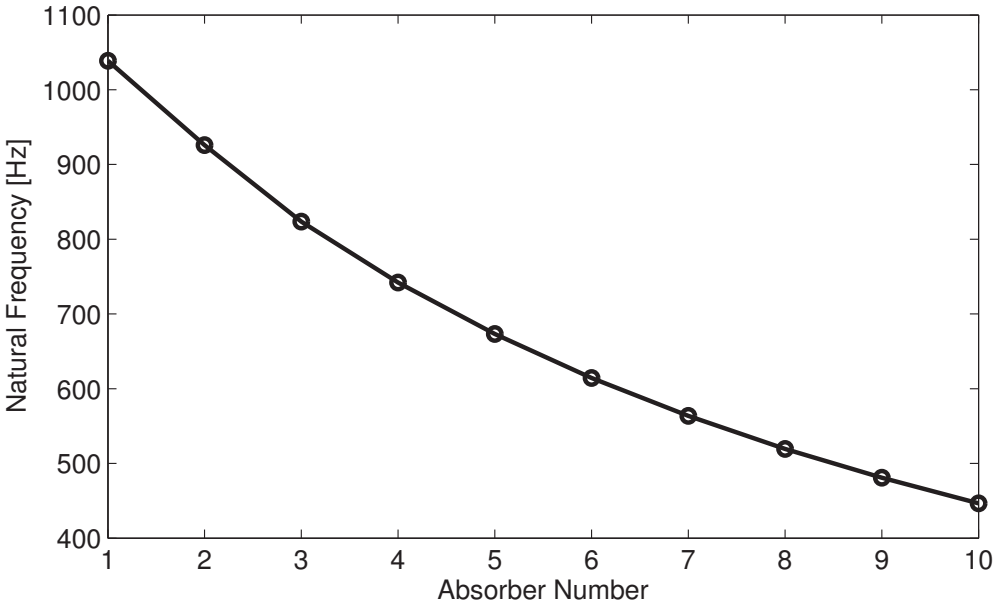

Figure 5.29: Natural frequencies of the vibration absorbers for the narrow frequency range design where absorber 1 is closest to the base and absorber 10 is closest to the tip

piezoelectric material results in a stiffer structure, the geometry must be modified to allow for the natural frequency of the absorber with the piezoelectric material to still be within the desired range.

For this design, the FRFs and impulse responses of the structure with the controller on and off are shown in Figures 5.31 and 5.32. As the gain value increase, the performance of the controller increases. In the impulse response, this is observed by the decrease in the settling time. The decrease in the amplitudes of the peaks is observed in the FRF. To get a better idea of how the gain influences the structure, the performance measures are plotted versus gain in Figure 5.33. For this distributed mass model design, the controller seems the effect the first two modes, whereas, for the lumped mass model, only one mode was effected.

For the other two designs, the closed loop FRFs for a gain value of 20,000 are shown in Figures 5.34 and 5.36. The plots of performance measure versus gain are shown in Figures 5.35 and 5.37. Comparing the designs of the higher frequency range and the lower frequency range, the mode that has the largest response is different. The higher frequency range design

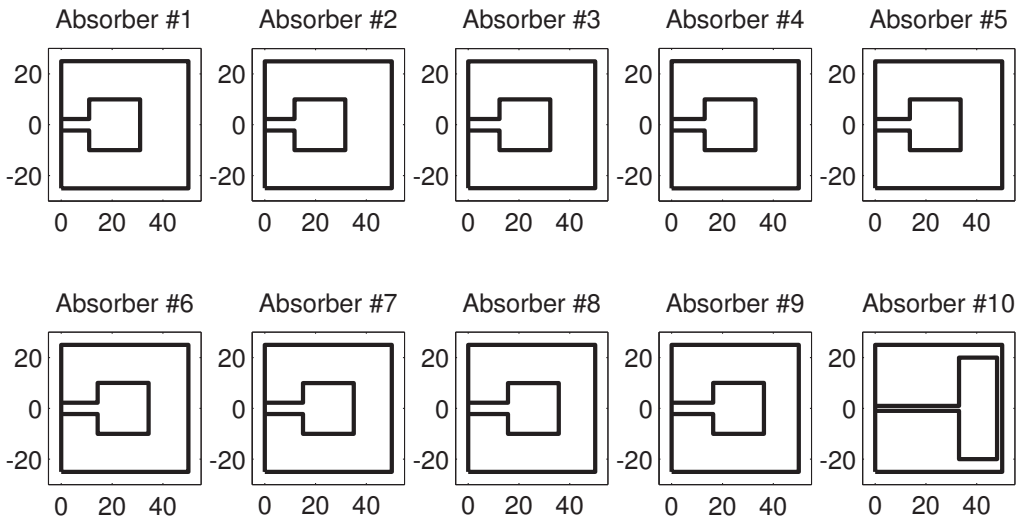

Figure 5.30: Geometry of absorbers for the higher frequency range design, dimensions in mm

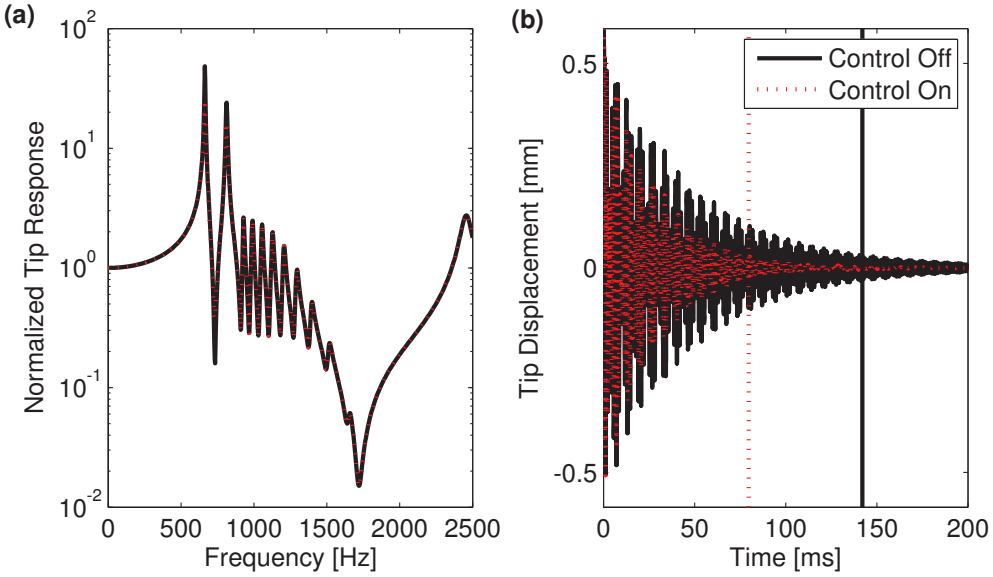

Figure 5.31: The (a) FRF and (b) impulse response of the tip of the higher frequency range metastructure design for a gain value of 10,000. Vertical lines represent the settling time of the corresponding structure.

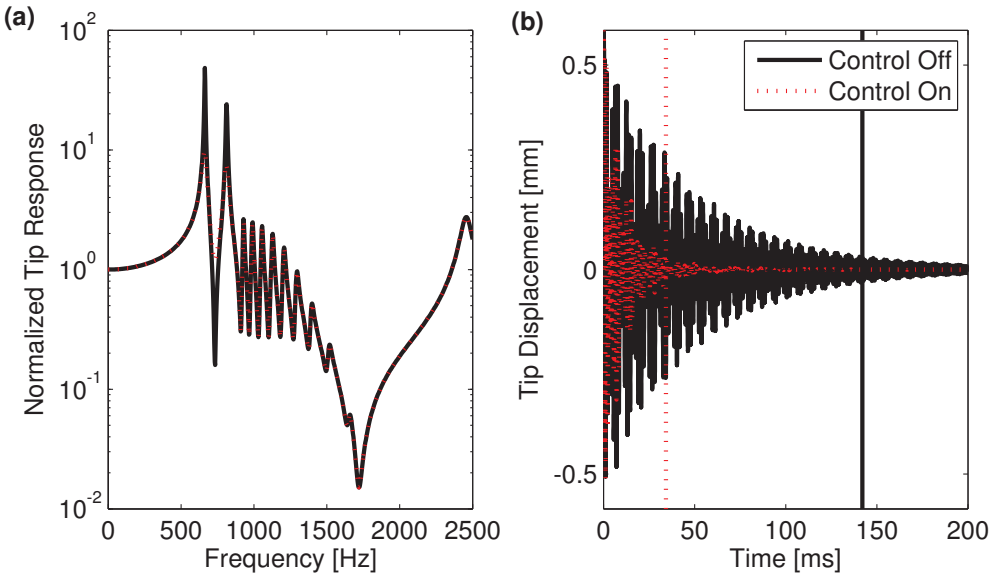

Figure 5.32: The (a) FRF and (b) impulse response of the tip of the higher frequency range metastructure design for a gain value of 20,000. Vertical lines represent the settling time of the corresponding structure.

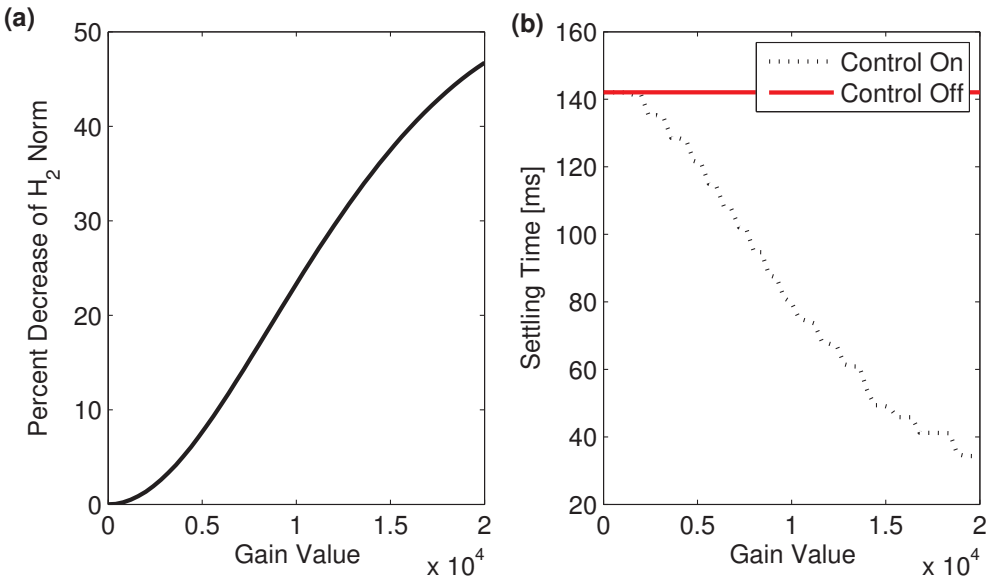

Figure 5.33: The (a) percent decrease in the H_2 norm and (b) settling time versus gain value for the higher frequency range metastructure design.

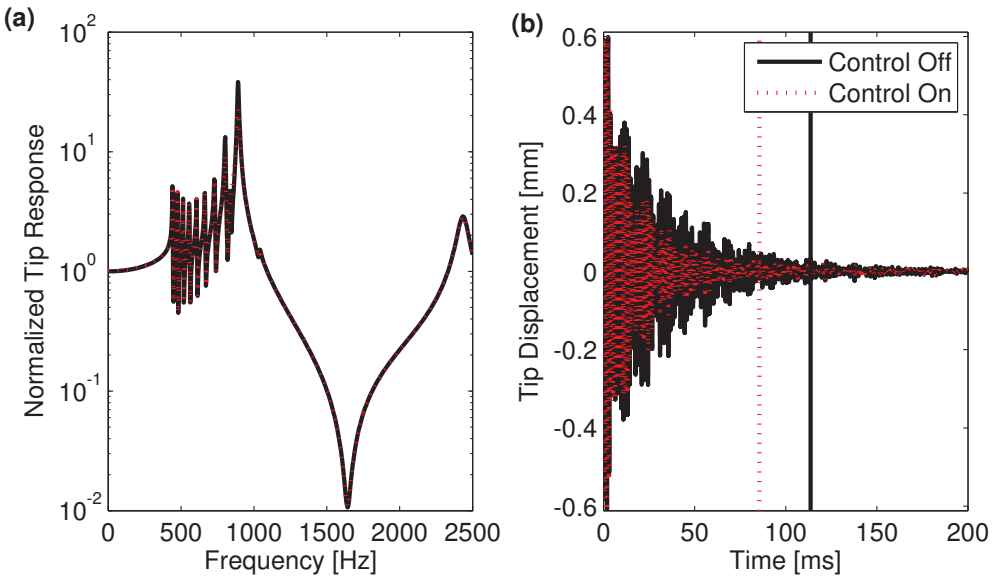

Figure 5.34: The (a) FRF and (b) impulse response of the tip of the lower frequency range metastructure design for a gain value of 20,000. Vertical lines represent the settling time of the corresponding structure.

has a large response of its first two nodes compared to the 11th mode of the lower frequency range design. The structure with the larger response also has better performance increases when the controller is added to the structure. This shows that the large the response of a single mode, the more effective the controller will be. For the design where all the absorbers are tuned to the same frequency, the effectiveness of the controller is not as significant. Since this design only has two natural frequencies within that 0 to 1500 Hz range, each mode has considerable motion of each absorber making a single active vibration absorber less effective. In conclusion, the larger the response of the mode of the corresponding absorber, the more effective the concept of adding a single active vibration absorber can be. For a metastructure without varying natural frequencies, a single active vibration absorber is less effective.

5.4 Chapter summary

This chapter examines the effectiveness of adding active vibration control to the metastructure designs explored previously. The chapter first examines a lumped mass model to

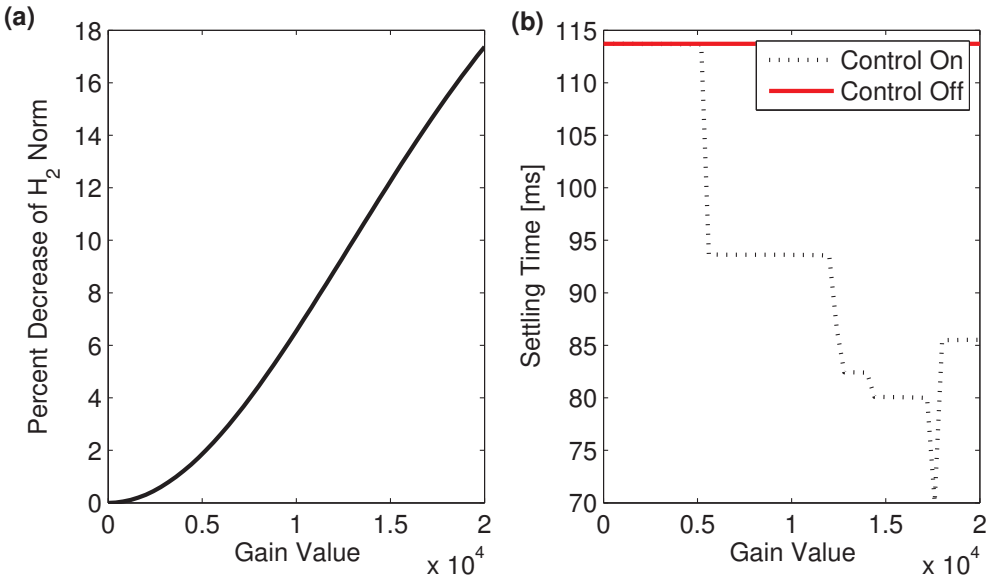

Figure 5.35: The (a) percent decrease in the H_2 norm and (b) settling time versus gain value for the lower frequency range metastructure design.

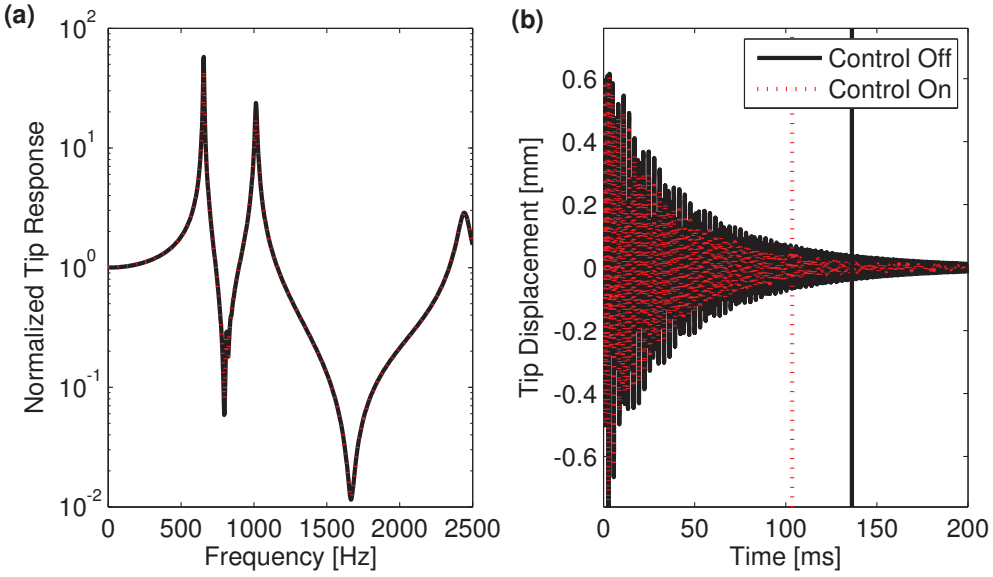

Figure 5.36: The (a) FRF and (b) impulse response of the tip of the constant frequency metastructure design for a gain value of 20,000. Vertical lines represent the settling time of the corresponding structure.

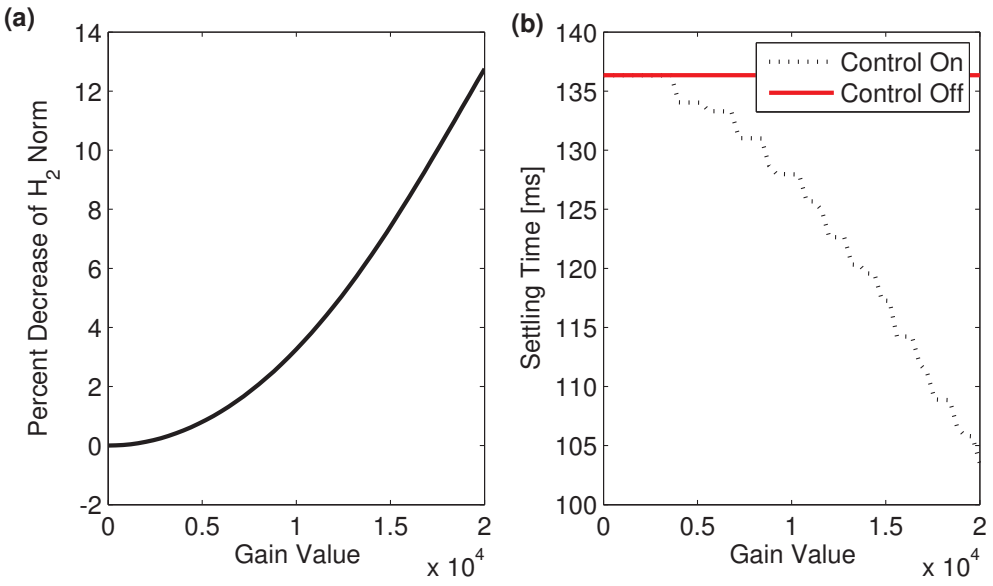

Figure 5.37: The (a) percent decrease in the H_2 norm and (b) settling time versus gain value for the constant frequency metastructure design.

determine trends and then extends the work to a distributed mass model using realistic piezoelectric material properties. The work shows that the concept of using a single active vibration absorber can be used to control the settling time of a metastructure.

For the lumped mass metastructure model utilized has vibration absorbers tuned to linearly varying natural frequencies. This design provides favorable decreases in the value of the H_2 norm but also leads to the appearance of beating behavior in the time response of the structure. Because of this beating response, a slight variation in the system can cause a jump in the settling time when a beat falls below the settling time threshold value. Another effect of the linearly varying natural frequencies is how the location of the actuator for the active control system affects various modes. When the actuator is placed on an absorber mass, one of the modes of the structure is damped which is seen on the FRF of the system.

Examining these designs shows that the best location for the actuator depends on the design of the structure. Although there is a rough pattern showing that placing the actuator closer to the tip of the structure can provide better performance, this is not always true. Once the metastructure design is finalized, the resulting FRF must be examined to determine

which mode is contributing the most to the response. Once that mode is determined, the corresponding absorber mass should have the actuator installed.

Once, the active control system is implemented, the nature of the beating behavior will always cause jumps in the gain versus settling time relationships. This cannot be avoided without removing the beating behavior. Additionally, there is a limit to the settling time values the controller can reach. Since the controller damps out a specific mode of the structure, once that mode is completely damped out, the controller cannot provide any additional performance increases. These are all important considerations that must be taken into account when designing an active control system for a metastructure with distributed vibration absorbers of varying natural frequencies.

For the distributed mass models, two different active vibration absorber designs were examined. The first design looked at using a stack actuator to control the displacement of a single absorber. The second design implemented the active vibration absorber using a piezoelectric bimorph design on a single vibration absorber. The models for both of these designs were presented along with the necessary equations to implement active control using the PPF control law. The active vibration absorber design using a stack actuator was shown to ineffective because the additional stiffness of the stack actuator prevented motion of the absorber in the lower frequency range only making it effective at higher frequencies.

For the active vibration absorber design using a piezoelectric bimorph configuration, the PPF control was successfully implemented to reduce the vibrations in the structure. Examining different designs showed that the larger the response of a mode, the more effective the active vibration absorber could be. Since the first modes of the structure correspond to the oscillations of a single absorber, making the absorber active is very effective at controlling that mode of the metastructure.

In conclusion, depending on the design of the metastructure and the desired performance, adding an active vibration absorber to the metastructure is a feasible solution to get an increased performance of the metastructure.

CHAPTER VI

Summary and Contributions

6.1 Summary

This dissertation studies the performance of one-dimensional metastructures. These structures use distributed vibration absorbers to suppress low-frequency vibrations in the longitudinal direction of the bar. The performance of the metastructures is determined by examining the frequency response and the time response of the tip of the metastructure bar. The metastructures are compared to a baseline structure that has the same mass, which shows that any increase in the performance is due to the addition of the vibration absorbers and not due to any additional mass being added to the structure. Both lumped mass and distributed mass models are used to capture the dynamic response of the metastructures. Additionally, the viscoelastic properties of 3D printed materials are characterized. The material properties are implemented into a viscoelastic model of the metastructure and the effects of temperature are studied. For situations in which high performance is required, the concept of adding active vibration control to the structure was also investigated. The following sections provide detailed summaries of the work completed in each chapter.

6.1.1 Chapter II

This chapter uses a lumped mass model to examine the response of a one-dimensional metastructure. The metastructure is compared to a baseline structure with equal mass.

This constraint shows that any increase in performance of the metastructure is due to the addition of vibration absorbers and not due to the additional mass. The development of the lumped mass model is shown, and different designs are explored. The metastructure model is characterized by the number of vibration absorbers, the natural frequencies of the absorbers, and the mass ratio. The mass ratio is defined as the mass of the absorbers over the total mass of the metastructure.

The parameters of the structure are optimized with respect to the H_2 norm to determine the best-performing structures. First, the effects of the mass and the stiffness distributions of the absorbers are studied. The results show that the primary factor influencing the performance is the ratio of the stiffness over the mass of the absorber, which is related to the natural frequency of the absorber. The best performance is achieved when the natural frequencies of the absorbers vary linearly, leading to broadband vibration suppression. For cases in which the mass ratio is high, the distribution of the mass of the absorbers also influences the performance.

Looking at metastructures with a varying number of vibration absorbers show that initially adding more vibration absorbers to the structure results in a better performing structure, but the performance reaches an asymptote. Once there are around ten absorbers, adding additional absorbers only increases the performance slightly. The mass ratio trends show that adding more mass to the absorbers initially increases performance, but after a certain point, the higher mass ratio leads to a decrease in performance. Lastly, the performance of the metastructure is compared to that of a structure with a single tuned mass damper. For structures with a lower mass ratio, the metastructure is more effective at reducing vibrations. This comparison has a strong dependence on the level of damping in the structure.

6.1.2 Chapter III

Chapter III examines the complex modulus of inkjet materials printed using VeroWhitePlus and TangoPlus on the Objet Connex 3D printer. These materials exhibit viscoelastic material behaviors which must be considered when used in vibration applications. Viscoelastic materials have material properties that vary significantly with temperature and frequency. The frequency dependence of the materials leads to hysteresis which greatly influences the amount of damping in the structure. The Objet Connex printer can print up to ten different materials using varying ratios of the two base materials; VeroWhitePlus and TangoPlus. TangoPlus is a rubber-like material which has material properties that vary significantly with temperature and frequency. VeroWhitePlus still exhibits viscoelastic properties but is substantially stiffer than TangoPlus.

Four of the ten materials the Objet Connex printer is capable of printing are tested to determine the frequency and temperature dependence of the complex modulus of the materials. This material characterization is done using a dynamic mechanical analyzer (DMA) machine. This device measures the modulus of the material in a dynamic sense while varying the frequency of the material of the applied load and the temperature of the material. Using the time-temperature superposition principle, the properties measured at various temperatures are shifted to represent the material properties at a single reference temperature over a larger frequency range. In addition to measuring these material properties, the effects of various printer parameters are also studied. Two in-plane print directions are investigated along with two testing configurations; a tensile configuration and a cantilever configuration. The print direction did not alter the results, but the testing configuration had a slight effect on the property values.

Using data obtained from the material characterization of the viscoelastic materials, the GHM model is used to model the response of a structure made from these materials. The GHM model uses internal variables to capture the viscoelastic effects of the material. The model parameters are curve-fit to the complex modulus data determined experimentally. Us-

ing the time-temperature superposition, the curve-fit is conducted at multiple temperatures allowing the GHM model to also capture the effects of temperature.

The GHM model is verified experimentally by measuring the natural frequency and damping ratio of a simple cantilevered beam at various temperatures and compared to the predicted values of the model. The results show the GHM model can accurately predict the fundamental natural frequency of the cantilevered beam at various temperatures.

6.1.3 Chapter IV

Chapter IV extends the work from Chapters II and III by using the material properties of the viscoelastic 3D printed materials for a distributed mass metastructure model. A physical design for a one-dimensional metastructure is proposed, consisting of a bar with a hollow square cross-section making up the host structure. The vibration absorbers are cantilevered beams with large tip masses which are distributed along the length of the bar and oriented such that the bending motion of the cantilevered beams absorbs vibrations along the axial direction of the bar. The effectiveness of this design is verified experimentally and by using a commercial finite element model.

The metastructure is then modeled using the GHM model developed in the Chapter III. The GHM model is beneficial as it allows the response of the metastructure to be calculated at various temperatures while also incorporating material damping into the model. The GHM model predicts the damping in a structure using the material properties, not by some arbitrarily defined damping value.

Next, a design procedure is explained for determining how various parameters affect the performance of the metastructure. Designs with varying mass ratios and number of absorbers are examined. For each of these cases, the influences of changing the natural frequencies of the absorbers are considered. This analysis shows similar results from the lumped mass model; using vibration absorbers with varying natural frequencies leads to more board-band suppression. From this analysis, a single metastructure design is chosen

to be experimentally tested. The GHM model was able to accurately predict the natural frequencies of the vibration absorbers within 20%.

The performance of this structure is analytically examined at various temperatures and compared to a baseline structure of the same weight. The results show the natural frequencies of the absorbers change at a similar rate to the host structure, allowing the metastructure to be effective at suppressing vibrations at a range of frequencies. Once the structure gets to higher temperatures, the damping of the material dominates the response. At these temperatures, the static response of the structure dominates the response, making the baseline structure more effective at higher temperatures.

6.1.4 Chapter V

Chapter V looks at improving the performance of a metastructure further by adding active vibration control to the structure. The previously developed lumped mass and distributed mass models are used for this examination. The models in which controls are implemented are metastructures with linearly varying natural frequencies. Understanding the effects of the active vibration absorber requires knowledge about the mode shapes of the metastructure. The lower-frequency mode shapes of these structures correspond to the movement a single absorber tuned to the same natural frequency of the natural frequency of the corresponding mode.

Using the lumped mass model, the controllability and observability norms are examined. These norms show that placing a sensor on a single absorber is good at sensing the mode that corresponds to the movement of that absorber. The same goes for an actuator affecting the controllability of the same mode. Next, the positive position feedback control law is implemented in the lumped mass model using collocated control, meaning the actuating and sensing occur at the same location. The control force is placed at various locations. At each location, the control parameters are optimized to achieve the best performance. This analysis shows the controller can effectively eliminate a single mode of the structure. Additionally,

increasing the gain on the controller causes the settling time of the structure to decrease. This trend occurs up to a limit, corresponding to when the mode has been eliminated. After this limit, the controller does not reduce the settling time any further.

For the distributed mass model, two different active vibration absorber designs are considered using piezoelectric materials. The first uses a stack actuator to control the force acting on a single absorber. Attaching the stack actuator to the structure results in significant additional stiffness, leading to the active vibration absorber only being effective at higher frequencies. The second design adds PZT materials to the beam of one of the vibration absorbers in a bimorph configuration. Once again, the PZT materials add additional stiffness to the structure, but for this design, the geometry of the absorber can be modified to account for the stiffness change.

The PZT bimorph design is implemented on a few different metastructure designs using material properties of actual materials. The results show that this design can effectively be integrated into an actual metastructure design to control the response of the structure. Additionally, the results show similar trends as the lumped mass model, where a single mode can be damped out. Furthermore, the larger the uncontrolled response of a mode, the more effective the controller is.

6.2 Main contributions

The major contributions of this dissertation are focused on the performance of a metastructure bar with linearly varying natural frequencies compared to a baseline structure of the same weight. The main contributions of this work are summarized as:

- Showing that the concept of using distributed vibration absorbers can effectively reduce vibrations without adding additional mass to the structure.
- Using vibration absorbers with linearly varying natural frequency leads to more broadband suppression.

- The creation of a physical one-dimensional metastructure model that experimentally exhibits the predicted metastructure behavior.
- The characterization of the frequency and temperature dependence of the Objet Connex 3D printed materials.
- Implementing the GHM model to predict the amount of damping in a metastructure from measured material properties.
- Using the GHM model to accurately predict the fundamental natural frequencies of cantilevered beams at various temperatures.
- Showing that the concept of adding a single active vibration absorber to a metastructure can control the response of a single mode of a metastructure with linearly varying natural frequencies.
- Developing an active vibration absorber design that is effective at reducing the vibrations in a metastructure.

6.3 Recommendations for future work

There are a few different directions the future work for this project could take. These directions are categorized into the three major parts of this dissertation: metastructures, viscoelastic modeling, and controls of metastructures. The recommendations for future work within these three areas are described in future detail below.

6.3.1 Metastructures

This work focused on a one-dimensional metastructure which provided insight into the general behavior of the metastructures. This work could be extended into two-dimensional bending metastructures. Beam structures behave differently than bar structures. Thus the trends for beam structures may look than those found for a metastructure bar here.

Additionally, the inverse problem could be considered. This work looked at how changing the parameters resulted in changes to the dynamic response of the structure. For the inverse problem, a desired dynamic response could be given and the necessary parameters to achieve that response could be determined. This would allow for metastructures to be designed for specific situations.

Another direction of this work could examine the robustness of the metastructure concepts This could be achieved by looking at how sensitive the performance of the metastructure is to specific parameters. If a vibration absorber is designed to suppress vibrations at a certain frequency, but the actual frequency of the absorber is off by 5%, how does that affect the performance of the metastructure?

Before these metastructure concepts can be implemented into real-life applications, the effects of fatigue on the vibration absorbers must be determined. Since the vibration absorbers absorb the energy from the rest of the structure, they move significantly. This cyclical nature can lead to fatigue failure and must be considered.

The work could also take a more application focus, where a specific scenario is chosen, and a metastructure is designed for that specific case. This would also allow for a more realistic comparison of the metastructure technique versus other vibration suppression solutions, such as a tuned mass damper or the addition of viscoelastic materials via constrained layer damping.

6.3.2 Viscoelastic modeling

This work made an essential first step in modeling the viscoelastic nature of 3D printed materials. More work could be done in examining the effects of the testing methods used to experimentally determine the complex modulus. An analysis in the effects of sample size could be examined. Additionally, the effects of modifying more printing parameters could be explored. This work examined the effects of two print directions, but a 3D printer has a total of six different print directions that could be tested.

This work solely used the GHM model to model the viscoelastic behavior of the printed materials. Other viscoelastic models could be used and compared to the GHM model, such as the augmenting thermodynamic fields model.

6.3.3 Controls

The controls work presented here considered the case in which only a single vibration absorber was an active vibration absorber. Future work could look at the benefits of using multiple active vibration absorbers and the trade-offs between adding more active vibration absorbers and the performance of the active structure.

Additionally, different methods for implementing an active vibration absorber could be explored. This work looked at using a stack actuator and also a piezoelectric bimorph configuration. Other designs could be considered and their performance could be compared to the results here. Additionally, different control laws could be considered.

6.4 List of publications

Journal Publications

1. K. K. Reichl and D. J. Inman, "Lumped mass model of a 1D metastructure for vibration suppression with no additional mass," *Journal of Sound and Vibration*, vol. 403, pp. 75-89, 2017.

2. K. K. Reichl and D. J. Inman, "Dynamic mechanical and thermal analysis of Objet Connex 3D printed materials," *Experimental Techniques*, vol. 42, pp. 19-25, 2018.

3. K. K. Reichl and D. J. Inman, "Temperature-dependent damping in 3D printed polymer structures," *Journal of Vibration and Acoustics*, 2018 (in review).

4. K. K. Reichl and D. J. Inman, "Implementation of an active vibration absorber in a 1D metastructure for vibration suppression," *Journal of Intelligent Materials Systems*

and Structures, 2018 (in preparation).

Conference Proceedings

1. K. K. Reichl and D. J. Inman, "Lumped mass model of a 1D metastructure with vibration absorbers with varying mass," in *36th International Modal Analysis Conference*, 2018.

2. M. L. Liu, K. K. Reichl and D. J. Inman, "Complex modulus variation by manipulation of mechanical test method and print direction," in *2017 Society of Engineering Mechanics Annual Conference*, 2017.

3. K. K. Reichl and D. J. Inman, "Constant mass metastructure with vibration absorbers of linearly varying natural frequencies," in *35th International Modal Analysis Conference*, 2017.

4. K. K. Reichl and D. J. Inman, "Metastructures and active vibration control," in *27th International Conference on Adaptive Structures Technologies*, 2016.

5. K. K. Reichl and D. J. Inman, "Dynamic modulus properties of Objet Connex 3D printer digital materials," in *34th International Modal Analysis Conference*, 2016.

6. K. K. Reichl and D. J. Inman, "Finite element modeling of longitudinal metastructures for passive vibration suppression," in *57th AIAA/ASCE/AHS/ASC Structures, Structural Dynamics, and Materials Conference*, 2016.

7. K. K. Reichl and D. J. Inman, "Modeling of low-frequency broadband vibration mitigation for a bar experiencing longitudinal vibrations using distributed vibration absorbers," in *20th International Conference on Composite Materials*, 2015.

APPENDICES

APPENDIX A

Complex Modulus Data Tables

This appendix provides the complex modulus data for the 3D printed material test for this work. The specimens tested to compile this data, were all printed from the Objet Connex 3D printer as described in Section 3.2.1. Two different studies were conducted as part of this work. The first examined the effects of printing direction and testing configuration (Section 3.2.2). Where as, the second study looked at the differences between four materials printed using the Objet Connex 3D printer. The following sections provide the complex modulus data for the eight different different testing scenarios using data collected from a dynamic mechanical analysis (DMA) machine. Using this data, a frequency-temperature analysis is performed, as described in Section 3.1 including the data for an Arrhenius shift factor relationship describing the relationship between the temperature and frequency.

A.1 Print direction and testing configuration comparison

This section provides additional details for the DMA testing preformed in Sections 3.2.3.3 and 3.2.3.4 where the effects of print direction and testing configuration were examined for the 3D printed material DM 8430. Four different specimens were used for this testing. Schematics showing the print directions and testing configuration are shown in Figures 3.1 and 3.2 respectively. The Arrhenius factor relationship for the four specimens is provided in Table A.1.

Table A.1: Arrhenius fit data for DM 8430 for various configurations

Testing Configuration	**Printing Direction**	**Reference Temperature [°C]**	**Arrhenius Temperature [K]**
tensile	horizontal	66	12,011
tensile	vertical	66	12,944
cantilevered	horizontal	65	15,071
cantilevered	vertical	65	15,271

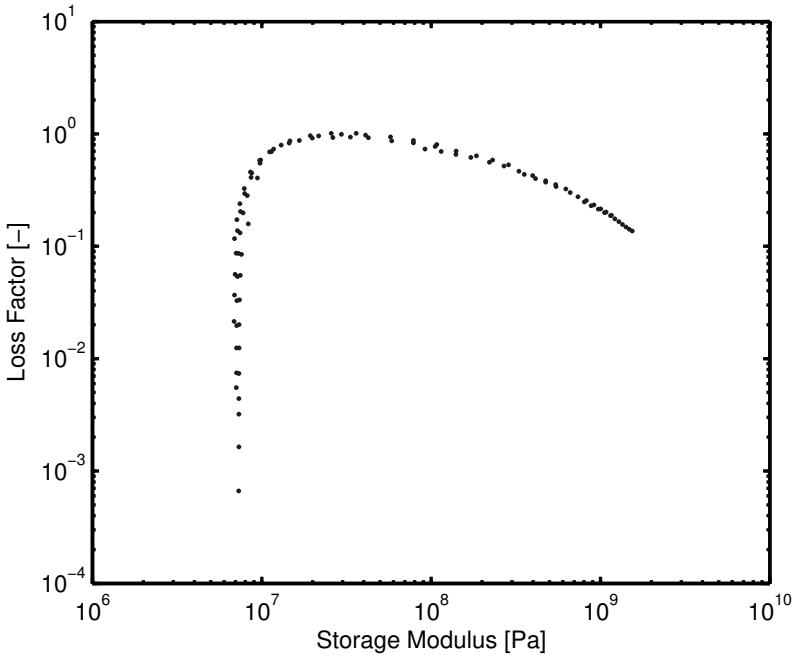

Figure A.1: Wicket plot of experimental data for DM 8420 printed in the horizontal direction and testing using the tensile configuration

A.1.1 Results for DM 8420 printed in the horizontal direction and testing using the tensile configuration

This sample was printed with approximate dimensions of 9 mm × 5 mm × 1 mm were used in the DMA machine. The complex modulus data is summarized in Table A.2 including the shift factor relationship determined from the frequency-temperature analysis. The Wicket plot is provided in Figure A.1.1. A plot of the shift factor, $\log[\alpha(T)]$ versus the inverses of the temperature with an Arrhenius fit is plotted in Figure A.2. Using the shift factors reported, the reduced frequency plot is in Figure 3.8.

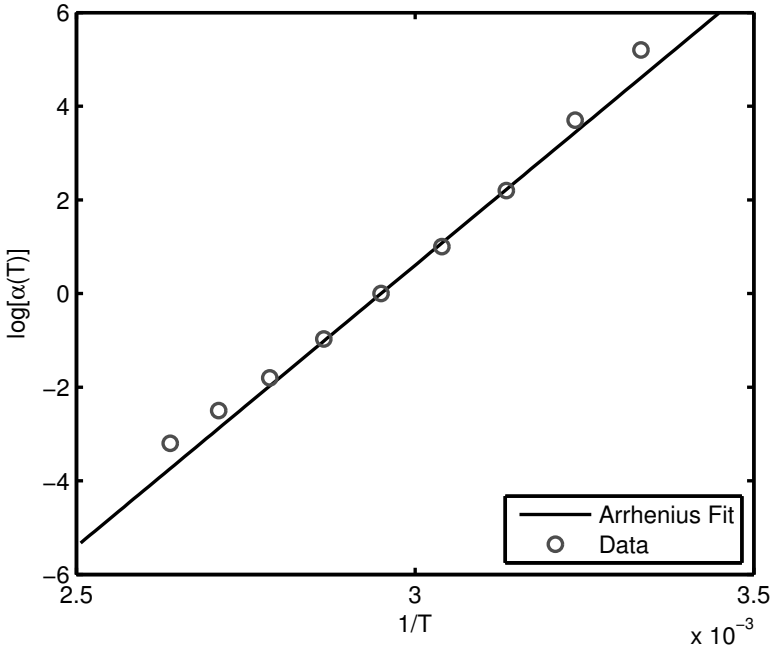

Figure A.2: Arrhenius fit for experimental data for DM 8420 printed in the horizontal direction and testing using the tensile configuration

Table A.2: Complex modulus data for DM 8420 printed in the horizontal direction and testing using the tensile configuration

Temperature [°C]	[°F]	**Frequency** [Hz]	**Storage Modulus** [MPa]	**Loss Factor** [-]	**Shift Factor** $\log[\alpha(T)]$
27	80.6	31.60	1540.71	0.136	5.2
		17.80	1479.48	0.141	
		10.00	1416.89	0.148	
		5.60	1351.22	0.156	
		3.20	1285.33	0.165	
		1.80	1215.66	0.175	
		1.00	1146.01	0.187	
		0.56	1058.06	0.199	
		0.32	970.63	0.214	
		0.18	882.22	0.230	
		0.10	804.27	0.248	
36	96.8	31.60	1163.92	0.189	3.7
		17.80	1080.56	0.202	
		10.00	1003.64	0.215	
		5.60	914.39	0.233	
		3.20	824.94	0.255	
		1.80	737.85	0.276	

Table A.2: Complex modulus data for DM 8420 printed in the horizontal direction and testing using the tensile configuration

Temperature [°C]	[°F]	**Frequency** [Hz]	**Storage Modulus** [MPa]	**Loss Factor** [-]	**Shift Factor** $\log[\alpha(T)]$
		1.00	662.88	0.301	
		0.56	547.65	0.340	
		0.32	474.35	0.372	
		0.18	413.32	0.401	
		0.10	355.16	0.436	
46	114.8	31.60	624.68	0.324	2.2
		17.80	544.09	0.353	
		10.00	475.31	0.383	
		5.60	398.03	0.425	
		3.20	330.04	0.466	
		1.80	269.31	0.517	
		1.00	221.10	0.559	
		0.56	171.70	0.617	
		0.32	140.29	0.656	
		0.18	114.77	0.697	
		0.10	92.08	0.732	
56	132.8	31.60	286.93	0.530	1.0
		17.80	230.70	0.584	
		10.00	185.48	0.638	
		5.60	140.43	0.704	
		3.20	105.73	0.771	
		1.80	78.62	0.830	
		1.00	58.51	0.865	
		0.56	42.62	0.925	
		0.32	33.39	0.935	
		0.18	26.32	0.930	
		0.10	19.89	0.918	
66	150.8	31.60	108.12	0.804	0.0
		17.80	78.65	0.873	
		10.00	57.63	0.939	
		5.60	41.03	0.974	
		3.20	29.56	0.990	
		1.80	21.69	0.959	
		1.00	16.69	0.873	
		0.56	13.04	0.794	
		0.32	11.14	0.691	
		0.18	9.72	0.581	
		0.10	8.58	0.457	
76	168.8	31.60	36.10	1.014	-1.0
		17.80	25.73	1.012	

Table A.2: Complex modulus data for DM 8420 printed in the horizontal direction and testing using the tensile configuration

Temperature [°C]	[°F]	**Frequency** [Hz]	**Storage Modulus** [MPa]	**Loss Factor** [-]	**Shift Factor** $\log[\alpha(T)]$
		10.00	19.34	0.965	
		5.60	14.67	0.865	
		3.20	11.74	0.733	
		1.80	9.85	0.586	
		1.00	8.72	0.449	
		0.56	7.88	0.326	
		0.32	7.43	0.239	
		0.18	7.13	0.172	
		0.10	6.90	0.117	
86	186.8	31.60	14.50	0.828	-1.8
		17.80	11.39	0.694	
		10.00	9.78	0.549	
		5.60	8.64	0.410	
		3.20	7.94	0.294	
		1.80	7.50	0.204	
		1.00	7.20	0.138	
		0.56	7.05	0.087	
		0.32	6.96	0.056	
		0.18	6.90	0.037	
		0.10	6.88	0.021	
96	204.8	31.60	9.44	0.406	-2.5
		17.80	8.21	0.282	
		10.00	7.76	0.198	
		5.60	7.46	0.132	
		3.20	7.29	0.086	
		1.80	7.19	0.054	
		1.00	7.13	0.033	
		0.56	7.11	0.020	
		0.32	7.10	0.012	
		0.18	7.09	0.007	
		0.10	7.09	0.006	
106	222.8	31.60	8.34	0.158	-3.2
		17.80	7.59	0.085	
		10.00	7.47	0.055	
		5.60	7.40	0.033	
		3.20	7.36	0.020	
		1.80	7.35	0.012	
		1.00	7.33	0.007	
		0.56	7.34	0.004	
		0.32	7.33	0.003	

Table A.2: Complex modulus data for DM 8420 printed in the horizontal direction and testing using the tensile configuration

Temperature [°C]	[°F]	**Frequency** [Hz]	**Storage Modulus** [MPa]	**Loss Factor** [-]	**Shift Factor** $\log[\alpha(T)]$
		0.18	7.33	0.002	
		0.10	7.32	0.001	

A.1.2 Results for DM 8420 printed in the vertical direction and testing using the tensile configuration

This sample was printed with approximate dimensions of 9 mm × 5 mm × 1 mm were used in the DMA machine. The complex modulus data is summarized in Table A.3 including the shift factor relationship determined from the frequency-temperature analysis. The Wicket plot is provided in Figure A.1.2. A plot of the shift factor, $\log[\alpha(T)]$ versus the inverses of the temperature with an Arrhenius fit is plotted in Figure A.4. Using the shift factors reported, the reduced frequency plot is in Figure 3.8.

Table A.3: Complex modulus data for DM 8420 printed in the vertical direction and testing using the tensile configuration

Temperature [°C]	[°F]	**Frequency** [Hz]	**Storage Modulus** [MPa]	**Loss Factor** [-]	**Shift Factor** $\log[\alpha(T)]$
28	82.4	100.00	1641.62	0.130	4.8
		56.00	1575.54	0.137	
		31.60	1506.84	0.137	
		17.80	1440.10	0.143	
		10.00	1372.69	0.150	
		5.60	1303.59	0.159	
		3.20	1233.85	0.168	
		1.80	1160.59	0.178	
		1.00	1084.45	0.191	
		0.56	997.89	0.203	
		0.32	908.02	0.220	
		0.18	820.51	0.238	
		0.10	745.95	0.250	
36	96.8	100.00	1330.82	0.169	3.7
		56.00	1254.55	0.177	
		31.60	1170.72	0.186	

Table A.3: Complex modulus data for DM 8420 printed in the vertical direction and testing using the tensile configuration

Temperature [°C]	[°F]	**Frequency** [Hz]	**Storage Modulus** [MPa]	**Loss Factor** [-]	**Shift Factor** $\log[\alpha(T)]$
		17.80	1088.74	0.198	
		10.00	1011.77	0.211	
		5.60	923.82	0.228	
		3.20	835.64	0.248	
		1.80	750.85	0.268	
		1.00	674.69	0.292	
		0.56	567.22	0.327	
		0.32	491.41	0.360	
		0.18	427.78	0.389	
		0.10	369.54	0.411	
46	114.8	100.00	815.58	0.274	2.4
		56.00	732.16	0.294	
		31.60	645.94	0.317	
		17.80	561.52	0.347	
		10.00	489.84	0.378	
		5.60	410.54	0.420	
		3.20	338.24	0.466	
		1.80	275.71	0.515	
		1.00	223.56	0.559	
		0.56	171.80	0.626	
		0.32	140.10	0.666	
		0.18	115.09	0.699	
		0.10	88.81	0.757	
56	132.8	100.00	418.92	0.449	1.2
		56.00	350.65	0.491	
		31.60	287.20	0.532	
		17.80	230.39	0.586	
		10.00	184.25	0.636	
		5.60	138.81	0.707	
		3.20	104.34	0.771	
		1.80	77.91	0.822	
		1.00	58.61	0.855	
		0.56	42.65	0.897	
		0.32	33.60	0.897	
		0.18	26.69	0.885	
		0.10	20.27	0.889	
66	150.8	100.00	184.71	0.684	0.0
		56.00	141.61	0.753	
		31.60	106.08	0.805	
		17.80	77.30	0.867	

Table A.3: Complex modulus data for DM 8420 printed in the vertical direction and testing using the tensile configuration

Temperature [°C]	[°F]	**Frequency** [Hz]	**Storage Modulus** [MPa]	**Loss Factor** [-]	**Shift Factor** $\log[\alpha(T)]$
		10.00	56.84	0.916	
		5.60	40.97	0.947	
		3.20	29.86	0.950	
		1.80	22.12	0.916	
		1.00	16.65	0.888	
		0.56	13.51	0.760	
		0.32	11.50	0.667	
		0.18	10.06	0.566	
		0.10	8.87	0.452	
76	168.8	100.00	67.34	0.940	-1.1
		56.00	49.20	0.995	
		31.60	35.76	0.980	
		17.80	25.80	0.970	
		10.00	19.67	0.913	
		5.60	15.03	0.824	
		3.20	12.09	0.704	
		1.80	10.16	0.572	
		1.00	8.86	0.449	
		0.56	8.07	0.327	
		0.32	7.59	0.243	
		0.18	7.26	0.176	
		0.10	7.04	0.121	
86	186.8	100.00	24.82	0.999	-2.1
		56.00	18.95	0.973	
		31.60	14.90	0.792	
		17.80	11.71	0.669	
		10.00	10.04	0.537	
		5.60	8.86	0.406	
		3.20	8.12	0.296	
		1.80	7.64	0.207	
		1.00	7.32	0.141	
		0.56	7.16	0.090	
		0.32	7.06	0.060	
		0.18	7.01	0.038	
		0.10	6.97	0.023	
96	204.8	100.00	12.75	0.689	-3.1
		56.00	11.11	0.632	
		31.60	9.70	0.399	
		17.80	8.38	0.283	
		10.00	7.91	0.201	

Table A.3: Complex modulus data for DM 8420 printed in the vertical direction and testing using the tensile configuration

Temperature [°C]	[°F]	**Frequency** [Hz]	**Storage Modulus** [MPa]	**Loss Factor** [-]	**Shift Factor** $\log[\alpha(T)]$
		5.60	7.59	0.134	
		3.20	7.41	0.090	
		1.80	7.30	0.056	
		1.00	7.25	0.035	
		0.56	7.21	0.020	
		0.32	7.20	0.012	
		0.18	7.19	0.008	
		0.10	7.17	0.004	

A.1.3 Results for DM 8420 printed in the horizontal direction and testing using the cantilevered configuration

This sample was printed with approximate dimensions of 17 mm × 12 mm × 3 mm were used in the DMA machine. The complex modulus data is summarized in Table A.4 including the shift factor relationship determined from the frequency-temperature analysis. The Wicket plot is provided in Figure A.1.3. A plot of the shift factor, $\log[\alpha(T)]$ versus the inverses of the temperature with an Arrhenius fit is plotted in Figure A.6. Using the shift factors reported, the reduced frequency plot is in Figure 3.9.

Table A.4: Complex modulus data for DM 8420 printed in the horizontal direction and testing using the cantilevered configuration

Temperature [°C]	[°F]	**Frequency** [Hz]	**Storage Modulus** [MPa]	**Loss Factor** [-]	**Shift Factor** $\log[\alpha(T)]$
35	95.0	17.80	1154.22	0.190	4.8
		10.00	1073.05	0.204	
		5.60	983.04	0.222	
		3.20	896.65	0.239	
		1.80	811.30	0.258	
		1.00	733.02	0.275	
		0.56	638.93	0.301	
		0.32	560.68	0.325	
		0.18	488.68	0.349	
		0.10	426.10	0.371	

Table A.4: Complex modulus data for DM 8420 printed in the horizontal direction and testing using the cantilevered configuration

Temperature [°C]	[°F]	**Frequency** [Hz]	**Storage Modulus** [MPa]	**Loss Factor** [-]	**Shift Factor** $\log[\alpha(T)]$
40	104.0	17.80	800.73	0.273	3.6
		10.00	720.76	0.294	
		5.60	636.90	0.320	
		3.20	559.11	0.346	
		1.80	484.74	0.373	
		1.00	418.46	0.399	
		0.56	346.88	0.437	
		0.32	289.95	0.471	
		0.18	241.11	0.504	
		0.10	199.44	0.535	
45	113.0	17.80	523.72	0.375	2.7
		10.00	453.36	0.405	
		5.60	384.50	0.440	
		3.20	323.80	0.475	
		1.80	268.05	0.512	
		1.00	219.77	0.550	
		0.56	175.90	0.589	
		0.32	142.37	0.623	
		0.18	114.13	0.655	
		0.10	90.62	0.684	
50	122.0	17.80	332.37	0.489	1.9
		10.00	275.40	0.528	
		5.60	222.91	0.571	
		3.20	179.33	0.612	
		1.80	141.89	0.654	
		1.00	111.60	0.692	
		0.56	85.72	0.725	
		0.32	67.47	0.748	
		0.18	53.01	0.762	
		0.10	41.24	0.770	
55	131.0	17.80	195.95	0.615	1.2
		10.00	155.47	0.660	
		5.60	120.51	0.704	
		3.20	93.28	0.742	
		1.80	71.46	0.774	
		1.00	54.89	0.795	
		0.56	41.76	0.802	
		0.32	32.81	0.796	
		0.18	26.03	0.776	

Table A.4: Complex modulus data for DM 8420 printed in the horizontal direction and testing using the cantilevered configuration

Temperature [°C]	[°F]	**Frequency** [Hz]	**Storage Modulus** [MPa]	**Loss Factor** [-]	**Shift Factor** $\log[\alpha(T)]$
		0.10	20.59	0.742	
60	140.0	17.80	109.18	0.734	0.6
		10.00	83.97	0.772	
		5.60	63.47	0.804	
		3.20	48.37	0.822	
		1.80	36.88	0.826	
		1.00	28.35	0.816	
		0.56	22.06	0.780	
		0.32	17.82	0.732	
		0.18	14.64	0.669	
		0.10	12.18	0.589	
65	149.0	17.80	59.79	0.816	0.0
		10.00	45.59	0.831	
		5.60	34.47	0.834	
		3.20	26.58	0.818	
		1.80	20.71	0.782	
		1.00	16.45	0.726	
		0.56	13.38	0.646	
		0.32	11.40	0.560	
		0.18	9.95	0.466	
		0.10	8.85	0.370	
70	158.0	17.80	34.08	0.823	-0.6
		10.00	26.32	0.807	
		5.60	20.35	0.773	
		3.20	16.21	0.718	
		1.80	13.21	0.640	
		1.00	11.09	0.546	
		0.56	9.66	0.442	
		0.32	8.75	0.350	
		0.18	8.10	0.266	
		0.10	7.62	0.191	
75	167.0	17.80	20.86	0.743	-1.1
		10.00	16.70	0.690	
		5.60	13.47	0.622	
		3.20	11.31	0.537	
		1.80	9.81	0.441	
		1.00	8.78	0.343	
		0.56	8.11	0.255	
		0.32	7.69	0.187	
		0.18	7.40	0.132	

Table A.4: Complex modulus data for DM 8420 printed in the horizontal direction and testing using the cantilevered configuration

Temperature [°C]	[°F]	**Frequency** [Hz]	**Storage Modulus** [MPa]	**Loss Factor** [-]	**Shift Factor** $\log[\alpha(T)]$
		0.10	7.24	0.088	
80	176.0	17.80	14.11	0.576	-1.7
		10.00	11.94	0.502	
		5.60	10.20	0.422	
		3.20	9.07	0.339	
		1.80	8.30	0.258	
		1.00	7.80	0.188	
		0.56	7.49	0.129	
		0.32	7.30	0.089	
		0.18	7.18	0.058	
		0.10	7.13	0.035	
85	185.0	17.80	10.69	0.361	-2.2
		10.00	9.61	0.296	
		5.60	8.63	0.236	
		3.20	8.04	0.181	
		1.80	7.66	0.130	
		1.00	7.42	0.088	
		0.56	7.28	0.057	
		0.32	7.21	0.036	
		0.18	7.16	0.021	
		0.10	7.11	0.009	

A.1.4 Results for DM 8420 printed in the vertical direction and testing using the cantilevered configuration

This sample was printed with approximate dimensions of 17 mm × 12 mm × 3 mm were used in the DMA machine. The complex modulus data is summarized in Table A.5 including the shift factor relationship determined from the frequency-temperature analysis. The Wicket plot is provided in Figure A.1.4. A plot of the shift factor, $\log[\alpha(T)]$ versus the inverses of the temperature with an Arrhenius fit is plotted in Figure A.8. Using the shift factors reported, the reduced frequency plot is in Figure 3.9.

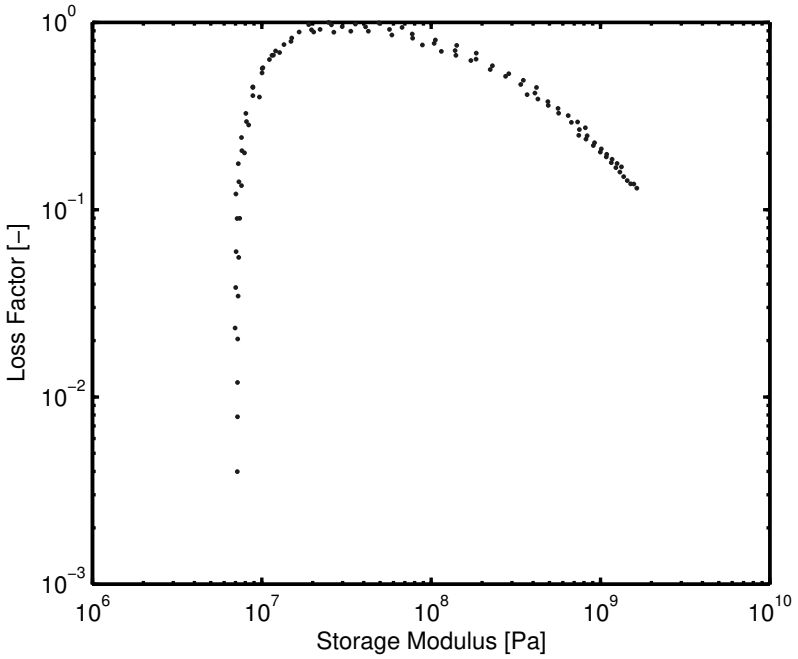

Figure A.3: Wicket plot of experimental data for DM 8420 printed in the vertical direction and testing using the tensile configuration

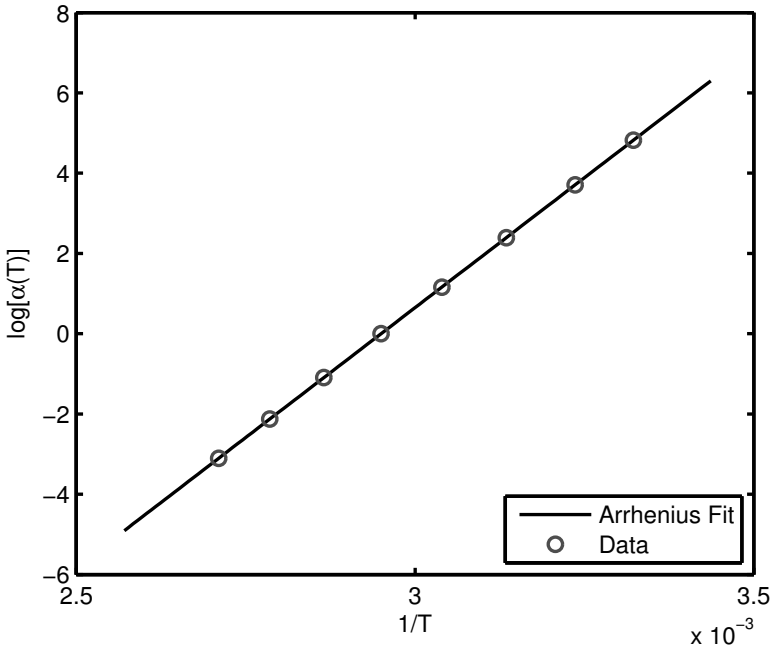

Figure A.4: Arrhenius fit for experimental data for DM 8420 printed in the vertical direction and testing using the tensile configuration

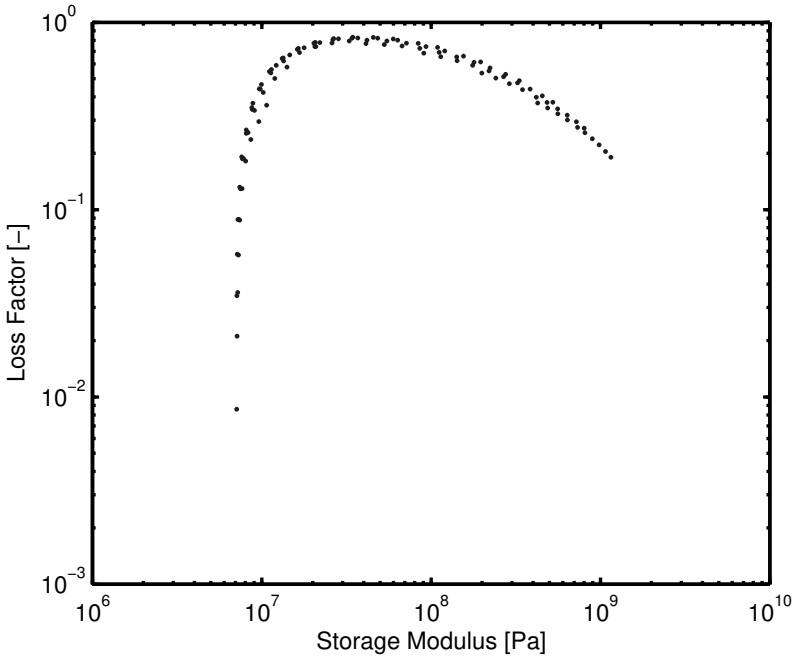

Figure A.5: Wicket plot of experimental data for DM 8420 printed in the horizontal direction and testing using the cantilevered configuration

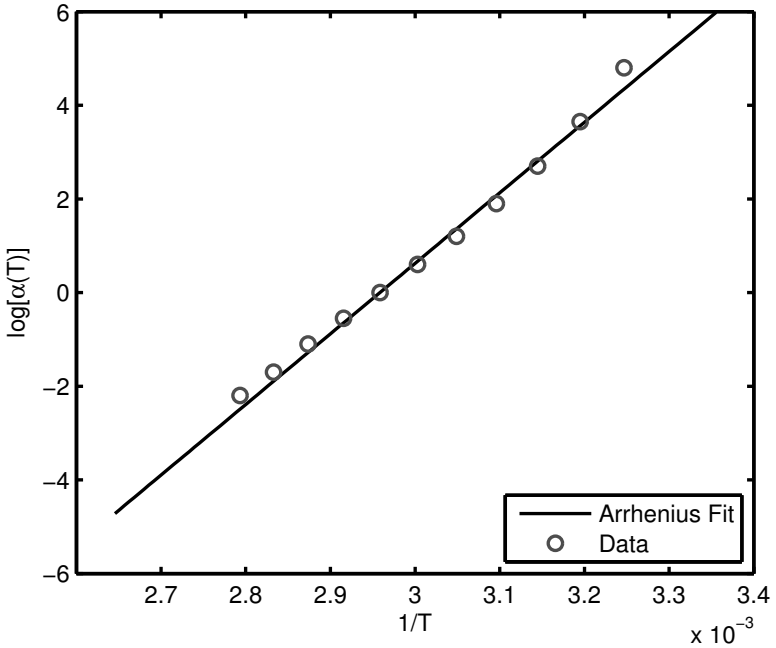

Figure A.6: Arrhenius fit for experimental data for DM 8420 printed in the horizontal direction and testing using the cantilevered configuration

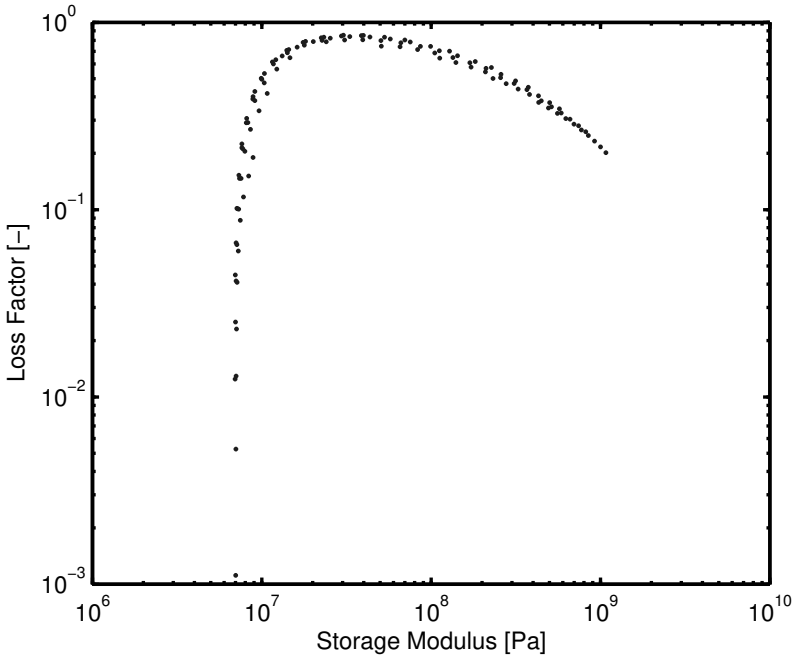

Figure A.7: Wicket plot of experimental data for DM 8420 printed in the vertical direction and testing using the cantilevered configuration

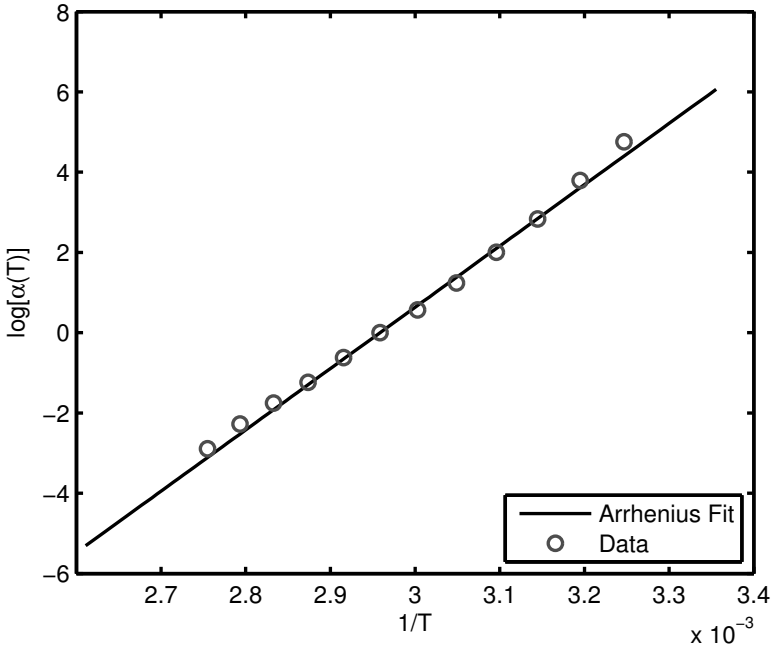

Figure A.8: Arrhenius fit for experimental data for DM 8420 printed in the vertical direction and testing using the cantilevered configuration

Table A.5: Complex modulus data for DM 8420 printed in the vertical direction and testing using the cantilevered configuration

Temperature [°C]	[°F]	**Frequency** [Hz]	**Storage Modulus** [MPa]	**Loss Factor** [-]	**Shift Factor** $\log[\alpha(T)]$
35	95.0	17.80	1077.53	0.201	4.8
		10.00	1000.55	0.216	
		5.60	922.66	0.232	
		3.20	848.01	0.249	
		1.80	772.59	0.266	
		1.00	697.40	0.286	
		0.56	624.69	0.306	
		0.32	557.99	0.327	
		0.18	493.90	0.349	
		0.10	432.05	0.374	
40	104.0	17.80	819.66	0.260	3.8
		10.00	742.28	0.281	
		5.60	661.80	0.304	
		3.20	586.94	0.328	
		1.80	514.31	0.354	
		1.00	447.92	0.381	
		0.56	381.44	0.412	
		0.32	326.68	0.440	
		0.18	277.44	0.470	
		0.10	232.29	0.502	
45	113.0	17.80	572.36	0.345	2.8
		10.00	501.09	0.373	
		5.60	430.59	0.405	
		3.20	367.61	0.437	
		1.80	309.29	0.471	
		1.00	257.41	0.507	
		0.56	209.60	0.544	
		0.32	172.34	0.577	
		0.18	140.16	0.611	
		0.10	112.45	0.644	
50	122.0	17.80	375.26	0.451	2.0
		10.00	315.16	0.487	
		5.60	258.82	0.528	
		3.20	211.35	0.568	
		1.80	169.59	0.609	
		1.00	134.75	0.648	
		0.56	105.06	0.687	
		0.32	83.22	0.716	
		0.18	65.64	0.741	

Table A.5: Complex modulus data for DM 8420 printed in the vertical direction and testing using the cantilevered configuration

Temperature [°C]	[°F]	**Frequency** [Hz]	**Storage Modulus** [MPa]	**Loss Factor** [-]	**Shift Factor** $\log[\alpha(T)]$
		0.10	50.79	0.745	
55	131.0	17.80	227.13	0.574	1.2
		10.00	182.50	0.618	
		5.60	143.23	0.664	
		3.20	112.02	0.706	
		1.80	86.47	0.744	
		1.00	66.37	0.778	
		0.56	50.52	0.798	
		0.32	39.49	0.807	
		0.18	30.85	0.804	
		0.10	24.02	0.787	
60	140.0	17.80	128.42	0.701	0.6
		10.00	99.41	0.744	
		5.60	75.36	0.785	
		3.20	57.42	0.815	
		1.80	43.51	0.834	
		1.00	33.13	0.839	
		0.56	25.38	0.823	
		0.32	20.13	0.790	
		0.18	16.20	0.738	
		0.10	13.20	0.662	
65	149.0	17.80	69.97	0.805	0.0
		10.00	53.12	0.833	
		5.60	39.86	0.852	
		3.20	30.34	0.853	
		1.80	23.27	0.832	
		1.00	18.12	0.791	
		0.56	14.46	0.716	
		0.32	12.09	0.631	
		0.18	10.38	0.533	
		0.10	9.11	0.428	
70	158.0	17.80	38.79	0.849	-0.6
		10.00	29.58	0.846	
		5.60	22.48	0.827	
		3.20	17.57	0.782	
		1.80	14.05	0.708	
		1.00	11.57	0.615	
		0.56	9.93	0.502	
		0.32	8.88	0.402	
		0.18	8.15	0.307	

Table A.5: Complex modulus data for DM 8420 printed in the vertical direction and testing using the cantilevered configuration

Temperature [°C]	[°F]	**Frequency** [Hz]	**Storage Modulus** [MPa]	**Loss Factor** [-]	**Shift Factor** $\log[\alpha(T)]$
		0.10	7.62	0.224	
75	167.0	17.80	22.72	0.802	-1.2
		10.00	17.86	0.755	
		5.60	14.16	0.689	
		3.20	11.72	0.600	
		1.80	10.01	0.496	
		1.00	8.86	0.389	
		0.56	8.11	0.291	
		0.32	7.64	0.214	
		0.18	7.32	0.153	
		0.10	7.13	0.102	
80	176.0	17.80	14.70	0.648	-1.8
		10.00	12.26	0.562	
		5.60	10.34	0.475	
		3.20	9.11	0.382	
		1.80	8.28	0.291	
		1.00	7.73	0.211	
		0.56	7.39	0.147	
		0.32	7.19	0.101	
		0.18	7.06	0.066	
		0.10	6.97	0.045	
85	185.0	17.80	10.76	0.417	-2.3
		10.00	9.63	0.337	
		5.60	8.58	0.268	
		3.20	7.95	0.205	
		1.80	7.55	0.147	
		1.00	7.30	0.101	
		0.56	7.14	0.065	
		0.32	7.06	0.042	
		0.18	7.00	0.025	
		0.10	6.95	0.012	
90	194.0	17.80	8.90	0.190	-2.9
		10.00	8.38	0.151	
		5.60	7.80	0.117	
		3.20	7.47	0.088	
		1.80	7.27	0.060	
		1.00	7.16	0.041	
		0.56	7.09	0.023	
		0.32	7.05	0.013	
		0.18	7.03	0.005	

Table A.5: Complex modulus data for DM 8420 printed in the vertical direction and testing using the cantilevered configuration

Temperature [°C]	[°F]	**Frequency** [Hz]	**Storage Modulus** [MPa]	**Loss Factor** [-]	**Shift Factor** $\log[\alpha(T)]$
		0.10	7.03	0.001	

A.2 Various 3D printed materials comparison

This section provides additional details for the DMA testing preformed in Section 3.2.2.1 where four different materials are compared. These materials are described in Table 3.1. The tensile configuration was used for testing all these materials the specimen have approximate dimensions of 9 mm × 5 mm × 1 mm. The complex modulus data is presented in the following sections. The Wicket plots for these four specimens is shown in Figure 3.4. The results of the temperature-frequency equivalence are plotted in Figure 3.6. The plots of the Arrhenius relationship is shown in Figure 3.5 and the parameters are given in Table 3.3.

A.2.1 Results for VeroWhitePlus

The VeroWhitePlus specimen was tested at temperatures between 0° and 100° C. The complex modulus data is summarized in Table A.6 including the shift factor relationship determined from the frequency-temperature analysis.

Table A.6: Complex modulus data for VeroWhitePlus

Temperature [°C]	[°F]	**Frequency** [Hz]	**Storage Modulus** [MPa]	**Loss Factor** [-]	**Shift Factor** $\log[\alpha(T)]$
0	32.0	21.50	2384.66	0.047	10.3
		10.00	2342.76	0.049	
		4.60	2322.34	0.050	
		2.20	2292.68	0.053	
		1.00	2248.75	0.057	
		0.46	2239.56	0.059	
		0.22	2208.62	0.062	
		0.10	2156.95	0.070	

Table A.6: Complex modulus data for VeroWhitePlus

Temperature [°**C**]	[°**F**]	**Frequency** [**Hz**]	**Storage Modulus** [**MPa**]	**Loss Factor** [**-**]	**Shift Factor** $\log[\alpha(T)]$
10	50.0	21.50	2281.23	0.053	9.1
		10.00	2235.47	0.056	
		4.60	2180.45	0.060	
		2.20	2121.15	0.065	
		1.00	2058.12	0.072	
		0.46	1964.55	0.081	
		0.22	1890.84	0.089	
		0.10	1818.17	0.095	
20	68.0	21.50	1969.47	0.076	7.5
		10.00	1909.80	0.082	
		4.60	1842.74	0.088	
		2.20	1773.41	0.095	
		1.00	1698.60	0.102	
		0.46	1593.90	0.115	
		0.22	1508.43	0.125	
		0.10	1432.96	0.134	
30	86.0	21.50	1569.42	0.114	5.7
		10.00	1492.38	0.123	
		4.60	1408.94	0.133	
		2.20	1330.00	0.144	
		1.00	1238.02	0.158	
		0.46	1136.25	0.172	
		0.22	1051.03	0.188	
		0.10	962.66	0.207	
40	104.0	21.50	1055.33	0.193	3.6
		10.00	961.30	0.213	
		4.60	861.61	0.237	
		2.20	773.71	0.260	
		1.00	676.98	0.289	
		0.46	595.90	0.322	
		0.22	496.55	0.368	
		0.10	412.04	0.422	
50	122.0	21.50	529.97	0.362	1.7
		10.00	443.30	0.410	
		4.60	356.27	0.471	
		2.20	279.87	0.535	
		1.00	208.33	0.622	
		0.46	167.85	0.667	
		0.22	126.17	0.742	
		0.10	86.81	0.835	
60	140.0	21.50	201.26	0.665	0.0

Table A.6: Complex modulus data for VeroWhitePlus

Temperature [°**C**]	[°**F**]	**Frequency** [**Hz**]	**Storage Modulus** [**MPa**]	**Loss Factor** [**-**]	**Shift Factor** $\log[\alpha(T)]$
		10.00	143.10	0.761	
		4.60	97.01	0.861	
		2.20	64.71	0.944	
		1.00	42.76	0.944	
		0.46	28.57	0.983	
		0.22	20.68	0.917	
		0.10	14.76	0.832	
70	158.0	21.50	51.23	1.023	-1.2
		10.00	33.33	1.046	
		4.60	22.11	0.993	
		2.20	15.92	0.859	
		1.00	12.30	0.669	
		0.46	10.15	0.484	
		0.22	9.05	0.338	
		0.10	8.31	0.214	
80	176.0	21.50	16.55	0.839	-2.3
		10.00	12.59	0.674	
		4.60	10.34	0.479	
		2.20	9.17	0.321	
		1.00	8.46	0.196	
		0.46	8.14	0.115	
		0.22	7.96	0.067	
		0.10	7.86	0.036	
90	194.0	21.50	10.46	0.365	-3.2
		10.00	9.25	0.249	
		4.60	8.58	0.148	
		2.20	8.31	0.085	
		1.00	8.17	0.046	
		0.46	8.13	0.024	
		0.22	8.10	0.013	
		0.10	8.08	0.007	
100	212.0	21.50	9.41	0.130	-3.8
		10.00	8.79	0.085	
		4.60	8.51	0.045	
		2.20	8.42	0.024	
		1.00	8.39	0.013	
		0.46	8.38	0.007	
		0.22	8.37	0.004	
		0.10	8.36	0.002	

A.2.2 Results for DM 8420

The DM 8420 specimen was tested at temperatures between 0° and 100° C. The complex modulus data is summarized in Table A.7 including the shift factor relationship determined from the frequency-temperature analysis

Table A.7: Complex modulus data for DM 8420

Temperature		**Frequency**	**Storage Modulus**	**Loss Factor**	**Shift Factor**
[°C]	**[°F]**	**[Hz]**	**[MPa]**	**[-]**	$\log[\alpha(T)]$
0	32.0	21.50	1576.09	0.083	9.1
		10.00	1529.75	0.088	
		4.60	1504.81	0.091	
		2.20	1481.40	0.095	
		1.00	1427.35	0.103	
		0.46	1432.05	0.103	
		0.22	1402.53	0.108	
		0.10	1342.69	0.116	
10	50.0	21.50	1503.99	0.090	8.0
		10.00	1449.15	0.097	
		4.60	1385.34	0.105	
		2.20	1318.21	0.115	
		1.00	1252.17	0.124	
		0.46	1142.88	0.141	
		0.22	1068.90	0.154	
		0.10	999.41	0.168	
20	68.0	21.50	1168.85	0.132	6.5
		10.00	1101.87	0.143	
		4.60	1029.63	0.156	
		2.20	956.23	0.169	
		1.00	880.04	0.189	
		0.46	781.66	0.205	
		0.22	714.97	0.221	
		0.10	647.62	0.242	
30	86.0	21.50	801.07	0.209	4.8
		10.00	723.85	0.230	
		4.60	648.89	0.253	
		2.20	575.70	0.277	
		1.00	499.44	0.310	
		0.46	422.42	0.343	
		0.22	369.25	0.371	
		0.10	308.42	0.400	
40	104.0	21.50	411.47	0.377	2.9

Table A.7: Complex modulus data for DM 8420

Temperature [°C]	[°F]	**Frequency** [Hz]	**Storage Modulus** [MPa]	**Loss Factor** [-]	**Shift Factor** $\log[\alpha(T)]$
		10.00	340.78	0.421	
		4.60	277.91	0.468	
		2.20	227.62	0.515	
		1.00	175.59	0.565	
		0.46	141.40	0.619	
		0.22	106.91	0.671	
		0.10	79.94	0.720	
50	122.0	21.50	160.54	0.641	1.2
		10.00	117.43	0.711	
		4.60	82.17	0.795	
		2.20	57.22	0.869	
		1.00	39.62	0.904	
		0.46	30.11	0.933	
		0.22	22.35	0.926	
		0.10	15.87	0.883	
60	140.0	21.50	53.13	0.925	0.0
		10.00	35.18	0.973	
		4.60	23.00	0.999	
		2.20	16.09	0.942	
		1.00	11.83	0.785	
		0.46	9.42	0.678	
		0.22	8.11	0.542	
		0.10	7.02	0.382	
70	158.0	21.50	18.87	0.978	-0.8
		10.00	13.20	0.892	
		4.60	9.91	0.715	
		2.20	8.16	0.535	
		1.00	7.04	0.366	
		0.46	6.53	0.241	
		0.22	6.23	0.161	
		0.10	6.01	0.099	
80	176.0	21.50	10.00	0.616	-1.6
		10.00	8.13	0.462	
		4.60	7.06	0.309	
		2.20	6.56	0.196	
		1.00	6.28	0.112	
		0.46	6.15	0.067	
		0.22	6.09	0.040	
		0.10	6.06	0.022	
90	194.0	21.50	7.79	0.261	-2.4
		10.00	6.93	0.182	

Table A.7: Complex modulus data for DM 8420

Temperature [°C]	[°F]	**Frequency** [Hz]	**Storage Modulus** [MPa]	**Loss Factor** [-]	**Shift Factor** $\log[\alpha(T)]$
		4.60	6.51	0.106	
		2.20	6.36	0.060	
		1.00	6.30	0.030	
		0.46	6.26	0.017	
		0.22	6.25	0.010	
		0.10	6.24	0.005	
100	212.0	21.50	7.36	0.093	-2.9
		10.00	6.81	0.071	
		4.60	6.56	0.037	
		2.20	6.50	0.020	
		1.00	6.49	0.011	
		0.46	6.47	0.006	
		0.22	6.46	0.004	
		0.10	6.46	0.002	

A.2.3 Results for DM 8430

The DM 8430 specimen was tested at temperatures between 0° and 100° C. The complex modulus data is summarized in Table A.8 including the shift factor relationship determined from the frequency-temperature analysis

Table A.8: Complex modulus data for DM 8430

Temperature [°C]	[°F]	**Frequency** [Hz]	**Storage Modulus** [MPa]	**Loss Factor** [-]	**Shift Factor** $\log[\alpha(T)]$
0	32.0	21.50	1739.90	0.114	8.5
		10.00	1680.76	0.120	
		4.60	1653.61	0.125	
		2.20	1628.34	0.128	
		1.00	1565.48	0.136	
		0.46	1587.35	0.136	
		0.22	1567.62	0.139	
		0.10	1501.24	0.146	
10	50.0	21.50	1728.68	0.113	7.8
		10.00	1659.79	0.122	
		4.60	1579.88	0.132	
		2.20	1499.57	0.141	
		1.00	1419.34	0.149	

Table A.8: Complex modulus data for DM 8430

Temperature [°**C**]	[°**F**]	**Frequency** [**Hz**]	**Storage Modulus** [**MPa**]	**Loss Factor** [**-**]	**Shift Factor** $\log[\alpha(T)]$
		0.46	1309.42	0.164	
		0.22	1230.43	0.175	
		0.10	1158.88	0.183	
20	68.0	21.50	1349.30	0.150	6.3
		10.00	1272.60	0.162	
		4.60	1191.36	0.174	
		2.20	1111.75	0.186	
		1.00	1027.38	0.198	
		0.46	926.46	0.218	
		0.22	845.36	0.234	
		0.10	766.70	0.248	
30	86.0	21.50	927.03	0.215	4.6
		10.00	844.37	0.235	
		4.60	764.68	0.254	
		2.20	686.74	0.275	
		1.00	602.08	0.306	
		0.46	520.47	0.334	
		0.22	463.97	0.358	
		0.10	397.66	0.395	
40	104.0	21.50	515.56	0.351	2.8
		10.00	436.51	0.392	
		4.60	366.69	0.434	
		2.20	306.63	0.479	
		1.00	242.60	0.529	
		0.46	200.54	0.594	
		0.22	151.43	0.645	
		0.10	109.72	0.752	
50	122.0	21.50	222.59	0.599	1.2
		10.00	164.83	0.689	
		4.60	116.65	0.770	
		2.20	82.99	0.851	
		1.00	57.09	0.906	
		0.46	41.32	0.954	
		0.22	30.03	0.962	
		0.10	20.85	0.935	
60	140.0	21.50	71.67	0.926	0.0
		10.00	47.20	0.989	
		4.60	30.32	1.036	
		2.20	20.83	0.991	
		1.00	15.04	0.852	
		0.46	11.61	0.724	

Table A.8: Complex modulus data for DM 8430

Temperature [°C]	[°F]	**Frequency** [Hz]	**Storage Modulus** [MPa]	**Loss Factor** [-]	**Shift Factor** $\log[\alpha(T)]$
		0.22	9.89	0.585	
		0.10	8.50	0.420	
70	158.0	21.50	23.66	1.023	-1.0
		10.00	16.49	0.919	
		4.60	12.13	0.758	
		2.20	9.86	0.571	
		1.00	8.48	0.384	
		0.46	7.75	0.260	
		0.22	7.36	0.173	
		0.10	7.07	0.102	
80	176.0	21.50	11.74	0.650	-1.9
		10.00	9.51	0.489	
		4.60	8.26	0.327	
		2.20	7.64	0.208	
		1.00	7.29	0.126	
		0.46	7.11	0.070	
		0.22	7.03	0.042	
		0.10	6.97	0.023	
90	194.0	21.50	8.90	0.284	-2.6
		10.00	7.96	0.192	
		4.60	7.49	0.112	
		2.20	7.32	0.064	
		1.00	7.24	0.033	
		0.46	7.20	0.018	
		0.22	7.18	0.010	
		0.10	7.17	0.006	
100	212.0	21.50	8.31	0.103	-3.2
		10.00	7.72	0.073	
		4.60	7.53	0.038	
		2.20	7.46	0.020	
		1.00	7.42	0.011	
		0.46	7.42	0.006	
		0.22	7.41	0.004	
		0.10	7.40	0.002	

A.2.4 Results for TangoPlus

The TangoPlus specimen was tested at temperatures between -40° and 60° C. The complex modulus data is summarized in Table A.9 including the shift factor relationship deter-

mined from the frequency-temperature analysis

Table A.9: Complex modulus data for TangoPlus

Temperature [°C]	[°F]	**Frequency** [Hz]	**Storage Modulus** [MPa]	**Loss Factor** [-]	**Shift Factor** $\log[\alpha(T)]$
-40	-40.0	10.00	1313.93	0.088	10.5
		4.60	1314.24	0.088	
		2.20	1303.20	0.090	
		1.00	1254.05	0.098	
		0.46	1262.37	0.099	
		0.22	1241.47	0.105	
		0.10	1183.27	0.120	
-30	-22.0	10.00	1158.59	0.107	9.1
		4.60	1086.65	0.120	
		2.20	1009.17	0.136	
		1.00	933.87	0.152	
		0.46	809.61	0.185	
		0.22	739.17	0.207	
		0.10	660.49	0.241	
-20	-4.0	10.00	690.53	0.205	7.2
		4.60	589.39	0.244	
		2.20	494.40	0.289	
		1.00	420.36	0.329	
		0.46	308.93	0.424	
		0.22	253.26	0.487	
		0.10	192.65	0.583	
-10	14.0	10.00	233.83	0.486	5.5
		4.60	177.90	0.601	
		2.20	117.50	0.805	
		1.00	78.31	0.978	
		0.46	56.98	1.185	
		0.22	39.17	1.276	
		0.10	21.67	1.523	
0	32.0	10.00	58.50	1.147	4.1
		4.60	31.56	1.537	
		2.20	16.87	1.745	
		1.00	8.49	1.959	
		0.46	4.34	2.023	
		0.22	2.79	1.892	
		0.10	1.86	1.585	
10	50.0	10.00	7.30	2.030	2.9
		4.60	4.03	1.968	
		2.20	2.47	1.663	

Table A.9: Complex modulus data for TangoPlus

Temperature [°C]	[°F]	**Frequency** [Hz]	**Storage Modulus** [MPa]	**Loss Factor** [-]	**Shift Factor** $\log[\alpha(T)]$
		1.00	1.77	1.230	
		0.46	1.19	0.925	
		0.22	0.98	0.708	
		0.10	0.83	0.529	
20	68.0	10.00	2.22	1.181	2.0
		4.60	1.45	1.014	
		2.20	1.11	0.775	
		1.00	0.90	0.557	
		0.46	0.76	0.378	
		0.22	0.69	0.260	
		0.10	0.64	0.166	
30	86.0	10.00	1.28	0.622	1.0
		4.60	0.93	0.513	
		2.20	0.78	0.377	
		1.00	0.70	0.251	
		0.46	0.65	0.155	
		0.22	0.62	0.101	
		0.10	0.61	0.059	
40	104.0	10.00	1.04	0.367	0.5
		4.60	0.77	0.274	
		2.20	0.69	0.183	
		1.00	0.65	0.112	
		0.46	0.63	0.067	
		0.22	0.62	0.041	
		0.10	0.61	0.021	
50	122.0	10.00	0.97	0.258	0.2
		4.60	0.73	0.166	
		2.20	0.67	0.099	
		1.00	0.65	0.053	
		0.46	0.64	0.032	
		0.22	0.64	0.018	
		0.10	0.63	0.008	
60	140.0	10.00	0.96	0.156	0.0
		4.60	0.73	0.118	
		2.20	0.68	0.067	
		1.00	0.66	0.032	
		0.46	0.66	0.017	
		0.22	0.65	0.008	
		0.10	0.65	0.003	

APPENDIX B

Golla-Hughes-McTavish (GHM) Model Parameters

This appendix presents the GHM parameters used for simulations in this dissertation. The GHM model approximates the material dissipation function as

$$s\tilde{G}(s) = G^{\infty}\left[1 + \sum_{j=1}^{n_{\mathrm{MOT}}} \hat{\alpha}_i \frac{s^2 + 2\hat{\zeta}_i\hat{\omega}_i s}{s^2 + 2\hat{\zeta}_i\hat{\omega}_i s + \hat{\omega}_i^2}\right] \tag{B.1}$$

where G^{∞}, $\hat{\alpha}_i$, $\hat{\zeta}_i$, and $\hat{\omega}_i$ are all parameters of the model and n_{MOT} represents the number of mini-oscillator terms and is chosen based on the desired accuracy of the model. Equation B.1 is evaluated along the imaginary axis ($s = \jmath\omega$) and curve fit to the experimental data over a frequency range. The curve fit is performed by optimizing the error fit for both the complex and the imaginary parts using an equal weighting. For each of the testing scenarios presented in Appendix A, a GHM fit is performed over the frequency range of 10 to 2,000 Hz at various temperatures. The number of terms, n in the GHM approximation depends on accuracy of the fit and ranges from $n = 3$ to $n = 5$ in this dissertation. For each temperature, the data is shifted on the reduced frequency scale using the procedure described in Section 3.3.3. This converts the reduced frequency to the frequency values for a specific temperatures. The temperatures used for the GHM fits, range the data set.

Table B.1: GHM parameters for DM 8420 printed in the horizontal direction and testing using the tensile configuration

Temperature	G^{∞} **[Pa]**	i	$\hat{\alpha}_i$ **[-]**	$\hat{\omega}_i$ **[rad/s]**	$\hat{\zeta}_i$ **[-]**
40° C	9.58e+03	1	2.70e+04	7.49e+05	1.33e+03
		2	8.37e+04	4.34e+04	1.38e+03
		3	2.47e+04	7.68e+05	2.10e+02
		4	3.58e+04	3.93e+06	1.64e+02
50° C	1.31e+05	1	3.08e+03	5.11e+04	1.34e+03
		2	1.94e+03	4.47e+06	1.31e+03
		3	1.93e+03	6.44e+05	1.38e+03
		4	2.46e+03	3.26e+07	1.45e+03
60° C	1.12e+08	1	1.66e+00	2.16e+05	6.17e+02
		2	2.10e+00	9.02e+06	1.32e+03
		3	1.27e+00	2.74e+06	1.54e+03
		4	1.92e+03	3.43e+07	8.78e-01
70° C	2.76e+07	1	1.90e+00	3.46e+05	1.41e+03
		2	5.94e+00	6.46e+06	1.21e+03
		3	2.86e+00	1.36e+06	1.26e+03
		4	1.13e+01	2.91e+07	7.74e+02
80° C	1.26e+07	1	9.07e-01	3.29e+05	1.27e+03
		2	4.85e+00	6.03e+06	1.31e+03
		3	1.88e+00	1.45e+06	1.42e+03
		4	1.61e+01	1.93e+07	6.92e+02
90° C	8.12e+06	1	3.00e-01	2.54e+05	1.02e+03
		2	1.81e+00	5.51e+06	1.44e+03
		3	5.68e-01	1.17e+06	1.60e+03
		4	1.16e+01	9.24e+06	3.44e+02
100° C	7.19e+06	1	7.91e-02	3.53e+05	1.69e+03
		2	7.65e-01	2.67e+06	5.38e+02
		3	1.78e-01	4.79e+05	3.40e+02
		4	6.85e+00	2.65e+07	4.67e+02
110° C	7.13e+06	1	7.67e-02	7.49e+05	5.24e+02
		2	5.99e-03	2.87e+07	1.50e+02
		3	1.27e-01	1.11e+07	1.39e+03
		4	2.01e+00	2.88e+07	6.14e+02

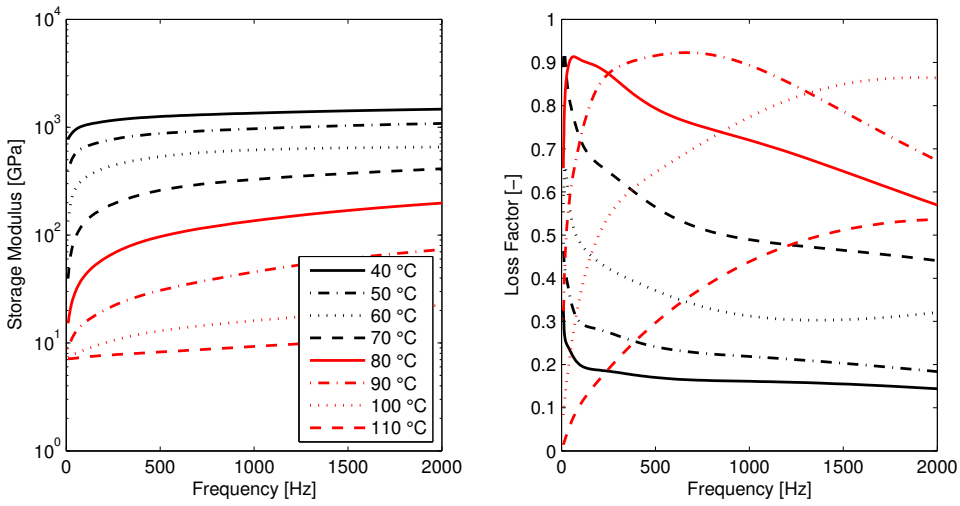

Figure B.1: GHM fit for DM 8420 printed in the horizontal direction and testing using the tensile configuration

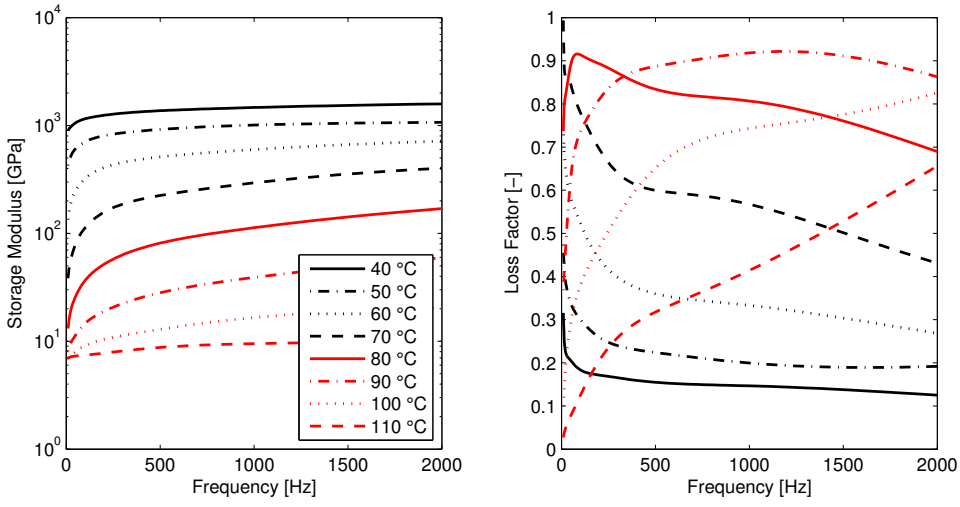

Figure B.2: GHM fit for DM 8420 printed in the vertical direction and testing using the tensile configuration

Table B.2: GHM parameters for DM 8420 printed in the vertical direction and testing using the tensile configuration

Temperature	G^{∞} **[Pa]**	i	$\hat{\alpha}_i$ **[-]**	$\hat{\omega}_i$ **[rad/s]**	$\hat{\zeta}_i$ **[-]**
40° C	3.16e+04	1	2.78e+04	6.40e+01	2.11e+00
		2	7.03e+03	7.75e+05	2.24e+02
		3	9.47e+03	4.38e+05	7.12e+02
		4	1.04e+04	7.51e+06	3.56e+02
50° C	3.14e+05	1	1.42e+03	5.26e+04	1.36e+03
		2	7.02e+02	8.74e+05	5.41e+02
		3	6.05e+02	6.85e+05	1.76e+03
		4	7.34e+02	1.11e+07	1.27e+03
		5	3.68e+03	3.29e+07	1.34e+02
60° C	4.04e+04	1	2.51e+03	4.64e+05	1.43e+03
		2	4.22e+03	2.71e+06	1.97e+03
		3	3.37e+03	1.30e+04	2.75e+02
		4	2.93e+03	3.56e+06	9.17e+02
		5	8.20e+03	1.16e+07	5.43e+02
70° C	7.25e+03	1	6.63e+03	8.38e+04	1.16e+03
		2	1.59e+04	3.51e+06	1.29e+03
		3	7.55e+03	7.95e+05	1.22e+03
		4	4.44e+04	2.29e+07	1.06e+03
80° C	9.64e+06	1	1.20e+00	2.63e+05	1.30e+03
		2	5.01e+00	4.67e+06	9.77e+02
		3	2.37e+00	1.77e+06	1.50e+03
		4	2.32e+01	2.76e+07	8.12e+02
90° C	6.61e+06	1	4.45e-01	1.53e+05	1.14e+03
		2	1.68e+01	3.10e+07	6.82e+02
		3	1.19e+00	9.63e+05	8.34e+02
		4	2.55e+00	9.19e+06	1.55e+03
100° C	6.86e+06	1	1.92e-01	5.12e+05	1.08e+03
		2	4.64e+02	3.42e+07	4.96e+00
		3	1.79e+00	1.39e+07	1.04e+03
		4	3.89e-01	2.72e+06	1.61e+03
110° C	7.02e+06	1	4.69e-02	4.43e+05	1.27e+03
		2	3.70e-01	1.00e+07	1.75e+03
		3	1.84e+00	4.56e+07	1.80e+01
		4	1.32e+02	2.76e+07	6.84e+00

Table B.3: GHM parameters for DM 8420 printed in the horizontal direction and testing using the cantilevered configuration

Temperature	G^{∞} **[Pa]**	i	$\hat{\alpha}_i$ **[-]**	$\hat{\omega}_i$ **[rad/s]**	$\hat{\zeta}_i$ **[-]**
50° C	1.03e+05	1	3.22e+03	6.24e+04	1.32e+03
		2	2.28e+03	4.53e+06	1.33e+03
		3	2.02e+03	8.14e+05	1.41e+03
		4	3.46e+03	3.32e+07	1.41e+03
60° C	6.88e+07	1	1.49e+00	3.53e+05	1.20e+03
		2	3.23e+00	4.56e+06	5.16e+02
		3	1.97e+00	2.22e+06	1.45e+03
		4	4.46e+02	3.31e+07	5.28e+00
70° C	1.66e+07	1	1.28e+00	1.83e+03	9.75e+00
		2	4.31e+00	4.07e+05	9.80e+01
		3	2.28e+00	1.25e+05	1.31e+02
		4	1.39e+01	2.67e+07	1.02e+03
80° C	8.97e+06	1	7.11e-01	4.07e+05	1.38e+03
		2	2.93e+00	4.69e+06	6.08e+02
		3	1.36e+00	2.63e+06	1.53e+03
		4	1.39e+01	2.84e+07	5.44e+02
90° C	7.17e+06	1	1.64e-01	3.42e+05	1.23e+03
		2	8.09e-01	5.37e+06	1.02e+03
		3	5.35e+00	3.30e+06	6.95e+01
		4	2.23e-01	2.07e+06	1.65e+03
100° C	7.11e+06	1	2.94e-02	1.09e+06	1.07e+03
		2	2.30e+00	1.80e+06	1.74e+01
		3	1.13e-01	5.29e+06	1.44e+03
		4	2.00e-01	6.82e+06	6.17e+02

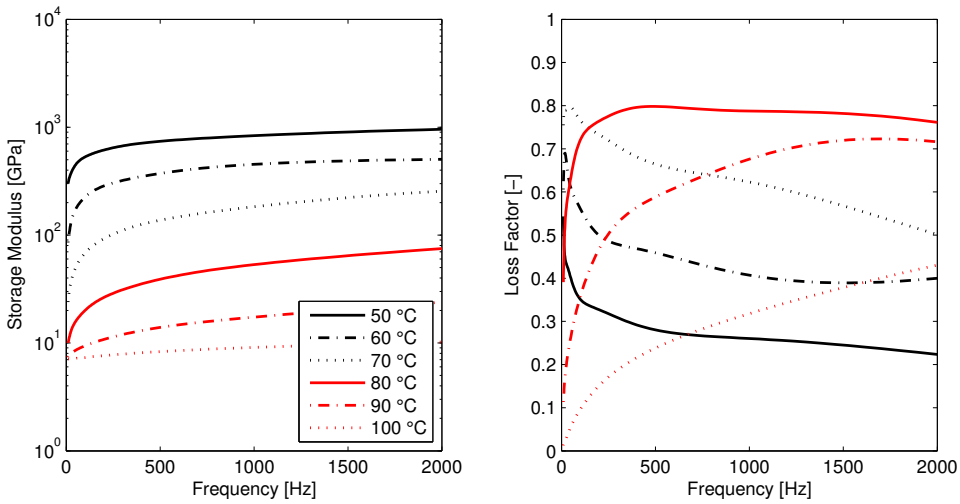

Figure B.3: GHM fit for DM 8420 printed in the horizontal direction and testing using the cantilevered configuration

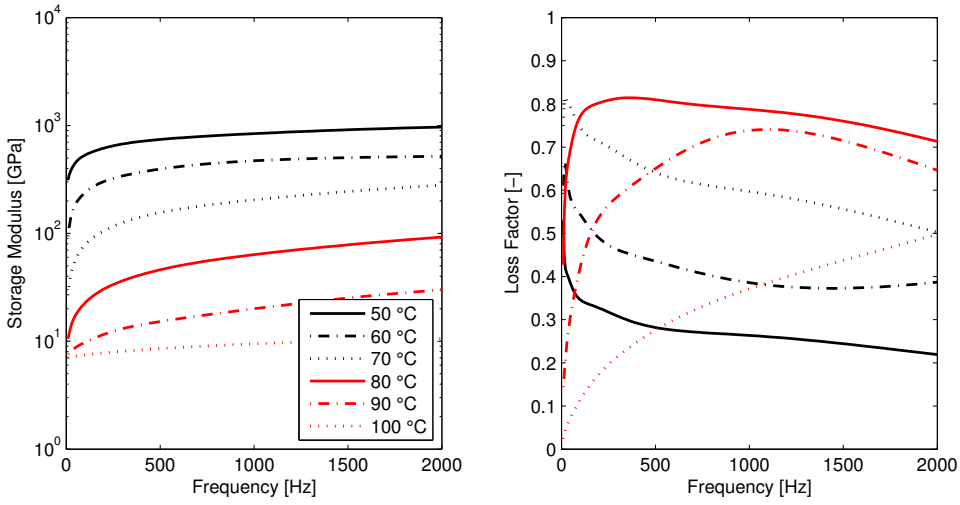

Figure B.4: GHM fit for DM 8420 printed in the vertical direction and testing using the cantilevered configuration

Table B.4: GHM parameters for DM 8420 printed in the vertical direction and testing using the cantilevered configuration

Temperature	G^{∞} **[Pa]**	i	$\hat{\alpha}_i$ **[-]**	$\hat{\omega}_i$ **[rad/s]**	$\hat{\zeta}_i$ **[-]**
50° C	1.28e+05	1	2.69e+03	6.31e+04	1.32e+03
		2	1.82e+03	4.25e+06	1.34e+03
		3	1.44e+03	8.25e+05	1.45e+03
		4	2.81e+03	3.07e+07	1.42e+03
60° C	7.53e+07	1	1.51e+00	3.80e+05	1.30e+03
		2	2.76e+00	3.52e+06	4.06e+02
		3	1.91e+00	2.51e+06	1.47e+03
		4	4.21e+03	2.77e+07	4.36e-01
70° C	1.98e+07	1	1.30e+00	3.58e+03	1.59e+01
		2	4.40e+00	7.37e+04	1.63e+01
		3	2.19e+00	3.74e+04	3.85e+01
		4	1.26e+01	2.81e+06	9.65e+01
80° C	9.48e+06	1	8.12e-01	5.37e+05	1.64e+03
		2	2.95e+00	3.33e+06	4.91e+02
		3	1.46e+00	1.77e+06	1.04e+03
		4	1.37e+01	2.65e+07	6.45e+02
90° C	5.57e+04	1	1.34e+02	5.26e+03	9.89e+02
		2	2.98e+01	7.58e+05	1.52e+03
		3	1.03e+02	4.55e+06	1.44e+03
		4	6.85e+02	2.82e+07	9.15e+02
100° C	7.03e+06	1	4.27e-02	7.03e+05	1.71e+03
		2	1.23e-01	1.40e+06	4.93e+02
		3	4.57e+00	1.35e+07	7.24e+01
		4	3.33e-01	1.15e+06	9.13e+01

Table B.5: GHM parameters for VeroWhitePlus

Temperature	G^{∞} **[Pa]**	i	$\hat{\alpha}_i$ **[-]**	$\hat{\omega}_i$ **[rad/s]**	$\hat{\zeta}_i$ **[-]**
20° C	1.78e+04	1	1.31e+04	1.74e+06	2.14e+02
		2	1.44e+04	1.56e+05	8.65e+02
		3	9.70e+03	5.93e+05	5.06e+02
		4	8.95e+04	2.00e+03	8.77e+02
30° C	1.46e+04	1	1.36e+04	4.59e+05	7.69e+02
		2	3.34e+04	1.29e+07	2.48e+02
		3	8.94e+03	1.84e+06	8.26e+02
		4	8.99e+04	2.72e+04	1.32e+03
		5	7.42e+03	2.83e+06	4.88e+02
40° C	2.15e+05	1	1.18e+03	8.80e+05	9.98e+02
		2	7.50e+02	7.29e+04	1.71e+03
		3	3.36e+03	4.08e+04	1.46e+03
		4	8.51e+02	4.82e+06	1.18e+03
		5	2.62e+02	7.35e+06	1.40e+03
		6	4.22e+04	2.98e+07	2.38e+01
50° C	8.08e+05	1	5.12e+02	1.18e+04	2.85e+02
		2	3.61e+02	2.59e+06	9.55e+02
		3	2.61e+02	2.75e+05	6.03e+02
		4	1.71e+03	4.38e+07	4.36e+02
60° C	7.02e+04	1	7.82e+02	7.05e+03	1.15e+02
		2	2.38e+03	8.25e+05	1.20e+03
		3	1.42e+03	7.31e+03	1.20e+02
		4	4.24e+03	3.38e+06	7.82e+02
		5	9.90e+04	3.87e+07	5.58e+01
70° C	4.84e+03	1	9.83e+03	8.73e+04	1.16e+03
		2	2.21e+04	6.87e+06	1.31e+03
		3	1.70e+04	1.63e+06	1.34e+03
		4	6.99e+04	2.48e+07	9.33e+02
80° C	1.07e+07	1	8.93e-01	4.39e+05	1.48e+03
		2	1.65e+01	2.86e+07	8.19e+02
		3	3.18e+00	2.80e+06	9.04e+02
90° C	8.51e+06	1	1.49e-01	6.85e+05	1.21e+03
		2	5.86e-01	1.60e+06	6.20e+02
		3	5.07e+00	3.72e+07	1.00e+03
100° C	8.03e+06	1	7.05e-02	3.13e+05	2.28e+02
		2	3.52e+00	3.64e+07	3.72e+01
		3	6.53e-01	2.40e+06	1.05e+02
		4	1.64e+00	3.66e+07	6.54e+01

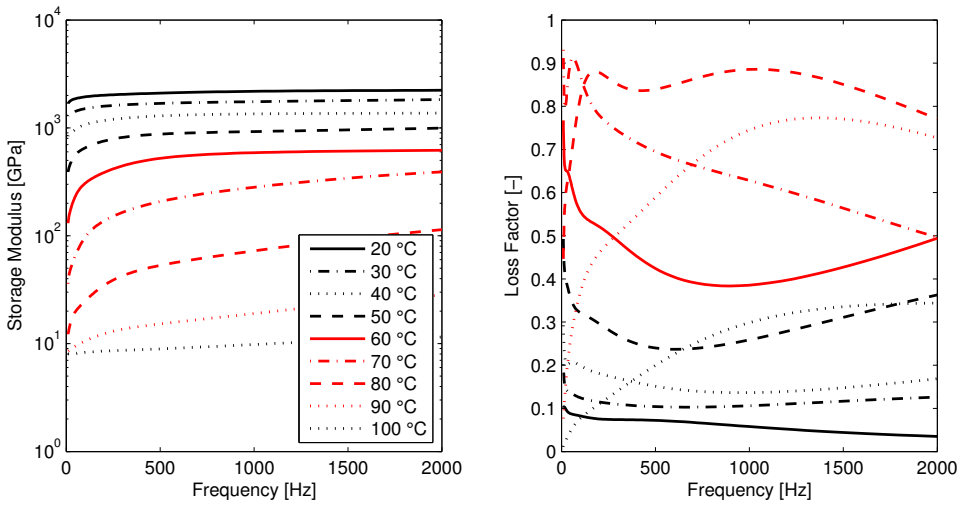

Figure B.5: GHM fit for VeroWhitePlus

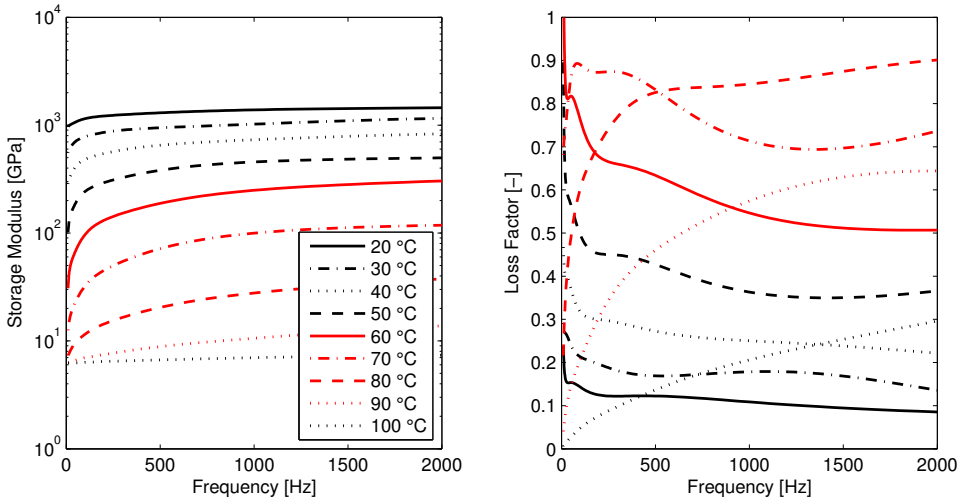

Figure B.6: GHM fit for DM 8430

Table B.6: GHM parameters for DM 8430

Temperature	G^{∞} **[Pa]**	i	$\hat{\alpha}_i$ **[-]**	$\hat{\omega}_i$ **[rad/s]**	$\hat{\zeta}_i$ **[-]**
20° C	2.14e+06	1	4.65e+02	3.81e+04	1.48e+03
		2	5.29e+01	6.86e+06	1.56e+02
		3	1.04e+02	1.42e+07	1.72e+03
		4	1.05e+02	6.34e+03	6.88e+00
30° C	6.86e+06	1	7.94e+01	2.86e+03	1.30e+02
		2	2.90e+01	8.56e+02	2.15e+00
		3	2.88e+01	8.56e+04	3.35e+01
		4	3.13e+01	1.29e+04	8.06e-01
40° C	4.50e+04	1	4.42e+03	9.47e+05	1.65e+03
		2	4.45e+03	2.60e+06	6.20e+02
		3	6.70e+03	4.98e+04	1.29e+03
		4	6.55e+03	3.37e+07	1.26e+03
50° C	5.83e+05	1	2.48e+02	5.60e+04	6.49e+02
		2	3.86e+02	5.28e+06	7.61e+02
		3	2.36e+02	6.70e+05	7.44e+02
		4	3.90e+03	3.89e+07	8.12e+01
60° C	6.53e+03	1	8.05e+03	8.43e+02	7.71e+00
		2	1.26e+04	1.57e+06	1.24e+03
		3	5.35e+03	1.29e+07	1.68e+02
		4	2.44e+04	2.44e+06	2.81e+02
		5	5.68e+04	4.91e+07	5.06e+02
70° C	8.88e+06	1	1.09e+00	2.35e+05	1.37e+03
		2	9.22e+00	6.87e+06	8.02e+02
		3	2.85e+00	2.40e+06	1.84e+03
		4	4.21e+02	4.20e+07	2.71e+01
80° C	6.98e+06	1	3.44e-01	5.53e+05	1.64e+03
		2	2.36e+00	6.09e+06	7.11e+02
		3	7.20e-01	9.65e+05	6.12e+02
		4	1.50e+01	2.87e+06	3.39e+01
90° C	6.24e+06	1	1.24e-01	1.08e+06	1.60e+03
		2	1.70e+00	1.90e+07	5.51e+02
		3	4.13e-01	6.42e+06	1.18e+03
		4	2.77e+00	2.90e+07	2.28e+02
100° C	6.24e+06	1	4.51e-02	3.11e+06	1.51e+03
		2	1.76e+00	4.17e+07	1.19e+01
		3	1.84e-01	1.70e+07	1.15e+03
		4	6.20e+01	2.62e+07	4.27e+00

Table B.7: GHM parameters for DM 8420

Temperature	G^{∞} **[Pa]**	i	$\hat{\alpha}_i$ **[-]**	$\hat{\omega}_i$ **[rad/s]**	$\hat{\zeta}_i$ **[-]**
20° C	5.98e+04	1	5.95e+03	3.29e+07	4.56e+02
		2	5.10e+03	1.20e+07	1.53e+03
		3	4.51e+03	1.23e+06	1.33e+03
		4	1.92e+04	4.55e+04	1.49e+03
30° C	9.63e+03	1	2.55e+04	1.01e+06	1.25e+03
		2	3.10e+04	6.33e+06	1.02e+03
		3	7.79e+04	1.04e+03	2.69e+01
		4	5.59e+04	3.17e+06	3.75e+01
40° C	1.50e+05	1	1.10e+03	1.10e+06	1.75e+03
		2	4.90e+02	1.11e+06	1.79e+03
		3	2.65e+03	1.81e+04	4.73e+02
		4	1.89e+03	2.11e+06	4.31e+02
		5	4.21e+04	3.78e+07	4.73e+01
50° C	1.11e+08	1	1.61e+00	3.33e+03	1.11e+01
		2	3.60e+00	7.26e+06	3.49e+02
		3	1.98e+00	4.01e+06	1.67e+03
60° C	1.03e+04	1	7.44e+03	9.73e+04	8.68e+02
		2	1.94e+04	4.99e+06	7.08e+02
		3	1.05e+04	6.82e+05	5.72e+02
		4	7.96e+04	3.49e+07	2.43e+02
70° C	8.11e+06	1	1.99e+00	2.55e+05	1.90e+03
		2	1.55e+01	1.78e+07	1.78e+03
		3	5.13e+00	2.60e+06	1.95e+03
		4	6.06e+02	4.79e+07	3.11e+01
80° C	8.07e+06	1	5.08e-01	2.69e+05	9.21e+02
		2	3.55e+00	1.63e+07	7.56e+02
		3	1.86e+00	1.30e+06	5.13e+02
		4	1.08e+01	4.93e+07	1.20e+03
90° C	7.33e+06	1	2.44e-01	7.37e+05	8.98e+02
		2	1.92e+01	3.16e+07	7.21e+01
		3	9.44e+00	3.02e+07	1.41e+02
		4	6.90e-01	8.18e+06	1.53e+03
100° C	7.18e+06	1	4.58e-02	1.06e+06	1.53e+03
		2	1.21e+00	3.60e+07	1.29e+02
		3	3.16e-01	6.04e+06	5.95e+02
		4	9.88e+00	3.16e+07	2.33e+01
		5	7.95e+01	3.28e+07	2.73e+00

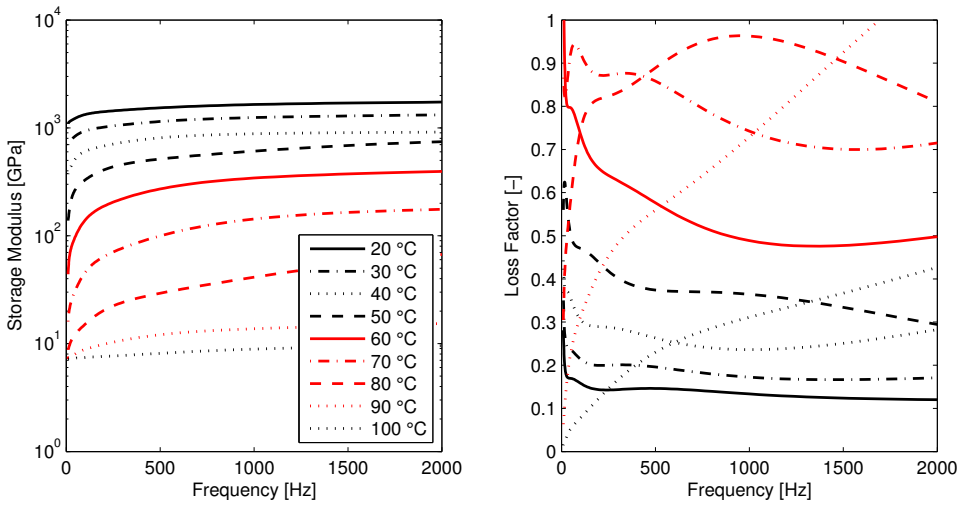

Figure B.7: GHM fit for DM 8420

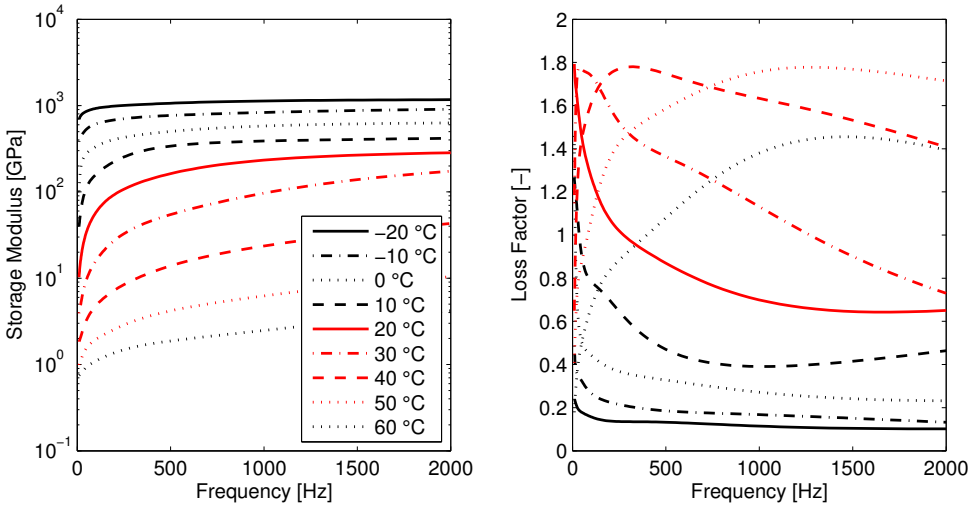

Figure B.8: GHM fit for TangoPlus

Table B.8: GHM parameters for TangoPlus

Temperature	G^{∞} **[Pa]**	i	$\hat{\alpha}_i$ **[-]**	$\hat{\omega}_i$ **[rad/s]**	$\hat{\zeta}_i$ **[-]**
-20° C	7.53e+03	1	2.54e+04	8.93e+06	1.21e+03
		2	2.82e+04	2.25e+05	1.36e+03
		3	5.81e+04	2.87e+07	1.58e+02
		4	8.10e+04	1.07e+04	1.32e+03
		5	2.18e+04	5.82e+04	5.98e+01
-10° C	5.49e+03	1	7.71e+04	6.17e+04	1.33e+03
		2	3.92e+04	8.47e+05	1.34e+03
		3	2.54e+04	4.14e+06	1.31e+03
		4	3.69e+04	2.81e+05	1.52e+01
° C	2.71e+04	1	1.01e+04	3.09e+04	1.88e+02
		2	7.80e+03	1.43e+07	1.65e+03
		3	6.09e+03	2.29e+06	1.43e+03
		4	4.05e+04	3.10e+07	7.76e+01
10° C	1.38e+04	1	7.69e+03	6.13e+05	1.28e+03
		2	1.87e+04	1.94e+05	5.36e+01
		3	2.80e+03	7.43e+04	1.34e+03
		4	8.66e+04	5.08e+06	2.68e+01
20° C	2.16e+06	1	4.70e+00	1.80e+05	1.86e+03
		2	3.29e+01	9.69e+03	4.87e+00
		3	1.11e+01	9.95e+02	2.06e+00
		4	9.13e+01	4.24e+05	4.49e+01
		5	5.39e+02	6.21e+06	9.06e+00
		6	1.17e+03	6.13e+06	6.93e+00
30° C	3.43e+06	1	2.42e+00	2.40e+05	4.43e+02
		2	7.15e+00	9.52e+05	1.56e+00
		3	9.72e+00	1.30e+05	4.27e+01
		4	7.10e+01	4.86e+05	2.05e+01
40° C	1.73e+06	1	1.35e+00	9.32e+05	1.55e+03
		2	8.05e+00	1.15e+07	1.40e+03
		3	2.00e+00	3.55e+06	1.54e+03
		4	9.27e+01	2.64e+07	4.30e+02
50° C	9.30e+05	1	1.02e+00	8.24e+05	1.61e+03
		2	1.89e+01	8.35e+06	2.34e+02
		3	2.91e+00	2.00e+06	4.39e+02
		4	1.53e+03	3.15e+07	7.99e+00
60° C	7.32e+05	1	5.82e-01	3.86e+06	1.41e+03
		2	6.20e-01	4.63e+06	1.32e+03
		3	3.73e-01	6.06e+05	1.22e+03
		4	2.25e+01	2.67e+07	4.31e+02

BIBLIOGRAPHY

BIBLIOGRAPHY

[1] R. Chandra, S. P. Singh, and K. Gupta, "Damping studies in fiber-reinforced composites - a review," *Composite Structures*, vol. 46, no. 1, pp. 41–51, 1999.

[2] O. Younossi, M. V. Arena, R. M. Moore, M. Lorell, J. Mason, and J. C. Graser, "Trends in Technological Innovation," in *Military Jet Engine Acquisition: Technology Basics and Cost-Estimating Methodology*, ch. 3, pp. 25–40, Santa Monica, CA: RAND, 2002.

[3] R. Singh, "Process capability study of polyjet printing for plastic components," *Evolutionary Ecology*, vol. 25, no. 4, pp. 1011–1015, 2011.

[4] H. Bikas, P. Stavropoulos, and G. Chryssolouris, "Additive manufacturing methods and modeling approaches: A critical review," *International Journal of Advanced Manufacturing Technology*, vol. 83, no. 1-4, pp. 389–405, 2016.

[5] S. Laszlo and E. Shamonina, "Preface," in *Waves in Metamaterials*, pp. vii –ix, Oxford University Press, 2009.

[6] R. W. Ziolkowski and N. Engheta, "Introduction, History and Selected Topics in Fundamental Theories of Metamateraials," in *Metamaterials: Physics and Engineering Explorations* (N. Engheta and R. W. Ziolkowski, eds.), ch. 1, pp. 1–41, Hoboken, NJ: John Wiley & Sons, Inc, 2006.

[7] S. A. Cummer, J. Christensen, and A. Alù, "Controlling sound with acoustic metamaterials," *Nature Reviews Materials*, vol. 1, no. 3, p. 16001, 2016.

[8] R. Martínez-Sala, J. Sancho, J. V. Sánchez, V. Gómez, J. Llinares, and F. Meseguer, "Sound attenuation by sculpture," *Nature*, vol. 378, no. 6554, pp. 241–241, 1995.

[9] M. I. Hussein, M. J. Leamy, and M. Ruzzene, "Dynamics of Phononic Materials and Structures: Historical Origins, Recent Progress, and Future Outlook," *Applied Mechanics Reviews*, vol. 66, no. 4, p. 040802, 2014.

[10] G. W. Milton and J. R. Willis, "On modifications of Newton's second law and linear continuum elastodynamics," *Proceedings of the Royal Society A: Mathematical, Physical and Engineering Sciences*, vol. 463, no. August 2006, pp. 855–880, 2007.

[11] Z. Liu, X. Zhang, Y. Mao, Y. Y. Zhu, Z. Yang, C. T. Chan, and P. Sheng, "Locally Resonant Sonic Materials," *Science Reports*, vol. 289, no. 5485, pp. 1734–1736, 2000.

[12] X. Zheng, H. Lee, T. H. Weisgraber, M. Shusteff, J. DeOtte, E. C. Duoss, J. D. Kuntz, M. M. Biener, Q. Ge, J. A. Jackson, S. O. Kucheyev, N. X. Fang, and C. M. Spadaccini, "Ultralight, Ultrastiff Mechanical Metamaterials," *Science Reports*, vol. 344, no. 6190, pp. 1373–1378, 2014.

[13] R. Zhu, X. N. Liu, G. K. Hu, F. G. Yuan, and G. L. Huang, "Microstructural designs of plate-type elastic metamaterial and their potential applications: a review.," *International Journal of Smart & Nano Materials*, vol. 6, no. 1, pp. 14–40, 2015.

[14] K. K. Saxena, R. Das, and E. P. Calius, "Three Decades of Auxetics Research Materials with Negative Poisson's Ratio: A Review," *Advanced Engineering Materials*, pp. 1–24, 2016.

[15] H. Sun, X. Du, and P. F. Pai, "Theory of Metamaterial Beams for Broadband Vibration Absorption," *Journal of Intelligent Material Systems and Structures*, vol. 21, no. 11, pp. 1085–1101, 2010.

[16] P. F. Pai, "Metamaterial-based Broadband Elastic Wave Absorber," *Journal of Intelligent Material Systems and Structures*, vol. 21, no. 5, pp. 517–528, 2010.

[17] T. Igusa and K. Xu, "Wide-Band Response of Multiple Subsystems with High Modal Density," in *2nd International Conference on Stochastic Structural Dynamics*, pp. 131–145, 1990.

[18] T. Igusa and K. Xu, "Vibration Control Using Multiple Tuned Mass Dampers," *Journal of Sound and Vibration*, vol. 175, no. 4, pp. 491–503, 1994.

[19] H. Yamaguchi and N. Harnpornchai, "Fundamental Characteristics of Multiple Tuned Mass Dampers for Supressing Harmonically Forced Oscillations," *Earthquake Engineering and Structural Dynamics*, vol. 22, no. February 1992, pp. 51–62, 1993.

[20] J. P. DenHartog, *Mechanical Vibrations*. New York: McGraw-Hill, 1947.

[21] J. Q. Sun, M. R. Jolly, and M. A. Norris, "Passive, Adaptive and Active Tuned Vibration AbsorbersA Survey," *Journal of Vibration and Acoustics*, vol. 117, pp. 234 – 242, 1995.

[22] N. Hoang and P. Warnitchai, "Design of multiple tuned mass dampers by using a numerical optimizer," *Earthquake Engineering & Structural Dynamics*, vol. 34, no. 2, pp. 125–144, 2005.

[23] L. Zuo and S. A. Nayfeh, "Minimax optimization of multi-degree-of-freedom tuned-mass dampers," *Journal of Sound and Vibration*, vol. 272, pp. 893–908, 2004.

[24] Y. Xiao, J. Wen, and X. Wen, "Longitudinal wave band gaps in metamaterial-based elastic rods containing multi-degree-of-freedom resonators," *New Journal of Physics*, vol. 14, 2012.

[25] A. Banerjee, R. Das, and E. P. Calius, "Frequency graded 1D metamaterials: A study on the attenuation bands," *Journal of Applied Physics*, vol. 122, no. 7, p. 075101, 2017.

[26] Y. Shanshan, Z. Xiaoming, and H. Gengkai, "Experimental study on negative effective mass in a 1D mass-spring system," *New Journal of Physics*, vol. 10, pp. 0–11, 2008.

[27] H. H. Huang, C. T. Sun, and G. L. Huang, "On the negative effective mass density in acoustic metamaterials," *International Journal of Engineering Science*, vol. 47, no. 4, pp. 610–617, 2009.

[28] R. Zhu, G. L. Huang, H. H. Huang, and C. T. Sun, "Experimental and numerical study of guided wave propagation in a thin metamaterial plate," *Physics Letters A*, vol. 375, no. 30-31, pp. 2863–2867, 2011.

[29] G. Wang, X. S. Wen, J. H. Wen, and Y. Z. Liu, "Quasi-One-Dimensional Periodic Structure with Locally Resonant Band Gap," *Journal of Applied Mechanics*, vol. 73, no. 1, pp. 167–170, 2006.

[30] A. Qureshi, B. Li, and K. T. Tan, "Numerical investigation of band gaps in 3D printed cantilever-in- mass metamaterials," *Scientific Reports*, vol. 6, no. 28314, pp. 1–10, 2016.

[31] J. D. Hobeck, C. M. V. Laurant, and D. J. Inman, "3D Printing of Metastructures for Passive Broadband Vibration Suppression," in *20th International Conference on Composite Materials*, (Copenhagen), 2015.

[32] E. D. Nobrega, F. Gautier, A. Pelat, and J. M. C. Dos Santos, "Vibration band gaps for elastic metamaterial rods using wave finite element method," *Mechanical Systems and Signal Processing*, vol. 79, pp. 192–202, 2016.

[33] F. Liravi, R. Darleux, and E. Toyserkani, "Additive manufacturing of 3D structures with non-Newtonian highly viscous fluids: Finite element modeling and experimental validation," *Additive Manufacturing*, vol. 13, pp. 113–123, 2017.

[34] M. M. Francois, A. Sun, W. E. King, N. J. Henson, D. Tourret, C. A. Bronkhorst, N. N. Carlson, C. K. Newman, T. Haut, J. Bakosi, J. W. Gibbs, V. Livescu, S. A. Vander Wiel, A. J. Clarke, M. W. Schraad, T. Blacker, H. Lim, T. Rodgers, S. Owen, F. Abdeljawad, J. Madison, A. T. Anderson, J.-l. Fattebert, R. M. Ferencz, N. E. Hodge, S. A. Khairallah, and O. Walton, "Modeling of additive manufacturing processes for metals : Challenges and opportunities," *Current Opinion in Solid State & Materials Science*, pp. 1–9, 2017.

[35] J. Mueller, K. Shea, and C. Daraio, "Mechanical properties of parts fabricated with inkjet 3D printing through efficient experimental design," *Materials and Design*, vol. 86, pp. 902–912, 2015.

[36] Y. Zhang, L. Hao, M. M. Savalani, R. A. Harris, and K. E. Tanner, "Characterization and dynamic mechanical analysis of selective laser sintered hydroxyapatite-filled polymeric composites," *Journal of Biomedical Materials Research - Part A*, vol. 86, no. 3, pp. 607–616, 2008.

[37] Q. Ge, Y. Mao, K. Yu, M. L. Dunn, and H. J. Qi, "Active Composites and 4D Printing," in *20th International Conference on Composite Materials*, 2015.

[38] Y. Wang and D. J. Inman, "Finite element analysis and experimental study on dynamic properties of a composite beam with viscoelastic damping," *Journal of Sound and Vibration*, vol. 332, pp. 6177–6191, nov 2013.

[39] Y. Liu, J. Yi, Z. Li, X. Su, W. Li, and M. Negahban, "Dissipative elastic metamaterial with a low-frequency passband Dissipative elastic metamaterial with a low-frequency passband," *AIP Advances*, vol. 7, no. 065215, pp. 1–7, 2017.

[40] B. C. Essink and D. J. Inman, "Optimized 3D Printed Chiral Lattice for Broadband Vibration Suppresion," in *Topics in Modal Analysis & Testing*, vol. 10, pp. 205–214, 2016.

[41] T. Yu and G. A. Lesieutre, "Damping of Sandwich Panels via Acoustic Metamaterials," *AIAA Journal*, vol. 55, no. 4, pp. 1–13, 2017.

[42] T. Li, Y. Chen, X. Hu, Y. Li, and L. Wang, "Exploiting negative Poisson's ratio to design 3D-printed composites with enhanced mechanical properties," *Materials & Design*, vol. 142, pp. 247–258, 2018.

[43] M. L. Liu, K. K. Reichl, and D. J. Inman, "Complex Modulus Variation by Manipulation of Mechanical Test Method and Print Direction," in *Society of Engineering Mechanics Annual Conference*, (Indianapolis, IN), 2017.

[44] D. I. G. Jones, *Handbook of Viscoelastic Vibration Damping*. John Wiley & Sons, 2001.

[45] "Objet Connex 3D Printers," 2015.

[46] "Stratasys Digital Materials Data Sheet," 2015.

[47] "Stratasys PolyJet Materials Data Sheet," 2014.

[48] Q. Ge, H. J. Qi, and M. L. Dunn, "Active materials by four-dimension printing Active materials by four-dimension printing," *Applied Physics Letters*, vol. 103, no. 131901, pp. 1–5, 2013.

[49] Q. Ge, C. K. Dunn, H. J. Qi, and M. L. Dunn, "Active Origami by 4D Printing," *Smart Materials and Structures*, vol. 23, no. 094007, pp. 1–15, 2014.

[50] K. Yu, A. Ritchie, Y. Mao, M. L. Dunn, and H. J. Qi, "Controlled Sequential Shape Changing Components by 3D Printing of Shape Memory Polymer Multimaterials," *Procedia IUTAM*, vol. 12, pp. 193–203, 2015.

[51] R. A. DiTaranto, "Theory of vibratory bending for elastic and viscoelastic layered finite-length beams," *Journal of Applied Mechanics*, vol. 32, no. 4, pp. 881–886, 1965.

[52] M. J. Yan and E. H. Dowell, "Governing Equations for Vibrating Constrained-Layer Damping Sandwich Plates and Beams," *Journal of Applied Mechanics*, vol. 39, no. 4, pp. 1041–1046, 1972.

[53] R. A. Christensen, *Theory of Viscoelasticity*. New York: Academic Press, Inc., 1982.

[54] R. S. Lakes, "Introduction : Phenomena," in *Viscoelastic Materials*, ch. 1, pp. 1–13, New York, New York: Cambridge University Press, 2009.

[55] L. B. Eldred, W. P. Baker, and A. N. Palazotto, "Kelvin-Voigt vs Fractional Derivative Model as Constitutive Relations for Viscoelastic Materials," *AIAA Journal*, vol. 33, no. 3, pp. 547–550, 1995.

[56] C. D. Johnson, D. A. Kienholz, and L. C. Rogers, "Finite Element Prediction of Damping in Beam with Constrained Viscoelastic Layers," *The Shock and Vibration Bulletin*, vol. 51, 1981.

[57] C. D. Johnson and D. A. Kienholz, "Finite element prediction of damping in structures with constrained viscoelastic layers," *AIAA Journal*, vol. 20, no. 9, pp. 1284–1290, 1982.

[58] M. A. Trindade, A. Benjeddou, and R. Ohayon, "Modeling of frequency-dependent viscoelastic materials for active-passive vibration damping," *Journal of Vibration and Acoustics*, vol. 122, no. 2, pp. 169–174, 2000.

[59] R. L. Bagley and P. J. Torvik, "Fractional calculus - a different approach to the analysis of viscoelastically damped structures," *AIAA journal*, vol. 21, no. 5, pp. 741–748, 1983.

[60] R. L. Bagley and P. J. Torvik, "Fractional calculus in the transient analysis of viscoelastically damped structures," *AIAA Journal*, vol. 23, no. 6, pp. 918–925, 1985.

[61] G. A. Lesieutre and D. L. Mingori, "Finite element modeling of frequency-dependent material damping using augmenting thermodynamic fields," *Journal of Guidance, Control, and Dynamics*, vol. 13, pp. 1040–1050, nov 1990.

[62] D. F. Golla and P. C. Hughes, "Dynamics of Viscoelastic Structures - A Time-Domain, Finite Element Formulation," *Journal of Applied Mechanics*, vol. 52, pp. 897–906, dec 1985.

[63] D. J. McTavish and P. C. Hughes, "Finite Element Modeling of Linear Viscoelastic Structures," in *1987 ASME Design Technology 11th Biennial Conference on Mechanical Vibration and Noise*, pp. 9–17, 1987.

[64] D. J. Inman, "Vibration Analysis of Viscoelastic Beams by Seperation of Variables and Modal Analysis," *Mechanics Research Communications*, vol. 16, no. 4, pp. 213–218, 1989.

[65] M. I. Friswell, D. J. Inman, and M. J. Lam, "On the realisation of GHM models in viscoelasticity," *Journal of Intelligent Material Systems and Structures*, vol. 8, no. 1, pp. 986–993, 1997.

[66] M. I. Friswell and D. J. Inman, "Finite Element Models with Viscoelastic Damping," in *17th International Modal Analysis Conference*, (Orlando, Florida), pp. 181–187, 1999.

[67] M. J. Lam, W. R. Saunders, and D. J. Inman, "Modeling Active Constrained Layer Damping Using Golla-Hughes-McTavish Approach," *Smart Structures & Materials' 95*, vol. 2445, pp. 86–97, may 1995.

[68] A. M. G. de Lima, M. H. Stoppa, and D. A. Rade, "Finite Element Modeling of Structures Incorporating Viscoelastic Materials," in *21st International Modal Analysis Conference*, (Orlando, Florida), 2003.

[69] C. M. A. Vasques, R. A. S. Moreira, J. Dias Rodrigues, and J. D. Rodrigues, "Viscoelastic Damping Technologies-Part II: Experimental Identification Procedure and Validation.," *Journal of advanced Research in Mechanical Engineering*, vol. 1, no. 2, pp. 96–110, 2010.

[70] ASTM D5026 - 06, "Standard Test Method for Plastics : Dynamic Mechanical Properties : In Tension 1," 2014.

[71] ASTM D5418 - 15, "Standard Test Method for Plastics: Dynamic Mechanical Properties: In Flexure (Three-Point Bending)," 2007.

[72] ASTM E756 - 05, "Standard Test Method for Measuring Vibration-Damping Properties of Materials," 2010.

[73] D. J. Inman, *Vibration with Control*. West Sussex, England: John Wiley, 2nd ed., 2017.

[74] A. Preumont, *Vibration Control of Active Structures: An Introduction*, vol. 179. New York: Springer-Verlag, 2011.

[75] M. A. Trindade, A. Benjeddou, and R. Ohayon, "Piezoelectric Active Vibration Control of Damped Sandwich Beams," *Journal of Sound and Vibration*, vol. 246, no. 4, pp. 653–677, 2001.

[76] T. Hegewald and D. J. Inman, "Vibration Suppression Via Smart Structures Across a Temperature Range," *Journal of Intelligent Material Systems and Structures*, vol. 12, pp. 191–203, mar 2001.

[77] A. Baz, "Robust Control of Active Constrained Layer Damping," *Journal of Sound and Vibration*, vol. 2720, no. 3, pp. 467–480, 1998.

[78] C. Sugino, M. Ruzzene, and A. Erturk, "Dynamics of hybird mechanical-electromechanical locally resonant piezoelectric metastructures," in *ASME 2017 Conference on Smart Materials, Adaptive Structures and Intelligent Systems*, (Snowbird, UT), 2017.

[79] S. Xiao, G. Ma, Y. Li, Z. Yang, and P. Sheng, "Active control of membrane-type acoustic metamaterial by electric field," *Applied Physics Letters*, vol. 106, no. 091904, 2015.

[80] A. M. Baz, "With Tunable Effective Density," *Journal of Vibration and Acoustics*, vol. 132, no. 041011, 2010.

[81] Y. Y. Chen, G. L. Huang, and C. T. Sun, "Band Gap Control in an Active Elastic Metamaterial With Negative Capacitance Piezoelectric Shunting," *Journal of Vibration and Acousti*, vol. 136, no. 061008, 2014.

[82] H. T. Chen, W. J. Padilla, J. M. O. Zide, A. C. Gossard, A. J. Taylor, and R. D. Averitt, "Active terahertz metamaterial devices," *Nature*, vol. 444, pp. 597–600, 2006.

[83] M. Nouh, O. Aldraihem, and A. Baz, "Periodic Metamaterial Plates with Smart Tunable Local Resonators," *Intelligent Material Systems and Structures*, vol. 27, no. 13, 2016.

[84] G. Hu, L. Tang, A. Banerjee, and R. Das, "Metastructure With Piezoelectric Element for Simultaneous Vibration Suppression and Energy Harvesting," *Journal of Vibration and Acoustics*, vol. 139, no. 1, p. 011012, 2016.

[85] J. D. Hobeck and D. J. Inman, "Simultaneous passive broadband vibration suppression and energy harvesting with multifunctional metastructures," in *SPIE Smart Structures and Materials*, vol. 10172, p. 101720K, 2017.

[86] J. Li, X. Zhou, G. Huang, and G. Hu, "Acoustic metamaterials capable of both sound insulation and energy harvesting," *Smart Materials and Structures*, vol. 25, no. 5, p. 045013, 2016.

[87] C. J. Goh and T. K. Caughey, "On the stability problem caused by finite actuator dynamics in the collocated control of large space structures," *International Journal of Control*, vol. 41, no. 3, pp. 787–802, 1985.

[88] S. Poh and A. Baz, "Active Control of a Flexible Structure," *Journal of Intelligent Material Systems and Structures*, vol. 1, no. July, pp. 273–288, 1990.

[89] M. K. Kwak and S. Heo, "Active vibration control of smart grid structure by multiinput and multioutput positive position feedback controller," *Journal of Sound and Vibration*, vol. 304, no. 1-2, pp. 230–245, 2007.

[90] D. J. Leo, "Piezoelectric Materials," in *Engineering Analysis of Smart Material Systems*, ch. 4, pp. 122–204, Hoboken, New Jersey: John Wiley & Sons, 2007.

[91] D. J. Leo, "Active Vibration Control," in *Engineering Analysis of Smart Material Systems*, ch. 10, pp. 467–510, Hoboken, New Jersey: John Wiley & Sons, 2007.

[92] J. J. Dosch, D. J. Inman, and E. Garcia, "A Self-Sensing Piezoelectric Actuator for Collocated Control," *Journal of Intelligent Material Systems and Structures*, vol. 3, no. 1, pp. 166–185, 1992.

[93] L. Jones, E. Garcia, and H. Waitest, "Self-sensing control as applied to a PZT stack actuator used as a micropositioner," *Journal of Smart Materials and Structures*, vol. 3, pp. 147–156, 1994.

[94] A. M. Kabe and B. H. Sako, "Issues with Proportional Damping," *AIAA Journal*, vol. 54, no. 9, pp. 2864–2868, 2016.

[95] H. P. Menard, *Dynamic Mechanical Analysis: A Practical Introduction*. Boca Raton, FL: Taylor & Francis Group, 2nd ed., 2008.

[96] X. Liu and G. Hu, "Elastic Metamaterials Making Use of Chirality: A Review," *Journal of Mechanical Engineering*, vol. 62, no. 7-8, pp. 403–418, 2016.

[97] K. K. Reichl and D. J. Inman, "Lumped Mass Model of a 1D Metastructure for Vibration Suppression with no Additional Mass," *Journal of Sound and Vibration*, vol. 403, pp. 75–89, 2017.

[98] ASTM D5026, "Standard Test Method for Measuring the Plastics : Dynamic Mechanical Properties of Plastics in Tension Properties : In Tension 1," Tech. Rep. November, ASTM, 2001.

[99] G. A. Lesieutre and U. Lee, "A finite element for beams having segmented active constrained layers with frequency-dependent viscoelastics," *Smart Materials and Structures*, vol. 5, pp. 615–627, oct 1996.

[100] G. A. Lesieutre, E. Bianchini, and A. Maiani, "Finite element modeling of one-dimensional viscoelastic structures using anelastic displacement fields," *Journal of Guidance Control and Dynamics*, vol. 19, no. 3, pp. 520–527, 1996.

[101] D. J. McTavish and P. C. Hughes, "Modeling of Linear Viscoelastic Space Structures," *Journal of Vibration and Acoustics*, vol. 115, pp. 103–110, jan 1993.

[102] D. J. McTavish and P. C. Hughes, "Finite element modeling of linear viscoelastic structures: the GHM method," in *33rd AIAA/ASME/ASCE/AHS/ASC Structures, Structural Dynamics and Materials Conference*, pp. 1753–1763, 1992.

[103] K. K. Reichl and D. J. Inman, "Dynamic Mechanical and Thermal Analyses of Objet Connex 3D Printed Materials," *Experimental Techniques*, vol. 42, pp. 19–25, 2018.

[104] K. K. Reichl and D. J. Inman, "Constant Mass Metastructure with Vibration Absorbers of Linearly Varying Natural Frequencies," in *35th International Modal Analysis Conference*, vol. 10, (Garden Grove, CA), pp. 153–158, 2017.

[105] K. K. Reichl and D. J. Inman, "Active Vibration Control and Metastructures," in *27th International Conference on Adaptive Structures and Technologies*, (Lake George, NY), 2016.

[106] R. E. Skelton and P. C. Hughes, "Modal cost analysis for linear matrix-second-order systems," *Journal of Dynamic Systems, Measurement, and Control*, vol. 102, no. 3, pp. 151–158, 1980.

[107] R. E. Skelton, *Dynamic Systems Control: Linear Systems Analysis and Synthesis*. John Wiley & Sons, 1988.

[108] A. Erturk and D. J. Inman, "Numerical Data for PZT-5A and PZT-5H Piezoceramics," in *Piezoelectric Energy Harvesting*, ch. Appendix E, pp. 373–374, West Sussex, England: John Wiley & Sons, 2011.

[109] D. J. Leo, "Piezoelectric material systems," in *Engineering Analysis of Smart Material Systems*, ch. 5, pp. 205–297, Hoboken, New Jersey: John Wiley & Sons, 2007.